Distortion Control during Welding

PROEFSCHRIFT

ter verkrijging van de graad van doctor
aan de Technische Universiteit Delft;
op gezag van de Rector Magnificus prof.ir. K.C.A.M. Luyben;
voorzitter van het College voor Promoties
in het openbaar te verdedigen op maandag 20 oktober 2014 om 15.00 uur

door

Amir Masoud AKBARI PAZOOKI

Master of Science in Material Science and Engineering
University of Tehran, Iran
Geboren te Tehran, Iran

Dit proefschrift is goedgekeurd door de promotor:
Prof.dr. I.M. Richardson

Copromotor: Dr.ir. M.J.M. Hermans

Samenstelling promotiecommissie:

Rector Magnificus,	voorzitter
Prof.dr. I.M. Richardson,	Technische Universiteit, Delft, promotor
Dr.ir. M.J.M. Hermans,	Technische Universiteit, Delft, copromotor
Prof.dr.ir. R. Benedictus,	Technische Universiteit, Delft
Prof.dr.ir. C. van Rhee,	Technische Universiteit, Delft
Prof.dr.ir. A. van Keulen,	Technische Universiteit, Delft
Prof.dr.ir. F.S.K. Bijlaard,	Technische Universiteit, Delft
Dr.ir. T. van der Veldt,	Tata Steel, RD&T, IJmuiden

Dr.ir. M.J.M. Hermans, heeft als begeleider in belangrijke mate aan de totstandkoming van het proefschrift bijgedragen.

Distortion Control during Welding
A.M.A.Pazooki
PhD thesis of Delft University of Technology - with summary in Dutch
ISBN 978-94-91909-18-4

Key words: Welding Distortion, Residual Stress, Thermal Tensioning, Side Heating, Numerical Modelling;

masoud.pazooki@gmail.com

Printed in The Netherlands.

Distortion Control during Welding

Amir Masoud AKBARI PAZOOKI

The research described in this thesis was performed in the department of Material Science and Engineering, Faculty of 3mE, Delft University of Technology, Mekelweg 2, 2628 CD, Delft, The Netherlands.

This research was carried out as part of the innovation program of the Materials innovation institute (M2i) (formerly, the Netherlands Institute for Metals Research) on Distortion Control during Welding, project number MC8.06252.

To my beloved late grandparents

Contents

Nomenclature

Symbol	Description	Units
$\mathbf{1}$	Forth order elasticity tensor	[Pa]
a	Half width of Goldak's double ellipsoid model	[m]
b	Depth of Goldak's double ellipsoid model	[m]
B_L	Length of the burners	[m]
B_s	Band width of the additional heating	[m]
c_1, c_2	Length of Goldak's double ellipsoid model	[m]
c_t	Temperature rate	[K s^{-1}], [^{o}C s^{-1}]
c , C_p	Heat capacity	[J kg^{-1} K^{-1}]
$\boldsymbol{C_p}$	Heat capacity matrix	[J kg^{-1} K^{-1}]
C_1 and C_2	Material constants	[K Pa^{-1}]
d_s	Hardening slope	[-]
d	Grain size	[m]
d_{tr}	Strain rate tensor due to phase transformation	[s^{-1}]
d_{hkl}	Distance between the (hkl) lattice-planes	[$\AA$]
$d_{0,hkl}$	Stress free lattice spacing	[$\AA$]
$\boldsymbol{d}$	Strain rate tensor	[s^{-1}]
$\boldsymbol{d^{elastic}}$	Elastic strain rate tensor	[s^{-1}]
$\boldsymbol{d^{plastic}}$	Plastic strain rate tensor	[s^{-1}]
$\boldsymbol{d^{thermal}}$	Thermal strain rate tensor	[s^{-1}]
$\boldsymbol{d^{phasetrans}}$	Phase transformation strain rate tensor	[s^{-1}]
D	Nozzle diameter	[m]
E	Effective power	[W]
$\boldsymbol{E}$	Fourth order elasticity tensor	[Pa]
f_1	Fraction of heat deposited at the leading part of the heat source	[-]
f_2	Fraction of heat deposited at the trailing part of the heat source	[-]
h	Planck's constant	[m^2 kg s^{-1}]
h_r	Heat transfer coefficient by radiation	[W m^{-2} K^{-1}]
h_c	Heat transfer coefficient by conduction	[W m^{-2} K^{-1}]
$h_{contact}$	Heat transfer coefficient due to contacts	[W m^{-2} K^{-1}]

$\dot{H}$	Enthalpy rate	[J kg^{-1} s^{-1}]
H, H$_1$	Enthalpy of system	[J kg^{-1}]
I	Welding current	[A]
j	Number of nozzles	[-]
k$_y$	Hall-Petch constant	[Pa m$^{-0.5}$]
k$_a$	Thermal diffusivity	[m^2 s^{-1}]
K$_s$	Spring stiffness	[N m^{-1}]
K$_t$	Plastic viscosity	[Pa s]
L	Distance to the centre of the heat source	[m]
L$_0$	Initial length	[m]
L$_s$	Additional heat source length	[m]
L$_1$	Distance from source to sample	[m]
L$_2$	Distance from sample to detector	[m]
m	Visco-plastic exponent	[-]
m$_n$	Neutron mass	[kg]
n	Exponent of phase kinetics, Avrami exponent	[-]
ND	Inter-distance of the nozzles	[m]
p	Plastic strain	[-]
q , q$_f$	Heat flux	[W m^{-2}]
q$_{radiation}$	Heat loss by radiation	[W m^{-2}]
q$_{convection}$	Heat loss by convection	[W m^{-2}]
q$_{contact}$	Heat loss by contact	[W m^{-2}]
q$_{front}$, q$_{rear}$	Heat flux per volume	[W m^{-3}]
q$_{max}$	Peak value of the Gaussian heat flux distribution	[W m^{-2}]
$\boldsymbol{q}$	Heat flux vector	[W m^{-2}]
Q	Power of heat source	[W m^{-3}]
Q$_{total}$	Total power in welding with additional heating	[W]
Q$_s$	Additional heating power	[W]
r	Radius of Gaussian distribution	[m]
r	Saturation exponent	[-]
r$_{flame}$	Flame radius	[m]
S	Hardening saturation	[Pa]
S$_{x1}$, S$_{x2}$, S$_{z1}$, S$_{z2}$	Parameters used to control the gradient of the heat flux at the side heater edges	[mm^{-1}]
t, t$_{hkl}$	Time	[s]
T	Temperature	[K], [^{o}C]
T$_0$	Initial temperature	[K], [^{o}C]
T$_\infty$	Ambient temperature	[K], [^{o}C]
T$_{A_1}$	A$_1$ temperature	[K], [^{o}C]
T$_{A_3}$	A$_3$ temperature	[K], [^{o}C]
T$_{M_s}$	Martensite start temperature	[K], [^{o}C]
T$_p$	Peak temperature	[K], [^{o}C]

U	Arc voltage	[V]
$\boldsymbol{u}$	Displacement vector	[m]
α , α_T	Thermal expansion coefficient	[^{o}C^{-1}]
ε	Strain	[-]
ε_{th}	Thermal strain	[-]
ε_{hkl}	Strains related to plane (hkl)	[-]
ε_m	Emissivity	[-]
$\boldsymbol{\varepsilon}$	Strain tensor	[-]
$\boldsymbol{\varepsilon^{elastic}}$	Elastic strain tensor	[-]
$\boldsymbol{\varepsilon^{plastic}}$	Plastic strain tensor	[-]
$\boldsymbol{\varepsilon^{Thermal}}$	Thermal strain tensor	[-]
$\boldsymbol{\varepsilon^{phasetrans}}$	Phase transformation strain tensor	[-]
γ	Width factor	[m^{-2}]
η	Heat source efficiency (side heating sources/welding torch)	[-]
$\boldsymbol{\lambda}$	Matrix for coefficients of thermal conductivity	[W m^{-1} K^{-1}]
λ	Thermal conductivity	[W m^{-1} K^{-1}]
λ_r	X-ray wavelength	[$\mathring{A}$]
υ_s	Velocity	[m s^{-1}]
ν	Poisson ratio	[-]
ρ	Material density	[kg m^{-3}]
ρ^i	Density of phase fraction i	[kg m^{-3}]
σ_B	Stefan-Boltzmann constant	[Wm^{-2} K^{-4}]
σ	Stress	[Pa]
$\boldsymbol{\sigma}$	Cauchy stress tensor	[Pa]
σ_y	Yield stress	[Pa]
σ_s , σ_R	Ultimate residual stress	[Pa]
σ_0	Hall-Petch constant	[Pa]
$\sigma_{I,II,III}$	Residual stress level 1 or 2 or 3	[Pa]
$\bar{\sigma}$	von Mises effective stress	[Pa]
σ_m	Mean stress	[Pa]
τ	Time constant related to phase growth	[s]
θ	Diffraction angle	[^{o}]
ϕ_2	Distance of the heaters to the weld line	[m]
$\dot{\phi}^i$	Phase fraction rate	[s^{-1}]
ϕ	Volumetric fraction of the considered phase	[-]
$\bar{\phi}$	Volumetric equilibrium phase fraction	[-]
ϕ_0	Volumetric initial phase fraction	[-]
$\phi^{\gamma}_{M_s}$	Volumetric fraction of austenite present at T$_{Ms}$	[-]
ϕ^m	Volumetric fraction of martensite	[-]
ϕ_i	Volumetric fraction of phase i	[-]
ψ, ϕ	Angle	[^{o}]

Abbreviation	Meaning
AC	Alternating Current
AHSS	Advanced High Strength Steel
AWS	American Welding Society
BCC	Body Centre Cubic
BOP	Bead-On-Plate
CBL	Critical Buckling Load
CCT	Continuous Cooling Transformation
CONV	Conventional welding
DC	Direct current
DIC	Digital Image Correlation
DIN	Deutsches Institut für Normung
DSNS	Damen Schelde Naval Shipyard
EDM	Electronically Discharge Machining
EWI	Edison Welding Institute
EXP	Experiment
FCC	Face Centre Cubic
FDM	Finite Difference Method
FEM/FE	Finite Element Model/Modeling
FWHM	Full Width at Half Maximum
GMAW	Gas Metal Arc Welding
GTAW	Gas Tungsten Arc Welding
HAZ	Heat Affected Zone
JMAK	Johnson-Mehl-Avrami-Kolmogorov
KM	Koistien and Marburger
LLB	Laboratoire Leon Brillouin
ND	Neutron Diffraction
NUM	Numerial Modelling
PSI	Paul Scherrer Institute
PSR	Plastic Strain Reset
SAW	Submerged Arc Welding
SH	Side Heating
TOF	Time Of Flight
TT	Thermal Tensioning
TTT	Transient Thermal Tensioning
TTT	Time Temperature Transformation
UTS	Ultimate Tensile Stress

Chapter 1

Introduction

1.1 Welding residual stress, distortion and mitigation methods

The locally introduced heating and cooling cycle of welding generates residual stresses and distortion [1]. During the Second World War, more than 1000 structural failures, related to welding, were found in over 5000 merchant ships built in the USA [2]. The fracturing of the Schenectady T-2 tanker is an example of such a failure, which is shown in **Figure 1.1** [3]. This oil tanker was the largest "navy oiler" at that time. The cause of the failure was the poor weld quality, combined with the presence of stress concentrations and low fracture toughness. After the Second World War, especially in the 1950s and 1960s research on welding residual stress and distortion was intensified to obtain a better understanding of these phenomena [2]. Later the advent of computational systems and the development of new computational methods, gave a boost in welding stress and distortion analysis. Nowadays, new techniques are being developed and introduced to industry, which are able to reduce and/or redistribute residual stress and mitigate distortion.

Figure 1.1. *T-2 tanker fractured in 1943 [3].*

Residual stresses are those that exist in a material without any external load. A common classification of welding residual stresses is based on their direction with respect to the weld centre line. In this regard, longitudinal, transverse and through thickness residual stresses can be defined. Welding distortion is the final permanent plastic deformation (or instability) due to processing of the workpiece by welding. Some examples of such deformations are bending distortion, buckling, longitudinal shrinkage and transverse shrinkage. Residual stresses and distortion are strongly linked as depicted in **Figure 1.2** [4]. In the case in which the distortion of a work piece is restricted by constraints (*i.e.* clamps or the construction), the residual stress levels will generally be high, whereas if the workpiece is allowed to move freely and distort, stresses will relax and will be lower.

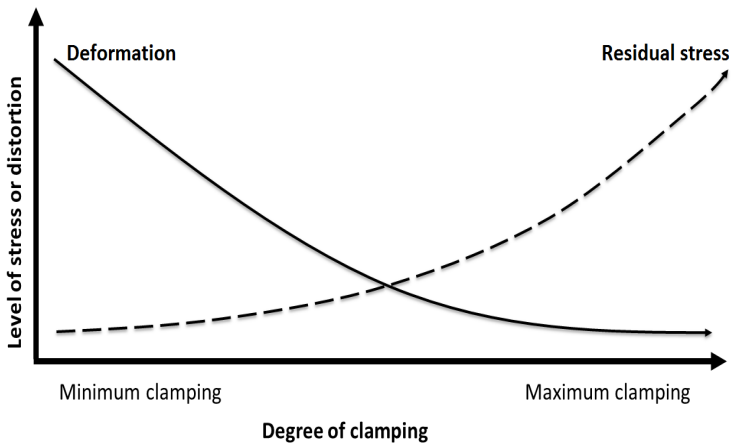

Figure 1.2. *The relationship between the level of stress and distortion and degree of clamping, adopted from [4].*

Many methods have been proposed and demonstrated by researchers [5-14] to control both residual stress and distortion, most of which are focused on distortion reduction. The selection of a suitable distortion mitigation method depends on the type of distortion.

A number of different classifications exists for distortion mitigation methods, but one of the most commonly used is based on the time during the manufacturing process when the technique is applied; *i.e.* pre-welding methods, post-welding methods and *in-situ* welding techniques.

Thermal Tensioning (TT) describes a group of *in-situ* methods to control welding distortion. In these methods local heating and/or cooling strategies are applied during welding. Additional heating and/or cooling sources can be implemented that are either stationary or transient. In static methods, a pre-set temperature distribution is imposed on the workpiece, while in transient methods, the temperature depends on position and time.

Although, many investigations related to thermal tensioning during welding (either with stationary or with moving sources) have been performed [15-17], a clear and uniform classification of different thermal tensioning methods is absent and not formalized. The names used and the classifications are mainly based on the mechanisms of distortion reduction in thermal tensioning.

In thermal tensioning with a cooling source, an active cooling source trails the welding heat source at a short fixed distance. The mitigation of residual stresses and distortion by means of active cooling during welding has been studied and demonstrated by van der Aa [18]. The results of the research showed that active cooling during welding changes the temperature profile around the weld. This modifies the stress state in such a way that the compressive stresses near the plate edges are reduced, thereby decreasing buckling distortion in welded plates considerably. A significant reduction of distortion upon welding of stainless steel sheet was achieved. Although the understanding of the phenomena related to the development of residual stresses in and around the weld and the influence of active cooling on the stress level and distribution has been improved, cooling can induce significant instability in the heat source, rendering the weld quality unacceptable. Thermal tensioning can be applied using additional heating sources or a combination of both heating and cooling sources. This latter method is known in the shipbuilding industry, where flame heating is combined with water cooling, causing mitigation of longitudinal residual stresses after welding [19].

The focus of the research presented in this thesis, is on Thermal Tensioning using additional heating sources and can be classified into two types, Transient Thermal Tensioning (TTT) and Side Heating (SH). The position of the heat sources in TTT is close to the weld centre line. The thermal field generated by the additional heaters

in TTT influences the thermal field generated by the arc. In contrast, in side heating the additional heaters are located further away from the weld and the thermal field induced by welding is not affected by the field generated by the additional heat sources.

Although, it is shown experimentally and numerically that thermal tensioning using additional heat sources is capable of producing welded plates with reduced distortion, the mechanisms of the process are still not completely understood.

1.2 Industrial valorisation

Over the past decade, designers in the transport industries have developed thinner lightweight steel structures to reduce weight and thereby reduce the consumption of energy. A good example can be found in the shipbuilding industry, where **Figure 1.3** shows the percentage of thin steel (10 mm or less) to thick-plate structures for vessels built at Northrop Grumman Ship Systems as a function of time [17].

Welding is a vital joining process in shipbuilding for a number of reasons including the ease of obtaining water and oil tightness and structural integrity using welded joints. The use of thinner sheets increases the production rates and results in a significant reduction in hull weight [20].

However, thin sheets deform more easily during welding. Welding distortion is a real quality concern for manufacturers of naval ships since welding distortion directly influences the performance (*e.g.* radar cross section) of the ship. Therefore, costly post weld treatments like flame straightening are often required and applied. Any possibility to avoid or reduce welding distortion will lead to cost-savings and thus to a clear economic advantage and will improve competitiveness. As an example, Romero [21] reports that rework can involve up to 20% of personnel time in the total metal working activities in shipbuilding, see **Figure 1.4** [21].

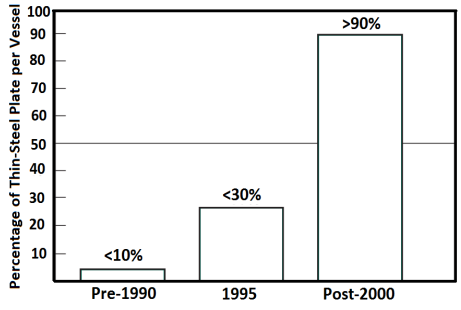

Figure 1.3. *The percentage of thin steel (10 mm or less) to thick-plate structures for some vessels built at Northrop Grumman Ship Systems [17].*

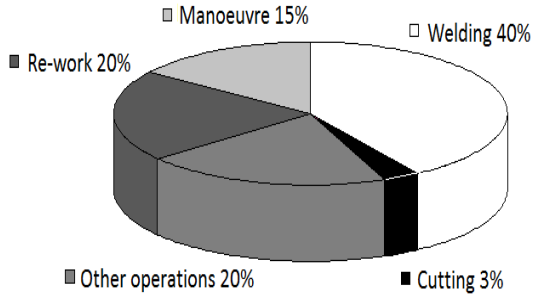

Figure 1.4. *Metalworking time required for building a large ship [21].*

In addition to the shipbuilding industry, steel producers have been attempting to improve strength and weight of plates used for automotive applications. Advanced High Strength Steel (AHSS) has been developed for such applications. For example, the Ford Motor Company uses Advanced High Strength Steel (AHSS) in the Ford 500 model shown in **Figure 1.5** [22]. The thin steel sheets have the necessary combination of strength and ductility but both welding distortion and welding residual stresses are challenges in the application of these materials.

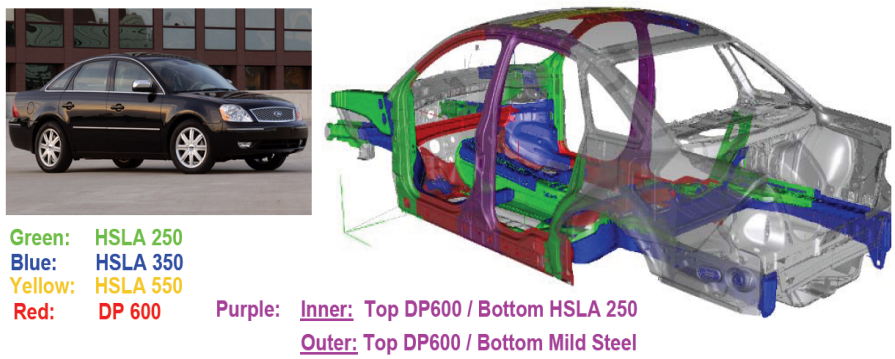

Figure 1.5. *Ford Motor Company usage of Advanced High Strength Steel (AHSS) in the Ford 500 model [22].*

1.3 Objectives and scope of the work

The motivation for this research is the need for a better understanding of what takes place in thermal tensioning using additional heating sources and what mechanisms are responsible for the reduction of welding distortion in this process. The main objective of the research is:

to increase the general understanding of distortion reduction mechanisms using thermal tensioning with additional heat sources during welding of steel;

To gain knowledge concerning distortion reduction mechanisms, the following sub-tasks are defined:

- to construct and develop two and three dimensional numerical models for the prediction of the thermal, metallurgical and mechanical behaviour of welds with thermal tensioning;
- to validate the models by experiments; in this sub-task, the development of a welding arrangement with thermal tensioning using additional heat sources is included;
- to investigate the influence of thermal tensioning on the microstructure and residual stress state of the welded samples;
- to investigate the mechanisms responsible for distortion reduction in thermal tensioning with additional heat sources using validated models.

The knowledge obtained is used for an industrial case.

1.4 Relevance and valorisation of this research

As described before, a number of mitigation techniques have been developed over the last decade. Published literature indicates the promising results of heating and cooling strategies, both from an experimental and a numerical point of view. The introduction of these techniques in industry is however limited. The reason for this delay is that the robustness of the techniques cannot always be guaranteed due to the large number of process parameters and the fact that not all parameters are fully evaluated. Furthermore, not all mechanisms involved on the interactions between these mechanisms are completely understood. For instance, the application of active cooling is hampered by the fact that arc instabilities reduce the weld quality and the fast cooling rates can negatively affect the development of the microstructure in ferritic steels. Thermal tensioning using additional heat sources could be favourable when welding steel plate, as cooling rates are reduced and the tendency toward formation of martensite is decreased. Furthermore, in industry, experience is available concerning the use of heating sources (burners for flame straightening), whereas familiarity with cryogenic conditions is, in general, limited.

1.5 Research approach

Due to the complex nature of welding and welding with additional heat sources, the experimental investigation of the processes cannot provide enough information about what is really going on, and the main reasons for distortion reduction. Moreover, a large number of experiments are required to cover all aspects involved in the processes. Experimental information related to stress and strain development during

both conventional welding and welding with additional heating is limited. For such reasons, a numerical approach combined with experimental validation has been used in this thesis. The numerical approach involves the modelling of thermal, microstructural and mechanical fields during conventional welding and welding with additional heat sources. This numerical approach has been validated by some dedicated experiments such as temperature measurements, distortion measurements, microstructure and material related analysis and residual stress determinations.

As the project is closely related to industrial partners (Damen Schelde Naval Shipyard [23] and Tata steel [24]), three case studies are defined for laboratory tests and one for industrial demonstration. The cases are selected in such a way that the complexity of the problem is disentangled. The cases are summarized as follows:

- *Case I, Set A and B (AISI-316L)*: The two sets involve AISI-316L stainless steel sheets with the dimensions of 200×100×1.5 mm^3 and 500×250×2 mm^3 respectively. The first set (set A) is used for preliminary welding (bead on plate) with additional heating experiments. The final tests were carried out using the larger plates (set B) and the Gas Tungsten Arc Welding (GTAW) process was applied. The benefit in this case is that the material does not undergo any solid state phase transformations.

- *Case II, Set A and B (DP600)*: Two different plate dimensions were used for the experiments on dual phase steel: 200×100× 1.5 mm^3 and 500×250×2 mm^3. The effects of solid state phase transformations on the residual stress and distortion were investigated numerically and experimentally in set A. Welding with additional heating experiments were performed with set B. The main difference between Case I and II is related to solid state phase transformations which occur in dual phase steels during the heating and cooling cycles. For all situations, the GTAW process was used.

- *Case III (AH36)*: In this case, AH36 steel plates with dimensions of 500×250×6 mm^3 were used. Similar to Case II, solid state phase transformations occur during welding of the plates. The use of filler metal is required and Gas Metal Arc Welding (GMAW) is employed.

- *Industrial implementation case*: In order to investigate the welding with additional heat sources in a real industrial environment, AH36 plates with dimensions of 3600×600×6 mm^3 were used. The experiments were performed at Damen Schelde Naval Shipyard (DSNS), where Submerged Arc Welding (SAW) was used to produce the welds.

1.6 Structure of the thesis

The results of the investigations described in this thesis, span 9 chapters. Following this introductory chapter, the state-of-the-art with regard to the origins of stresses,

welding residual stresses, welding distortion and methods to control residual stress and distortion, in-process methods and thermal tensioning processes are described in **Chapter 2**. The modelling approach adopted is described in **Chapter 3**. This chapter contains a description of the three fields involved in the simulations; *i.e.* the thermal, the microstructural and the mechanical fields. The experimental set-up used in both conventional welding and welding with additional heat sources is discussed in **Chapter 4**. In **Chapters 5** the experimental results for thermal, microstructure, distortion and residual stress fields are shown. The results are not only useful to investigate the parameters involved in the processes (conventional welding and welding with additional heating), but are also used to validate the numerical models. The modelling results are compared to the experimental results in **Chapters 6**. The validated numerical models at this stage are used to understand both processes and to predict the out-of-plane deformation of plates in different situations. After comparing the conventional welding model and the welding with additional heating model, mechanisms responsible for distortion reduction in thermal tensioning are then proposed. The industrial implementation is presented in **Chapter 7**. A detailed general discussion is provided in **Chapter 8** and finally in **Chapter 9** general conclusions are presented including a number of recommendations for future research.

Reference

[1] K. Masubuchi, *Analysis of welded structures*, Pergamon Press, USA, 1980.

[2] L. Troive, *Deformations and stresses in welded pipes*, PhD thesis, Lulea University of Technology, Sweden, 1996.

[3] http://en.wikipedia.org/wiki/T2-tanker.

[4] H. Porzner, *Possibilities of Numerical Simulation for Evaluation and Optimisation of Welded Designs. Principles*, Mathematical Modelling of Weld Phenomena 5, Seggau, Graz, Austria, pp. 701-724, 2001.

[5] S. W. Williams, S. A. Morgan, A. Wescott, M. Poad and S. W. Wen, *Stress engineering, control of residual stresses and distortion in welding*, Proceedings of 2nd International Workshop on Thermal Forming and Welding Distortion IWOTE 2008, Bremen, pp. 229-239, 2008.

[6] W. Liu, X. Tian and X. Zhang, *Preventing weld hot cracking by synchronous rolling during welding*, Welding Research Supplement, pp. 297s-304s, 1996.

[7] W. Xu, C. Fan, H. Fang and X. Tian, *New development in welding thin-shell aluminium alloy structures with high strength*, China Welding, Vol. 13, No. 1, pp. 27-30, 2004.

[8] C. Fan, H. Fang, J. Tao and X. Wang, *Strain field analysis of welding with trailing impact rolling for reduction of residual stress and distortion and prevention of hot*

cracking, Transactions of the China Welding Institution (in Chinese), Vol. 25, No. 6, pp. 47-50, 2004.

[9] C. Fan, H. Fang, J. Tao, Y. Tian and M. Li, *Weld with trailing impact rolling to control the residual distortion of the thin-walled planar circumferential weldment*, Journal of Harbin Engineering University (in Chinese), Vol. 26, No. 2, pp. 238-241, 2005.

[10] Q. Guan, *A few issues with promoting application of weld rolling process*, Aeronautical Process Technology (in Chinese), Vol. 2, pp. 21-26, 1980.

[11] Q. Guan, *Development of weld mechanics and distortion control in aircraft thin-shell structures*, Proceedings of the 8th National Congress of Welding (in Chinese), Publisher of Chinese Mechanical and Machinery Industry, Vol. 1, pp. 51-57, Beijing, 1997.

[12] Q. Guan, C. X. Zhang and D. L. Guo, *Dynamic Control of Welding Distortion by Moving Spot Heat Sink (Controle dynamique des deformations lors du soudage grace a un puits thermique mobile)*, Welding in the World, Vol. 33, No. 4, pp. 308-313, 1994.

[13] Q. Guan, C. X. Zhang and D. L. Guo, *Dynamically Controlled Low Stress No Distortion Welding Method and its Facility*, Chinese patent No. 93101690.8, 1993.

[14] F. Soul and Z. Yanhua, *Numerical analysis of stresses and strain behaviour in trailing heat sink mitigation technique*, Materials Science and Technology, Vol. 4, pp. 15-28, 2005.

[15] P. Michaleris, and X. Sun, *Finite Element Analysis of Thermal Tensioning Techniques Mitigating Weld Buckling Distortion*, Welding Journal, Vol. 76, No. 11, pp. 451s-457s, 1997.

[16] M. V. Deo and P. Michaleris, *Mitigation of welding induced buckling distortion using transient thermal tensioning*, Science and Technology of Welding and Joining, Vol. 8, No. 1, pp. 49-54, 2003.

[17] T. D. Huang, R. Dull, C.Conrardy, N. Porter, L. DeCan, N. Evans, A. Davis, L. Kvidahl and P. Keene, *Transient Thermal Tensioning and Prototype System Testing of Thin Steel Ship Panel Structures*, Journal of Ship Production, Vol. 24, No. 1, pp. 25-36, 2008.

[18] E. M. van der Aa, *Local cooling during welding: Prediction and control of residual stresses and buckling distortion*, PhD thesis, Delft University of Technology, 2007.

[19] D. Radaj, *Heat Effects of Welding: temperature field, residual stress, distortion*, Springer-Verlag, 1992.

[20] D. J. Eyres, *Ship Construction*, Elsevier Ltd, 2007.

[21] P. Romero, N. Otero, A. Lopez, J. Otero, *Experimental comparison and analytical modelling of different industrial heating sources for thermal forming*, Proceedings of 3rd International Workshop on Thermal Forming and Welding Distortion IWOTE 2011, Bremen, pp. 121-132, 2011.

[22] http://www.autosteel.org//AM/Template.cfm?Section=Automotive2

[23] http://www.schelde.com/

[24] http://www.tatasteel.nl/

Chapter 2

Welding residual stress, distortion and control methods

Welding involves local heating and cooling of the workpiece. During the heating and the cooling cycles, the material experiences non-uniform expansion and contraction. Furthermore, the material might undergo plastic deformation, phase transformations, recovery and recrystallization. All these phenomena, in combination with the constraints imposed, contribute to the formation of stresses within the workpiece, which may cause permanent welding distortion.

In this chapter a theoretical background is presented on residual stresses and distortion in welding. This overview includes the classification and the origin of welding induced residual stresses and distortion as well as the transient behaviour of these stresses during welding. Furthermore, methods for controlling both residual stress and distortion are presented. In **Section 2.4**, a more detailed description is given on the thermal tensioning distortion mitigation technique.

2.1 Welding residual stresses

Residual stresses are the stresses existing in a material, when no external loads act on the material [1]. These stresses are often referred to as internal stresses or inherent stresses [2]. It is important to note that internal stresses are already introduced by fabrication processes. Subsequent treatments like welding and peening may redistribute and alter the stress state. When, no external loads are present, the resultant forces and the moments of these forces should be zero for any cross section in the material.

Residual stresses can be classified according to the length scale over which they are acting. Three types of stresses, shown schematically in **Figure 2.1** [3], can be distinguished being:

- *Type I or first order stresses (σ_I)* cover residual macro-stresses. The length scale in this category should be large enough to cover all phases present in the material and should contain a sufficient number of crystallites. Releasing this type of stress causes macroscopic shape changes of the material [3].
- *Type II or second order stresses (σ_{II})* act between adjacent grains and are referred to as micro-stresses. In the case that there are deformation gradients introduced between neighbouring grains, this type of residual stress will be generated. The release of this type of stress also causes macroscopic distortions [3].
- *Type III or third order stresses (σ_{III})* act on an inter-atomic level within individual grains. Substitution atoms, vacancies, dislocations or coherent precipitates generate such stress fields. The release of this type of stress will not result in a macroscopic distortion [3].

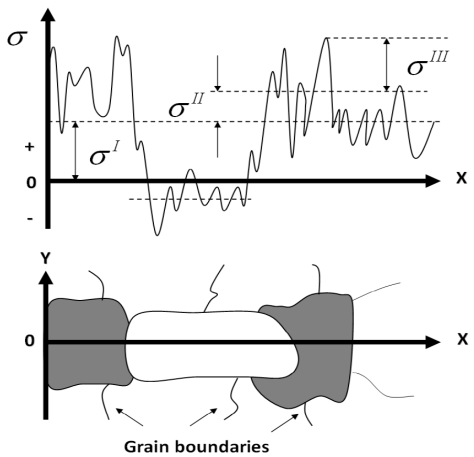

Figure 2.1. *The classification of residual stresses based on length scale, adopted from [3].*

The classification mentioned above is based on the length scale and not on the magnitude of the stresses. The ultimate residual stress (σ_R) in a material is the sum of σ_I, σ_{II} and σ_{III} stresses:

$$\sigma_R = \sigma_I + \sigma_{II} + \sigma_{III}. \tag{2.1}$$

Residual stresses will also develop in materials during welding, *i.e.* residual welding stresses, where the classification mentioned above is also valid. Apart from the order, a common classification of residual welding stresses is based on the direction of the residual stresses compared to the welding direction, as can be seen in **Figure 2.2**. If

the residual stresses are parallel to the welding direction, they are called longitudinal residual stresses, while traverse residual stresses are the residual stresses perpendicular to the welding direction and in the plane of the workpiece. Normal stresses (or through-thickness stresses) are perpendicular to both the welding direction and the plane of the workpiece. The through-thickness stresses are assumed to be of minor importance in thin material, since both top and bottom surfaces of the material experience more or less a similar thermal cycle during welding. For thick plates, normal stresses are responsible for deformation, due to a significant temperature gradient in the thickness direction.

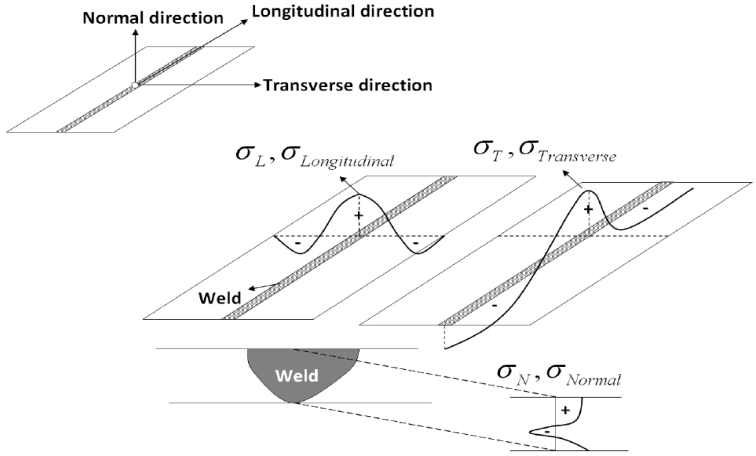

Figure 2.2. *Schematic representations of longitudinal (L), transverse (T) and normal (N) residual welding induced stresses. A positive sign indicates tensile and a negative sign indicates compressive stresses. Adopted from [1].*

2.1.1 Origin of residual welding stresses

The origin of welding induced residual stresses is the misfit between different regions [3]. The misfits act over different length scales and are due to temperature gradients, deformation gradients and material defects.

The origin of the residual welding stresses is complex and results from the interaction of (i) the temperature distribution, (ii) plastic deformation and (iii) microstructural changes.

A non-uniform temperature (*i.e.* the temperature distribution) in the workpiece due to welding results in non-uniform expansion and contraction of the material. If a material is heated and then cooled to room temperature homogeneously, it will be free of macroscopic stresses. When the heating is non-uniform, the cooler parts of the workpiece constrain the expansion and stresses are generated. Upon cooling a similar

behaviour occurs. Apart from the internal constraints, (*i.e.* the cooler parts of the workpiece) external constraints can be applied to the workpiece.

When the elastic limit is exceeded during the thermal cycle, plastic deformation will take place and residual stresses will be introduced. As the workpiece experiences a thermal gradient, the material softens locally and plastic deformation shows a gradient. Due to softening of materials at elevated temperatures, which is the case during welding, non-uniform plastic deformation will take place.

Finally, material related phenomena such as grain growth, solid-state phase transformations, re-crystallization and aging may occur by temperature changes. These changes will have an effect on the stress state.

The origins of residual welding stresses in steels are explained in more detail in the subsequent sections.

Thermally induced strains due to welding

Temperature changes cause thermal strains in solids as defined by the temperature dependant thermal expansion coefficient:

$$\varepsilon_{th} = \int_{T_0}^{T_p} \alpha_T dT; \tag{2.2}$$

in which ε_{th} is the thermal strain, α_T is thermal expansion coefficient and T_0 and T_p are the initial and peak temperatures respectively. The thermal expansion coefficient is a temperature dependent material property.

During welding heat is locally introduced into the workpiece. Furthermore, the latent heats of melting, solidification and solid-state phase transformations affect the temperature distribution. The heat is distributed by the thermal material properties: the thermal conductivity (λ) and the specific heat (C_p). Both properties are combined in the thermal diffusivity (k_a).

$$k_a = \frac{\lambda}{\rho C_p}; \tag{2.3}$$

where ρ is the density. The temperature dependant thermal expansion coefficient can be obtained experimentally by dilatometer experiments, in which the dilatation Δl over a certain measuring length l_0 is measured as a function of the temperature. It should be noted that also volumetric changes related to solid state phase transformations will be included in the dilatometer results, see **Figure 2.3** [4].

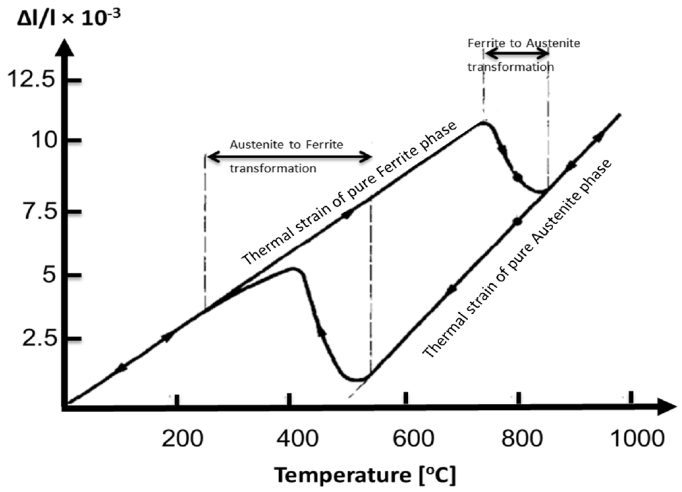

Figure 2.3. *Free dilatometric diagram of a A508 C13 steel [4].*

Plastic deformation

Under constrained conditions the thermal strains due to temperature changes in the material may produce elastic or plastic stresses. In welding this constrained condition is present as the heated area is constrained by the surrounding cold base metal. Moreover, the construction or a clamping system induces additional constraints on the workpiece.

The temperature dependency of the mechanical material properties determines the stress and strain fields in welding. The mechanical material properties which affect the residual stresses are the yield stress, Young's modulus, Poisson's ratio and the work hardening behaviour. The yield strength of materials decreases with increasing temperature. **Figure 2.4** [5] depicts the yield strength of carbon steels as a function of temperature. As a result, plastic deformation will more easily occur near the fusion zone.

The effect of microstructural changes during welding on the stress/strain state

As mentioned in the previous sections, the temperature distribution and the induced plastic deformation affect the stress state in the workpiece. However, the temperature cycle in combination with the stresses generated, will also affect the microstructure. This effect is mutual.

Solid state phase transformations in steels are accompanied by specific volumetric changes, as was already shown in **Figure 2.3**. During heating, the material expands

and therefore the thermal strain increases. At approximately 770 ^{o}C, the ferrite to austenite (BCC to FCC) transformation takes place, upon which the strain decreases. In the cooling stage, the austenite to ferrite, pearlite, bainite or martensite transformation occurs. These phase transformations are accompanied by an increase in volume.

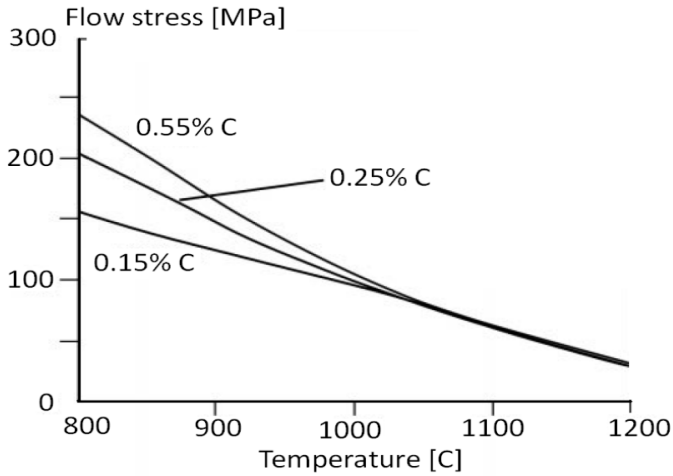

Figure 2.4. *Flow stress of carbon steels with different carbon content as a function of the temperature [5].*

In steels, the new constituents formed depend critically on the chemical composition of the steel and the thermal cycle applied during welding, in particular the peak temperature reached and the cooling rate. **Table 2.1** [3] shows the volume changes of different solid state phase transformations, including the effect of the carbon content of the steel. This will affect the residual stress levels and distribution.

Table 2.1. *Volumetric changes of different solid state phase transformations in steels, indicating the dependency of the carbon content of the steel [3].*

Phase transformation	**Volume change**
Pearlite to Austenite	$-4.64 - 2.21 \times wt.\%C$
Austenite to Upper Bainite or Pearlite	$4.64 - 2.21 \times wt.\%C$
Austenite to Lower Bainite	$4.64 - 1.43 \times wt.\%C$
Austenite to Martensite	$4.64 - 0.53 \times wt.\%C$

Apart from the volumetric changes, the constituents formed upon solid state phase transformations, change the material mechanical properties. For example, the formation of hard phases like martensite increase the yield strength of a material. **Figure 2.5** [6] shows the change in the yield strength and ultimate tensile stress (UTS) as function of volume fraction of martensite in dual phase steel.

Transformation plasticity

Transformation induced plasticity is the increased plasticity due to stresses present during a phase transformation. **Figure 2.6** [7] shows the dilatation curve for free expansion, labelled $\sigma = 0$, but also includes the effects of external stresses on the strain changes during a thermal cycle. This plastic deformation can occur even for external stresses smaller than the yield stress of the material [8]. The transformation plasticity should be taken into account to obtain a correct estimation of residual stresses and distortion in welding. However, it is not yet clear how much the influence of transformation plasticity contributes to residual stress levels (compared to the volume change effects) [9].

Grain size and re-crystallization

Due to the thermal cycle, especially near the fusion zone, grain growth may occur. The Hall-Petch [10] relationship expresses the variation in yield strength with grain size as:

$$\sigma_y = \sigma_0 + k_y\sqrt{d}; \tag{2.4}$$

where σ_y is the yield stress, σ_0 and k_y are constants for a particular material and d is the grain size. At elevated temperature grain growth occurs to reduce the Gibbs free energy by reduction of grain boundaries.

During welding, different locations experience different thermal cycles. Regions close to the fusion line are heated to very high temperatures. For steels that do not experience solid state transformation (such as AISI-316L), re-crystallization and growth of the generated grains occur based on the temperature. For a material exhibiting solid state transformations, the grains close to the fusion line transform to austenite. Since the temperature is very high, the austenite grains grow and form a coarse grained region. As the peak temperature reduces with distance to the fusion line, a fine grained zone is formed close to the coarse grained region. The region next to the fine grained zone is only partially transformed to austenite. Other regions do not transform into austenite and become tempered or remain unaffected. The formation of different regions with different microstructures is schematically shown in **Figure 2.7** [11]. It is obvious that such changes in grain size and microstructure will have an influence on the stress and strain fields.

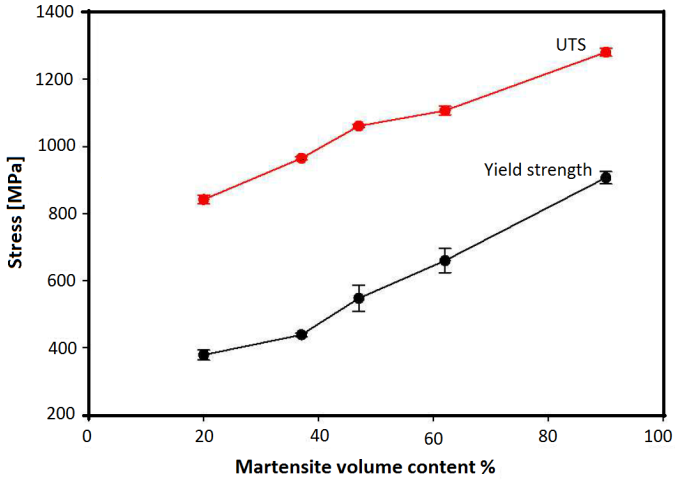

Figure 2.5. *The relation between stress increase (yield strength and UTS) and the martensite volume content in a dual phase steel [6].*

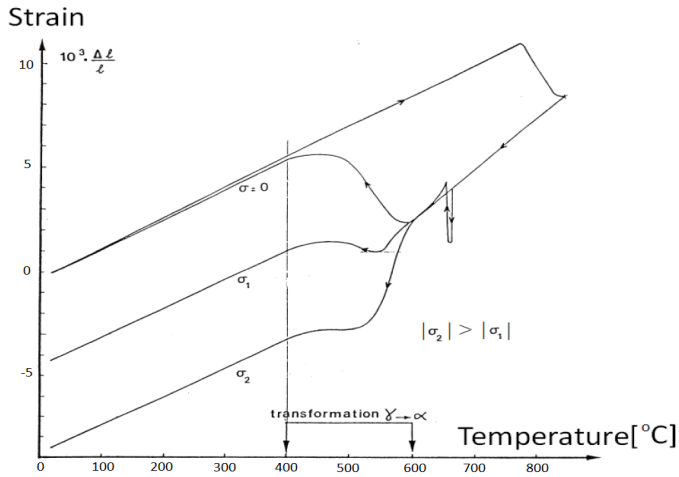

Figure 2.6. *Free dilatometer and transformation plasticity test [7]. Phase transformations in the presence of stresses can result in plastic deformation.*

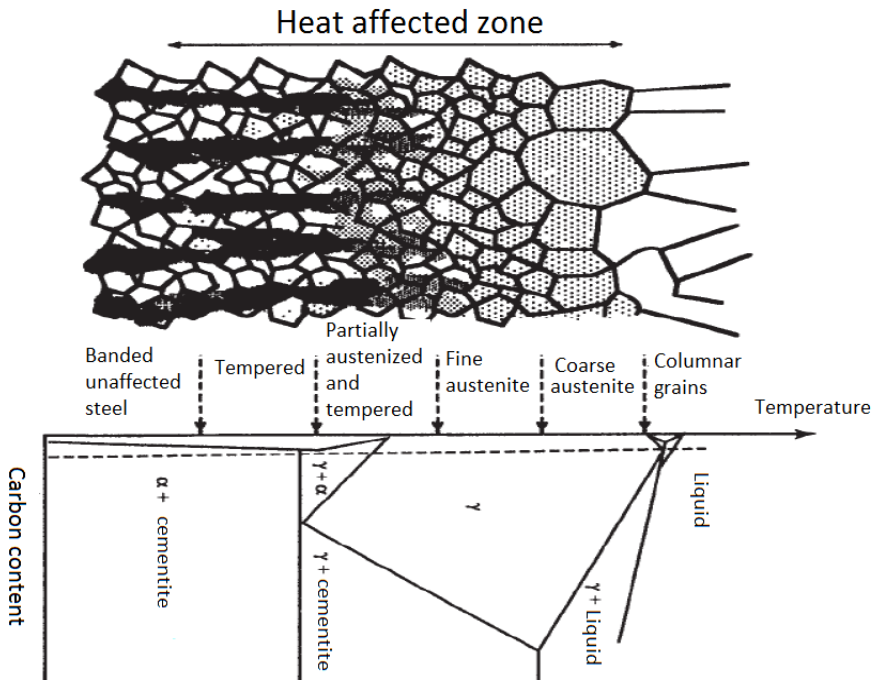

Figure 2.7. *Schematic illustration of the microstructural variation to be expected in the HAZ of low carbon steel welds [11].*

2.1.2 Transient behaviour of stresses and strains during welding

Stresses introduced by the factors discussed in the previous sections, will alter during the welding cycle. In this section the transient behaviour or development of stresses is described, starting from simulated heating cycles in hypothetical situations to real welding conditions. For the latter case the development of stresses is presented in the longitudinal, transverse and through thickness directions.

Stress development under constrained condition

The effect of a thermal cycle during welding on the stress state can be simulated by the Satoh test. In the Satoh test, a constrained bar is uniformly heated using induction heating, **Figure 2.8a** [12]. The axial stress formation in this bar is comparable to the welding induced stresses in the heat affected zone (HAZ). The clamps (*i.e.* the walls) simulate the surrounding cold material. In this test, the heating, expansion and softening of the surrounding material are ignored [5]. During testing, temperature (**Figure 2.8b**) as well as the axial force per unit area (**Figure 2.8c**) is measured. If the material undergoes solid state phase transformations the effects on the axial

stress will also be captured.

By increasing the temperature, the material tries to expand, which is limited by the clamps. Consequently, compressive stresses are formed in the bar. If the stress reaches the yield strength of the material, plastic deformation occurs. Since the yield stress is reduced by the elevated temperature (softening), the compressive stresses are reduced at high temperature. When the temperature approaches the melting point, the material shows a softening behaviour and the stress approaches zero. During cooling, the material contracts, but is again constrained by the clamps, and tensile stresses are introduced.

If a solid state phase transformation occurs during the cooling cycle, a change in cooling rate is observed in the temperature-time curve and the associated volume changes alter the tensile stresses during cooling. This is indicated in **Figure 2.8c** for example by the dip in the stress in the cooling curve.

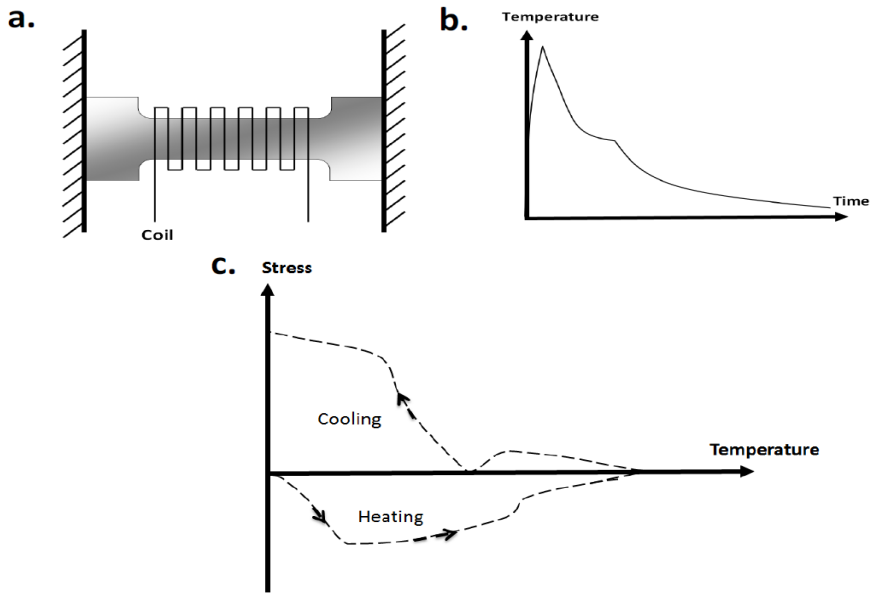

Figure 2.8. *Schematic representation of (a) the Satoh test, (b) schematic temperature profile applied on the sample (the discontinuity indicates the thermal effect of a solid state phase transformation) and (c) the stress development as a function of temperature, adopted from [12].*

Longitudinal residual stresses due to welding

Similar to the Satoh test, longitudinal contraction of the weld during cooling introduces residual stress in the weld seam direction because the shrinkage of the weld is

constrained by the surrounding colder and therefore stronger material.

The development of stresses in the weld direction can be understood by a simple model [13] shown in **Figure 2.9**. In this model, the temperature and the development of strain and stress, of a specific point are shown as a function of time. A thin plate, with thickness h, has been assumed in order to neglect the temperature gradient in the through-thickness (z) direction. Welding is performed in the x-direction. An elementary volume element ($h.dx.dy$) is selected in the heat affected zone and the stress development is described for this arbitrary element. The material properties are assumed to be elastic-perfectly plastic in order to simplify the situation. Furthermore, it is assumed that the stress in the y-direction (y) and the strain in the x-direction (ε_x) are equal to zero. The numbering in the graphs corresponds to specific times in the thermal cycle.

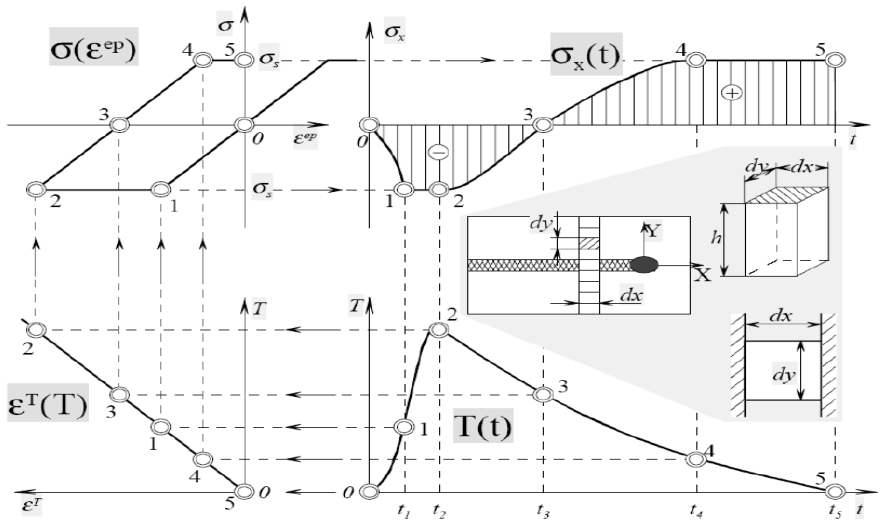

Figure 2.9. *Longitudinal stress development during welding for a simple case. An elementary volume element (h.dx.dy) in the heat affected zone is selected and the stress and strain development is described for this arbitrary element following a specific temperature profile [13].*

As can be seen from the temperature profile $T(t)$, the total thermal cycle takes t_5 seconds. Heating takes place up to t_2, after which the cooling starts. The thermal strain profile ε_T is plotted on the left side of the temperature profile. During the heating cycle, the element expands. Therefore the thermal strain increases. The maximum thermal strain is reached at point 2. During cooling, the thermal strain is reduced until it reaches zero at room temperature. The thermal strain consists of elastic and plastic strains. The relationship between the strain and stress is plotted above the thermal strain profile. Until t_1 (point number 1), the material behaves

elastically, after which the perfect plastic deformation starts. At t_2 the cooling cycle starts, accompanied by contraction of the material. The compressive elastic stress turns into tensile stresses until point 4. From point 4, yielding occurs in the contraction cycle. Finally, when the temperature reaches room temperature at point 5, an internal stress is generated in the material. The longitudinal stress as a function of time σ_x is plotted above the temperature profile. During the heating cycle, the element expands. However, this expansion is limited by the surrounding material. A compressive stress is generated in this part of the cycle. In the cooling stage, contraction occurs in the element, which is again constrained by the surrounding material. Therefore, the absolute value of the compressive stress is reduced until it reaches zero (t_3). The stress becomes tensile in nature with decreasing temperature. At point 4, the maximum tensile stress is reached.

This figure is only valid in a certain area of the welded plate, if the elementary volume is selected further away from the weld, plastic deformation will not occur and only elastic strains will be present upon heating. Even further away, the cold elementary volume will not experience a change in temperature, but will be affected by the fact that an equilibrium situation has to be maintained. Therefore, in this region compressive force might be present.

The plastic deformation zones during welding are shown in **Figure 2.10** [13, 14]. The temperature of the region leading the heat source (in the figure left of the curve indicated by T_{max}) increases when the welding arc approaches and thus the yield stress reduces. This region experiences a compressive stress, because the surrounding material limits the expansion of this region. The region very close to the welding heat source has temperatures very close to or above the melting point of the material. In this region softening is apparent. The region trailing the heat source (in the figure right of the curve indicated by T_{max}) is in the cooling stage. After the heat source has passed, this region is still at elevated temperature and has a low yield stress. The contraction of this region is limited by the surrounding materials and therefore this region will finally experience tensile stresses. Plastic deformation occurs locally and is non-uniform.

Apart from the cold material surrounding the weld, the application of clamping devices constrains the plates to be welded even further and prohibits distortion of the plate during welding. The larger the constraining forces, the larger the residual stresses. The build-up of large stresses locally generates plastic deformation. After releasing the clamps the workpiece will distort in order to achieve equilibrium. However, less distortion is observed when plastic deformation has occurred. The level of the residual stresses remains relatively high. The clamping distance to the weld line is an important issue with respect to welding distortion. The closer the clamps are situated to the weld centre line, the less final distortion is observed [15].

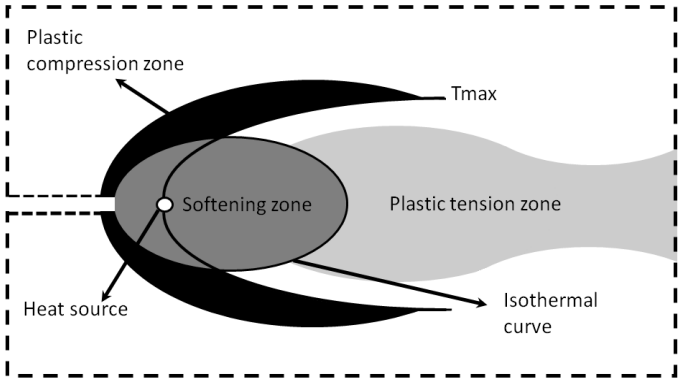

Figure 2.10. *Plastic tensioned and compressed zones during welding [13, 14].*

An example of a 3D representation of the calculated longitudinal stress distribution (as a function of time) for a 2 mm thick stainless steel sheet (AISI-316L) is shown in **Figure 2.11**. This figure helps to create an overall notion about the complexity of the stress-state caused by welding. The distribution of the longitudinal residual stress shows high tensile stresses in the weld metal and regions close to the weld, changing to compressive stresses at a certain distance from the fusion line in order to fulfil the requirements of equilibrium. The maximum level of longitudinal residual stress in the weld is close to the yield stress of the material at room temperature. It should be mentioned, that in this model the effects of solid state phase transformations are not included.

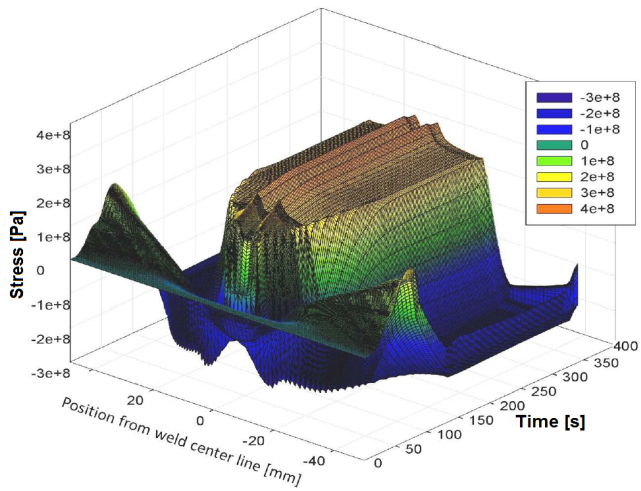

Figure 2.11. *A typical 3D representation of the longitudinal stress distribution as a function of distance to the weld centre line for a cross section in the middle of the plate over time for a 2 mm thick AISI-316L steel plate. The welding time is 80 s. After 400 s the plate has cooled to room temperature.*

Transverse and through thickness residual stresses

Both longitudinal and transverse contraction of the weld cause transverse residual stresses during welding. The magnitude of residual stresses in the transverse direction is less than the longitudinal stresses, due to the limited amount of metal that is heated by the passing heat source compared to the total width of the plate. The principles are however basically the same as for the longitudinal case. An element as in **Figure 2.9** will undergo a similar behaviour. An example of the welding transverse stress development in an unconstrained plate is shown in **Figure 2.12** [13]. The stress evolution is traced along the line transverse to the welding direction. As can be seen from the figure, the distribution of transverse residual stresses is complex.

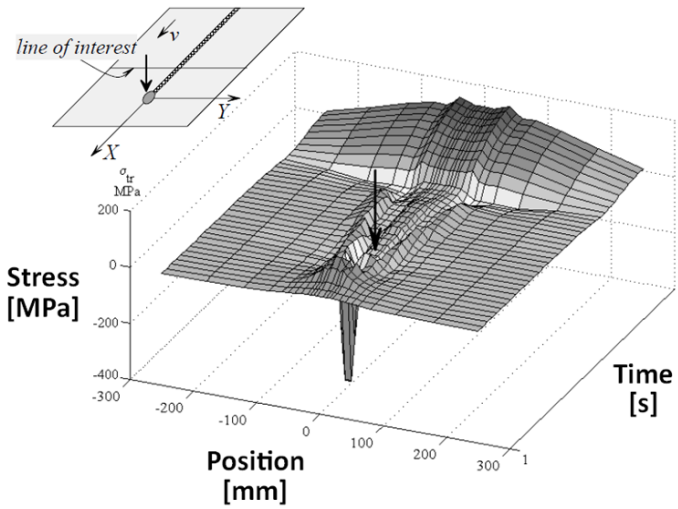

Figure 2.12. *A typical 3D representation of the transverse residual stress distribution at different positions over time. Position is the distance from the weld centre line [13]. The bold arrows indicate the location of the heat source.*

Usually, when the plate thickness is over 25 mm, residual stresses in the thickness direction can become significant [1]. Despite the importance of these stresses in thick welded material, limited information is available especially for multi-pass welds. The main difficulty is the availability of measurement methods. As an example, **Figure 2.13** shows the distribution of stresses along the thickness direction of a low carbon steel butt joint obtained by hole drilling [1]. The welds were made with covered electrodes and the welding operations were conducted from both sides.

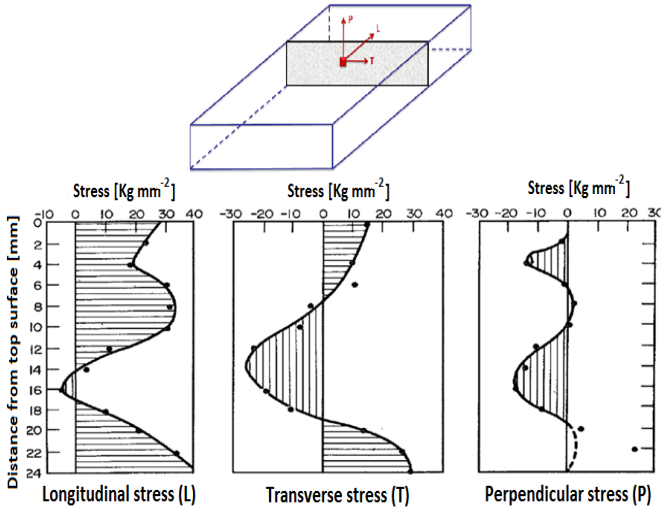

Figure 2.13. *An example of the distribution of stresses along the thickness direction of a low carbon steel butt joint [1].*

2.2 Welding distortion

Welding distortion is a permanent change in shape of a component (or an instability) due to the welding induced stresses [16]. Six types of welding distortion are defined [1, 13]:

- transverse shrinkage (shrinkage perpendicular to the weld),
- longitudinal shrinkage (shrinkage in the direction of the weld),
- rotational distortion (angular distortion in the plane of the plate due to thermal expansion or contraction),
- angular distortion (shrinkage caused by a non-uniform temperature distribution in the through-thickness direction of the workpiece),
- bending distortion (distortion in a plane through the weld line and perpendicular to the plate) and
- buckling (distortion caused by compressive stresses).

Figure 2.14 shows the different types of welding distortion [17]. It should be mentioned that in reality multiple types of welding distortion may occur at the same time and that it is sometimes difficult to distinguish the types of distortion present in a workpiece [17].

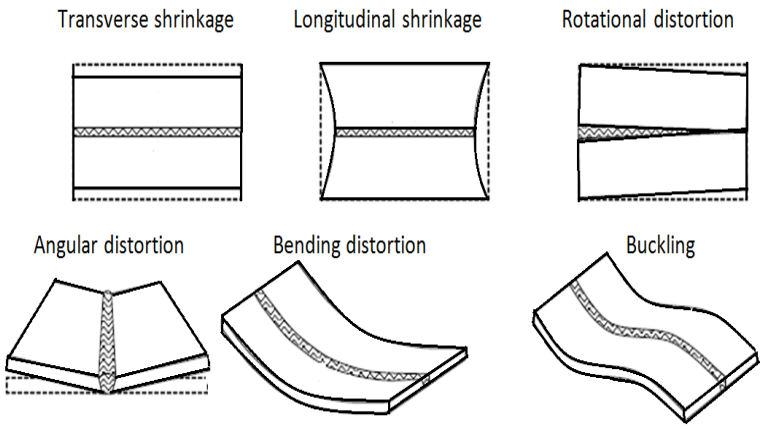

Figure 2.14. *Different types of welding distortions [17].*

2.2.1 Transverse and longitudinal shrinkage

The mechanism of transverse shrinkage is schematically shown in **Figure 2.15** [13]. The mechanism is studied for a cross section of a plate with thickness dx, subdivided in three regions, labelled 1 to 3. The first region represents the softened metal inside the T isotherm, while the second region indicates the region in which the temperature gradually drops to the initial temperature T_0. The third region is the zone in which the temperature remains at the initial temperature. If a cross section is subdivided into rectangles, then the change in shape of these rectangles shows the shrinkage in the transverse direction (see **Figure 2.15b**). During welding, when the arc reaches the cross section (dx), the temperature of region 1 is high and therefore this region tries to expand much more than region 2. However, the expansion of this region is limited/suppressed by the colder region (region 2). Therefore region 1 deforms more than region 2. This deformation is mainly towards the centre line of the weld. In region 3, the temperature remains at the initial temperature of the plate and shows no deformation. During cooling all elastic stresses are released. The final deformation of the plate after cooling, is shown by Δ_{tr}, which is in the transverse direction and is called the transverse shrinkage.

Research [18-22] has been carried out for this type of distortion, especially for butt welds. Transverse shrinkage of fillet welds is less compared to butt welds, because the restraint in a fillet weld (due to its shape) minimises the distortion.

The mechanism of longitudinal shrinkage is similar to that of transverse shrinkage. The amount of shrinkage in the transverse direction is larger than in the longitudinal direction, *i.e.* parallel to the weld. Because the cold metal resists the contraction of the hotter metal more in the longitudinal direction than in the transverse direction.

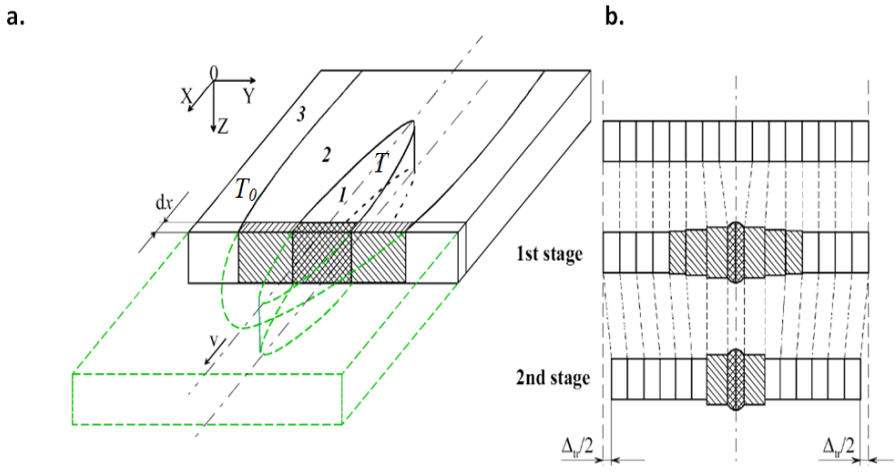

Figure 2.15. *Schematic representation of the transverse shrinkage mechanism in a weld, a) considered cross section, b) transverse shrinkage stages [13].*

2.2.2 Rotational distortion

The rotational distortion is an in-plane distortion resulting in a change of the angle between the welded plates. This type of deformation strongly depends on the welding condition as well as the material properties [23]. For the cases in which a high welding power and a high welding speed is applied, like submerged arc welding (SAW), a gap forms or expands. In situations with a relatively low power and a low speed, the gap closes [13]. For a material with low diffusivity (such as AISI-316L), the heat generated by the arc is localized while for a material with high diffusivity (such as DP600 and AH36) a lower temperature is obtained (with same heat input) in the weld region and therefore less distortion occurred.

2.2.3 Angular distortion

Angular distortion, which is also referred to as butterfly distortion, is the change in the out-of-plane angle between the materials to be joined [13]. This type of deformation occurs because of the non-uniform temperature distribution in the through-thickness direction of the plate. The mechanism of angular distortion has been studied by Pilipenko [13] and is shown schematically in **Figure 2.16**.

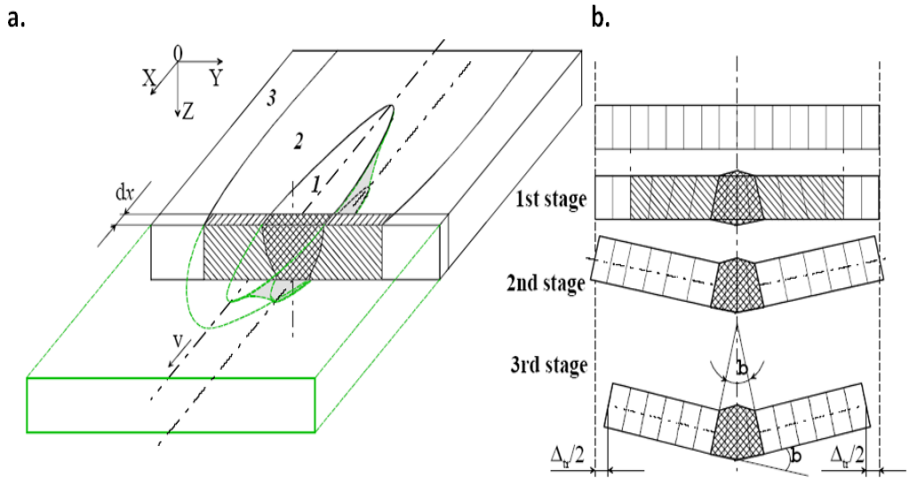

Figure 2.16. *Schematic representation of the angular distortion mechanism, a) cross section considered and b) stages of angular distortion [13].*

Similar to **Figure 2.15**, three regions can be distinguished according to the temperature reached. In region 1, the temperature is higher than in regions 2 and 3. During the heating cycle, the temperature in regions 1 and 2 increases, while the temperature in region 3 remains at room temperature. The material at high temperature is very weak, ductile and will deform easily. In region 1 of the cross section with thickness dx, the material tries to expand when the welding arc approaches, but the colder regions (2 and 3) limit this expansion. Therefore, this region deforms significantly. As the temperature at the top surface is higher than the bottom surface, the contraction during the cooling stage is much larger for the top surface compared to the rear surface. This finally leads to an out-of-plane (angular) distortion.

As there are always through-thickness temperature variations in welding, this type of deformation appears in the majority of welding processes. The angular distortion depends to a large extent on the plate thickness and the heat input as shown in **Figure 2.17** for steel [24]. As can be seen from the figure, thinner plates show less angular distortion than thicker plates until a critical thickness is reached, because of the more uniform temperature profile in through-thickness direction of thinner plates compared to thicker plates. By increasing the plate thickness from this critical point, the stiffness of plate increases and the angular distortion reduces.

2.2.4 Bending distortion

An uneven through-thickness temperature distribution produces an uneven residual stress distribution over the plate thickness. This generates a bending moment, which causes bending distortion in the welded structure. Bending distortion can be produced also when the weld line is offset from the neutral axis of the component.

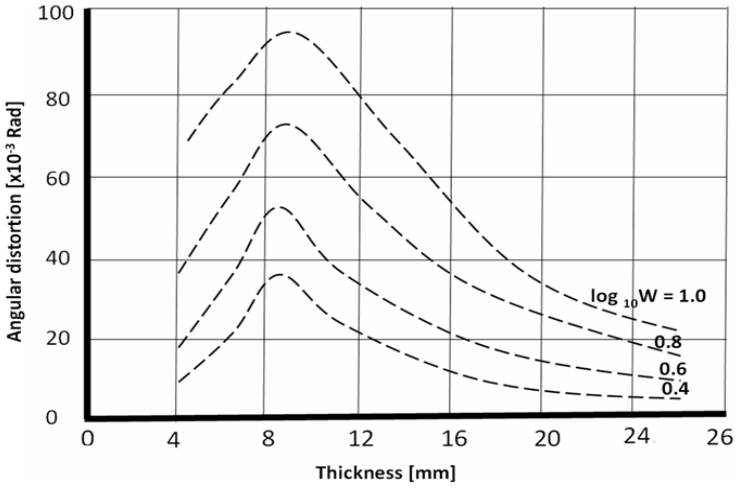

Figure 2.17. *The angular distortion of steel plates with different thicknesses, the lines represent the heat input (W), adopted from [24].*

2.2.5 Buckling

Buckling is a distortion mode resulting from an instability of a structure under compressive stresses. The structure buckles and collapses when these compressive stresses reach the critical buckling stress. Buckling differs from other types of distortion because buckling is an instable type of deformation and usually there are more than one deformation modes [1]. The critical buckling load depends on the material properties (Young's modulus, Poisson's ratio), boundary conditions and the dimensions of the structures.

2.2.6 Factors affecting distortion

In summary, the main factors affecting distortion are [22]:

- *Initial stress state*: If there is an initial stress state in the plate before welding, the residual stress and distortion of the plate after welding can be increased or decreased.

- *Constraints*: Since constraints act against shrinkage of the weld, it reduces distortions. However, by increasing the degree of constraint, the residual stresses in the plate also increase, see **Figure 1.2**.

- *Thermo-mechanical properties of the material*: The material properties, both thermal and mechanical, influence the magnitude and distribution of the residual stresses and distortion in the welded joint.

- *Welding parameters and sequence*: The higher the welding heat input, the larger the welding residual stress and distortion. The sequence of welding has a significant effect on the residual stress state and distortion after welding [11]. Two main effects of welding sequences are preheating and reheating (the weld) which can increase or decrease welding distortion.

- *Weld and joint design*: The more uniform the joint geometry, the lower the welding distortion. For example, U-grooves produce less distortion than V-grooves. The bigger the volume of the weld, the larger the welding residual stress and distortion.

2.3 Controlling residual welding stresses and distortion

Many methods are proposed and demonstrated in industry to control both residual stress and distortion. However, most of these techniques aim to reduce distortion. Any change in distortion reflects a change in the residual stress level. Some methods can reduce welding distortion significantly, whilst the residual stress level in the workpiece is increased. It should be mentioned that the selection of a suitable distortion reduction method depends on the type of distortion to be reduced.

A classification of mitigation methods is based on when they are applied during the manufacturing stage [14]:

- Pre-welding methods,

- Post-welding methods,

- In-situ welding techniques.

2.3.1 Pre-welding stress/distortion mitigation methods

Appropriate welding design considerations before welding can be very helpful to reduce welding distortion. The design of the groove cross section [14] should be as narrow as possible in order to minimize heat input. For good welds, sufficient heat input is required. However, high heat inputs cause more welding distortion. In this respect, the U-groove shape is much more preferred to a V-groove shape.

Pre-shaping is another method which can be applied prior to welding. The design of a structure is altered in such a way that after welding distortion, the preferred final shape will be achieved. **Figure 2.18** shows two common methods used in design modification named pre-setting and pre-bending [16].

Pre-heating can reduce both welding residual stress and distortion. This method

reduces the high temperature gradient in welding. Preheating can also be applied for material with low thermal diffusivity [14]. For materials such as steel which can produce unwanted hard constituents like martensite upon welding, pre-heating can be used to reduce the cooling rate.

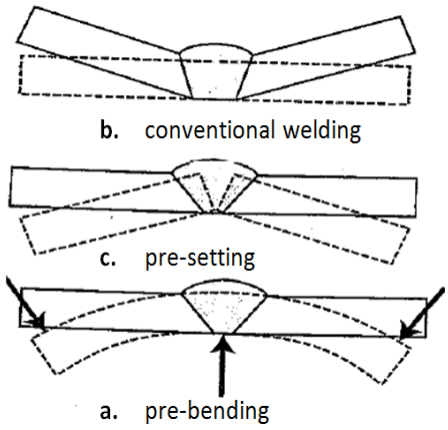

Figure 2.18. *Pre-setting and pre-bending methods used in distortion reduction, the dashed lines indicate the initial state [16].*

2.3.2 Post-welding stress/distortion mitigation methods

Stress relieving (annealing) is a method to improve the microstructure, to reduce the risk of cracking by heating the material to above the recrystallization temperature and thus relieve stresses. Stress relaxation occurs in this method as a result of a creep mechanism. This method will reduce both macroscopic and microscopic residual stresses. **Figure 2.19** shows schematically the temperature profile as a function of time for this method [14] for mild steel. The annealing temperature is in the range of 450 ^{o}C to 700 ^{o}C and the annealing time takes 1 to 3 hours. The relief of stresses may results in distortion.

Vibration stress relieving reduces the residual stresses by vibrating the material of its eigen frequency with a small amplitude. In this method the residual stresses are reduced as a result of global or local plastic deformation. The method has many benefits such as short time and low energy and avoids thermal distortion [14].

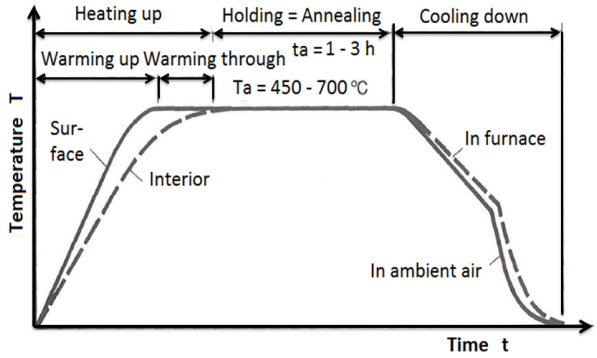

Figure 2.19. *Schematic representation of temperature as a function of time for stress relief annealing of mild steel [14].*

2.3.3 In-situ mitigation methods

Rolling can be applied during welding either on top of the weld (direct rolling) or alongside of the weld (roller tensioning). This method has been investigated by many researchers [25-33]. Research in this topic was focused on the control of residual stress (and distortion) but also on associated issues like the prevention of hot cracking and improvement of mechanical properties of the weld. An example of the application of rolling in welding engineering was shown by Wen [33] for the friction stir welding process. Two types of rolling conditions were used, as shown **Figure 2.20a**. The longitudinal residual stress profile after rolling is shown in **Figure 2.20b**. For both cases, significant reduction of residual tensile stresses can be seen, mainly because of plastic deformation of the weld.

One of the methods which can be used for mitigation of residual stress and distortion during welding is mechanical tensioning. In this method (as can be seen in **Figure 2.21**), a load is applied uniformly before clamping of the plates prior to welding. The tensioning load is present during welding and is released together with the clamps after welding. The experimental and numerical investigation of mechanical tensioning in friction stir welding has been presented by Richards *et al.* [34].

The development of the longitudinal, transverse, normal and von Mises stresses as a function of the distance to the tool centre along the weld centre line is predicted by numerical modelling for mechanical tensioning of 3 mm aluminium AA2024-T6 friction stir welded plates and is shown in **Figure 2.22** [34]. The investigated conditions were: (a) un-tensioned (b) 35% tensioned (of the room temperature yield point of the material) and (c) 70% tensioned (of the room temperature yield point of the material) welds. As can be seen, mechanical tensioning affects both the compressive yielding ahead, and tensile yielding behind the friction stir tool. The imposed tensile

stress reduces the amount of compressive yielding that occurs ahead of the weld and the resultant misfit formed. Behind the tool, tensioning encourages increased longitudinal tensile straining of the cooling material in the softened (hot) zone. The tensile misfit thus generated, can either decrease the magnitude of the tensile stress (for tensioning levels less than 40%) or introduce significant compressive residual stresses (for tensioning levels greater than 40%). A further observation is that tensioning in the welding direction has hardly any influence on the other stress components.

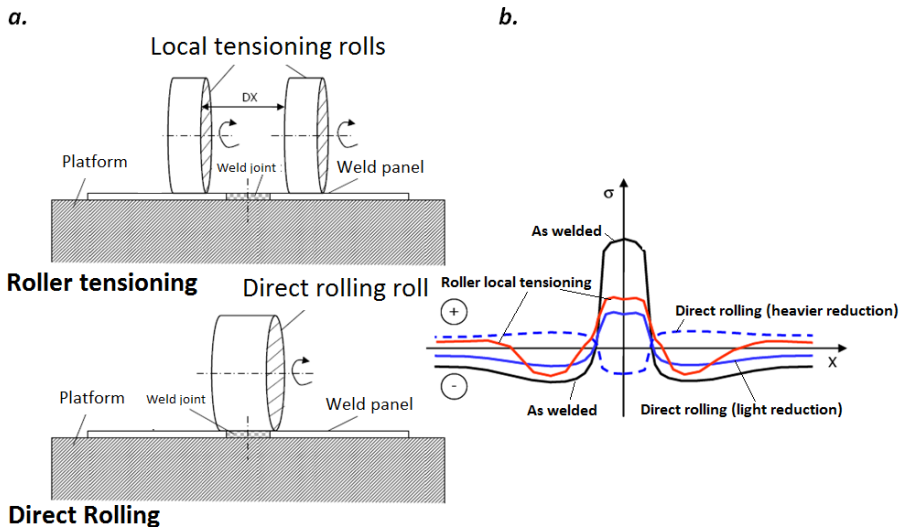

Figure 2.20. *Application of rolling in friction stir welding (a) using roller tensioning and direct rolling and (b) the final longitudinal residual stress profile generated by these two types of rolling and conventional welding [33].*

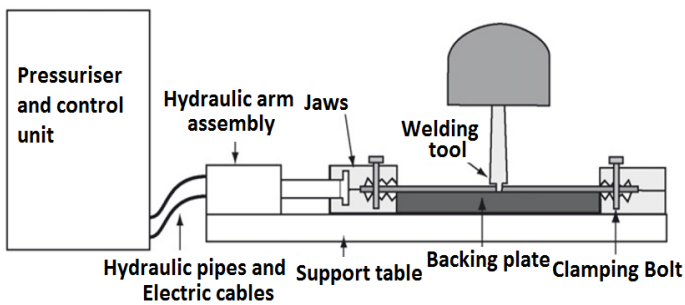

Figure 2.21. *Schematic representation of mechanical tensioning method used for friction stir welded plates [34].*

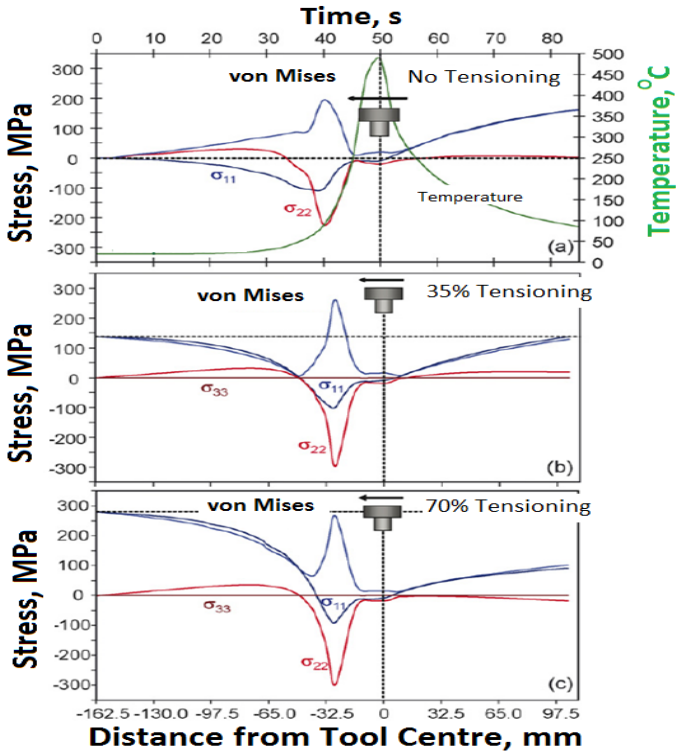

Figure 2.22. *Development of the longitudinal (σ_{11}), transverse (σ_{22}) and normal (σ_{33}) and von Mises stresses with distance from the tool centre along the weld centreline predicted by numerical modelling, for (a) un-tensioned (b) 35% tensioned and (c) 70% tensioned welds in AA2024-T6 3 mm plates, the arrow indicates the welding direction [34].*

2.4 In-situ thermal tensioning stress/distortion mitigation techniques

In the previous section, the effects of mechanical tensioning on the stress state of a weld were described. Tensioning can also be achieved by heating the specimen, *i.e.* thermal tensioning. Thermal tensioning, first applied by Burak *et al.* [35] and later patented by Guan [36, 37], describes a group of in-process methods to control deformation. In these methods local heating and/or cooling strategies are applied during welding. Generally speaking, two types of thermal tensioning can be distinguished:

1. Thermal tensioning with stationary heating and/or cooling sources (static thermal tensioning);
2. Thermal tensioning with moving heating and/or cooling sources (dynamic thermal

tensioning).

In the static methods, there is a pre-set temperature distribution in the workpiece, while in the dynamic or transient methods no pre-set temperature is applied. In both cases, different heating and/or cooling sources are used, such as gas flames, electric arcs, high energy density beams, solid CO_2-snow, water or liquid nitrogen.

Although, many studies have been performed related to the thermal tensioning either with stationary or with moving sources [35-40], a clear classification of the different thermal tensioning methods is not present. The adopted names and the classifications are mainly based on the mechanisms of distortion reduction.

The mechanisms of distortion reduction in thermal tensioning are complex. The complicated nature of welding stress and strain fields is increased by large number of parameters involved in thermal tensioning. Type, intensity and characteristics of the additional heating and/or cooling sources play an important role in the development of the stress and strain fields during welding with thermal tensioning. The positioning of the additional sources with respect to the weld centre line and the welding torch are other critical parameters involved in thermal tensioning.

In this thesis, a classification of thermal tensioning is adopted as shown in **Figure 2.23**.

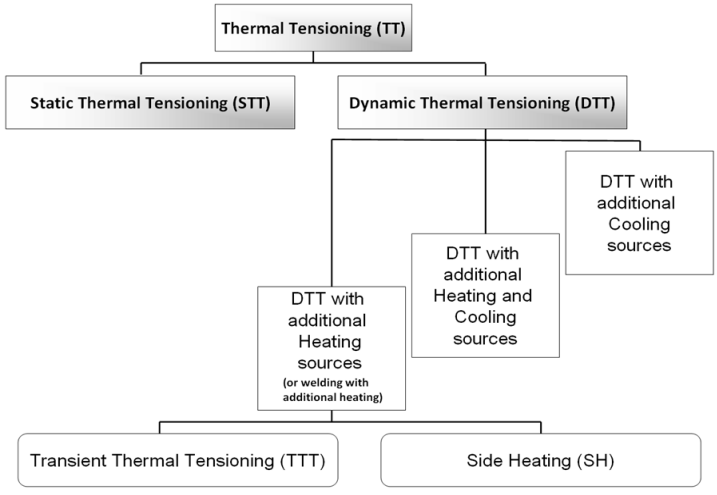

Figure 2.23. *The classification of thermal tensioning adopted in this research.*

2.4.1 Static Thermal Tensioning (STT)

The stationary thermal tensioning technique includes pre-stretching the weld area along the entire weld length by means of heating and cooling blocks. In this way a

specific temperature profile is generated in the specimen, which provides a certain *stretching* effect due to thermal expansion/shrinkage. This effect is super-imposed on the thermal effects of welding. The applied temperature gradient produces tensile stresses to prevent the formation of plastic strains during welding.

A schematic representation of stationary thermal tensioning using both heating and cooling sources is shown in **Figure 2.24**.

Resistive heating blocks in combination with a cooling water-spray on the reverse side of the plate, underneath the weld zone, create a specific temperature distribution. The stress field causes yielding, and reduces the peak tensile stress in the weld. The final resulting stresses (due to the applied temperature profile) lead to a reduction of the compressive plastic stress zone and it's stress level during welding [38].

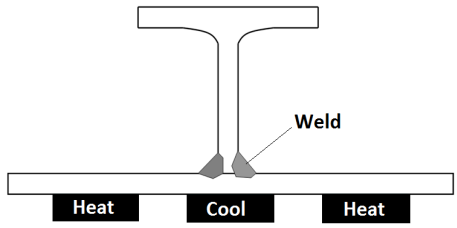

Figure 2.24. *Schematic representation of static thermal tensioning process.*

2.4.2 Dynamic Thermal Tensioning (DTT)

It is not always practical to use stationary sources. Therefore, developments upon the introduction of stationary thermal tensioning were directed in thermal tensioning with additional moving (heat and/or cooling) sources.

Dynamic thermal tensioning can be applied using both heating and cooling sources. This method is known in the shipbuilding industry. Flame heating combined with water cooling causes mitigation of longitudinal residual stresses after welding. However, the combination of both heating and cooling sources increases the complexity of the process.

In thermal tensioning with a cooling source, a cooling source follows the welding torch at a short and fixed distance, see **Figure 2.25**. The abnormal temperature field created by the trailing heat sink causes a modification of the residual stresses in such a way that the compressive stresses near the plate edges are reduced [17]. Therefore, this technique is particularly suited to reduce buckling distortion.

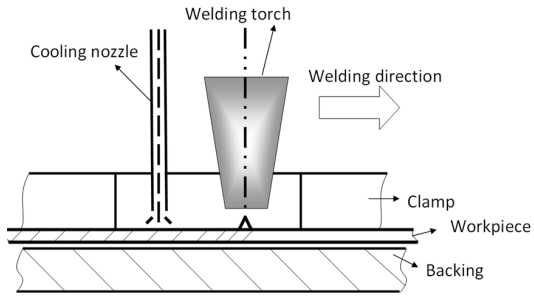

Figure 2.25. *Schematic representation of dynamic thermal tensioning process using cooling sources, adopted from [39].*

Usually, solid CO_2-snow, water or liquid nitrogen is used as a cooling medium. The main disadvantages of this method are the interaction of the cooling source with the welding arc and the high cooling rates which may result in the formation of hard constituents such as martensite in some types of steel.

Figure 2.26, schematically shows the dynamic thermal tensioning in which two additional heating sources are applied together with the welding torch to reduce welding distortion.

As shown in **Figure 2.23**, thermal tensioning using additional heating sources is classified into two types, Transient Thermal Tensioning (TTT) and Side Heating (SH). The position of the heat sources in TTT is close to the weld centre line in comparison to that of Side Heating. The thermal field generated by the burners in TTT influence the thermal field generated by the arc. The thermal field of the weld zone is not affected by the generated temperatures by the burners in SH.

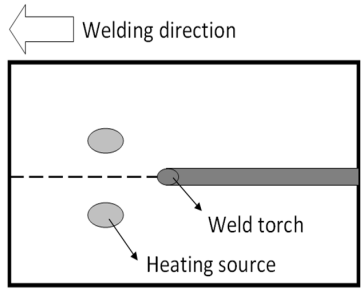

Figure 2.26. *Schematic presentation of dynamic thermal tensioning using heat sources.*

2.4.3 Dynamic Thermal Tensioning using heat sources

As stated before, dynamic thermal tensioning can be divided into two main strategies; TTT and SH. In this section both methods are discussed in more details.

The distortion reduction can be achieved during welding with TTT based on a thermal tensioning or stretching effect. It is provided by establishing a required specific temperature gradient in a localized area near the welding arc zone. This stretching effect depends on material and process parameters. Influencing factors are: the material and thickness of the welded plate, the welding related parameters, the shape, size, intensity, location and velocity of the additional heat sources.

The TTT was studied and further developed at the Edison Welding Institute (EWI) from 1990 [38]. The technique was first tested at Northrop Grumman Ship Systems in 1999 for lightweight ship panel application on U.S. Navy vessel class DDG-51. Deo and Michaleris [40] presented the elimination of welding-induced bowing distortion in welded T-type stiffeners by TTT at the stiffener web plate. The effectiveness of using numerical analysis and optimization to design the TTT process has been presented by Michaleris *et al.* [41]. Preston *et al.* [16] used a finite element analysis with shell elements to model the optimum parameters of TTT by means of laser heating. Angled heat sources were predicted to provide a better solution than conventional orthogonal heat distributions. With orthogonal heat distributions the longitudinal and transverse strains act over the same area, resulting in beneficial high levels of longitudinal tension, but also in transverse compression which is undesirable. With the angled heat source, the transverse expansion is accommodated over a fairly large area. Most of the plate is still cool and capable of supporting the expansion without permanent deformation, and thus limiting the localized transverse compression, whilst still concentrating the longitudinal expansion in a small area around the arc.

In a Japanese patent, a technique to prevent buckling distortion in the welding of thin metal sheets using Side Heating (SH) is described [42]. This method is not only based on the thermal tensioning effect but is mainly based on the additional heating-induced plastic strains near the edges of the plate. A suitable contracted zone is formed in the areas away from the weld to level out the incompatible plastic zone in the welded area [43].

Yanga and Juang [44] reported that plate edge waves were eliminated by the SH method, due to tensile stresses introduced in the areas near the edges. **Figure 2.27** shows a comparison of distortion after welding with and without Side Heating (SH). Nagy *et al.* [45] applied SH during welding of $500 \times 12 \times 4\ mm^3$ DH36 ship panel to eliminate buckling distortion. It is claimed that in the SH method the compressive residual stresses are reduced and that is the main reason for reduction of buckling distortion [46].

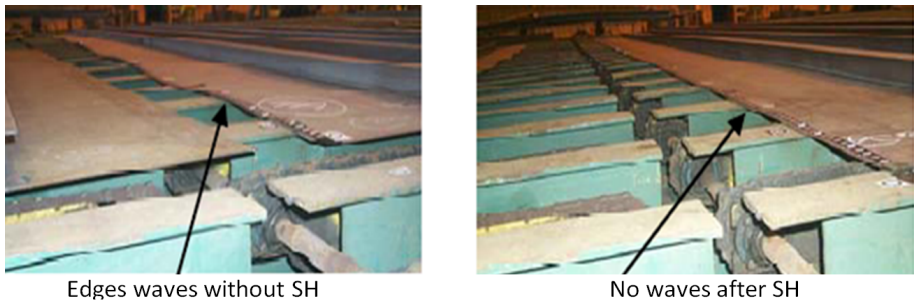

Figure 2.27. *Side Heating (SH) technique used in shipbuilding application [44].*

A simplified representation of the mechanism of side heating (SH) is shown in **Figure 2.28** [47]. The welding process induces tensile stress in the weld zone and compressive stresses near the edges of plates. The application of two heat sources during welding causes expansion, yielding and shrinkage. Residual tensile stresses are produced in the panel by the side heating in opposition to the residual compressive stresses induced by welding. The specific pattern of the residual stress distribution shown in **Figure 2.28** in the case of side heating is capable to prevent buckling. Because of the newly created residual tensile stress zones located between the compressive residual stresses; the residual compressive stresses, cannot cause buckling. Even the maximum values of the compressive stresses are higher than the critical buckling load. In other words, the plastically yielded regions with tensile stresses act as specific stiffening supports against possible buckling [43].

Although promising results are obtained in TTT and SH, the mechanisms of these methods are still not completely clear. This is the main reason why dynamic thermal tensioning has not been applied in industry to any great extent.

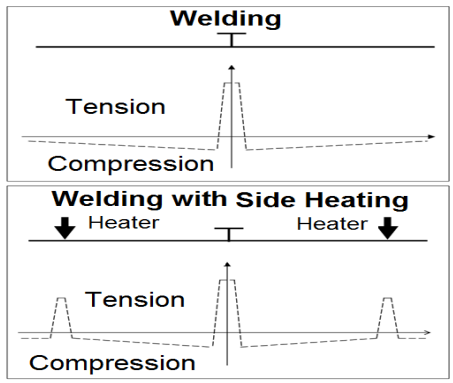

Figure 2.28. *A simple representation of the mechanism of distortion reduction by applying side heating, adopted from [47].*

Published literature agrees that dynamic thermal tensioning using additional heat sources can reduce welding distortion significantly. However, literature does not fully agree on how this method works. The relevant literature proposes three different mechanisms of distortion reduction by these methods:

(A) The redistribution and not a reduction of longitudinal residual welding stresses increase the critical buckling load. Therefore, buckling distortion is prevented [43, 48].

(B) The compressive longitudinal welding stresses are reduced by means of the heat sources [16, 46].

(C) Thermal tensioning generates tensile stresses, which increase the tensile stress level in the weld zone. The stresses reach the yield stress of the material and therefore local plastic deformation occurs. During cooling the final residual stresses are reduced due to this plastic deformation [48, 49].

2.4.4 Heating sources overview for thermal tensioning

In addition to the welding arc, two additional heat sources are applied in either TTT or SH. In the literature three main types of heat sources are reported for transient thermal tensioning or side heating experiments: flames [50-53], resistance heaters [54] and laser beams [16]. Most of the reported results are based on experiments using flames, which is also adopted in this study.

A wide range of oxy-gas combinations can be used for welding with additional heating, in which oxygen is combined with different fuel gases like acetylene, natural gas, propane and hydrogen. The combustion of the fuel gasses create flames with different maximum temperatures, based on the chemical reactions taking place.

In **Table 2.2** [55], four different oxy-fuel and air-fuel gases combination are compared.

Table 2.2. *Some properties of oxy-fuel and air-fuel gases [55].*

Properties	O_2	C_2H_2	C_3H_8	CH_4	H_2
Density [kg m^{-3}]	1.337	1.095	1.874	0.671	0.084
Boiling temperature [^oC]	-183	-84	-43	-162	-253
Max flame temp.					
with air [^oC]	-	2325	1925	1920	2045
with O_2 [^oC]	-	3200	2850	2750	2650
Power of flame[kJ cm^{-2} s^{-1}]	-	45	11	13	14

The most common type of flame used in welding with additional heating is the oxy-acetylene flame. The combustion of oxygen and acetylene produces a flame with a maximum temperature of approximately 3200 ^{o}C. **Figure 2.29** [55] shows different regions in a neutral oxy-acetylene flame.

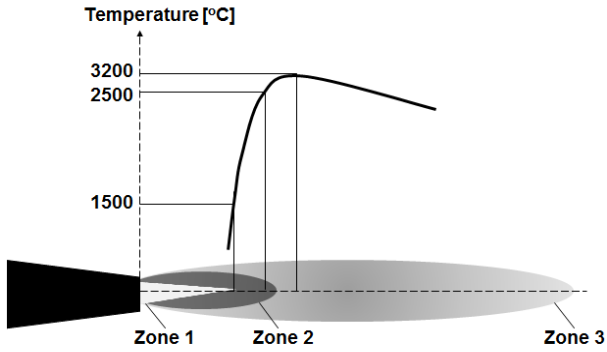

Figure 2.29. *Different regions in a neutral oxy-acetylene flame [55].*

In the flame, acetylene is combusted with oxygen in the torch nozzle and the mixture flows at a high speed. The oxygen from the surrounding air then reacts with the mixture. These chemical reactions can be summarized as [14]:

$$C_2H_2 + O_2 = 2CO + H_2 + Q_1(Q_1 = 0.021 Jmm^{-3}), \tag{2.5}$$

$$2CO + H_2 + 1.5O_2 = 2CO_2 + H_2O + Q_2(Q_2 = 0.027 Jmm^{-3}), \tag{2.6}$$

The heat produced is mainly transferred to the plate by convection. The size of the flame depends on the nozzle diameter and the velocity of the gas mixture. According to reference [14], the effective heat output of the flame is influenced by the following factors:

1. the mixing ratio of oxygen and acetylene (maximum heat is generated when the ratio $\frac{O_2}{C_2H_2}$ is 2.0 to 2.4);
2. the velocity of the gas and the nozzle size (maximum heat is obtained with a high velocity and a small nozzle size);
3. the distance between the nozzle and the plate (maximum heat with decreasing distance, but the workpiece should not be within the primary combustion regime);
4. the speed of the flame over the material surface;
5. the thickness of the plate;
6. the thermal conductivity or thermal diffusivity of the plate material.

This effective heat flow has a Gaussian distribution. The maximum value of heat distribution is localized in the centre and decreases sharply towards the edges mainly due to the rapid decrease of flow velocity.

2.5 Concluding remarks

The heating and cooling cycle in welding, produce high tensile stresses in and around the weld zone, which are balanced by compressive stresses further away from the weld. Different types of welding distortion may occur simultaneously after welding, when constrains are released.

Control of residual welding stresses and distortion are significant topics in welding engineering. Several techniques have been proposed to reduce welding distortions. Thermal tensioning is a group of in-process techniques to reduce welding distortion using heating and/or cooling strategies. The main focus of this thesis is on thermal tensioning using additional moving heat sources. Although promising results are obtained, the mechanisms of these methods are still not completely understood. This is the main reason why the method has not been widely adopted by industry.

Reference

[1] K. Masubuchi,*Analysis of welded structures*, Pergamon Press, USA, 1980.

[2] *Welding Handbook*, 7th edition, American Welding Society, Miami, USA.

[3] W. Reimers, A.R. Pyzalla, A. Schreyer, H. Clemens, *Neutron and Synchrotron Radiation in Engineering Material Science*,Wiley-VCH Verlag GmbH Co., 2008.

[4] J. B. Leblond, G. Mottet and J. C. Devaux, *A Theoretical and Numerical Approach to the Plastic Behaviour of Steels During Phase Transformations I: Derivation of General Relations*, Journal of Mechanics and Physics of Solids, Vol. 34, No. 4, pp. 395-409, 1986.

[5] L-E. Lindgren,*Computational Welding Mechanics*, Woodhead Publishing, 2007.

[6] C. Tomser, *Modelling of the mechanical properties of Dual Phase Steels based in microstructure*, PhD thesis, RWTH Aachen, 2009.

[7] L. Taleb, N. Cavallo, and F. Waeckel, *Experimental Analysis of Transformation Plasticity*, International Journal of Plasticity, Vol. 17, pp. 1-20, 2001.

[8] W. Mitter, *Umwandlungsplastizitat Und Ihre Berucksichtigung Bei Der Berechnung Von Eigenspannungen*, Materialkundlich-Technische, Vol.7, 1987.

[9] P. Ferro, H. Porzner, A. Tiziani and F. Bonollo, *The influence of phase transformations on residual stresses induced by the welding process-3D and 2D numerical models*, Modelling and Simulation in Material Science and Engineering, Vol. 14, pp. 117-136, 2006.

[10] W. F. Smith, J. Hashemi, *Foundations of Materials Science and Engineering*, Fourth edition, McGraw-Hill, 2006.

[11] H. K. D. H. Behadeshia, R. W. K. Honeycombe, *Steel microstructure and properties*, Third edition, Elsevier Ltd., 2006.

[12] H. M. Aarbogh, M. M'Hamdi, A. Mo and H. G. Fjær, *On using the SATOH test for extracting parameters in constitutive equations for modelling welding stresses in phase transforming steel*, Mathematical Modelling of Weld Phenomena 8, pp. 105-118, Verlag der Technischen Universitt Graz, 2007.

[13] A. Pilipenko, *Computer simulation of residual stress and distortion of thick plates in multi-electrode submerged arc welding*, PhD thesis, Norwegian University of Science and Technology (NTNU), Trondheim, 2001.

[14] D. Radaj, *Heat Effects of Welding: temperature field, residual stress, distortion*, Springer-Verlag, 1992.

[15] T. Schenk, *Modelling welding distortion-Influence of clamping and sequencing*, PhD thesis, Delft University of Technology, 2010.

[16] R. V. Preston, *Modelling of residual stresses in welded aerospace alloys*, PhD thesis, University of Cambridge, 2000.

[17] E. M. van der Aa, *Local cooling during welding: Prediction and control of residual stresses and buckling distortion*, PhD thesis, Delft University of Technology, 2007.

[18] S. Matsui, *Investigation of shrinkage, restraint stresses and cracking in arc welding*, PhD thesis, Osaka University, 1964.

[19] T. Naka, *Shrinkage and cracking in welds*, Tokyo, Komine Publishing Co., 1950.

[20] Y. Iwamura, *Reduction of transverse shrinkage in aluminium butt welds*, M.Sc. Thesis, M.I.T., 1974.

[21] R. H. Leggatt, *Distortion in welded steel plates, PhD thesis*, Magdalene College, Cambridge, UK, 1980.

[22] G. Verhaeghe, *Predictive formulae for weld distortion, a critical review*, TWI Ltd., 1998.

[23] C. Conrardy and R. Dull, *Practical techniques for distortion*, report Edison Welding Institute, 1995.

[24] S. Hirai, I. Nakamura, *Research on angular change in fillet welds*, Ishikawa jiama Review, Japan, pp. 59-68, 1955.

[25] S. W. Williams, S. A. Morgan, A. Wescott, M. Poad and S. W. Wen, *Stress engineering, control of residual stresses and distortion in welding*, Proceedings of 2nd International Workshop on Thermal Forming and Welding Distortion IWOTE 2008, Bremen, pp. 229-239, 2008.

[26] W. Liu, X. Tian and X. Zhang, *Preventing weld hot cracking by synchronous rolling during welding*, Welding Research Supplement, pp. 297s-304s, 1996.

[27] W. Xu, C. Fan, H. Fang and X. Tian, *New development in welding thin-shell aluminium alloy structures with high strength*, China Welding, Vol. 13, No. 1, pp. 27-30, 2004.

[28] C. Fan, H. Fang, J. Tao and X. Wang, *Strain field analysis of welding with trailing impact rolling for reduction of residual stress and distortion and prevention of hot cracking*, Transactions of the China Welding Institution (in Chinese), Vol. 25, No. 6, pp. 47-50, 2004.

[29] C. Fan, H. Fang, J. Tao, Y. Tian and M. Li, *Weld with trailing impact rolling to control the residual distortion of the thin-walled planar circumferential weldment*, Journal of Harbin Engineering University (in Chinese), Vol. 26, No. 2, pp. 238-241, 2005.

[30] Q. Guan, *A few issues with promoting application of weld rolling process*, Aeronautical Process Technology (in Chinese), Vol. 2, pp. 21-26, 1980.

[31] Q. Guan, *Development of weld mechanics and distortion control in aircraft thin-shell structures*, Proceedings of the 8th National Congress of Welding (in Chinese), Publisher of Chinese Mechanical and Machinery Industry, Vol. 1, pp. 51-57, 1997.

[32] H. Yue, H. Zhao, Z. Cai, J. Zhang, J. Lin and S. Ni, *Investigation of numerical simulation on controlling welding stress and distortion of thin aluminium alloy plate by rolling after welding*, Chinese Journal of Mechanical Engineering (in Chinese), Vol. 42, No. 6, pp. 217-220, 2006.

[33] S. W. Wen, *Development and Evaluation of a Roller System for Mitigation of Weld Residual Stress and Distortion*, Corus Research, Development and Technology, Swinden Technology Centre, Reference Source No. 135908 (internal report), 2007.

[34] D. G. Richards, P. B. Prangnell, S. W. Williams and P. J. Withers, *Global mechanical tensioning for the management of residual stresses in welds*, Materials Science and Engineering A, 489, pp. 351-362, 2008.

[35] Y. I. Burak, L. P. Besedina, Y. P. Romanchuk, A. A. Kazimirov and V. P. Morgun, *Controlling the Longitudinal Plastic Shrinkage of Metal during Welding*, Avt. Svarka (Automated Welding), Vol. 3, pp. 27-29, 1977.

[36] Q. Guan, *A Survey of Development in Welding Stress and Distortion Controlling in Aerospace Manufacturing Engineering in China*, Welding in the World, Vol. 43, No. 1, pp. 64-74, 1999.

[37] Q. Guan, D. L. Guo, C. Q. Li and R. H. Leggatt, *Low Stress Non-Distortion (LSND), Welding - a New Technique for Thin Materials*, Welding in the World (UK), Vol. c33(3), pp. 160-167, 1994.

[38] R. M. Dull, J. R. Dydo, J. J. Russell and J. Shanghvi, *Method of reducing distortion by transient thermal tensioning*, US Patent 6861617.

[39] J. Li, Q. Guan, Y. W. Shi and D. L. Guo, *Stress and distortion mitigation technique for welding titanium alloy thin sheet*, Science and Technology of Welding and Joining, Vol. 9, pp. 451-458, 2004.

[40] M. V. Deo and P. Michaleris, *Mitigation of welding induced buckling distortion using transient thermal tensioning*, Science and Technology of Welding and Joining, Vol. 8, No. 1, pp. 49-53, 2003.

[41] J. Song, J. Y. Shanghvi, P. Michaleris, *Sensitivity analysis and optimization of thermo-elasto-plastic processes with applications to welding side heater design*, Computational Methods in Applied Mechanical Engineering, 193, pp. 4541-4566, 2004.

[42] S. Takeno, *Method for preventing welding distortion of sheet metals*, Japanese Patent JP 4052079, 20 February 1992.

[43] Z. Feng, *Processes and Mechanisms of Welding Residual Stress and Distortion*, Woodhead Publishing Ltd, 2005.

[44] Y. P. Yanga and G. Juang, *Advancement in Prediction and control of Welding Residual Stress and Distortion*, Materials Science Forum, Vols. 539-543, pp. 3943-3948, 2007.

[45] T. Nagy, S. Williams, P. Colegrove, C. Ikegu, I. Fafiolu, *Distortion mitigation in welded ship panels*, Proceedings of 2nd International Workshop on Thermal Forming and Welding Distortion IWOTE 2008, Bremen, pp. 265-275, 2008.

[46] *Minimization of Welding Distortion and Buckling, Modeling and Implementation*, Edited by P. Michaleris, Woodhead Publishing, May 2011.

[47] C. Conrardy, T. D. Huang, D. Harwig, P. Dong, L. Kvidahl, N. Evans, and A. Treaster, *Practical Welding Techniques to Minimize Distortion in Lightweight Ship Structures*, Journal of Ship Production, Vol. 22, No. 4, pp. 239-247, 2006.

[48] T. Nagy, *Investigation of thermal techniques to mitigate buckling distortion in welded panels*, PhD thesis, Cranfield University, 2012.

[49] N. A. McPherson, *Thin plate distortion - The ongoing problem in shipbuilding*, Journal of Ship Production, May 2007.

[50] Y. C. Lin and C. P. Chou, *A new technique for reducing the residual stress induced by welding in type 304 stainless steel*, Journal of Materials Processing Technology, No.48, pp. 693-698, 1995.

[51] http://www.cnst.us/Documents/Presentations/SNAME2006TTT2.pdf

[52] P. Michaleris, J. Dantzig, D. Tortorelli, *Optimization of the thermal tensioning process for minimum residual stress and distortion*, ASM Proceedings of the International Conference: Trends in Welding Research, Pine Mountain, GA, pp. 988-992, 1998.

[53] P. Michaleris, L. Zhang, S. R. Bhide and P. Marugabandhu, *Evaluation of 2D, 3D and applied plastic strain methods for predicting buckling welding distortion and residual stress*, Science and Technology of Welding and Joining, Vol. 11, No. 6, pp. 707-716, 2006.

[54] G. Shaoqing, X. Wenli, Y. Hong, G. Weihua and T. Xitang, *Numerical simulation of distortion control by static thermal tensioning in welding of thin aluminium alloy plates*, Materials Science Forum, Vols. 475-479, pp. 3263-3266, 2005.

[55] *International Welding Engineering (IWE) Course*, SLV, Germany, 2002.

Chapter 3

Finite element modelling of conventional welding and welding with additional heating

In this chapter, the modelling approaches for simulation of conventional welding and welding with additional heating are introduced and discussed. The thermal, microstructural and mechanical modelling of the processes is explained subsequently.

The results of numerical modelling are presented and compared to the experimental results, such as temperature, distortion and residual stress measurements, in **Chapter 6**.

3.1 Introduction

The main goal of computational welding mechanics is to provide useful models to predict the performance. The models can be used to perform virtual experiments, visualising, designing, optimising and analysing aspects of the welding process [1].

The multi-physics in the welding process necessitate the consideration of different fields in the models. Three main interacting fields can be distinguished; the thermal, microstructural and mechanical fields, as shown in **Figure 3.1** [2]. In order to predict residual welding stresses and distortion, the models should contain all three fields. Coupled models contain all these fields; however, computational time can be reduced significantly when some weak interactions are ignored or when decoupled models are used (for example, when the thermal field calculation forms the input for the micro-

structural/mechanical determination).

The effect of the mechanical field on the thermal field (path 4, **Figure 3.1**) is generally ignored [3]. The main reason for such an assumption is that the heat generated by the welding heat source is much greater than the heat generated by plastic deformation of the material.

Many models exclude the effects of the microstructure changes on the thermal (path 2, **Figure 3.1**) and mechanical fields (path 5, **Figure 3.1**) [4-5], while it is also reported that these effects cannot be ignored [6-7]. The effect of latent heat of transformation on the thermal field is often ignored, again, this is mainly due to the high amount of heat generated by the heat source compared to the heat associated by transformations. The effect of solid state phase transformations on the mechanical field depends to a significant extent upon the type of material and the type of transformation.

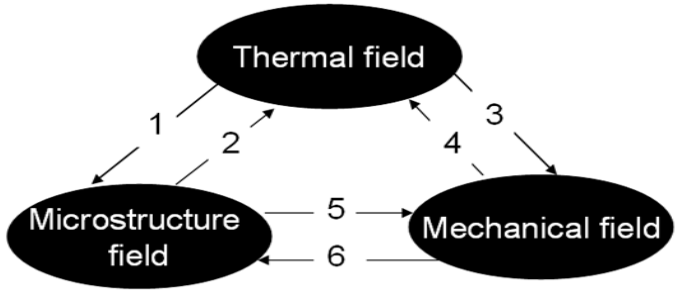

Figure 3.1. *The interaction among three modelling fields in welding. The meaning of the numbers is as follows: (1) Microstructure evolution depends on the temperature, (2) Latent heat of phase transformation and thermal material properties depend on the microstructure, (3) Mechanical properties depend on temperature, (4) deformation changes thermal boundary condition, (5) phase transformations generate stress and strain and (6) Microstructure evolution depends on deformation [2].*

In this study a de-coupled analysis is employed. The thermal field is calculated first ignoring the heat generated by plastic deformation and the results are used in the mechanical field (path 3, **Figure 3.1**). If there are solid state phase transformations in the material, the fraction of phases is calculated based on the thermal field output (path 1, **Figure 3.1**) and the results are used to evaluate the mechanical field (path 5, **Figure 3.1**). **Figure 3.2** shows the modelling approach as well as the validation experiments used throughout this thesis. In all calculations the fluid behaviour is excluded. The effect of mechanical field on the microstructure is also ignored (path 6, **Figure 3.1**)).

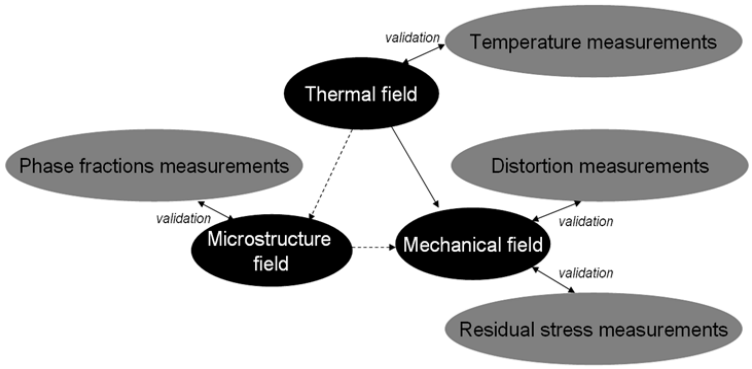

Figure 3.2. *The modelling approach used in the simulations as well as the validation experiments. The dashed lines indicate that the phase transformation is modelled only for dual phase steel (DP600). The effects of the mechanical field on the thermal field have been ignored.*

Nowadays, software makes it possible to solve the thermal, microstructural and mechanical problems numerically. Two methods are generally applied to obtain approximate solutions of the differential equations: the Finite Difference Method (FDM) and the Finite Element Method (FEM). Although using the FDM analysis can explain cases on physical principles, it is difficult to use for complicated weld geometries. The finite element method is the dominant technique used in welding simulations [8]. Modelling of the welding process is difficult, due to the complex interactions of many parameters.

In this study, the Finite Element Method (FEM) is used to simulate both conventional welding and welding with additional heating. All finite element models described in this thesis were run on an HP Proliant ML 570 workstation with four Intel Xeon 64EMT processors. The commercial finite element code $Msc.Marc$ was used in the simulations. $Thermocalc^{TM}$ software was used for thermo-dynamical calculations. An in-house $Matlab$ code was written to calculate the phase fractions. All subroutines were written in $Fortran77$.

Figure 3.3 shows the coordinate system used in the models throughout this thesis. The welding direction is defined as the longitudinal or x-direction. The in-plane direction perpendicular to the welding direction is defined as the transverse or y-direction. The z-axis is the through-thickness direction. The origin in the numerical calculations is selected at the edge of the plate in the x-direction at the centre of the plate in the y-direction. The origin of the z-axis is at the top surface of the workpiece. SI units (kg, m, s) are employed in the models.

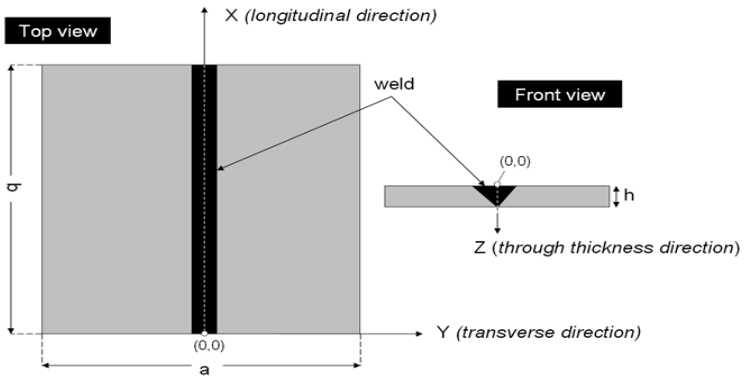

Figure 3.3. *The coordinate system used in the models.*

The Lagrangian formulation or the Eulerian formulation can be adopted. The Lagrangian formulation uses finite element meshes which are attached to the materials and move along with the material. In the Eulerian approach the finite element mesh is fixed and the material flows through the mesh [9]. The Eulerian approach is very suitable for steady state processes [10-16]. The generality and availability of Lagrangian codes lead to the selection of the Lagrangian formulation as a more or less common choice in welding simulation [1] and is adopted in this study. Two classifications of the Lagrangian approach are the total Lagrangian and the up-dated Lagrangian method. In the first method the original un-deformed state of the workpiece is set as the reference, while in the latter approach, the current configuration (frequently updated) is used as reference state. Since, excessive deformation occurs during welding, the up-dated Lagrangian formulation is preferred and adopted in this investigation. The main reason is that when excessive deformation occurs, mesh elements are distorted significantly and therefore re-meshing of these elements is required.

3.2 Thermal analysis

During arc welding, an arc is established between a consumable or a non-consumable electrode and the workpiece. A welding arc is an electrical discharge between electrodes in a gas or vapour environment [17]. The temperature of the arc column varies in various gases and may reach temperatures beyond 15000 K in an argon atmosphere [17]. A certain fraction of the power provided by the heat source is transferred to the workpiece, while the remaining part is lost to the surroundings by several mechanisms: radiation, convection and conduction as shown in **Figure 3.4**. The efficiency of the heat transfer is process dependant. The heat entering the workpiece is redistributed primarily by conduction, while at the workpiece boundaries heat is lost by conduction, convection and radiation. This determines the spatial and temporal thermal distribution and the development of the microstructure in the weld and the

heat affected zone. This non-uniform temperature distribution of the workpiece is one of the sources of welding induced residual stress and distortion.

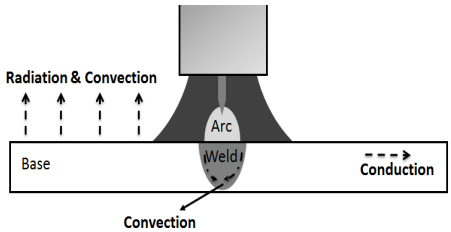

Figure 3.4. *Schematic overview of heat transfer during welding.*

Thermal analysis includes the heat flow in the electrode, the weld pool, the arc and the solid workpiece. Both arc and weld pool phenomena are necessary for the development of a numerical model of the arc welding process, because there is close interaction between the electrode, the arc plasma and the weld pool. A unified numerical model accounting for the weld pool, the arc plasma and the electrode is under development for predicting the properties of the weld [18]. Experimentally, it is difficult to perform temperature measurements within the weld pool and the arc. In order to simplify the analysis, the thermal analysis throughout this study assumes a volumetric heat input in the workpiece excluding all physical phenomena taking place in the arc and the weld pool. This approach was used by other researchers [19-21]. Satisfactory agreements between temperature measurements and the numerical predictions have been reported using such approach [22]. Using such simplifications, the thermal analysis can be classified into two main parts: a heat input model and the modelling of heat losses.

3.2.1 Basic equation

The basic equation in the heat transfer analysis is the energy conservation law. The energy conservation law leads to a balance between a change in stored energy and heat flux as:

$$\rho\dot{H} = Q - \bigtriangledown q; \tag{3.1}$$

where ρ is the material density, $\dot{H}$ is the enthalpy rate, Q is the power of the heat source per unit volume and q is the heat flux. The enthalpy rate is related to the temperature rate by the heat capacity c:

$$\frac{dH_1}{dt} = c\frac{dT}{dt}; \tag{3.2}$$

where H_1 is the enthalpy. Fourier's law of isotropic heat conduction gives:

$$\mathbf{q} = -\boldsymbol{\lambda} \bigtriangledown T; \tag{3.3}$$

where $\mathbf{q}$ is the heat flux vector, $\boldsymbol{\lambda}$ is a matrix of thermal conductivity coefficients and T is the temperature. The thermal conductivity coefficient depends on the chemical

composition, microstructure and temperature [23]. The combination of the above equations leads to the classical equation of conservation of energy:

$$\rho c \frac{dT}{dt} = Q + \bigtriangledown(\boldsymbol{\lambda} \bigtriangledown T). \tag{3.4}$$

Room temperature is assumed to be the initial condition. The simulation of the transient thermal field in welding contains the modelling of heat input and heat losses. The heat losses due to clamp contacts, heat convection and radiation to the environment are modelled as boundary conditions. The input by the heat source into the workpiece is modelled using Q in **Equation 3.4**.

3.2.2 Modelling of the welding heat source

As stated before, a part of the heat generated in the arc is transferred to the workpiece. The term *heat source efficiency* or *process efficiency* is defined as the fraction of the heat transfer from the heat source to the workpiece to the nominal power of the heat source [24]. The process efficiency can be measured with a calorimeter [25], but this is rather difficult and incorporates relatively large errors. Different values have been reported for the process efficiency [22, 26]. In this investigation, the process efficiency is used as a fitting factor and was varied until a good agreement with experimental results was obtained.

Table 3.1 shows values for the process efficiency for GTA and GMA welding from the literature and includes the values adopted in this study. The process efficiency for GMAW is higher than GTAW. The main reason is that in GTAW heat is lost to the cooled tungsten electrode, while in GMAW the heat entering the wire electrode is transported to the weld pool by the transferring droplets.

Table 3.1. *Values for the process efficiency for GTA and GMA welding from the literature and this study.*

Reference	**Process efficiency for** GTAW	**Process efficiency for** GMAW
[22]	0.6	-
[27]	-	0.64
[24]	0.6-0.8	0.75-0.85
[26]	0.75	0.85
This thesis	0.65	0.75

The effective power of the arc (E), which is transferred to the workpiece is determined by the welding current (I), the arc voltage (U) and the efficiency of the process (η):

$$E = \eta U I. \tag{3.5}$$

Several heat input models have been introduced in the literature such as point, line, plane and volume heat source models [28]. Rosenthal [29] assumed a point heat source

model with the steady state heat flow and neglected the heat of fusion and heat losses. These assumptions made it possible to derive an analytical solution to the differential equation. Many other analytical models have subsequently been derived for two and three dimensional welding heat flow [28]. Some disadvantages such as inaccurate temperature predictions near the fusion zone and the heat affected zone limit the application of these models to the cases where solutions are sought far from the weld fusion line. The main source of the inaccuracies is the assumptions of a point heat source and the use of temperature independent material properties.

An early suggestion for a distributed heat source model was made by Pavelic *et al.* [30]. In this model a Gaussian distribution of a surface heat flux was proposed. Such a distributed heat flux model predicts the temperature of the weld pool and the heat affected zone better than the older models. However, the presented temperature distribution in the through thickness direction below the surface of the workpiece was inadequate. This led to the introduction of the first volumetric heat source models [31].

One of the most commonly used volumetric heat source models in welding simulations nowadays was proposed by Goldak [32]. The Goldak model, also called the double ellipsoid heat source model, defines two volumetric heat fluxes in front and behind the arc centre, as shown in **Figure 3.5**.

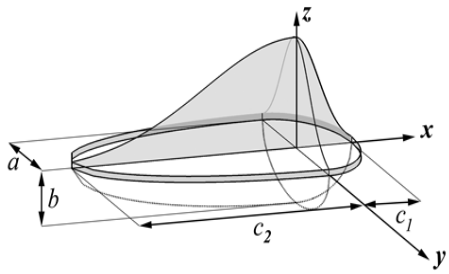

Figure 3.5. *Goldak's double ellipsoid heat source model [32].*

The volumetric heat flux with a Gaussian distribution is expressed for the region in front of the arc centre as:

$$q_{front} = \frac{6\sqrt{3}f_1E}{abc_1(\pi)^{3/2}} e^{-3(\frac{y}{a})^2} e^{-3(\frac{z}{b})^2} e^{-3(\frac{x_0+vt}{c_1})^2}; \tag{3.6}$$

and for the region trailing the arc centre the heat flux is expressed by:

$$q_{rear} = \frac{6\sqrt{3}f_2E}{abc_2(\pi)^{3/2}} e^{-3(\frac{y}{a})^2} e^{-3(\frac{z}{b})^2} e^{-3(\frac{x_0+vt}{c_2})^2}; \tag{3.7}$$

in which E is the effective power of the arc (see **Equation 3.5**), v is the travel speed along the x-direction (welding direction), f_1 and f_2 are the fractions of heat deposited at the leading and trailing side of the heat source, respectively (with the centre of x_0, y_0, and z_0). As can be seen from the equations, the shape of the volumetric heat flux is defined by arbitrary parameters a, b and c. The fusion zone geometry in the experiments is used as a starting point for selection of these parameters.

In general, the boundary of the heat flux is set as the location where the flux has dropped to 5% of its maximum value. Outside of this volume, no heat flux is assumed. The parameters used in the Goldak model are derived from experiments. Good agreement between predicted and measured temperatures of both GTAW and GMAW processes have been reported using this model [1, 27, 33].

In order to ensure the continuity of the heat input at the centre the following condition, as presented in [27], is used in the simulations.

$$\frac{f_1}{c_1} = \frac{f_2}{c_2} \Rightarrow q_{front} = q_{rear}. \tag{3.8}$$

The values of the parameters of the Goldak model used in the simulations of this study are described in **Chapter 6**.

3.2.3 Modelling of heat losses

The heat generated in the workpiece is lost to the backing plate, the clamping system and the surroundings. The mechanism of heat losses by contacting bodies (*i.e.* backing plate, clamping system) is based on conduction and can be described by:

$$q_{contact} = h_{contact}(T_\infty - T_0); \tag{3.9}$$

in which $h_{contact}$ is the heat transfer coefficient to the contacting body, T is the surface temperature of the plate, and T_∞ is the ambient temperature.

Since there are contacts between the clamps, the workpiece and the backing plate; the temperature of the plate changes at the location of the contacting bodies. The heat flow is determined by two factors: (a) the interface thermal resistance between the workpiece and the contacting bodies and (b) the heat conductivities of the contact bodies. The thermal resistance of the interface depends on the degree of clamping. When there is a very good contact, the heat transferred across the interface can be comparable to the conductive heat flow within the plate. In many studies these clamping condition effects are neglected [6, 34-36]. However, it was shown in [27 and 33] that the heat transfer conduction into the backing plate is the dominant heat loss mechanism during welding. Van der Aa [22] used a parameter study to fit the models with different heat transfer coefficients due to the contact bodies ranging from 25 to 100 W m^{-2} K^{-1} to the experimental temperature measurements. It appeared that a

fixed value of 50 W m^{-2} K^{-1} (for the heat transfer coefficient to contacting bodies) is suitable. In this thesis, a similar approach to [22] is employed. The heat transfer coefficients for contact bodies are varied ranging from 10 to 1000 W m^{-2} K^{-1}. It was found that the heat transfer due to contacting bodies plays an important role (see **Figure 3.6**). The backing plate has a large mass compared to the plates to be welded and it can be assumed that the temperature of the backing plate is constant. However, the temperature of the clamping system may change, as it experiences direct radiation of the arc and therefore in **Equation 3.9** is affected. This effect is included in the models, by measuring the thermal cycle of a clamp exposed to the radiation of the arc.

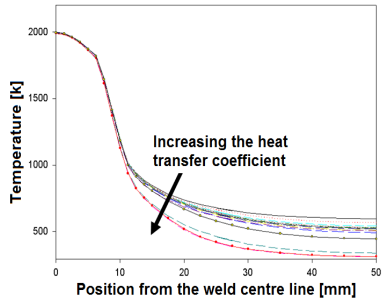

Figure 3.6. *Effects of heat transfer coefficient due to the contacting bodies on the temperature profile for different positions from the weld centre line (Material: AH36).*

The heat is also lost by convection and radiation to the surroundings. The heat lost by convection is described by:

$$q_{convection} = h_c(T_\infty - T_0); \tag{3.10}$$

where h_c is the convective heat transfer coefficient and T_∞ is the ambient temperature. The flow of a liquid or gaseous medium over a heated surface causes heat transfer by convection. The convection heat transfer coefficient is difficult to measure. The main reason is that it depends on fluid temperature, fluid and surface properties. For non-forced cooling in air, the range for the convective heat transfer coefficient is often selected to be between 1 to 10 W m^{-2} K^{-1} [33]. However, values as high as 30 W m^{-2} K^{-1} are reported [23].

As stated before, the heat transfer coefficients are temperature dependent. However, it has been reported in [22] that there is no real benefit using temperature dependent heat transfer coefficients. Therefore, a temperature independent value of 10 W m^{-2} K^{-1} is used for the convective heat transfer coefficients in this study. This value was also reported in [22, 37].

Heat lost by radiation is described as:

$$q_{radiation} = \varepsilon_m \sigma_B (T^4 - T_\infty^4); \tag{3.11}$$

where ε_m is the emissivity, σ_B is the Stefan-Boltzmann constant (5.6703×10^{-8} W m^{-2} K^{-4}), T is the surface temperature of the plate, and T_∞ is the ambient temperature.

The emissivity is an experimentally determined parameter ranging from 0.0 to 1.0. It is usually difficult to measure this parameter as it is dependent on the surface conditions and temperature. In the literature, there is little information available on this parameter for different materials and surface conditions. For shiny metallic surfaces the emissivity is reported to be between 0.2 and 0.4. The emissivity increases with temperature to values as high as 0.95 before melting [22, 38, 39]. Preliminary results of thermo-mechanical modelling showed that this parameter does not significantly influence the residual stress and distortion. It is therefore assumed to be constant in many publications [32, 37]. However, in this thesis, the emissivity is assumed to be a temperature dependent parameter for each of the materials. **Table 3.2** shows the dependencies used in the simulations.

The heat losses due to radiation are negligible at low temperatures, while at high temperatures the heat losses increase significantly, exceeding the convective losses for temperature above 200 ^{o}C to 300 ^{o}C [33]. As a result, it is rarely modelled explicitly. Heat losses by radiation occur mainly close to the arc during welding. Therefore, it can be assumed that the heat source efficiency includes this effect.

Table 3.2. *The parameter values for the emissivity used in the simulations.*

Emissivity	Materials	Reference
$\varepsilon_m = 0.7 - 0.02e^{\frac{900}{T}}; \varepsilon_{min} = 0.2$	AISI-316L	[22]
$\varepsilon_m = 0.7 - 0.02e^{\frac{900}{T}}; \varepsilon_{min} = 0.2$	DP600	[22]
$\varepsilon_m = 0.6367(1 - e^{-0.002266T}); \varepsilon_{min} = 0.2$	AH36	[39]

Detailed information on the heat transfer coefficients used in the simulations as well as the temperature of the clamps for the selected cases can be found in **Chapter 6**.

3.2.4 Thermal material properties

Thermal material properties used in the simulation include solidius and liquidius temperatures, latent heat of solid state phase transformations and fusion, specific heat, thermal conductivity, and density.

Solidius and liquidus temperatures have been calculated based on the chemical composition (see **Chapter 4**) of the materials used in this study using $ThermoCalc^{TM}$ and are shown in **Table 3.3**.

Table 3.3. The solidius and liquidus temperatures used for different materials in the simulations.

Parameter	AISI-316L	DP600	AH36
Solidius Temperature [K]	1673	1760	1749
Liquidus Temperature [K]	1732	1790	1788

Options for the implementation of the release of latent heat of fusion in the models are shown in **Figure 3.7**. The latent heat of fusion can be released uniformly in the temperature range between the solidius and liquidus temperature of the materials, **Figure 3.7a**. Another option is to define the temperature-dependent latent heat, if sufficient experimental data is available, and to implement this in Msc.Marc, see **Figure 3.7b**. **Table 3.4** shows the latent heat of fusion for different materials used in the simulations. The latent heats of some solid state phase transformations in steel are shown in **Table 3.5.** Comparing the values mentioned for the latent heat of fusion for different materials (**Table 3.4**) with the values of latent heat of solid state transformations (**Table 3.5**), it can be concluded that the latent heat of fusion is much higher. The latent heat of solid state phase transformations is therefore often ignored in modelling of the thermal field in welding [1]. In **Figure 3.8** temperature dependant specific heat data in which latent heat of fusion is included for dual phase steel DP600 is shown, whereas for AH36 and AISI-316L this data is not available.

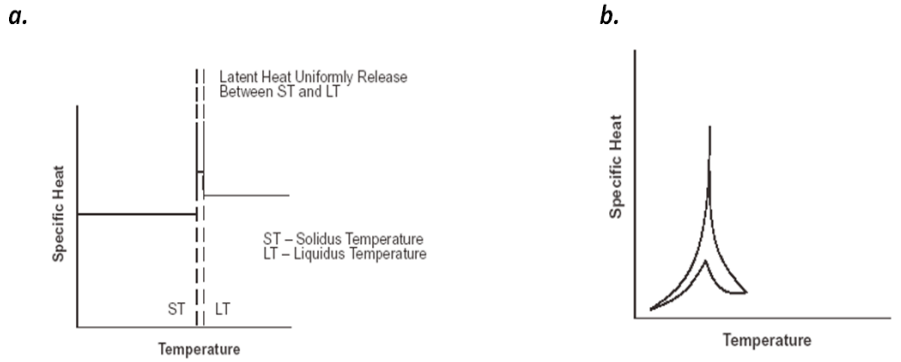

Figure 3.7. Different modelling methods for the release of latent heat: (a) uniform release of latent heat between solidus and liquidus and (b) temperature dependant release [9].

Table 3.4. The latent heat of fusion for different materials used in the simulations.

Parameter	AISI-316L	DP600	AH36
Latent heat of fusion $[kJkg^{-1}]$	330 [22]	See **Figure 3.8**	270 [40]

Table 3.5. *Latent heat of solid state phase transformation for some phase transformations in steel.*

Phase transformation	**Ferrite to Austenite**	**Austenite to Pearlite**	**Austenite to Martensite**
Latent heat $[kJkg^{-1}]$	75 [41]	92 [42]	83 [42]

Thermal conductivity is a temperature dependent property. The values used for thermal conductivity of the materials in this investigation are obtained from several sources and are shown in **Figure 3.9** as a function of the temperature.

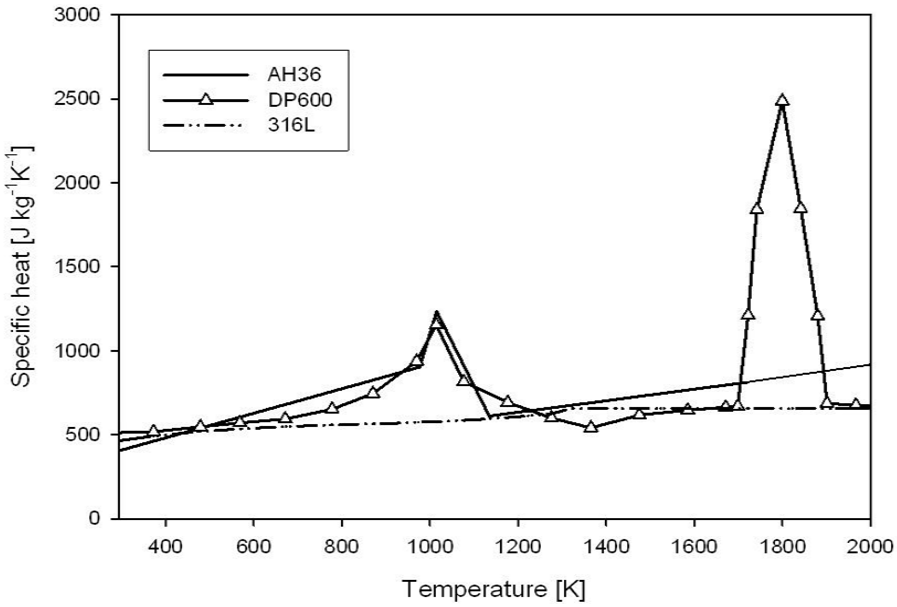

Figure 3.8. *Specific heat of AH36 [23], DP600 [22] and AISI-316L [22] as a function of the temperature. This data is used in the simulations.*

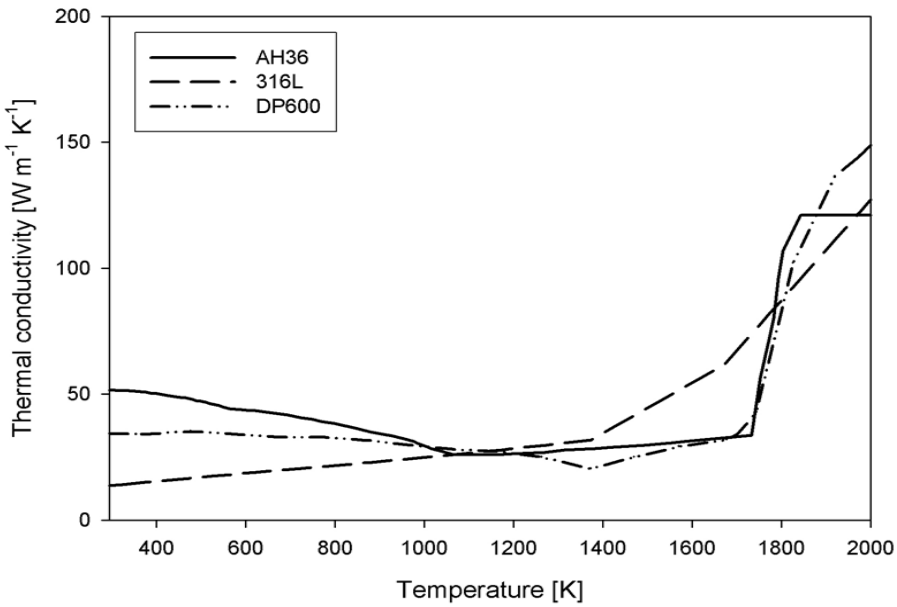

Figure 3.9. *Thermal conductivity of AH36 [43], DP600 [22] and AISI 316L [22] as a function of the temperature.*

Density is another material property which should be defined in the thermal analysis. Again, this property is temperature dependent. As stated in reference [22], density is assumed to be a constant material property in Msc.Marc. **Table 3.6** shows the values used for density of the materials in the simulations.

Table 3.6. *Density of different materials at room temperature used in the simulations.*

Parameter	**AISI- 316L**	**DP600**	**AH36**
Density $[kgm^{-3}]$	8030 [22]	8020 [22]	7860 [40]

3.2.5 Element and mesh study

Important considerations in finite element modelling are related to selecting an appropriate element and the mesh for the calculations. In this section, first different aspects of element selection in the thermal analysis are described. This is followed by consideration of meshing issues.

Element type is the first issue. There are a large number of element types available for finite element calculations. Continuum and shell elements are mainly used in arc welding simulations.

In welding the heat flow can be described as either a two or a three dimensional problem, mainly depending on the dimensions of the workpiece. Two dimensional models are generally used when the thickness of the material is much less than the length. It can be assumed that the temperature gradient (as well as the stress gradient) in the through thickness direction of the plate can be neglected. For this condition, shell elements are used. For thicker materials this boundary condition is not valid and the use of 2-D models would overestimate the temperature especially in the weld zone and HAZ. The main reason is the heat flow in the through thickness direction. This limitation of two dimensional modelling is usually compensated by reducing the process efficiency, but the 3-D problems are better described by continuum elements.

The order of the element indicates the order of the polynomial used to express the element behaviour [33]. The higher the order of an element the greater potential variation of the properties across the element. For example, in a first order element, a linear variation is allowed, while in a second order element a quadratic variation is possible. Although the accuracy is improved using high order elements, the calculation time will also increase.

In elements with a reduced integration, the calculation is done at a lower number of integration points. Thus the accuracy will be less, although the computational time is reduced. In this study, it was found that in the thermal analysis, the predictions of the temperature distributions by reduced or full integration are in close agreement.

In this investigation, the modelling has been performed using two dimensional (Cases I and II) and three dimensional (Case III) models. Therefore, different element types have been used in the thermal analysis.

For two dimensional modelling, a four-node heat transfer shell element (Element 85) with temperature as nodal degree of freedom has been used. Bilinear interpolation is applied to calculate the temperature in the plane of the shell and either a linear or a quadratic temperature distribution is assumed in the shell thickness direction [9]. This element uses four integration points. **Figure 3.10** shows the shell element used in two dimensional models.

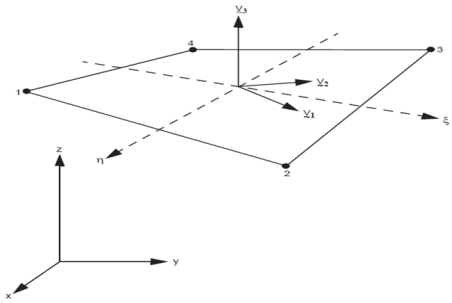

Figure 3.10. *Shell element used in two dimensional modelling. The element is defined geometrically by the (x,y,z) coordinates of the four corner nodes and local orthogonal surface directions (V1, V2, and V3) [9].*

In the three dimensional models two types of elements have been used: Element 123 and Element 71. Element 123 is an eight-node isoperimetric arbitrary hexahedral element for three dimensional heat transfer applications using reduced integration. A single integration point at the centre of the element is used in the calculations [9]. Element type 71 is a 20-node, isoperimetric, arbitrary quadrilateral element used for three dimensional heat transfer applications using reduced integration. The linear variation of the thermal gradients allows a realistic prediction of temperature field. There are eight integration points in this element. These two elements are shown in **Figure 3.11**.

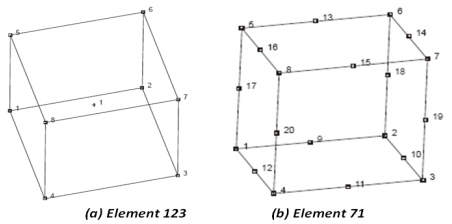

Figure 3.11. *Solid elements used in 3D modelling: (a) Element 123 with 8 nodes and 1 integration point and (b) Element71 with 8 nodes and 8 integration points [9].*

The mesh size should be fine enough to capture the peak temperature and the steep thermal gradients during welding. A fundamental guideline expressed in reference [1] indicates that the model should use finer meshes wherever needed and coarse meshes elsewhere. Therefore, the elements around the weld centre line (weld and HAZ of welding) are smaller than those at the plate edges (base material) shown in **Figure 3.12**.

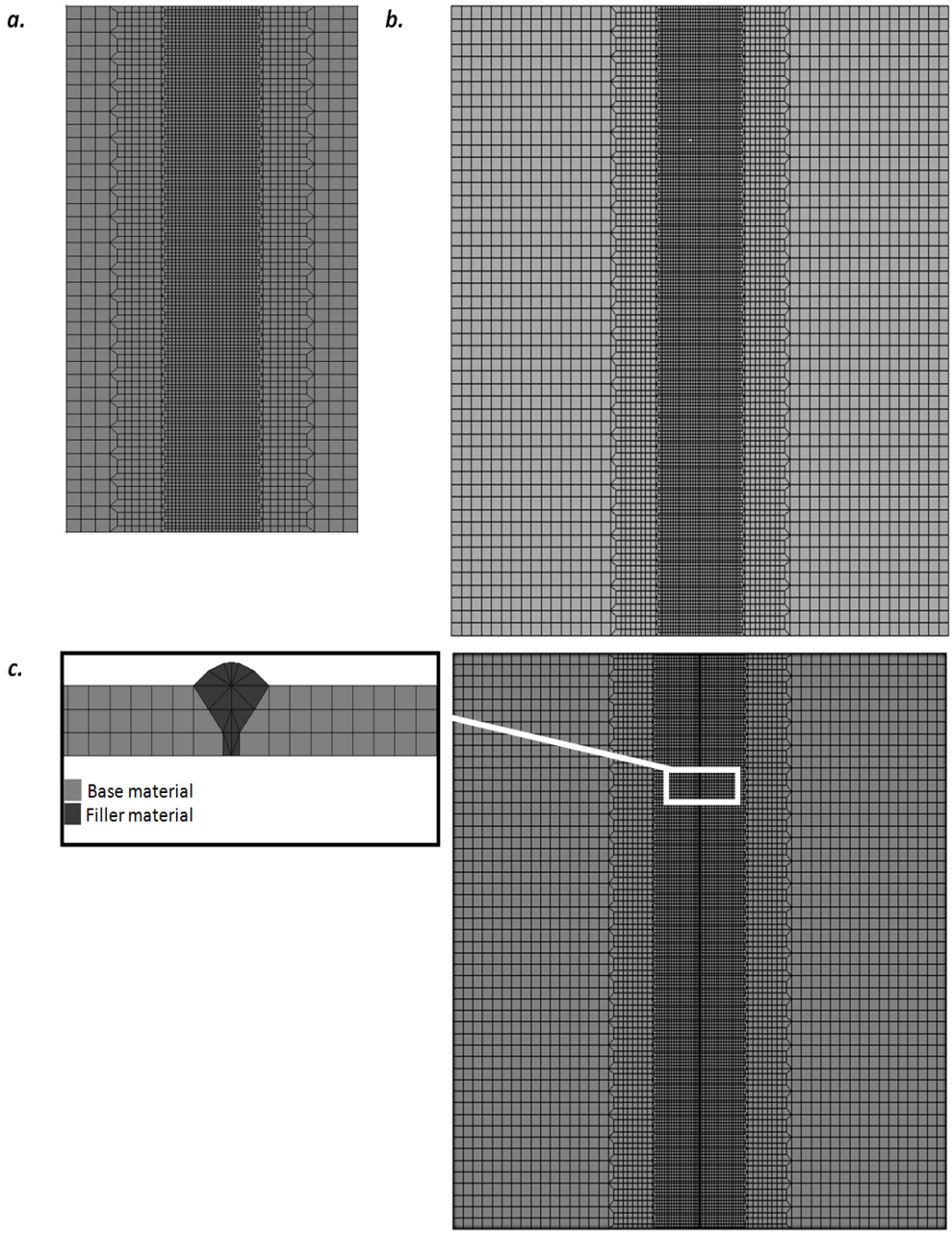

Figure 3.12. *The models used in the simulations with (a) 200 ×100×1.5 mm^3 (b) 500×500×2 mm^3 and (c) 500×500×6 mm^3 (The cross section is shown on the left side).*

The adaptive meshing criteria for thermal analysis in Msc.Marc [9] are classified into two methods: temperature gradient based criterion and the node in box criterion. In the latter case, nodes that fall in a defined box are refined during the analysis. This criterion was used in the fusion zone and the HAZ.

In order to check the effects of element size and meshing style on the predicted temperature profiles, some case studies were conducted. In the first trial, three models were used with different element size, but similar meshing style. The first model uses elements with dimensions of $0.5\times0.5\times0.5$ mm^3, while the element size for the second and third model is $1\times1\times1$ mm^3 and $2\times2\times2$ mm^3, respectively. **Figure 3.13** shows the maximum temperature predictions and the calculation time for these three models. It is clear that by increasing the element size, the maximum temperature prediction increases and the computational time decreases. However, the trends are not linear.

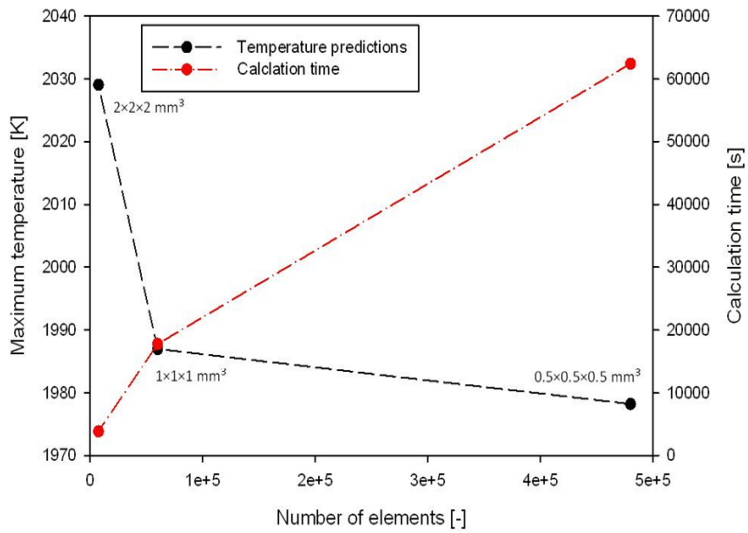

Figure 3.13. *Relations among number of elements, maximum temperature prediction and the calculation time.*

Another issue in the thermal modelling is the meshing style. For this purpose some case studies are compared. In this exercise, the models are meshed with different element sizes in the plane of the plate. The models have a similar element size of 1 mm (1 element) in the through-thickness direction, see **Figure 3.14**.

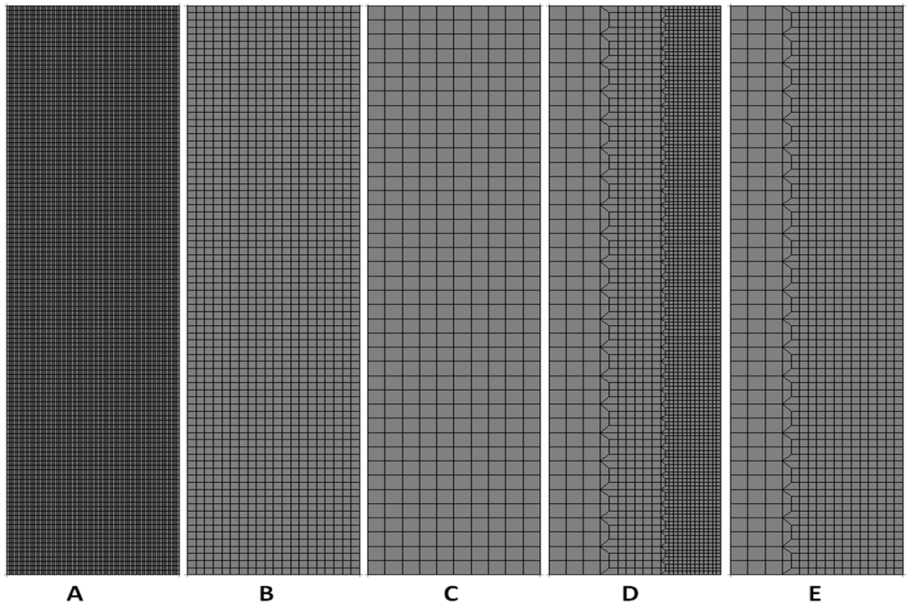

Figure 3.14. *Different models used in the simulations in order to investigate the effect of the mesh style in the plane of the plate on the maximum temperature predictions and the calculation time.*

The results of this study are summarized in **Table 3.7**. The different meshing styles lead to a difference in the predicted maximum temperature of around 214 K. This indicates that the element size and the meshing style play an important role in the calculation of the thermal field. It can also be concluded that homogeneous meshing does not improve the temperature prediction and the calculation time.

Table 3.7. *The calculation time and the predicted maximum temperature for different cases with different meshing style in the plane of the plate (see* ***Figure 3.14****).*

Cases	**No. of elements**	**Calculation time [s]**	**Max temp. [K]**	**Min element size [mm^3]**
A	60000	18665	2003	$0.625 \times 1.6 \times 1$
B	9600	3817	2007	$2.5 \times 2.5 \times 1$
C	2400	630	2209	$5 \times 5 \times 1$
D	16800	4425	1995	$1.25 \times 1.25 \times 1$
E	7200	1670	2028	$2.5 \times 2.5 \times 1$

3.2.6 Modelling of filler wire addition

In the GMAW process a consumable wire electrode is used. Droplets detached from the tip of the wire and are transferred towards the weld pool via the arc. For the case

described in **Chapter 1** where the GMAW process is applied, the addition of filler wire should be adopted in the models. In this section the approach of modelling the metal deposition in the thermal analysis is described.

There are two approaches to model the addition of filler wire in numerical simulations [44]: (a) the quiet element method and (b) the deactivated element method.

In the quiet element method, filler elements are initially present in the model with scaled down material properties. By default the scaling factor in *Msc.Marc* is 10^{-5} [9]. When the heat source approaches, the thermal properties of the filler elements are restored. This method is often applied in welding simulations [27, 45-47]. Since the geometry of the weld to be made is included in the model from the beginning, the implementation of this method is relatively easy.

In the second method, filler elements are initially not present (deactivated) in the analysis. When the heat source approaches the elements are created. This approach was used in [23, 48-49].

The first method was adopted in the simulation of the GMAW process in this investigation.

3.2.7 Modelling of additional heat sources

In the literature, thermal tensioning is modelled using different modelling methods [50-51]. The modelling of thermal tensioning by additional heat sources mainly depends on an appropriate description of the selected heat sources used in the experiments. In **Chapter 4**, the experimental options for thermal tensioning heat sources will be explained. It appears that in general oxy-acetylene/air-acetylene flames are used in practice. This heat source is also selected in the current study. Therefore, the modelling of the additional heat sources for thermal tensioning is restricted to the modelling of oxy-acetylene/air-acetylene flames.

In general, a Gaussian heat flux distribution is assumed for modelling of the gas flame with a circular shape [52]. This heat flux distribution can be expressed by:

$$q_f = q_{max} e^{-\gamma r^2}; \tag{3.12}$$

in which q_f is the heat flux at the position with a distance r to the centre of the heat source, q_{max} is the peak value of the Gaussian distribution and γ is the width factor of the Gaussian heat flux distribution. The total heat can be calculated as the integral of the distribution by:

$$Q_{total} = \int_0^{2\pi} \int_0^{\infty} q_f r dr d\theta. \tag{3.13}$$

Usually, a term (flame radius, r_{flame}) is defined for the proper selection of the flame width γ. The flame radius is the distance where q is reduced to 1% of q_{max}. Therefore, it can be expressed by:

$$0.01q_{max} = q_{max}e^{-\gamma r_{flame}^2} \Rightarrow \gamma = \frac{\ln 100}{r_{flame}^2}. \tag{3.14}$$

Figure 3.15 shows the Gaussian heat flux distribution explained above. The heat flux can be calculated from temperature measurements during heating.

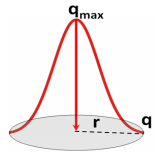

Figure 3.15. *Heat flux with Gaussian distribution over a circle.*

Circular heat sources are not the only types of heaters. Rectangular heaters can also be applied in thermal tensioning. Song *et al.* [53] used an averaged heat flux distributed over a rectangular area shown in **Figure 3.16** with dimensions of $B_s \times L_s$ by defining two functions to control the heat flux at the edges of the side heater as:

$$\bar{q} = \frac{Q_s \eta}{B_s L_s} M_x M_z; \tag{3.15}$$

$$\begin{aligned} M_x = {} & \frac{(\tanh S_{x2}(x + \phi_2 + \frac{B_s}{2}))}{2} - \frac{(\tanh S_{x1}(x + \phi_2 - \frac{B_s}{2}))}{2} \\ & + \frac{(\tanh S_{x1}(x - \phi_2 + \frac{B_s}{2}))}{2} - \frac{(\tanh S_{x2}(x - \phi_2 - \frac{B_s}{2}))}{2}; \end{aligned} \tag{3.16}$$

$$M_z = \frac{(\tanh S_{z1}(z - \frac{L_s}{2})) - (\tanh S_{z2}(z + \frac{L_s}{2}))}{2}; \tag{3.17}$$

in which Q_s is the side heating flux, η is the side heating efficiency, B_s is the band width of the side heating, L_s is the length of the side heating, x and z are local coordinates, ϕ_2 is the distance of the heaters to the weld line and S_{x1}, S_{x2}, S_{z2} and S_{z1} are parameters used to control the gradient of the heat flux at the side heater edges.

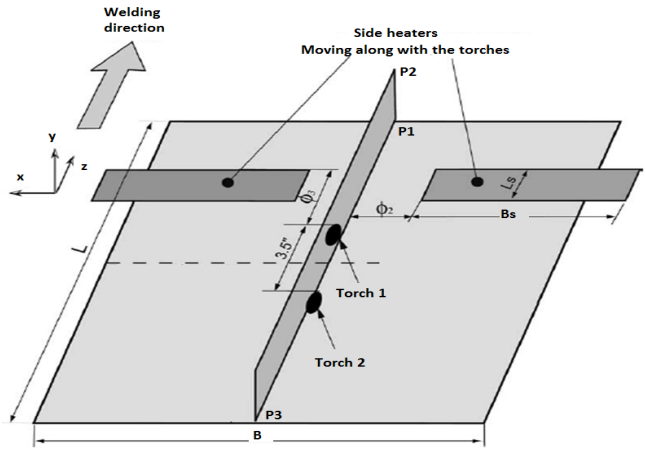

Figure 3.16. *An averaged heat flux distributed over a rectangle in order to model transient thermal tensioning burners [53].*

In this study, preliminary experiments have been conducted with a single flame while in the final experiments a burner consisting of eight flames with a separation distance of 30 mm is applied, as will be described in **Chapter 4**. For this reason, the flames have been characterized by a Gaussian heat flux distribution in the models. In the final series of experiments, a set of eight Gaussian heat flux distributions have been used, as shown in **Figure 3.17**.

Several calculations by FE thermal analysis have been carried out to determine the most suitable power density distribution, which matches the experimental results. The power density distribution is varied (by changing the heat input) until a good fit is achieved to the measured temperatures at the rear surface of the plate. The parameter values used in the modeling of the thermal tensioning heat sources are discussed in **Chapter 6**.

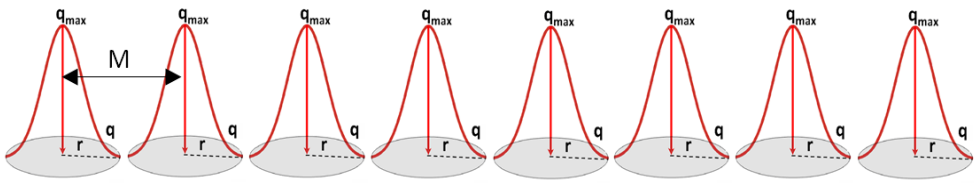

Figure 3.17. *The burners have been modelled by eight circular Gaussian heat flux distributions with radius r and separation distance of M in this thesis. The maximum heat flux for each flame is the same.*

3.2.8 Subroutines in the thermal analysis

The following subroutines were used in the thermal analysis:

1. FILM: In order to include non-uniform film coefficients for the calculation of convective boundary conditions, the FILM user subroutine has been used. This subroutine is called at each time step for each integration point for each surface element [9].

2. FLUX: This subroutine allows surface or volume fluxes to be specified as functions of time, and position. This user subroutine is called at each time step for each integration point and element listed with an appropriate flux type [9].

3. UADAPBOX: This subroutine is used to define and move the box used with the adaptive criterion node within a box for local adaptive meshing.

4. UADAP: is used to define an error criterion for local adaptive meshing. The output is the user error criteria

3.3 Microstructure analysis

Material properties are altered when new phases are created. Microstructural changes in the welded area due to thermal cycling should be considered when modelling the stress field. Solid state phase transformations may occur in steels during the heating and cooling cycle of the welding process and might also take place in the side heated areas, depending on the temperature reached. The effects of phase transformation on welded structures are the result of [54, 22]:

* changes in the material properties when new phases are formed,

* changes in specific volume when new phases are formed and

* transformation plasticity which may occur in the presence of stresses.

In this section, the procedures of phase transformation modelling adopted in this study are presented. A phase diagram presents the equilibrium fractions of the phases in an alloy (or a pure metal) at a given temperature. The two steels used in this study which undergo phase transformations are dual phase steel (DP600) and mild steel (AH36). They nominally contain 0.09 wt.% and 0.12 wt.% carbon, respectively. Depending on the heating and cooling rates either diffusion controlled (reconstructive) or displacive phase transformations occur resulting in different constituents (see **Figure 3.18**). In the **Sections 3.3.1** and **3.3.2** these groups of transformations are described. The implementation of these effects in the models is discussed in subsequent sections.

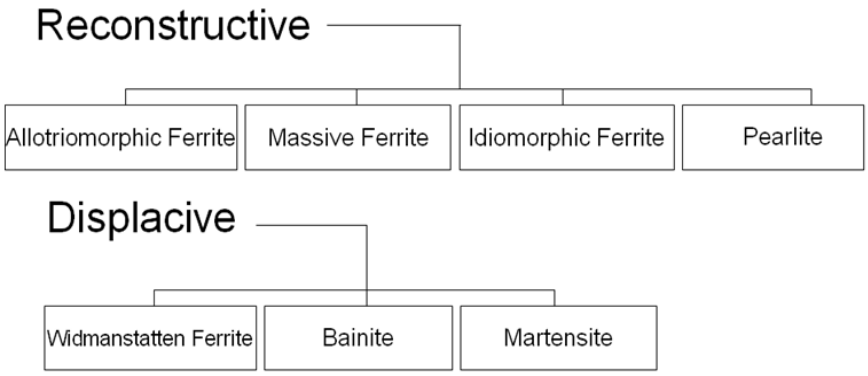

Figure 3.18. *Classification of microstructural constituents, reconstructive and displacive [54].*

3.3.1 Reconstructive phase transformations

In reconstructive or diffusion controlled transformations, the transformation occurs by rearranging the atoms into an alternative pattern [54]. The formation of pearlite, allotriomorphic and idiomorphic ferrite from austenite in steels are examples for this kind of phase transformations (see **Figure 3.18**). This type of transformation requires an incubation time to occur. Temperature and cooling rate are two main factors of the transformation kinetics. In the next section the kinetics of diffusion controlled phase transformations are presented. Although the kinetics (as well as the thermodynamics) are changed due to mechanical strains (elastic and plastic strains), it can be assumed that this effect is less significant with respect to this type of phase transformation. However, volumetric changes occur as a result of reconstructive transformations.

Kinetics of diffusion controlled phase transformations

The transformation has three stages: Initial nucleation, growth of initial nuclei in combination with steady nucleation and finally site saturation and impingement of grains [55-57]. The new phases nucleate at preferred lattice sites and each nucleus starts to grow steadily. Different mathematical models have been proposed to describe the transformation kinetics based on either isothermal or non-isothermal transformations.

(i) Isothermal transformation

In isothermal transformations the phase fraction of the newly formed phase is assumed to follow:

$$\phi(t) = kt^n; \tag{3.18}$$

where ϕ is the volume fraction of the considered phase, k and n are a temperature dependent time coefficient and a time exponent respectively. The exponent n depends

on the ratio between nucleation rate and growth rate. The parameter k, the Avrami coefficient, depends on the absolute values of the nucleation and the growth rate [55-58]. The values of k and n are usually calculated either from Time Temperature Transformation (TTT) or Continuous Cooling Transformation (CCT) curves or determined experimentally. Rather than using the Avrami coefficient k, it is preferable to use a time constant τ. Both n and τ are functions of the temperature T. The phase fraction as a function of time can then be expressed as:

$$\phi(t) = \left(\frac{t}{\tau}\right)^n . \tag{3.19}$$

With progressing transformation the available nucleation volume becomes exhausted [58]. The general rate equation is:

$$\dot{\phi}(t) = (1 - \phi(t))^r \frac{n}{\tau} \left(\frac{t}{\tau}\right)^{n-1} ; \tag{3.20}$$

where r is the saturation exponent depending on the growth mode [58] (lineal, planar, or spherical). Generally, this saturation exponent is also temperature dependent.

The Johnson-Mehl-Avrami-Kolmogorov (JMAK) expression for diffusional phase changes is obtained by integrating **Equation 3.20** over time. This equation was corrected by Leblond and Devaux [59] to account for incomplete transformations, *i.e.* full saturation is not achieved:

$$\phi(t) = \phi_0 + (\bar{\phi} - \phi_0)(1 - e^{-(\frac{t}{\tau})^n}); \tag{3.21}$$

where $\bar{\phi}$ is the volumetric equilibrium phase fraction, ϕ_0 is the volumetric initial phase fraction.

During isothermal transformation, τ is the time required to produce a certain fraction of a phase. In a TTT diagram, τ can be used to indicate the start of a reaction, the end of the reaction or any constant phase fraction curve in between.

(ii) Non-isothermal transformation

In thermally activated transformations, the thermal history determines the state of transformation. If three different thermal paths are considered (see **Figure 3.19**), each path will result in different phase fractions while the paths start and end at the same temperature and time. This indicates that functions like $\phi(T, t)$ cannot be relied upon. Thus, a new state variable which depends on the thermal path has to be defined for non-isothermal processes.

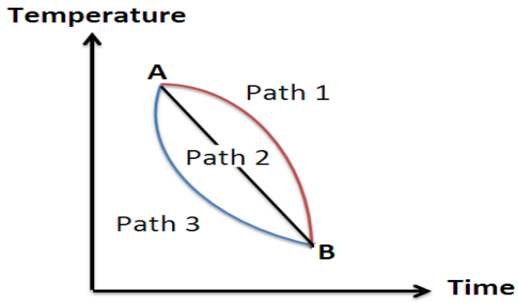

Figure 3.19. *Different phase transformations for three thermal paths with similar starting and ending time and temperature [60].*

The additivity rule proposed by Scheil [60] can be used for this purpose. The concept is extended later to solid state phase transformations by Cahn [61] and generalized by Christian [62]. According to Scheil's additivity rule, if τ_1 is the isothermal time required to reach a certain amount of transformed phase τ, the same transformation amount will be reached under non-isothermal conditions when the following Scheil's sum equals to unity [60]:

$$\int_0^{t1} \frac{dt}{\tau_1(T)} = 1. \tag{3.22}$$

Assuming the additivity rule holds, the following rate equation is valid:

$$\dot{\phi} = (1-\phi)\frac{n}{\tau}(-\ln(1-\phi))^{\frac{n-1}{n}}. \tag{3.23}$$

This expression can be approximated by:

$$\phi \approx (1-\phi)^{\frac{r+n-1}{n}} \frac{n}{\tau}\phi^{\frac{n-1}{n}}. \tag{3.24}$$

Estimation of time constants for non-isothermal transformation is based on CCT diagrams. If the cooling rate is constant, the time and the temperature are related:

$$dt = \frac{dT}{c_t}; \tag{3.25}$$

where c_t is the temperature rate. According to the additivity rule:

$$\int_0^{t_1} \frac{dt}{\tau_1(T)} = \frac{1}{c_t}\int_{T_0}^{T_1} \frac{dt}{\tau_1(T)} = 1. \tag{3.26}$$

For a small variation in the temperature rate (dc_t) and temperature (dT_1) the following equation can be obtained:

$$\tau_1 = \frac{dT_1}{dc_t}. \tag{3.27}$$

3.3.2 Displacive phase transformations

During displacive phase transformations, the transformation occurs homogeneously by deforming the original pattern into a new crystal structure [54]. A martensitic transformation is a well-known example of this category (see **Figure 3.18**). In numerical investigations the main difference of this type of transformation compared to the diffusion controlled transformations is that this transformation is considered as an instantaneous change in the crystal lattice. The martensitic transformation in steel is the only transformation that occurs just by this displacive mechanism. Bainite and Widmansttten ferrite also transform by a displacive mechanism, however the growth of bainite and Widmansttten ferrite requires the partitioning of the interstitial carbon. For this reason, their growth is controlled by diffusion although the transformation from the FCC to the BCC crystal structure is via a displacive mechanism [60]. This type of transformation results in both volume and shape changes for single crystals and in isotropic volume change and anisotropic shape change in polycrystals. In the following section the martensite transformation in steel is briefly discussed.

Martensite transformation

When the temperature drops below the martensite start temperature, M_s, martensite starts to form by a time independent transformation. Although the transformation consists of nucleation and growth stages, the growth rate is so high (*e.g.* at the speed of sound in solids) that the rate of transformation is controlled by nucleation. An equation describing the fraction of martensite formed as a function of time was proposed by Koistien and Marburger [60]:

$$\phi^m(T) = \phi^{\gamma}_{M_s}(1 - e^{\beta(T - T_{M_s})}); \tag{3.28}$$

where ϕ_{M_s} is the fraction of austenite present at M_s, the martensite start temperature and β is usually set to 0.011 [58]. The martensite-start temperature depends on the austenization conditions (carbon enrichment), stress state and prior plastic deformation. It should be noted that also the prior austenite grain size affects the martensitic transformation.

3.3.3 Modelling of phase transformation

Phase transformation can be simulated either explicitly or implicitly. The explicit methods can predict the microstructure morphology as part of the solution, while in the implicit method the results are phase fractions or the average grain size in a domain. It should be mentioned that although the implicit method does not recover the microstructure morphology, it is still widely used in welding computational mechanics. In reference [63] a review of phase transformations during welding is described.

Explicit methods include Monte Carlo, Cellular Automaton and Phase Field methods. The Monte Carlo method operates with a fixed grid of points, each being assigned

an orientation. Grains are then determined by clusters of points with identical orientations. To simulate grain growth and re-crystallization, grid points are given a probability of changing orientation within a time step. The main drawback of this method is that in the calculations there is no inherent coupling to real time. The relation between the real time and the simulation time is dependent on the assumption that the material follows the classical grain growth law. Since the grain growth laws are derived for isothermal conditions, it is questionable if it can be used as the basis for coupling measurement time and simulation [63].

In the Cellular Automaton method a lattice of contacting cells is defined as a domain. The cells can be in one of a finite number of states. Transitions which determine the cell evolution are defined according to the neighbours states. Although this method is faster than other methods, it has to be applied to the spatial and temporal temperature gradient during welding [64].

In the Phase Field method, a state variable is defined over the entire computational domain. This state (or phase-field variable) can be dependent on variables such as composition, orientation, long-range order and lattice structure. A diffuse border is represented as the region where the state variable can vary between two extreme values. This method has been used for many simulations of phase transformation.

The implicit method consists of empirical models, which are based on a large number of experiments for different welding processes and controlled heating or cooling stages. The main models commonly used in welding simulation are Continuous Cooling Transformation diagrams, the Johnson-Mehl-Avrami-Kolmogorov equation and the Koistien-Marburger equation. In previous sections the details of such models were presented. The main drawback of these methods is that the methods are composition and peak temperature dependent. The grain size of austenite above A_3 plays an important role, which is not captured in all equations. Above A_3 the austenite grains continue to grow. The coarseness of austenitic grains affects the nucleation and causes a delay of the ferrite nucleation upon cooling, which cannot be neglected. The implicit method is widely used in the modelling of welding and is adopted in this study.

3.3.4 Implementation of phase transformation

The temperature history calculated in the thermal analysis is used in the microstructure calculations. The phase fraction of the different phases is calculated. This information is used in the mechanical analysis in order to calculate the residual stress and deformation fields after welding. Different subroutines can be used before and at the end of each pass of the thermo-mechanical analysis.

The analysis starts with a thermal analysis. As stated before, the effect of solid state phase transformation on the thermal field is ignored due to the high amount

of heat generated by the welding arc and also because of the high values of latent heat of fusion compared to the latent heat of solid state phase transformations. The temperature profile for any point at any time is read by an in-house code written in *Fortran*77 to calculate phase fractions.

The literature concerning the microstructural evolution is often available in the form of time temperature transformation and continuous cooling transformation diagrams. In welding continuous cooling takes place and therefore CCT diagrams are generally used. In this study, the phase fractions are calculated at each position in the workpiece as a function of time using the appropriate CCT diagrams. The mechanical analysis is performed after the thermal analysis and phase fraction calculations. The stresses and strains due to solid state phase transformations for the area where such transformations take place, are added to the other stresses/strains in the mechanical field. Detailed information regarding interactions of mechanical and microstructural fields are discussed in **Section 3.4.5**.

3.4 Mechanical analysis

The mechanical analysis uses the results from the thermal analysis as input files. The meshes used in the thermal analysis are also used in the mechanical analysis. The main outputs of the mechanical model are the residual stress and deformation fields. In this section, the mechanical analysis of the weld employed in this thesis is discussed. The principles of the mechanical analysis apply both to the cases of welding and welding with side heating.

3.4.1 Basic equations

The equilibrium condition with respect to stresses can be written as:

$$\boldsymbol{\sigma}.\bigtriangledown = \mathbf{0}; \tag{3.29}$$

where $\boldsymbol{\sigma}$ is the Cauchy stress tensor. The stresses depend on the strains and the strains are displacement dependent:

$$\boldsymbol{\varepsilon} = \frac{1}{2}(\boldsymbol{u} \bigtriangledown + \bigtriangledown \boldsymbol{u}); \tag{3.30}$$

where $\boldsymbol{\varepsilon}$ is the strain tensor and is $\boldsymbol{u}$ the displacement vector. It can be assumed that the strain includes a number of independent terms:

$$\boldsymbol{\varepsilon} = \boldsymbol{\varepsilon}^{\boldsymbol{elastic}} + \boldsymbol{\varepsilon}^{\boldsymbol{plastic}} + \boldsymbol{\varepsilon}^{\boldsymbol{phasetrasnformation}} + \boldsymbol{\varepsilon}^{\boldsymbol{thermal}}; \tag{3.31}$$

where $\boldsymbol{\varepsilon}$ is the total strain tensor, $\boldsymbol{\varepsilon}^{\boldsymbol{elastic}}$ is the elastic strain tensor as a result of mechanical loading, $\boldsymbol{\varepsilon}^{\boldsymbol{plastic}}$ is the plastic strain tensor as a result of mechanical loading, $\boldsymbol{\varepsilon}^{\boldsymbol{thermal}}$ is the thermal strain tensor due to thermal loading and

$\boldsymbol{\varepsilon^{phasetransformation}}$ is the phase transformation strain tensor. The elastic part can be summarized as:

$$\boldsymbol{\varepsilon_{elastic}} = \frac{\boldsymbol{\sigma}}{\boldsymbol{E}}; \tag{3.32}$$

where $\boldsymbol{E}$ is the fourth order elasticity tensor. From **Equation 3.31**, the strain rate tensor ($\boldsymbol{d}$) can be defined as:

$$\boldsymbol{d} = \boldsymbol{d^{elastic}} + \boldsymbol{d^{plastic}} + \boldsymbol{d^{phasetrasnformation}} + \boldsymbol{d^{thermal}}; \tag{3.33}$$

where $\boldsymbol{d}$ is the total strain rate tensor, $\boldsymbol{d^{elastic}}$ is the elastic strain rate tensor, $\boldsymbol{d^{plastic}}$ is the plastic strain rate tensor, $\boldsymbol{d^{thermal}}$ is the thermal strain rate tensor and $\boldsymbol{d^{phasetransformation}}$ is the phase transformation strain rate tensor. The thermal strain rate tensor depends on the thermal expansion coefficient and the temperature rate:

$$\boldsymbol{d^{thermal}} = \alpha \dot{T} \mathbf{1}; \tag{3.34}$$

where α is the thermal expansion coefficient, $\dot{T}$ is the temperature rate and $\boldsymbol{1}$ is a second order unit tensor. The strain rate due to phase transformation can be expressed by:

$$\boldsymbol{d^{phasetransformation}} = \frac{-1}{3} \sum_i \frac{\rho^i}{\rho} \dot{\phi}^i \mathbf{1}; \tag{3.35}$$

where ρ is the average density of material, ρ^i is the density of each phase present and $\dot{\phi}^i$ is the phase fraction transformation rate.

3.4.2 Modelling of clamps

In almost all welding applications the workpiece is restrained. This can either be by the whole construction or by clamping devices. The plates are welded in clamped condition and after welding, the clamps/restraints are released. When the plates are fixed, the residual stresses are high, while the residual distortion is low. When the plates are allowed to move freely, the residual stresses are low and the resulting distortion is high. The influence of clamps and restraints on the welding residual stress and distortion is studied extensively [65-67]. Some critical points concerning the influence of clamping on residual stresses and distortion and the modelling of clamps are addressed below.

(i) The clamping position: Positioning of the clamps closer to the weld centreline leads to a reduction in both welding residual stress and distortion [27]. In the experimental conditions adopted in this study the position of the clamps were situated at locations that also allowed the application of side heaters. The effect of the clamp positions on the residual stress and distortion was not the scope of this investigation. A detail explanation of the clamp positions is included in **Chapter 4**.

(ii) The releasing time of the clamps: It is reported by Roeren *et al.* [36] that if a plate is clamped outside of the heat affected zone, the releasing time of clamps has

no influence on distortion. However, results presented by Schenk [27] indicate that for buckling, bending and angular distortion, longer clamping times leads to larger restraints at the weld centre line and HAZ. Therefore, the plastic deformation increases and the final deformation of the plate after releasing the clamps is reduced. The effect of the releasing time of the clamps has been investigated for a case where the clamps are released immediately after the welding process stopped. The plate cools after welding in an un-clamped condition. The results indicated that the final distortion of the plate is higher when the clamps are released directly after welding. In order to compare different situations in this work, *e.g.* conventional welding and welding with additional heating sources, and to exclude the effect of clamp release time, the clamps were always released when the temperature of the plate reached room temperature.

(iii) The clamping forces: Clamping forces have been measured in several welding applications [27, 68-69]. The force measurement sensors should be included in the system. In **Chapter 4** a common clamping system is described, which is employed in this investigation to prevent the movement of the plate. The clamping forces are not measured and just estimated in the numerical modelling.

(iv) Modelling of the clamps: Different approaches from simply fixing the displacement of clamped nodes to three dimensional modelling of clamps explicitly can be used to simulate a clamping system. Three common modelling approaches are used depending on the goal of the modelling:

(1) Fixed displacement: Fixing the displacement of the clamped nodes can change the residual stress profile [27]. Also the direction in which the nodes are fixed will affect the residual stress predictions. Although this method can be used for fast calculations of residual stresses and distortion, it is in general not recommended [22, 37].

(2) The application of springs: A very common approach used in welding mechanics modelling is the application of spring elements to describe the boundary condition in the models. The clamping system is modelled by applying spring links with certain stiffness between nodes on the plate edges and a series of fixed nodes outside the plate [22]. During welding, the plate is clamped and therefore high spring stiffness is defined in the model. The releasing the clamps is modelled by gently reducing the spring stiffness. It is shown by [22, 33 and 70] that clamping in the out-of-plane direction has far less influence on the longitudinal residual stress distribution than clamping in the transverse direction. This approach can predict the residual stresses more accurately than the first approach, as is also shown by van der Aa [22]. Another advantage of this approach is the low computational time.

(3) Using contact bodies: The third approach is the modelling of the clamping system using contact bodies. In this method the contacting bodies are modelled together with the plate. Although this approach can predict the residual stresses closer to reality [34] than the approaches described above, there are some drawbacks which limit the

application of this method. These drawbacks include the more expensive computational time, the unknown friction coefficient between the surfaces of the workpiece and the contact body and problems related to numerical convergence. In the present study the clamping is modelled by applying spring links as shown in **Figure 3.20a** for small plates and in **Figure 3.20b** for large plates.

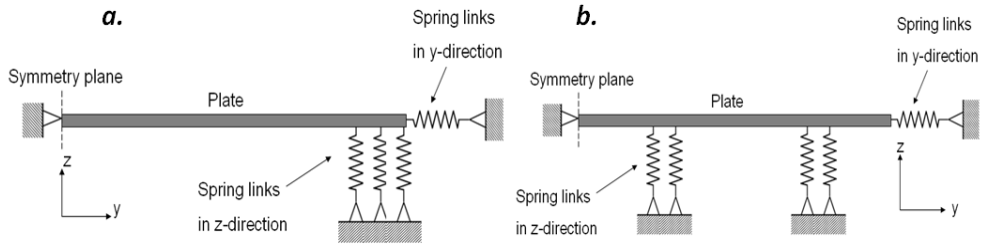

Figure 3.20. *Modelling approach for the clamping system for (a) small plates of 200×100×1.5 mm^3 and (b) large plates of 500×500×2 or 6 mm^3.*

The user subroutine USPRNG is used to manipulate the spring stiffness during and after welding. The spring stiffness applied in the calculation is based on comparison of the calculations to the experimental results. The best value which gives a close prediction to the measurement is selected. In the clamped condition a value of 2×10^7 Nm^{-1} for the spring stiffness in all directions is used. In the clamp release stage, the spring stiffness K_s is defined as a function of the releasing time (t) and can be expressed as follows:

$$K_s = 2 \times 10^7 \times (1 - t^7). \tag{3.36}$$

3.4.3 Temperature dependant mechanical material properties

The temperature dependant mechanical material properties used in the simulations of the materials used in this study are shown in **Figure 3.21** [22, 27].

Figure 3.22 shows the stress-strain relationship for the materials used in this thesis as well as the work hardening behaviour of the materials at elevated temperatures.

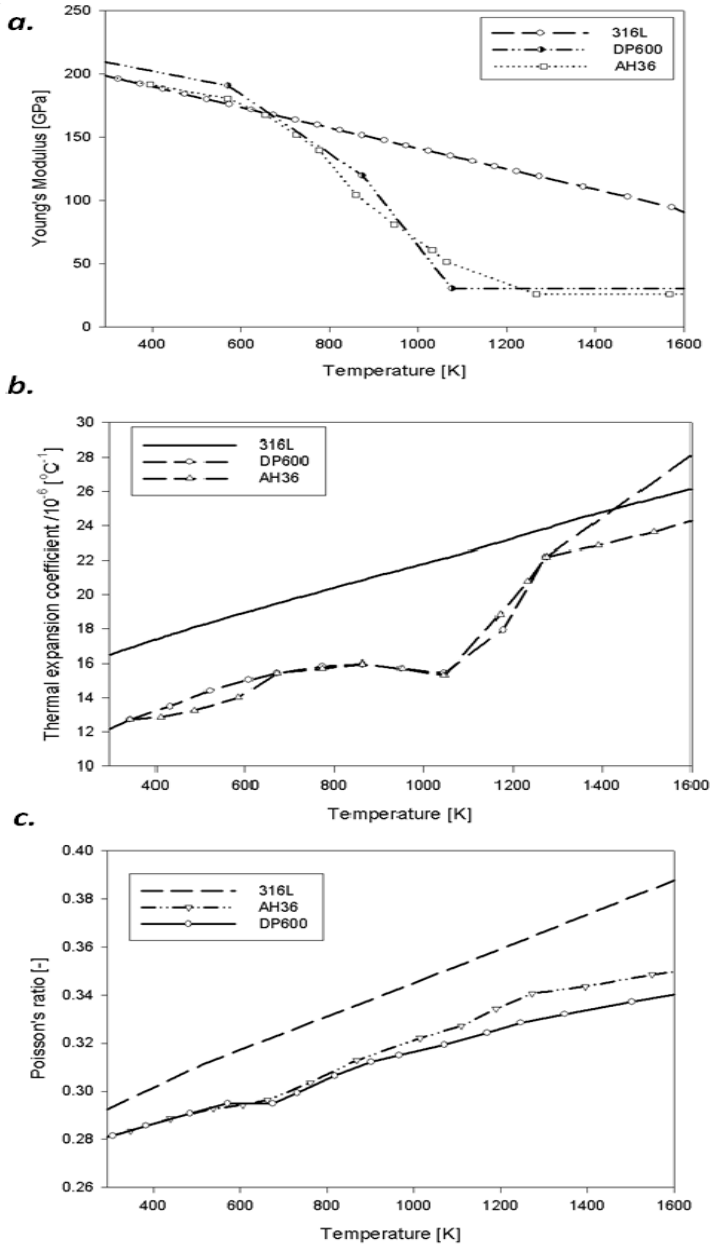

Figure 3.21. *Mechanical material properties used in the simulations: (a) Young's modulus as a function of temperature, (b) Thermal expansion coefficient as a function of temperature and (c) Poisson's ratio as a function of temperature for AISI-316L [22], DP600 [27] and AH36 [27].*

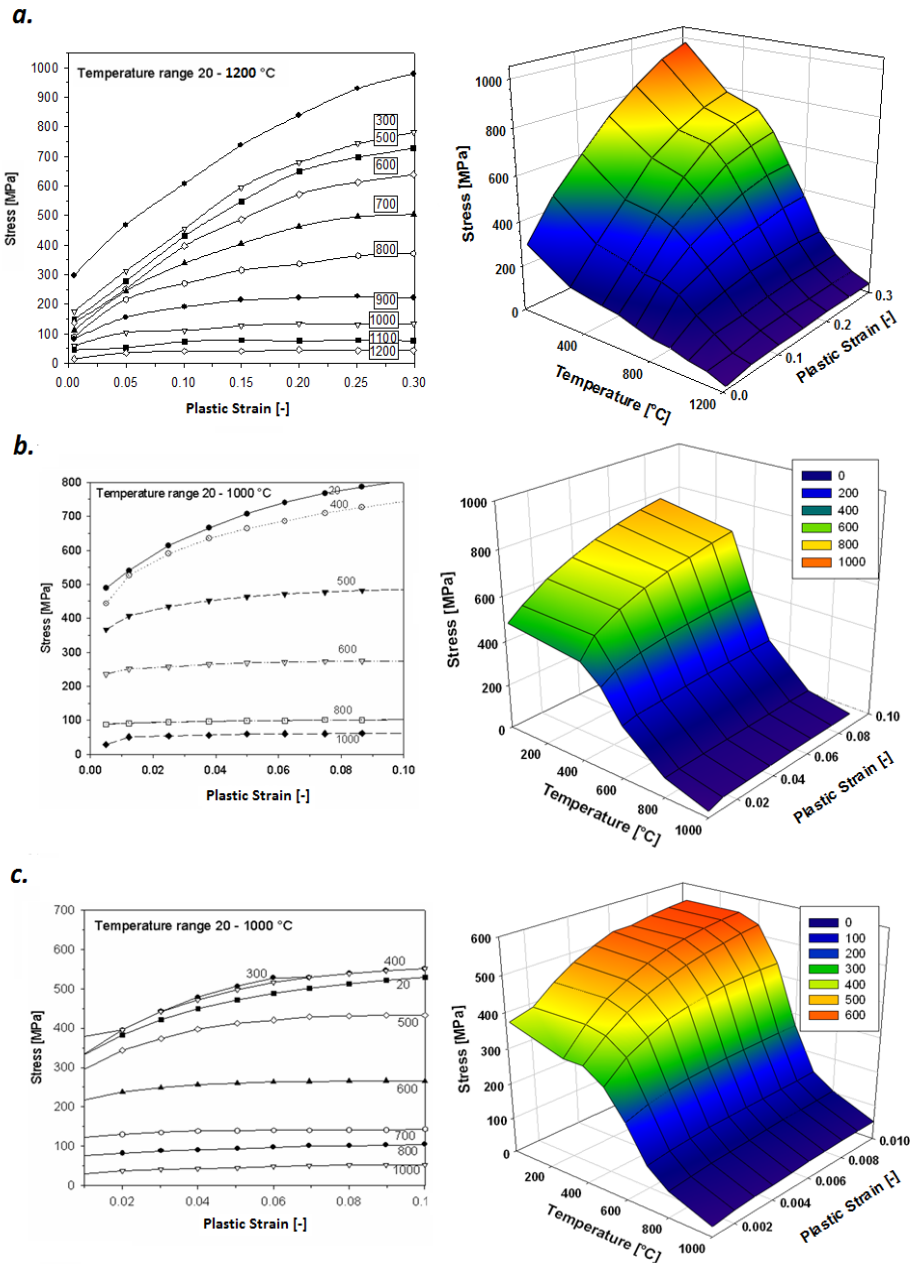

Figure 3.22. *Stress-Strain relationship of (a) AISI-316L [22], (b) DP600 [27] and (c) AH36 [27] as a function of temperature.*

The work hardening behaviour of the material has been represented by two different hardening models:

Isotropic hardening: In an isotropic hardening model, it is assumed that the centre of the yield surface is fixed in stress space, while the size of the yield surface increases. In **Figure 3.23a**, a stress-strain curve of a uniaxial loading history is shown, while in **Figure 3.23b** the corresponding points are plotted in the stress space. From the origin to point 1, the material behaves elastically. From point 1 to point 2 the material is plastically deforming and the size of the yield surface is increased. During releasing of the tensile load and reversing to compression, elastic deformation will occur from point 2 to point 3. By plastically loading the material from point 3 to point 4, the size of the yield surface is further increased [71].

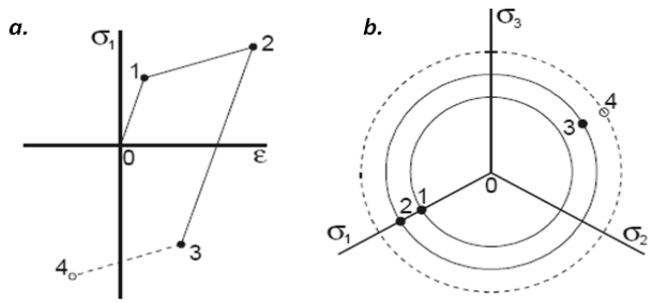

Figure 3.23. *Isotropic hardening model: (a) uniaxial loading history and (b) the corresponding points in the stress space [71].*

In the *Kinematic model*, the size of the yield surface is constant while the work hardening is represented by translating the centre of the yield surface. As can be seen from **Figure 3.24**, the material behaves elastically until the yield surface is reached at point 1. From point 1 to point 2 the material is plastically loaded and the yield surface now moves from point 1 to point 2 in the corresponding stress space. However, the size remains constant. Upon reversing the loading direction at point 2, elastic unloading and reloading occurs. Due to the work hardening in the loading stage, the compressive yield stress at point 3 is reduced. By plastically loading the material from point 3 to point 4, the yield surface now moves in the opposite direction [71].

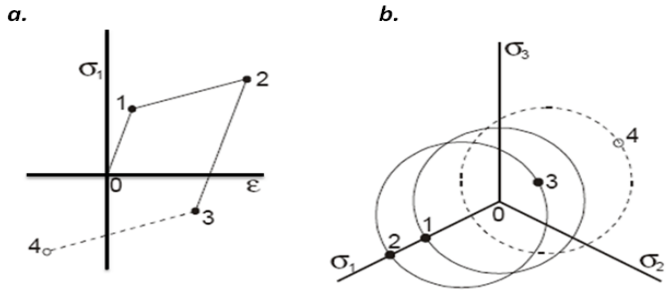

Figure 3.24. *Kinematic hardening model: (a) loading history (b) corresponding points in stress space [71].*

Mixed isotropic-kinematic hardening model: This model is based on the following equation [72]:

$$\sigma = \sigma_y + K_t \dot{\varepsilon}^m + S(1 - e^{-d_s p}); \tag{3.37}$$

in which σ_y is the yield stress, K_t is the plastic viscosity, m a visco-plastic exponent, d_s is the hardening slope, S is the hardening saturation and p is the plastic strain.

All relevant parameters of the isotropic hardening model are used from [72]. From tensile tests the parameter values for the second hardening model (mixed hardening model) can be derived.

Both isotropic and mixed hardening models were applied in the residual stress prediction of DP600 steel and the results were compared. It was found that the isotropic hardening model slightly overestimates the final residual stresses. The mixed hardening model predicts the residual stresses more accurately. However, the mixed hardening model depends on a large number of temperature dependent material properties. These properties are hard to obtain from the literature and difficult and time consuming to measure. The isotropic hardening model was therefore used in all simulations.

3.4.4 Modeling of filler wire addition

As stated in **Section 3.2.6**, filler wire is modeled using the quiet element method. This means that filler elements are initially available in the model with scaled down material properties [9].

3.4.5 Interactions of mechanical and phase transformation fields

During phase transformation, new phases with new material properties are created, which is accompanied by changes of the specific volume of the material (*transformation strains*). The new phases like martensite can increases the strength of the material. In the first part of this section the effects of phase transformation on the

stress field is presented. The modification of the kinetics of the phase transformation in the presence of stresses will be discussed subsequently.

Transformation strains

The mass density of a material with different phase fractions can be expressed by [58]:

$$\rho = \sum_{i=1}^{i=n} \rho_i \phi_i; \tag{3.38}$$

where ρ is the mass density of the material, ρ_i is the mass density of a specific phase i, ϕ_i is the phase fraction of that phase while n is the number of phases present in the material. The mass density of the phases is a temperature dependent property. The rate of change of the mass density can be written as:

$$\frac{d\rho}{dt} = \sum_{i=1}^{i=n} (\rho_i \dot{\phi}_i + \frac{d\rho_i}{dT} \dot{T} \phi_i); \tag{3.39}$$

where t indicates the time and T is the temperature. The term $\rho_i \dot{\phi}_i$ is the density change due to the phase transformations.

Kinetics modifications

Both hydrostatic pressure and deviatoric stresses alter the kinetics of phase transformation. If the positive hydrostatic pressure is positive, both T_{A_1} and T_{M_s} are lowered [73]. Moreover, the pearlitic transformation as well as the martensitic transformation is enhanced by deviatoric stresses.

Stress effects of pearlitic and ferritic transformations Most of the approaches used to model the effect of stress on the ferritic and the pearlitic transformation are based on modifications of the JMAK equation and Scheils additivity rule. The influence of stress on the kinetics of the pearlite transformation during cooling is present as a stress dependent time constant τ in the Avrami equation [73]:

$$\tau(T, \sigma_{eq}, p) = f(\sigma_{eq}, p)\tau(T) = \tau(T) e^{-A_\tau \sigma_{eq} + B_\tau p}. \tag{3.40}$$

Stress effects of martensitic transformations

The martensite start temperature (T_{M_s}) is affected by the stress and plastic deformation. There are some models developed [74-77], which include the effect of stresses on the martensitic transformation. Denis *et al.* [78] proposed a model, which relates the change of T_{M_s} to the mean stress (σ_m) and the von Mises effective stress ($\bar{\sigma}$):

$$\triangle T_{M_s} = C_1 \sigma_m + C_2 \bar{\sigma}; \tag{3.41}$$

where C_1 and C_2 are material constants.

The stress effects on the martensitic transformations and the kinetic modification are not included in the model because of the lack of the experimental parameter values. The transformation strains and the increase of strength due to formation of martensite are calculated and incorporated in the model.

Subroutines for effects of microstructure on the mechanical field

Two main subroutines were used in the microstructure analysis:

(i) ANEXP: This subroutine is used to specify anisotropic thermal strain increments. The ANEXP user subroutine is called for all elements at all integration.

(ii) WKSLP: This user subroutine makes it possible for the user to program the yield stress and the corresponding work-hardening slope directly as a function of equivalent plastic strain and temperature. The user needs to define the value of the slope of the equivalent stress versus the equivalent plastic strain.

Subroutines in the mechanical analysis

The following subroutines were used in the mechanical analysis:

(i) UACTIVE: This subroutine either activates or deactivates elements. The user subroutine is called at the beginning of the analysis and at the end of each increment. A deactivated element does not contribute to load, mass, stiffness, or internal force calculations [9].

(ii) USPRNG: This subroutine permits the introduction or further modification of non-linear spring constants [9]. This is mainly used in the modelling of clamps (see **Section 3.4.2**).

3.4.6 Simplified mechanical models

The first simplification in an analysis is related to the model symmetry. This means that only half of the model is created and included in the analysis. The second simplification is related to the material properties. In general, material properties used in analyses are specified to a certain temperature (cut-off temperature) [72]. The mechanical properties of the steels are not implemented above this temperature. The main reason for such an assumption is related to the reduction of the elastic modulus of steel to low values above this temperature. Therefore, strains acquired, when the temperature exceeds the cut-off temperature, do not contribute significantly to the final residual stress state [79].

In this study, shell models have been used for the large sheets of less than 6 mm thickness. It is assumed that due to the full penetration welds obtained, the bottom surface of the plates experiences the same temperatures as the top surface. Through-thickness stresses can therefore be ignored. For thick plates solid elements were applied.

3.5 Concluding remarks

The finite element modelling background and procedures used to investigate the thermal, the microstructural and the mechanical fields in both conventional welding and welding with additional heating are presented in this chapter. The assumptions used in all three fields are explained in more detail. It should be mentioned that the models and the procedures explained here result in a reasonably good agreement with the experimental measurements. Since the main goal of these models is the investigation of additional heating during welding, the current models are satisfactory. The results of numerical modelling are presented and experimentally validated in **Chapter 6**.

Reference

[1] L-E. Lindgren, *Computational Welding Mechanics*, Taylor and Francis Group, 2007.

[2] J. A. Goldak, M. Akhlaghi, *Computational Welding Mechanics*, Springer, 2005.

[3] E. Friedman, *Thermomechanical Analysis of the Welding Process Using the Finite Element Method*, Journal of Pressure Vessel Technology, Vol 97, pp. 206-213, 1975.

[4] Y. Shim, Z. Fng, D. Kim, J. Jaeger, J. C. Papritan, C. L. Tsai, *Determination of Residual Stresses in Thick-Section Weldments*, Welding Journal, Vol. 71(9), pp. 305-312, 1992.

[5] H. D. Hibbit, P. V. Marcal, *A Numerical Thermo-Mechanical Model for the Welding and subsequent Loading of a fabricated Structure*, Computers and Structures, 3, pp. 1145-1174, 1973.

[6] P. Ferro, H. Porzner, A. Tiziani, F. Bonollo, *The influence of phase transformations on residual stresses induced by the welding process-3D and 2D numerical models*, Modelling and Simulation in Material Science and Engineering, Vol. 14, pp. 117-136, 2006.

[7] L. Fuglsang-Andersen, *Residual Stresses and Deformations in Steel Structures*, PhD thesis, DTU, 2000.

[8] M. Goodarzi, *Mathematical modelling of gas tungsten arc welding and gas metal arc welding processes*, PhD thesis, University of Toronto, 1997.

[9] *Msc.Marc Manuals*, MSC.Software, 2007.

[10] D. Balagangadhar, *A displacement-based reference frame formulation for steady-state thermo-elasto-plastic material processes*, International Journal of Solids and Structures, Vol. 36, No. 16, pp. 2397-2416, 1999.

[11] S. Rajadhyaksha, P. Michaleris, *Optimization of thermal processes using an Eulerian formulation and application in laser hardening*, International Journal for Numerical Methods in Engineering, Vol. 47, pp. 1807-1823, 2000.

[12] J. Shanghvi, and P. Michaleris, *Thermo-elasto-plastic finite element analysis of quasi-state processes in Eulerian reference frames*, International Journal for Numerical Methods in Engineering, Vol. 53, pp. 1533-1556, 2002.

[13] S. Paul, P. Michaleris, and J. Shangvi, *Optimization of thermo-elasto-plastic processes using Eulerian sensitivity analysis*, International Journal for Numerical Methods in Engineering, Vol. 56, pp. 1125-1150, 2003.

[14] L. Zhang, P. Michaleris, *Investigation of Lagrangian and Eulerian finite element methods for modelling the laser forming process*, Finite Elements in Analysis and Design, Vol. 40, pp. 383-405, 2004.

[15] J. Goldak, M. Gu, *Computational weld mechanics of the steady state*, Mathematical Modelling of Weld Phenomena 2, The Institute of Materials, 1995.

[16] D. Atteridge, *3D Eulerian modeling of electroslag welding*, 5th International Conference on Trends in Welding Research, Pine Mountain, Georgia, USA, 1998.

[17] J. F. Lancaster, *Metallurgy of Welding*, Chapman and Hall, 1994.

[18] M. Tanaka and J. Lowke, *Predictions of weld pool profiles using plasma physics*, Journal of Physics D: Applied Physics, No. 40, R1-R23, 2007.

[19] T. Schenk, I. M. Richardson, G. Esser, M. Kraska, S. Ohnimus, *Welding Distortion of DP600 Overlap Joints and Influence of Clamping and Phase Transformation*, Proceedings of 2nd International Workshop on Thermal Forming and Welding Distortion, IWOTE 2008, Bremen, pp. 83-96, 2008.

[20] T. Schenk, D. Tikhomirov, M. Kraska, I. M. Richardson, *Modelling clamping conditions for welding simulations of 1mm thick DP600 overlap joints*, 9th International Seminar on Numerical Analysis of Weldability, Seggau, Austria, 2009.

[21] J. Dike, C. Cadden, R. Cordeman, *Finite Element Modelling of Multipass GMA Welds in Steel Plates*, Proceedings of 4th International Conference on Trends in Welding Research, Gatlinburg, Tennessee, USA, pp. 57-65, 1995.

[22] E. M. van der Aa, *Local cooling during welding: prediction and control of residual stress and buckling distortion*, PhD thesis, Technische Universiteit Delft, 2007.

[23] A. Pilipenko, *Computer simulation of residual stress and distortion of thick plates in multi-electrode submerged arc welding Their mitigation techniques*, PhD thesis, NTNU Trondheim, 2001.

[24] S. Kou, *Welding metallurgy*, John Wiley and Sons, 2002.

[25] W. H. Giedt, L. N. Tallerico, P. W. Fuerschibach, *GTA Welding Efficiency Calorimetric and Temperature Field Measurements*, Welding Journal, Vol. 68, No. 1, pp. 28-31, 1989.

[26] P. W. Fuerschbach and G. A. Knorovsky, *A Study of Melting Efficiency in Plasma Arc and Gas Tungsten Arc Welding*, Welding Journal, 70, pp. 287s-297s, 1991.

[27] T. Schenk, *Modelling welding distortion: Influence of clamping and sequencing*, PhD thesis, Delft University of Technology, 2011.

[28] N. T. Nguyen, *Thermal Analysis of Welds*, WIT press, 2004.

[29] D. Rosenthal, *Mathematical theory of heat distribution during welding and cutting*, Welding Journal, Vol. 20, No. 5, pp. 220-234, 1941.

[30] V. Pavelic, R. Tanbakuchi, O. A. Uyehara and P.S. Myers, *Experimental and computed temperature histories in Gas Tungsten Arc Welding of thin plates*, Welding Journal, Vol. 48, No. 7, pp. 295s-305s, 1969.

[31] Z. Paley, P. D. Hibbert, *A new finite element model for welding heat sources*, Welding Journal Research Supplement, Vol. 54, pp. 385-392, 1975.

[32] J. Goldak, *A finite element model for welding heat sources*, Metallurgical Transactions, Vol. 15B, pp. 299-305, 1984.

[33] R. V. Preston, *Modelling of residual stress in welded aerospace alloys*, PhD thesis, University of Cambridge, 2000.

[34] T. Böllinghaus, T. Kannengieβer, *Effect of filler material selection and shrinkage restraint on stress strain buildup in component welds*, Proceedings of the 6th International Trends in Welding Research Conference, Callaway Gardens Resort, Phoenix, Arizona USA, pp. 906-911, 2003.

[35] Y. Wei, Z. Dong, R. Liu, Z. Dong, Y. Pan, *Numerical simulation and prediction of weld solidification cracking*, Mathematical Modelling of Weld Phenomena 7, pp. 651-669, 2005.

[36] S. Roeren, C. Schwenk, M. Rethmeier, *Different approaches to model clamping conditions within a weld simulation*, Proceedings of the 8th Conference on Mathematical Modelling of Weld Phenomena, S. 1093-1106, 2006.

[37] P. Tekriwal, J. Mazumder, *Finite Element Analysis of Three-Dimensional Transient Heat Transfer in GMA Welding*, Welding Journal, Vol. 67, No. 5, pp. 150-156, 1988.

[38] S. Allmeier, *Untersuchung von Schweißeigenspannungen an Aluminiumkonstruktionen*, PhD thesis, TU München, 2005.

[39] S. Brown, H. Song, *Finite Element simulation of welding of large structures*, Journal of engineering for industry, 114, pp. 441-445, 1992.

[40] P. Michaleris, A. DeBiccari, *Prediction of welding distortion*, Welding Journal, Vol. 76, pp. 172s-180s, 1997.

[41] R. Pehlke, A. Jeyarajan, and H. Wada, *Summary of Thermal Properties for Casting Alloys and Mold Materials*, University of Michigan, 1982.

[42] Y. V. L. N. Murthy, G. V. Rao and P. K. Iyer, *Numerical simulation of welding and quenching processes using transient thermal and thermo-elasto-plastic formulations*, Computers and Structures, Vol. 60, No.1, pp. 131-154, 1996.

[43] S. A. Tsirkas, P. Papanikos, Th. Kermanidis, *Numerical simulation of the laser welding process in the butt joint specimens*, Journal of Material Processing and Technology, 134, pp. 59-69, 2003.

[44] R. Pietzsch, *Simulation und Minimierung des Verzuges von Stahlprofilen beider Abkühlung*, PhD thesis, University of Magdeburg, 2000.

[45] N. Ma, Y. Ueda, H. Murakawa, H. Maeda, *FEM Analysis of 3D Welding Residual Stresses and Angular Distortion in T-type Fillet Welds*, Transactions of joining and welding research institute of Osaka University, Vol. 24, No. 2, pp. 115-122, 1995.

[46] T. L. Teng, P. H. Chang, W. C. Tseng, *Effect of welding sequences on residual stresses*, Computers and Structures, Vol. 81, No. 5, pp. 273-286, 2003.

[47] J. A. Free, R. F. D. P. Goff, *Predicting residual stresses in multi-pass weldments with the finite element method*, Computers and Structures, Vol. 32, No. 2, pp. 365-378, 1989.

[48] C. Hackmair, *Messung und numerische Simulation der Schweißverzge an Aluminium-Fahrwerkskomponenten*, PhD thesis, University of Technology München, 2003.

[49] W. W. Wilkening, J. L. Snow, *Analysis of Welding-Induced Residual Stresses With the Adina System*, Computers and Structures, Vol. 47, No. (4/5), pp. 767-786, 1993.

[50] P. Michaleris, and X. Sun, *Finite Element Analysis of Thermal Tensioning Techniques Mitigating Weld Buckling Distortion*, Welding Journal, Vol. 76, No. 11, pp. 451s-457s, 1997.

[51] M. V. Deo and P. Michaleris, *Mitigation of welding induced buckling distortion using transient thermal tensioning*, Science and Technology of Welding and Joining, Vol. 8, No. 1, pp. 49-53, 2003.

[52] H. B. Clausen, *Plate forming by line heating*, PhD thesis, Technical University of Denmark, April, 2000.

[53] J. Song, J. Y. Shanghvi, P. Michaleris, *Sensitivity analysis and optimization of thermo-elasto-plastic processes with applications to welding side heater design*, Computational Methods in Applied Mechanical Engineering, Vol. 193, pp. 4541-4566, 2004.

[54] H. Bhadeshia, R. Honeycombe, *Steels: Microstructure and Properties*, Third Edition, Butterworth-Heinemann, 2006.

[55] M. Avrami, *Kinetics of Phase Change I. General Theory*, Journal of Chemical Physics, 7:1103, 1939.

[56] M. Avrami, *Kinetics of Phase Change II. Transformation-Time Relations for Random Distribution of Nuclei*, Journal of Chemical Physics, 8:212. 1940.

[57] M. Avrami, *Kinetics of Phase Change III. Granulation, Phase Change, and microstructure*, Journal of Chemical Physics, 9:177, 1941.

[58] H. J. M. Geijselaers, *Numerical Simulation of Stresses due to Solid State Transformations*, PhD thesis, Twente University, 2003.

[59] J. Leblond, J. Devaux, *Mathematical Modelling of Transformation Plasticity in Steels I: Case of Ideal-Plastic Phases*, International Journal of Plasticity, Vol. 5, pp. 551-572, 1989.

[60] C. Simsir, *3D finite element simulation of steel quenching in order to determine the microstructure and residual stresses*, Middle East Technical University, PhD thesis, 2008.

[61] J. W. Cahn, *Transformation Kinetics During Continuous Cooling*, Acta Metallurgica, 4:572, 1956.

[62] J. W. Christian, *The Theory of Transformations in Metals and Alloys*, Pergamon Press, Oxford, 1975.

[63] I. M. Richardson, M. Amirthalingam, M. J. M. Hermans, N. J. den Uijl, M. K. Wibowo, *The influence of welding on advanced high strength TRIP and DUAL PHASE steels*, 9th International Seminar on Numerical Analysis of Weldability, Graz-Seggau, pp. 185-214, 2009.

[64] R. G. Thiessen, *Physically-based Modelling of Material Response to Welding*, PhD thesis, Technische Universiteit Delft, 2007.

[65] M. Watanabe, K. Satoh, *Effect of welding conditions on the shrinkage distortion in welded structures*, Welding Journal, August, pp. 377-384, 1961.

[66] M. Watanabe, K. Satoh, K. Kimura, R. Hoshi, *Effect of Welding Methods and Sequences on the Residual Stress Distribution of Welded Joints*, Japan Welding Society, Vol. 24, No. 4, pp. 146-153, 1955.

[67] M. Staubach, R. Müller, S. Jüttner, *Messung und Minimierung schweißtechnisch bedingter Verzüge an Profil-T-Stoßverbindungen*, Schweißen und Schneiden, Vol. 58, No. 10, pp. 520-523, 2006.

[68] T. Boldt, *Clamping systems for laser welding processes*, Ölhydraulik und Pneumatik, Vol. 48, No. 2, pp. 1-26, 2004.

[69] B. Lenz, *Finite Elemente-Modellierung des Laserstrahlschweißens für den Einsatz in der Fertigungsplanung*, PhD thesis, TU München, 2001.

[70] R. V. Preston, H.R. Shercliff, P. J. Withers, D. J. Huges, S. D. Smith and P. J. Webster, *Synchrotron X-Ray Measurement and Finite Element Analysis of Residual Strain in TIG Welded Aluminium 2024*, Metallurgical and Materials Transactions A, Vol. 37, No. 12, pp. 3629- 3637, 2006.

[71] C. H. L. J. ten Horn, *Cyclic plastic deformation and welding simulation*, PhD thesis, Delft University of Technology, 2002.

[72] T. Schenk, I. M. Richardson, M. Karska, *Influence of the hardening model on the predicted welding distortion of DP600 Lap Joints*, Proceedings of the THERMEC 2009, Berlin, Vol. 638-642, pp. 3710-3715, 2009.

[73] S. Sarkani, V. Tritchkov, G. Michaelov, *An efficient approach for computing residual stresses in welded joints*, Finite Elements in Analysis and Design, Vol. 35, pp. 247-268, 2000.

[74] F. Fischer, *A micromechanical model for transformation plasticity in steels, Acta Metallurgical et Materialia*, Vol. 38, No. 8, pp. 1535-1546, 1990.

[75] K. Tanaka, and Y. Sato, *A mechanical view of transformation plasticity*, Ingenieur-Archiv, Vol. 55, pp. 147-155, 1985.

[76] T. Inoue, and Z. Wang, *Finite element analysis of coupled thermo-inelastic problem with phase transformation*, Numerical Methods in Industrial Forming Processes, Pineridge Press, Swansea, pp. 391-400, 1982.

[77] T. Inoue, and Z. Wang, *Coupling between stress, temperature, and metallic structures during processes involving phase transformations*, Materials Science Technology, Vol. 1, pp. 845-850, 1985.

[78] S. Denis, *Stress-phase-transformation interactions - basic principles, and calculation of internal stresses*, Materials Science and Technology, No. 1, pp. 805-814, 1985.

[79] P. Tekriwal, J. Mazumder, *Transient and residual thermal strain-stress analysis of GMAW*, Journal of Material Technology, Vol. 113, pp. 337-343, 1991.

Chapter 4

Experimental investigations

This chapter starts with an introduction to the base materials used in this study. It was indicated in **Chapter 1**, that three case studies are defined for the laboratory tests and one case study is set for industrial implementation. This industrial case study is the topic of **Chapter 7**. For the three cases of the laboratory tests, different sets of experiment are defined related to specific types of steel as shown in **Table 4.1**.

Table 4.1. *Weld and joint design for preliminary and final stages.*

Cases	**Materials**	**Dimensions mm×mm×mm**	**Weld design**	**Joint design**
Case I-A	AISI-316L	200×100×1.5	BOP[1]	-
Case I-B	AISI-316L	500×250×2	Butt	Square
Case II-A	DP600	200×100×1.5	BOP[1]	-
Case II-B	DP600	500×250×2	Butt	Square
Case III	AH36	500×250×6	Butt	Y-groove

1. BOP=Bead On Plate.

The welding equipment and set-up are discussed in **Section 4.2**. The arrangement for welding with additional heating experiments is explained in the subsequent section. The experimental procedures of additional laboratory tests, *i.e.* distortion, temperature measurements, microstructure investigation and residual stress measurements, are explained in the last part of this chapter.

4.1 Base materials and specimens size

Three different types of steel were selected: an austenitic stainless steel AISI-316L, a dual phase steel DP600 and a fine grained construction steel AH36.

AISI-316L is an austenitic stainless steel with approximately 4 to 6 wt.% δ-ferrite.

The material properties of such steel are well known and the temperature dependent mechanical properties have been measured by van der Aa [1]. During the weld thermal cycle, this material does not undergo any significant solid state phase transformations. **Table 4.2** shows the typical chemical composition of AISI-316L stainless steel.

Table 4.2. *Typical chemical composition of AISI-316L stainless steel [2], Fe balance.*

	C	**Mn**	**Si**	**Cr**	**Ni**	**Mo**	**N**	**P**	**S**
Max wt.%	0.030	2.00	0.75	16-18	10-14	2-3	0.10	0.045	0.030

DP600 steel is a dual-phase steel, commonly used in thin sheet automotive applications, due to its strength and formability properties. This alloy consists of a matrix of soft ferrite (approximately 90%) with islands of martensite 10%. A specific inter-critical annealing heat treatment is applied to produce this microstructure with optimum mechanical properties.

During welding dual phase steel, the material undergoes solid state phase transformations. Therefore, the engineered microstructure is destroyed and the amount of hard constituents like martensite increases in the fusion zone (FZ) and the Heat Affected Zone (HAZ). The typical chemical composition of DP600 is shown in **Table 4.3**.

Table 4.3. *Typical chemical composition of DP600 steel [3], Fe balance.*

	C	**Mn**	**Si**	**P**	**V**	**Ti**
Max wt.%	0.090	1.72	0.263	0.014	0.008	0.002

AH36 steel is a grade of ASTM A131 steel. This is a moderate strength hot rolled steel, mainly used in shipbuilding [4]. The steel has a ferritic-pearlitic microstructure. The material undergoes solid state phase transformations during welding. **Table 4.4** shows the chemical composition of such steel.

Table 4.4. *The chemical composition of AH36 steel [4], Fe balance.*

	C	**Mn**	**Si**	**Cr**	**Ni**	**Al**	**Cu**	**V**	**Ti**	**Nb**
Max wt.%	0.124	1.42	0.465	0.026	0.017	0.040	0.018	0.003	0.003	0.020

4.2 Welding equipment and welding conditions

The experimental welding arrangement and equipment are adjusted for the defined cases and sets. However, three main units can be identified for all of the experimental welding experiments:

the welding power sources,

the clamping systems and

the movement and control units.

The thin sheets (Case I and II) were welded by means of gas tungsten arc welding (GTAW), whereas for thick plate welding (Case III), the gas metal arc welding (GMAW) process was employed. GTA welding was carried out using a Migatronic inverter type power source Commander TIG 400 AC/DC. A 2 mm diameter tungsten 2 wt.%-ThO_2 electrode (DIN EN 26848 [5]) with the shielding cup of 10 mm diameter and an electrode tip angle of 60^o was used. The electrode stick-out was around 2 mm. Argon was used as shielding gas and backing gas with typical flow rates of 12 l min^{-1} and 6 l min^{-1}, respectively.

The welding power source used for GMA welding (Case III) was a Cloos-Quinto Profi 503. The welding torch was tilted to an angle of around 60^o to the plane of the plate (leading the weld pool). A Lincoln electric LNM 25TM filler wire with a diameter of 1.2 mm was used for GMA welding. According to AWS A5.18 specification [6], the electrode is classified as ER70S-3 with a chemical composition given in **Table 4.5**.

Table 4.5. *Chemical composition for ER70S-3 filler wire [6], Fe balance.*

	C	Mn	Si	Cu	P	S	Cr, V, Mo, Ni
Max wt.%	0.06-0.15	0.9-1.4	0.45-0.75	0.5	0.025	0.035	total<0.5

In order to achieve a fully penetrated weld in Case III (6 mm thick AH36 steel), a Y-groove joint was employed with dimensions shown in **Figure 4.1**.

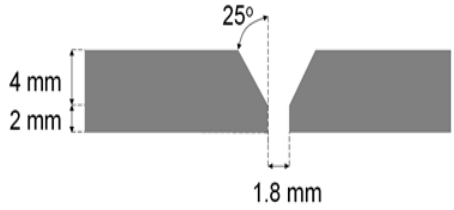

Figure 4.1. *The Y-groove joint design used during welding of 6 mm thick AH36 steel.*

A ceramic strip with a rounded groove was used for backing during GMA welding and is shown schematically in **Figure 4.2**.

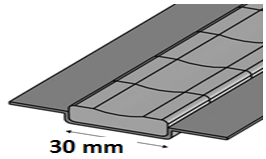

Figure 4.2. *Ceramic backing strip with rounded groove used in GMA welding.*

The shielding gas used for GMA welding was 85% Ar-15% CO_2. This mixture of shielding gasses provides a stable arc, low spatter losses and acceptable weld bead profile. The shielding gas flow rate was 15 l min^{-1}.

The clamping system prevents movement of the samples during welding and is released after the cooling stage. The releasing temperature of the clamps plays an important role in the final deformation [7]. In all experiments of this study, the clamps were released when the temperature of the plate had reached room temperature. The clamping unit for Case I-A and Case II-A (**Table 4.1**) consists of a 20 mm thick steel grooved backing plate with a width of 220 mm and a length of 330 mm and four toggle clamps on each side. Two copper strips ($4\times25\times280$ mm^3) were used to evenly distribute the clamping pressure to the work piece. **Figure 4.3** shows the clamping system for this configuration.

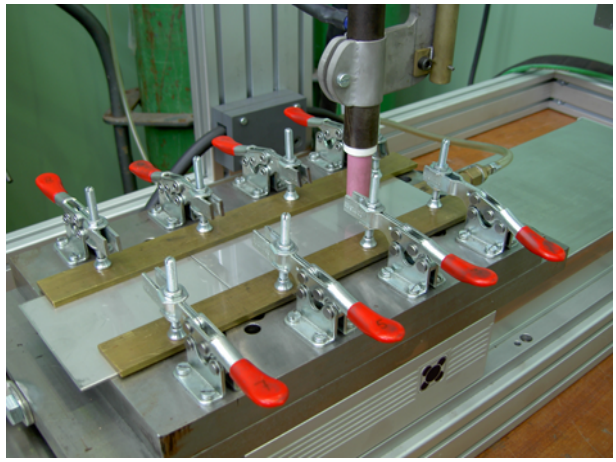

Figure 4.3. *The clamping system used for thin sheets of $200\times100\times1.5$ mm^3 (Case I-A and Case II-A).*

For the larger plates (Case I-B, Case II-B and Case III, **Table 4.1**), the clamping system consists of a steel backing frame with dimensions of $735\times1200\times30$ mm^3 with a top plate with a thickness of 4 mm. A 30 mm deep and 20 mm wide groove is located at the centre of the backing plate in order to apply the backing gas (and the ceramic backing) as shown in **Figure 4.4** and **Figure 4.5**. Four steel strips with dimensions of $660\times32\times10$ mm^3 were used to evenly distribute the clamping pressure to the workpiece.

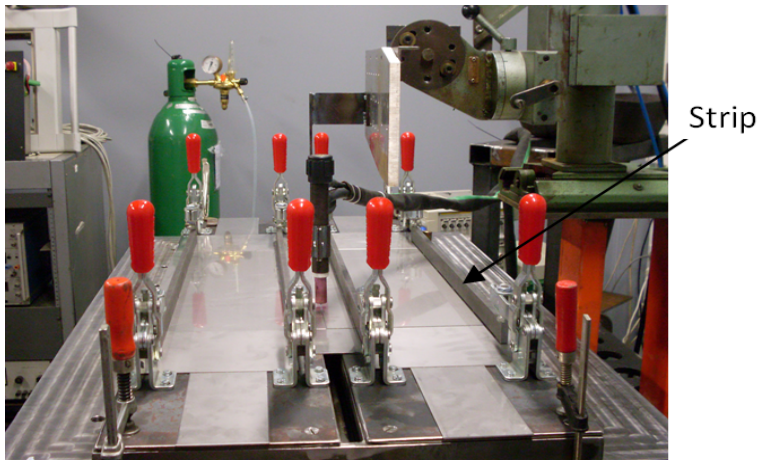

Figure 4.4. *The clamping system used for the larger plates of 500×250×2 (and 6) mm^3 (Case I-B, Case II-B and Case III).*

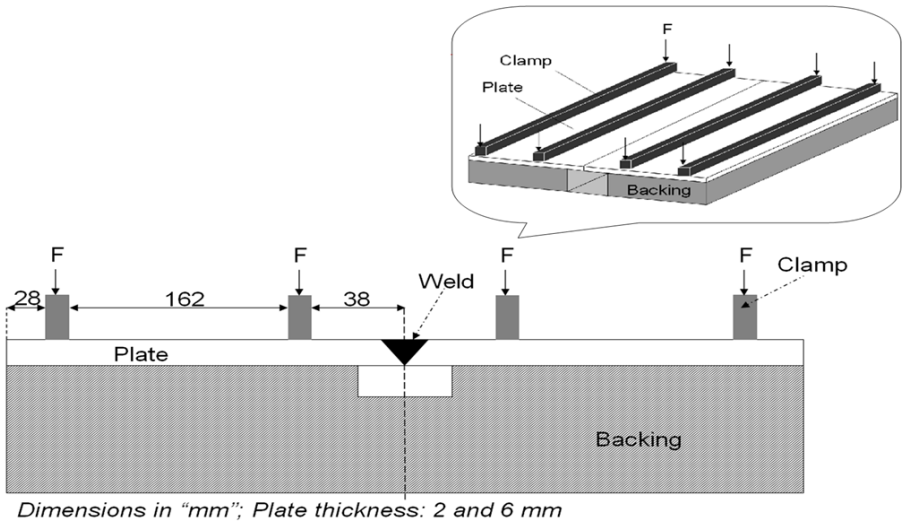

Figure 4.5. *Schematic drawing of the positions of the clamps for large plates.*

In addition to the groove at the centre of the backing plate, a similar groove was made at 250 mm (125 mm for Case I-A and Case II-A) from the starting point of welding, perpendicular to the welding direction, to allow temperature measurements by means of thermocouples at the underside surface of the workpiece. During welding, the thin plates (1.5 and 2 mm thick plates) could move, even though clamps were used. The movement of the plates leads to partially penetrated welds and gap opening. To prevent the plate movements, tack welds were used at the starting and the finishing

position of the weld.

The movement and the control units consist of a computer, a motion controller (DMC), a shunt and a monitor to measure the welding current and the welding voltage. The welding parameters are summarized for different materials in **Table 4.6**.

Table 4.6. *Welding parameters for the different materials.*

Materials / Parameters	**AISI-316L**			**DP600**			**AH36**
	$200 \times 100 \times 1.5\ mm^3$		$500 \times 250 \times 2\ mm^3$	$200 \times 100 \times 1.5\ mm^3$		$500 \times 250 \times 2\ mm^3$	$500 \times 250 \times 6\ mm^3$
Welding process	GTAW		GTAW	GTAW		GTAW	GMAW
Weld type	BOP		Butt	BOP		Butt	Butt
Joint type	-		Square	-		Square	Y-groove
Welding electrode	W-2 wt.%ThO_2			W-2 wt.%ThO_2			LNM25
Electrode diameter $[mm]$	2		2	2		2	1.2
Electrode tip angle $[^o]$	60		60	60		60	-
Electrode stick out $[mm]$	2		2	2		2	12
Arc length $[mm]$	2		2	2		2	-
Contact tube to workpiece $[mm]$	N.A.		N.A.	N.A.		N.A.	12
Averaged welding current, $[A]$	80.5		88.7	110.6		99.4	200.2
Averaged welding voltage $[A]$	10.8		10.6	11.1		10.7	25.9
Welding speed $[mm\ s^{-1}]$	2.5		2.5	5		2.5	4.5
Wire feed speed $[mm\ s^{-1}]$	N.A.		N.A.	N.A.		N.A.	5.7
Shielding gas	Ar		Ar	Ar		Ar	85% Ar+ 15% CO_2
Shielding gas flow rate $[l\ min^{-1}]$	12		12	12		12	15
Shielding cup diameter $[mm]$	10		10	10		10	16
Backing gas	Ar		Ar	Ar		Ar	Ar
Backing gas flow rate $[l\ min^{-1}]$	4		6	6		6	-

4.3 Welding with additional heating equipment and arrangement

In the experimental arrangement, a frame is designed in order to position the heat sources at any desired location. As introduced before, preliminary tests were carried out on small specimens. For these tests, a single nozzle burner approach was followed. After examining several tests, the set-up was redesigned and extended for larger plates using multiple nozzle burners. Although, the first approach was not very successful, the approach should not be rejected. Therefore, it is worthwhile mentioning both the preliminary approach and the final set-up here.

4.3.1 Single flame approach

The first trials were based on simple single nozzle oxy-acetylene burners. AISI-316L stainless steel sheets, with dimensions of $200 \times 100 \times 1.5$ mm^3 (Case I-A), were tested using two oxy-acetylene burners. The burners have a single nozzle with a diameter of 0.5-1 mm. **Figure 4.6** shows the experimental set-up for both conventional bead on plate welding (**Figure 4.6a**) and welding with additional heating (**Figure 4.6b**). Two oxy-acetylene burners were installed above the top surface of the plate at different positions to the weld torch and to each other using simple fixtures. Neutral flames (in which the amount of oxygen is suitable for burning, and neither oxidation nor reduction occurs) were used in the experiments. In all experiments throughout this study, the burners are symmetrically placed. Several tests were conducted with different maximum burner induced temperatures, distances to the weld torch (side heating and transient thermal tensioning), burner separations and distances of the burner to the plate. The burners were ignited and installed manually during the experiments. The welding torch and the heaters remained stationary, while the clamped plate moved underneath the heat sources at a desired speed. The temperature was measured on the underside surface of the plates.

The main problem in the experiments was the repeatability of the tests. Setting similar flame characteristics for both burners and the precise positioning of the burners were difficult. Welding distortion was reduced occasionally. **Figure 4.7** shows one of these samples.

The burner induced temperature is defined as the temperature of the underside surface of the plate at the location of the burner. If the burners are located in such a way that the plate is heated first by the burners and then by the arc, the situation is called *leading*. In the *trailing* situation, the burners are located in such a way that the arc is heating the plate first and followed by the burners.

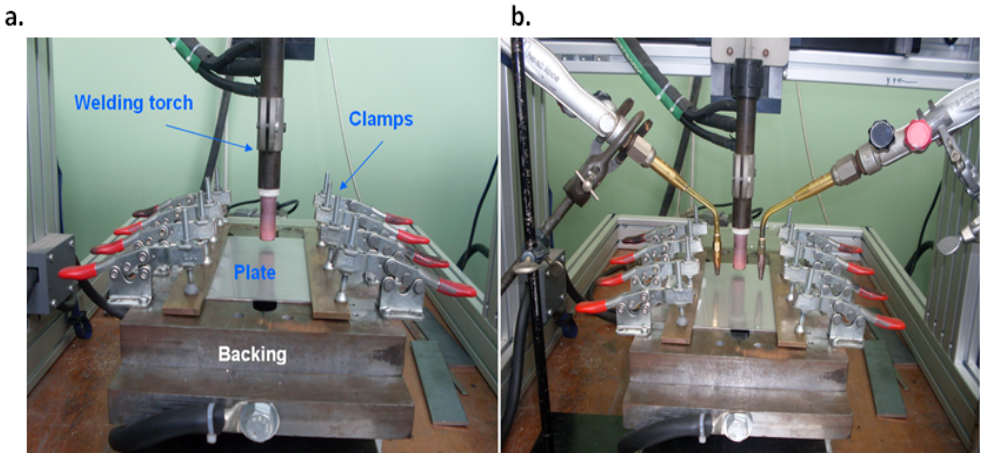

Figure 4.6. *(a) Set-up for conventional welding and (b) welding with additional heating used in the first series of the experiments.*

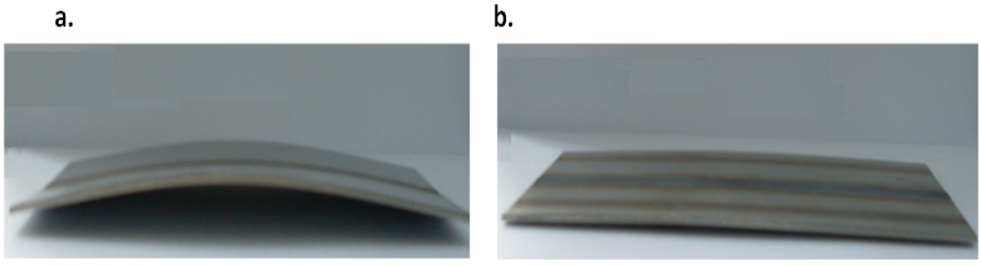

Figure 4.7. *(a) Out-of-plane deformation after conventional welding and (b) after welding with additional heating using two single nozzle burners.*

The maximum out-of-plane deformation for conventional welding was reduced by 50% using this approach. **Figure 4.8** shows the maximum out-of-plane deformation of plates with experimentally obtained maximum reduction of welding distortion for different situations. It was found that distortion reduction with single nozzle burners is very sensitive to the position of the burners with respect to the welding torch.

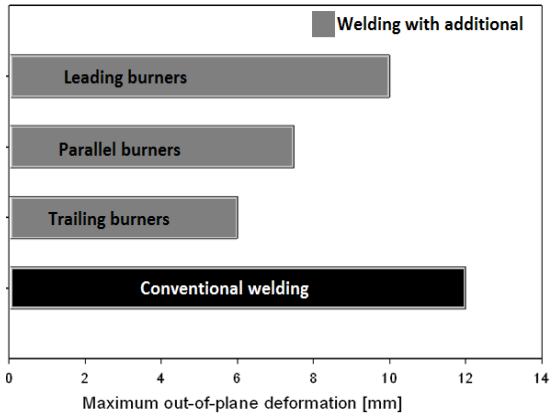

Figure 4.8. *Maximum out-of-plane deformation after conventional welding and welding with additional heating for different situations using two single nozzle burners.*

4.3.2 Multiple burners approach

The first series of experiments were successful for just a few samples. This may be attributed to the heat flow pattern as shown in **Figure 4.9**. The figure shows schematically the heat flow pattern for a single nozzle burner with a circular shape and a multi-nozzle burner with a rectangular shape. The heat flow in the case of a single nozzle burner is in all directions, while in the elongated burner, it is mainly in the direction of the burner width.

In welding with additional heating, the burners can be installed either parallel or perpendicular to the weld centre line [8]. It was practically impossible to test the burner assembly perpendicular to the weld centre line due to geometric limitations. Therefore, in all experiments the burners were installed parallel to the weld centre line. Beside the practical limitation of perpendicular burners, it is mentioned in literature [8] that the burners perpendicular to the weld centre line are not suitable for distortion reduction. The process parameters involved in welding with additional heating, shown schematically in **Figure 4.10**, can be summarized as:

1 Maximum temperature of the underside surface of the plate beneath the flame;

2 Burner separation (BB);

3 Burner distance to the welding torch (BT);

4 Burner distance to the plate (BP).

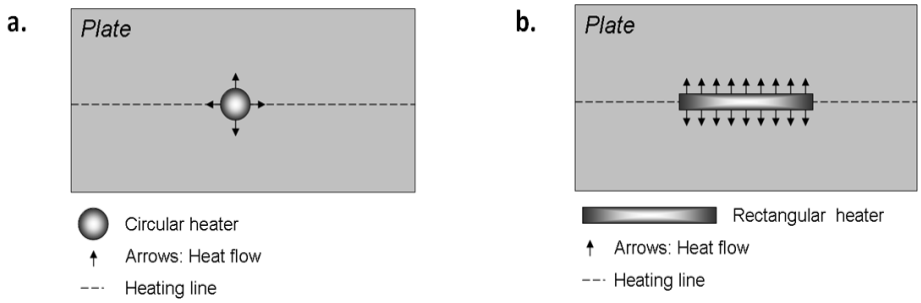

Figure 4.9. *(a) Schematically representation of heat flow for a single burner and (b) for an elongated burner.*

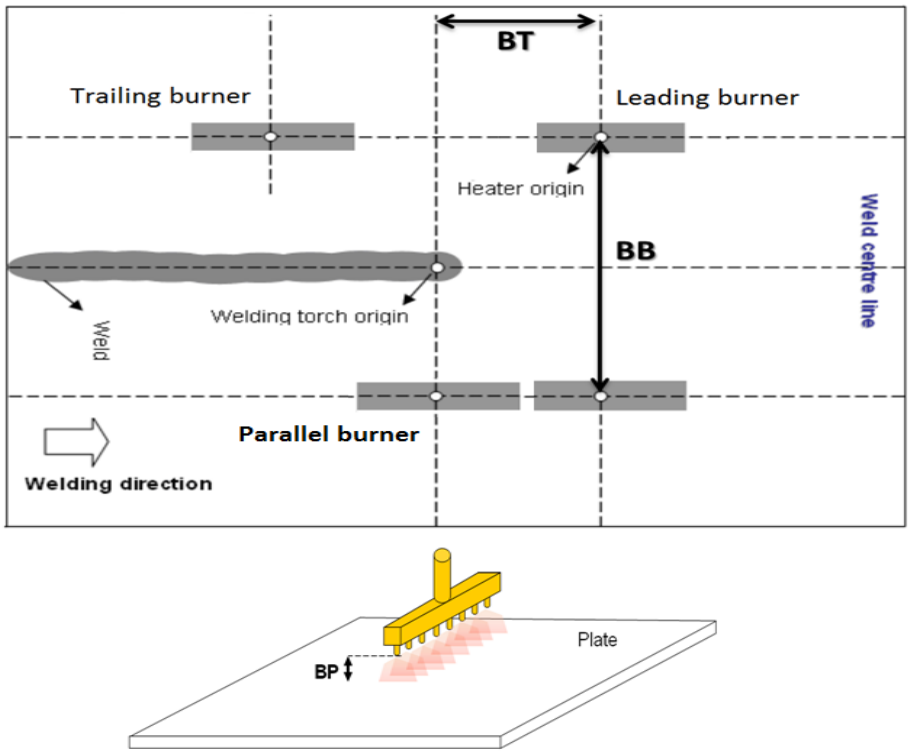

Figure 4.10. *A schematic drawing of the positional process parameters involved in welding with additional heat sources: Burner separation (BB), Burner distance to the welding torch (BT) and Burner distance to the plate (BP).*

The new set-up is based on the rectangular *LINDOFLAMM*® [9] special short lance burners, shown in **Figure 4.11**.

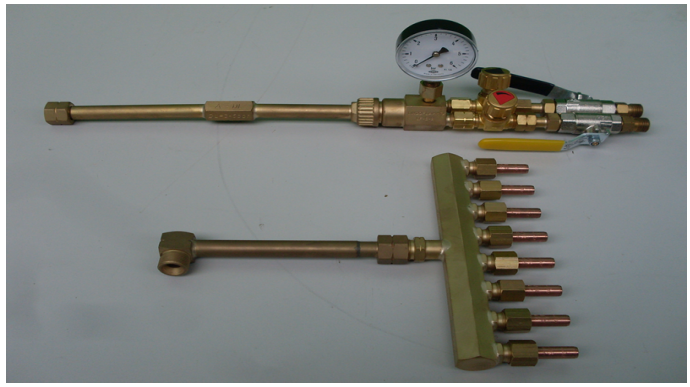

Figure 4.11. *LINDOFLAMM® special short lance burner used in the series of experiments for Case I-B, Case II-B and Case III [9].*

The burner operates according to DIN EN ISO 5172 [10] with compressed air and acetylene. Basically, it consists of a burner head, a mixing pipe, a mixing chamber with a pressure regulator and a handle. The total length of the burner is 240 mm and includes 8 nozzles with 30 mm separation distance. The width of the burner is 27 mm. The working pressure at the burner inlet is 0.5 bar for acetylene and 1.5-4.0 bar for compressed air. This gives a consumption of 0.3-3.2 m^3 h^{-1} for acetylene and 2.1-22.4 m^3 h^{-1} for compressed air. The burners were adjusted by turning the acetylene and oxygen valves on the regulator to control the gas flow and to obtain the required flame for welding with additional heating.

The welding with additional heating experimental set-up with the rectangular burners is shown in **Figure 4.12a**. In order to investigate the process parameters such as the distance of the burners to the weld centre line, large sheets are required. For this reason the size of samples was changed to 500×250×2 mm^3 (Cases I-B and II-B) and 500×250×6 mm^3 (Case III). The burner parameters (like the distances to the weld centre line and the distance of the nozzle tips to the plate) are adjustable (**Figure 4.12b**).

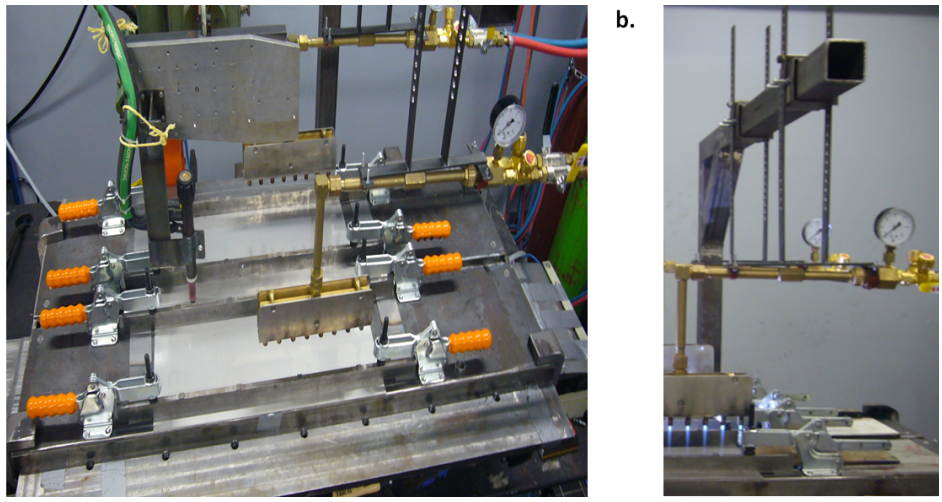

Figure 4.12. *(a) Welding with additional heating set-up for larger plates (500×250×2 mm^3 and 500 ×250×6 mm^3) and (b) fixture with adjustable height.*

4.3.3 Welding with additional heating

The first step in the experiments is the setting of the burners for different peak temperatures. The maximum temperatures for different burner settings were measured at the underside surface of the plate by means of thermocouples (see **Chapter 5**). A series of trials was performed for a number of pressurised air-acetylene flame settings, *i.e.* different peak temperatures. In this way, the mixtures were calibrated for different peak temperatures. These tests were repeated for the different base materials.

Table 4.7 shows the range of the maximum temperatures obtained and position parameters.

Table 4.7. *The range of process parameters used in the experiments for different materials.*

Cases / Sets	Case I-B	Case II-B	Case III
Separation of burners [mm]	177 to 367	177 to 407	227 to 427
Welding torch to burners distance [mm]	-220 to 220	-185 to 195	-220 to 220
Maximum temperature at the underside surface of the plate [°C]	Up to 520	Up to 520	Up to 400

The distance of the burners to the plate (BP) was set to 50 mm for AISI-316 and DP600 in all experiments. This distance was then reduced to 40 mm for AH36 sheets in order to increase the heat input.

An example of the final out-of-plane deformation of a plate after welding with additional heating compared to the conventional welding is shown in **Figure 4.13**.

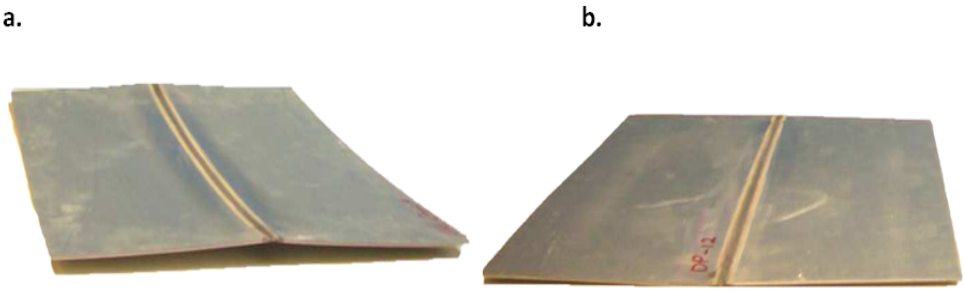

Figure 4.13. *An example of the final out-of-plane deformation after a) conventional welding and b) welding with additional heating compared for DP600 steel, Case II-B.*

One of the practical challenges in welding with additional heating using pressurised air-acetylene burners is the difference between the maximum temperatures obtained for the two burners. With the same burner settings, differences in maximum temperature were always observed for the two. **Figure 4.14** shows one of these examples in which the maximum temperature deviates by approximately 50 ^{o}C. This asymmetric heating may reduce the effectiveness of distortion mitigation.

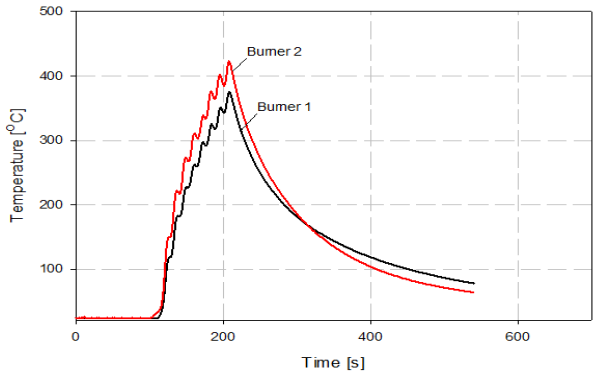

Figure 4.14. *Temperature profiles for two burners with similar settings, heating a 2 mm thick AISI-316L sheet (Case I-B).*

Another practical challenge is the movement of the plate during the heating cycle by pressurised air-acetylene multiple burners, even using tack welds and in a clamped condition, as shown in **Figure 4.15**. During heating, the regions beneath the burners are locally deformed. The higher the maximum temperature, the more deformation will occur. This localized deformation can change the final deformation mode of the plate.

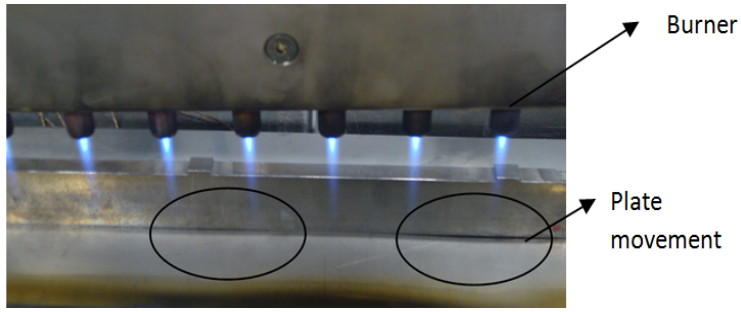

Figure 4.15. *An example of plate movement during welding with additional heating beneath the burner in the clamped condition.*

4.4 Measurement methods and errors

4.4.1 Distortion measurement method

Devices to measure distortion can be classified into two main groups: contact and non-contact methods. Examples of contact measuring tools are mechanical dial gauges and Linear Variable Differential Transducers (LVDT). Laser scanning and Digital Image Correlation (DIC) are two examples of non-contact measuring tools. The contact measurement method should not be placed close to the weld because high temperatures near the weld may damage the tool and will affect the experimental results.

The DIC method is a full-field image analysis method, which can determine the contour and the displacement of a plate in three dimensions. The method is based on the principle of stereovision. The three dimensional measurement is carried out using two cameras. A speckle pattern is applied on the plate surfaces. The stereo correlation between the images of the left and right camera allows the measurement of the geometry and the position of the plate [11].

The out-of-plane distortions of the plates before and after welding and welding with additional heating were measured by means of the DIC method with an accuracy of 50 μm. In this study speckle patterns were applied on all plates before and after welding. **Figure 4.16a** shows one example of such pattern for an AISI-316L plate before welding. The experimental arrangement is shown in **Figure 4.16b**.

During the distortion measurements, no external loads are applied on the samples. The results of the measurement are the relative out-of-plane deformations. The relative deformation of the plate is defined as the difference between the initial shape (before welding) and the final shape (after welding). In order to make the comparison of the experiments simple and fast, a distortion index is defined based on the result of DIC measurements. The distortion index is the difference between the maximum and

the minimum out-of-plane deformation of a plate. In all measurements, a constant arbitrary reference surface is used. The out-of-plane deformation of the plate above this surface is always positive. The negative values in the distortion measurement results indicate that the plate is deformed below the reference surface.

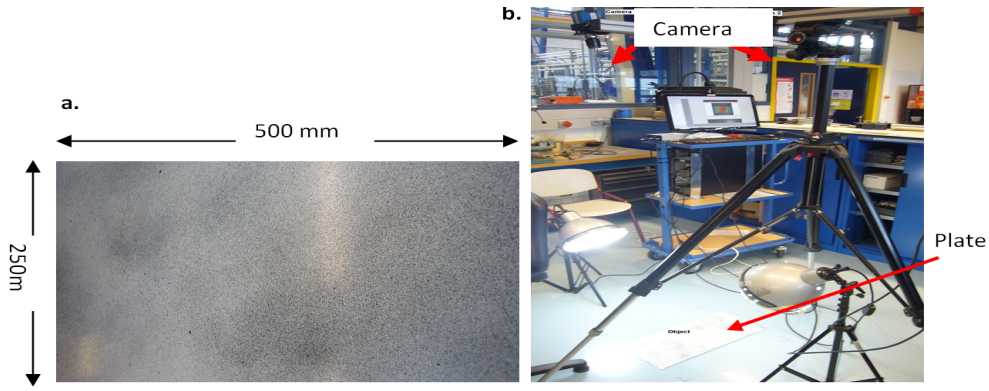

Figure 4.16. *(a) An example of a speckle pattern used for distortion measurement of AISI-316L plate before welding and (b) the experimental arrangement.*

4.4.2 Temperature measurement method

The temperature of the workpiece during both conventional welding and welding with additional heating was measured by means of thermocouples. Standard 0.25 mm (diameter) glass insulated k-type thermocouples (Chromel-Alumel) were used to measure temperature. These thermocouples measure temperatures within a temperature range of -270 ^{o}C to 1372 ^{o}C. The measurement accuracy is ± 2.2 ^{o}C [1]. The thermocouple wires were welded to the cleaned surface of the workpiece at different positions at the underside surface of the workpieces using a Labfacility L60+ electric discharge thermocouple welder. In order to isolate the thermocouple wires, ceramic tubes were used. The thermocouples were installed along or perpendicular to the heating (or welding) line. The exact position of thermocouples was measured after welding.

As stated earlier, the burner induced temperature is defined as the temperature at the underside surface of the plate beneath the burner.

4.4.3 Microstructure investigation

The microstructure of the weld metal, the heat affected zone of the weld (HAZ-welding), the base metal and the heated area beneath the burners (HAZ-welding with additional heating) were studied at a cross section perpendicular to the weld and in the middle of the plate for all materials.

For AISI-316L, after mounting and polishing, the microstructures were revealed using Kalling's No.2 etchant for 25 s. In DP600, Marder and Benscoter was used as the etchant solution. The micrograph of the AH36 samples was obtained using a 5% Nital etching solution for 10 s.

Hardness profiles were also taken across the welds, the heat affected zones and the heated areas beneath the additional heating burners, for different materials using Vickers micro hardness measurements with an indentation load of 300 g.

4.4.4 Residual stress measurement method

Residual stress measurements were performed on AISI-316L and DP600 steel plates by means of the neutron diffraction (ND) method at the Paul Scherrer Institute (PSI) Switzerland. At the Laboratoire Leon Brillouin (LLB) France the stress profiles of AH36 plates were measured by ND.

The principle of residual stress measurements by means of diffraction is based on measuring the lattice strains. Lattice strains can be derived from shifts in the diffraction peaks. The diffraction occurs when an incident beam with a certain wavelength interacts with the lattice planes. The diffraction condition for X-rays or neutrons in crystalline materials is described by Bragg's law [12, 13]. If the incident radiation with a specific wavelength (λ_r) is diffracted by the lattice (see **Figure 4.17**), the relation between the lattice plane spacing and the diffraction angle is expressed by:

$$\lambda_r = 2d_{hkl}sin\theta; \tag{4.1}$$

where d_{hkl} is the distance between the *(hkl)* lattice-planes and θ is the diffraction angle.

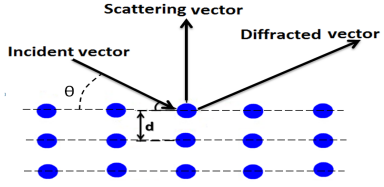

Figure 4.17. *Diffraction of incident radiation by a set of lattice planes with spacing* d_{hkl}.

When residual stresses are present in a material, the lattice spacing (d_{hkl}) deviates from its stress free value ($d_{0,hkl}$). This deviation will be reflected as shifts of the diffraction peak positions [14]. Therefore, measuring these peak positions can be used to calculate the residual strains (ε_{hkl}):

$$\varepsilon_{hkl} = \frac{d_{hkl} - d_{0,hkl}}{d_{0,hkl}}; \tag{4.2}$$

The measurement of the lattice spacing is in the direction of the scattering vector, which is the difference of the diffracted and the incident vectors. This means that the measurements are always in the normal direction to the lattice plane. The intersection of the incident and the diffracted beams is usually called the sampling volume or gauge volume. From this volume, the diffraction signal is obtained.

In many cases, the peaks can be fitted with a simple Gaussian distribution. When there is significant peak broadening due to defects, other peak profile functions can be involved. To obtain the peak position accurately, numerous peak fitting programs are available which yield the reflection position, and the full width at half maximum (FWHM) of the reflection. The FWHM of the reflection profiles depends on the experimental conditions, especially the divergence of the beam and the state of the material. Small grain size and micro-strains lead to a broadening of the reflection profiles [15].

In the above equations, there are two material dependent elasticity constants; Young's modulus and Poisson's ration. These two parameters can be obtained experimentally from tensile tests. However, the results of such tests generate bulk elasticity constants, expressing the macroscopic material behaviour. The strain measured in the diffraction experiments depends on specific crystallographic planes. To calculate stresses, the elastic constants of these planes are required. Therefore, the bulk elasticity constants cannot be used. The measurements of elasticity constants for each plane are based on both diffraction and tensile tests. There are also analytical and numerical approaches to derive these constants [16, 17].

The neutron source and the detectors cannot move. Therefore, the sample is moved or rotated in order to measure the strains in different directions. **Figure 4.18** shows two situations in order to measure longitudinal and transverse residual strains. The width of the incident and diffracted neutron beams is selected according to the desired spatial resolution and the thickness of the plate.

Preferred diffraction angles for residual stress measurement by neutrons is as close as possible to 90^o and preferably not outside of the range 60^o to 120^o [14]. The longitudinal direction is defined as the direction parallel to the welding direction, while the direction perpendicular to the welding direction is defined as the transverse direction.

The stresses determined by diffraction methods are the sum of macro and micro-stresses calculated from peak shifts. Micro-stresses can also lead to peak broadening. Inter-granular micro-stresses have different influences on different lattice planes due to the elastic anisotropy of the crystallites [15]. It is recommended to avoid certain reflections for the determination of macroscopic stresses and use reflections for which the influence of inter-granular strains is small [15]. In FCC and BCC materials the use of the (200) reflection is strongly discouraged; instead the use of the (111) or (311) reflections for FCC and the (110) or (211) reflections for BCC is recommended.

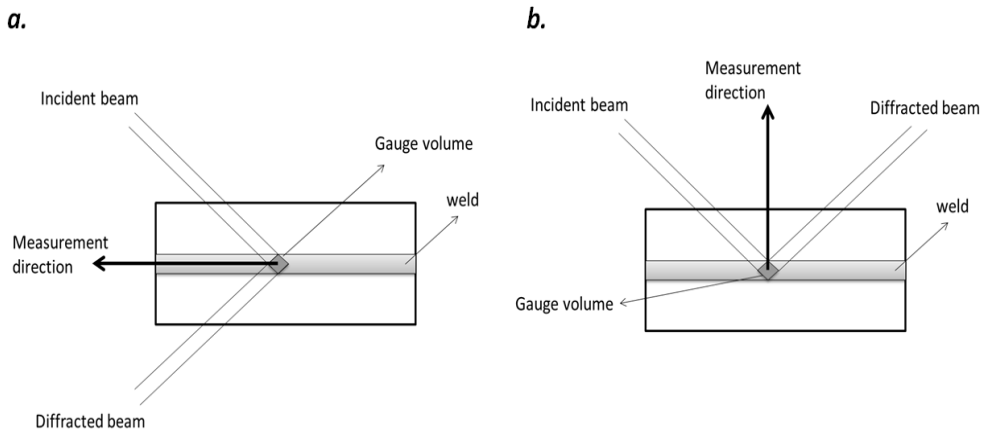

Figure 4.18. *Measurement geometries for (a) longitudinal residual stresses, and (b) transverse residual stresses.*

Neutron diffraction residual strain measurements were conducted on $500 \times 250 \times 2$ mm^3 AISI-316L (Case I-B) and DP600 (Case II-B) samples at PSI. The samples were welded conventionally and welding with additional heating and full penetration was obtained. The sample geometry and measuring positions are shown in **Figure 4.19**.

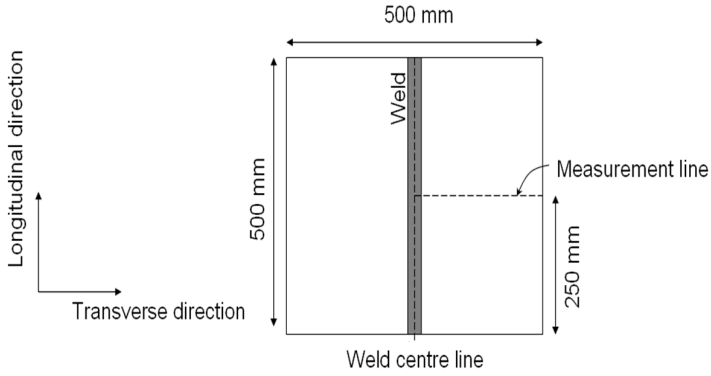

Figure 4.19. *Sample geometry for the neutron diffraction measurements at PSI.*

In **Figure 4.20** [18], a sketch of the instrument is presented. Stress measurements were performed by a strain scanner, a Multi Pulse Overlap diffractometer. **Figure 4.21** shows a picture of the arrangement.

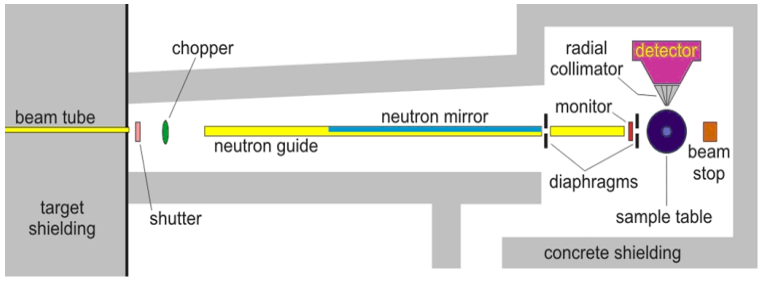

Figure 4.20. *A sketch of the POLDI instrument [18].*

A neutron beam with a flux of approximately 6×10^6 neutrons $s^{-1}cm^{-2}$ passes the neutron guide. The size of the incoming beam is defined by the horizontal and vertical incoming beam slits. The diffracted beam passes the radial collimator and is detected. The diffraction measurements were performed on the Fe(311) and (211) planes for AISI-316L and DP600 respectively. As stated before, these two planes are known to be the least sensitive to the inter-granular stress effects. The gauge volume was set to $1.5\times1\times1$ mm^3.

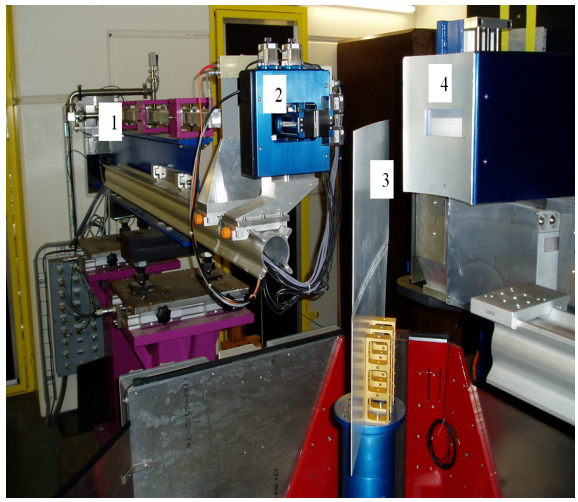

Figure 4.21. *Overview of the set-up for the neutron diffraction measurements at PSI. The numbers indicate: (1) Neutron guide, (2) the diaphragm, (3) the sample and (4) the radial collimator.*

Neutron diffraction residual stress measurements at LLB were performed on $500\times250\times6$ mm^3 AH36 samples (Case III). In **Figure 4.22** [19], a sketch of the instrument at LLB with a diffractometer called DIANE is presented. The instrument is a two axis diffractometer, consisting of a monochromator, a sample table and a multi-detector,

which is situated on the G5 cold guide of the Orphee reactor. Orphee is a swimming pool type reactor with a thermal power of 14 MW and a neutron flux of 3×10^{14} neutrons cm^{-2} s^{-1}. The monochromator is a pyrolytic graphite single crystal (using the (002) or the (004) reflection) providing a continuous wavelength spectrum between 2.3 *Å* and 5 *Å*. Different sized cadmium masks, ranging from 0.3 mm to 25 mm in width, just before and after the sample, are available to define the size and the shape of the gauge volume, according to the different experimental requirements [11].

The samples were welded conventionally and with additional heating. The diffraction measurements were performed on the Fe(211) planes. An overview of the arrangement for the measurements at LLB is shown in **Figure 4.23**.

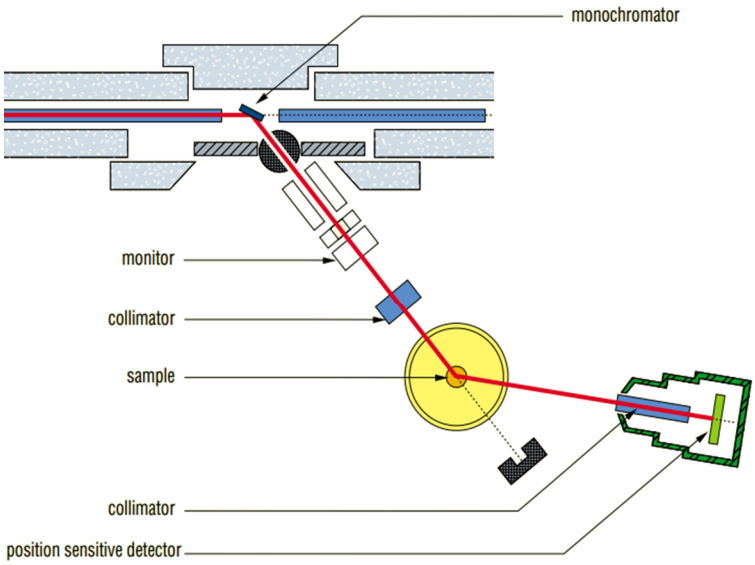

Figure 4.22. *A sketch of the instrument at LLB [19].*

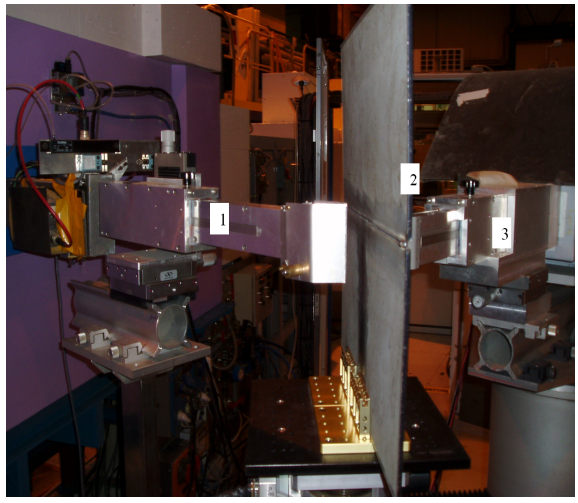

Figure 4.23. *Overview of the set-up for the neutron diffraction measurements at LBB. The numbers indicate: (1) Neutron guide, (2) the sample and (3) the collimator.*

Finally, for AH36 plates in the clamped conditions, the residual stresses were obtained from portable X-Ray equipment.

4.5 Concluding remarks

This chapter described the experimental procedures for conventional welding and welding with additional heating. The produced welds are characterised *in-situ* (*i.e.* temperature) and ex-situ (microstructure, residual stresses and distortion). A welding arrangement has been developed, which can be used for both conventional welding and welding with additional heating. The LINDOFLAMM® special short lance burners were used to apply the heating profile during welding with additional heating. The set-up was extended to cover larger sheets. Increasing the plate size makes the problem of welding distortion more pronounced. The repeatability of the experiments is of some concern; however the set-up mentioned above can be used to successfully reduce welding distortion.

Reference

[1] E. M. van der Aa, *Local Cooling during Welding: Prediction and Control of Residual Stresses and Buckling Distortion*, PhD thesis, Delft University of Technology, 2003.

[2] *Engineering Properties of Steel Handbook*, ASM International, 1982.

[3] R. G. Thiessen, *Physically-Based Modelling of Material Response During Welding*, PhD Thesis, Delft University of Technology, 2006.

[4] *ASTM A 131/A 131 M-08: Standard Specification for Structural Steel for Ships*, ASTM International (http://www.astm.org/Standards/A131.htm).

[5] *DIN EN 26848: Tungsten electrodes for inert gas shielded arc welding and for plasma cutting and welding*, 1991.

[6] *AWS A5.18: Specification for Carbon Steel Electrodes and Rods for Gas Shielded Arc Welding*, AWS, 2001.

[7] T. Schenk, *Modelling welding distortion: The influence of clamping and sequencing and sensitivity analyses*, PhD thesis, Delft University of Technology, 2011.

[8] I. Fafiolu, *Evaluating the heating methods to reduce the distortion of 4 mm thick DH36 ship panels*, Master thesis, Cranfield University, 2007.

[9] http://www.lindegas.com/

[10] *DIN EN ISO 5172: Gas welding equipment, Blowpipes for gas welding, heating and cutting-Specifications and tests*, 2006.

[11] http://www.limess.com/

[12] W. L. Bragg, *The Diffraction of Short Electromagnetic Waves by a Crystal*, Proceedings of the Cambridge Philosophical Society, 17, pp. 43-57, 1913.

[13] B. D. Cullity, *Elements of X-ray diffraction*, Prentice Hall, New Jersey, 2001.

[14] C. Ohms, *Residual stresses in thick bi-metallic fusion welds: a neutron diffraction study*, PhD thesis, Delft University of Technology, 2013.

[15] W. Reimers, A. R. Pyzalla, A. Schreyer and H. Clemens, *Neutron and Synchrotron Radiation in Engineering Material Science*, WILEY-VCH, 2008.

[16] B. Eigenmann, E. Macherauch, *Rontgenographische Untersuchung von Spannungszustanden in Werkstoffen - Teil II*, Mat.-Wiss. u. Werkstofftech., 26, pp. 199-216, 1995.

[17] B. Eigenmann, E. Macherauch, *Rontgenographische Untersuchung von Spannungszustanden in Werkstoffen - Teil III*, Mat.-Wiss. u. Werkstofftech., 27, pp. 426-437, 1996.

[18] http://poldi.web.psi.ch/index.shtml

[19] http://www-llb.cea.fr/en/fr-en/pdf/g52-llb.pdf

Chapter 5

Experimental results and discussion

In **Chapter 4**, different case studies were defined and the procedures of the experiments were described. The preliminary experiments were conducted with single nozzle oxy-acetylene burners and then developed to eight nozzle compressed air-acetylene burners. The results of out-of-plane deformation, temperature, microstructure and residual stress measurements for these cases will be presented in this chapter.

As stated earlier, many parameters are involved in welding with additional heating such as the intensity of the burners and the position of the burners with respect to the weld centre line and the welding torch. The first part of the experiments is related to determine the condition where distortion is reduced by welding with additional heating as compared to conventional welding. This condition is referred as 'experimentally obtained minimum distortion'. The temperature measurements, microstructure investigations and the residual stress measurements for the experimentally obtained minimum distortion cases are then performed. The results of the experiments are not only used to investigate the distortion reduction, but are also vital for model validations. The numerical models were subsequently used to gain a better understanding of the welding with additional heating process and are discussed in **Chapter 6**.

This chapter starts with the results of distortion measurements for the different cases (Case I-B, Case II-B and Case III). The experimentally obtained minimum distortion condition for different materials is defined. The chapter then continues with the results of temperature measurements, microstructure analysis and residual stress measurements for conventionally welded plates and plates with the experimentally obtained minimum distortion after welding with additional heating.

5.1 Distortion measurement results

Several experiments have been conducted to realize a distortion reduction after welding with additional heating by varying the parameters involved in the process, *i.e.* the intensity of the burners, the burner separation distance and the burner distance to the welding torch.

5.1.1 Measurement of the initial deformation

The initial distortion of the plate plays an important role in the final deformation both in the experiments and the numerical simulations [1]. Although for many of the plates used in this investigation, the initial out-of-plane deformation was found to be near zero, there were some plates with considerable initial deformation. **Figure 5.1** shows the maximum initial out-of-plane deformation measured for AISI-316L, DP600 and AH36 plates (Case I-B, Case II-B and Case III). For example for the DP600 plate, the initial deformation of the plate exceeds 3 mm. The initial deformation of a plate can have different sources related to the production process such as rolling, coiling, and cutting. In this study, the initial deformation of the plates was measured for all samples.

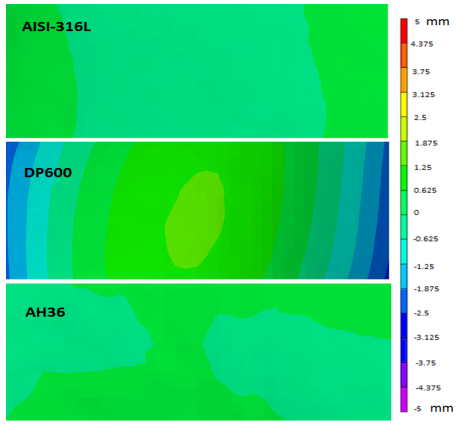

Figure 5.1. *The initial out-of-plane deformation for different materials (with considerable deformation). The scale is -5 to 5 mm.*

5.1.2 Experimental results of the out-of-plane deformation after welding and welding with additional heating of AISI-316L (Case I-B)

It was shown in **Chapter 4** that in welding with additional heating experiments, a large number of process parameters are involved; the most important being the intensity of the heat source, the positions of the burners to the weld centre line and the

weld torch. A systematic series of experiments was carried out with respect to these parameters, as the situation in which the out-of-plane deformation after welding with additional heating was reduced, compared to that of conventional welding.

The starting point was based on the literature. It was reported by Nagy *et al.* [2] that the distortion of welded steel plates can be reduced significantly in welding with additional heating when the burners are located far from the weld centre line with a burners induced temperature of approximately 270 ^{o}C. The burners induced temperature is defined as the measured temperature at the underside surface of the plate at the location of the burner. In this study, the same temperature was used and the burners were located at the farthest possible position with respect to the weld centre line as starting point. The experiments were repeated with different burners induced temperatures, burner separation distances and the welding torch distances to the burners.

In first instance, the effect of the burner induced temperature on the distortion index was evaluated for AISI-316L (Case I-B) at a fixed position of the burners as shown in **Figure 5.2**. The burners are located 143.5 mm to the weld centre line and a leading distance of 145 mm to the welding torch.

The result of conventional welding is also included in the figure, being welding with additional heating with a burner induced temperature of room temperature. As can be seen from the figure, by increasing the burner induced temperature, the distortion index decreases after which again it increases. The suitable burner induced temperature was found to be around 380 ^{o}C. This temperature is found to be a suitable temperature and not the optimum temperature. In other words, it might be possible that the distortion is minimized at a different temperature between 250 to 550 ^{o}C. It can also be seen that the distortion is still high, but slightly reduced in comparison to that of conventional welding. This is attributed to high thermal expansion coefficient and low thermal conductivity of AISI-316.

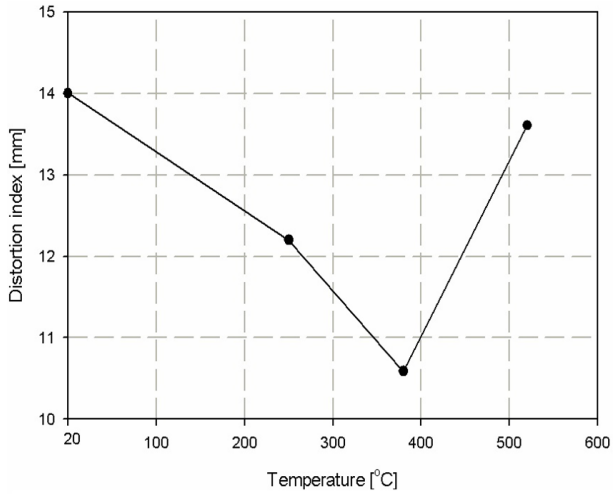

Figure 5.2. *The effect of the burner induced temperature on the distortion index for AISI-316L plate (Case I-B).*

Figure 5.3 shows the effect of the separation distance of the burners on the distortion index of AISI-316L after conventional welding and welding with additional heating. The burners were positioned leading and trailing to the welding torch. In the leading situation the burners are positioned in front of the welding torch in the welding direction while in the trailing situation the burners are located behind the welding torch. The burner induced temperature is set to 380 ^{o}C.

It can be seen that when the burners are close to each other, the distortion is large. By increasing the burner separation, the distortion index first decreases and then it increases again. The experimentally obtained minimum distortion is achieved where the burners are located approximately at the middle of each plate (143.5 mm from the weld centre line). Although welding with additional heating for both leading and trailing burners can reduce the distortion index, it can be seen from the figure that the experimentally obtained minimum distortion condition is obtained by the welding with the burners in the leading position.

The effect of the position of the burners to the welding torch, *i.e.* leading or trailing, on the distortion index is shown in **Figure 5.4** where the burner separation was set to 287 mm and the burner induced temperature was 380 ^{o}C.

The trend of distortion change as a function of the burner distance relative to the welding torch is non-linear. The strain (distortion) field in conventional welding is very complex in nature. There are many parameters involved, which contribute in the strain field. Small variations in the parameters may change the strain field significantly; for example, the clamping forces. Although the clamping system and the

positions of the clamps were all the same in the experiments, the clamping forces can vary in different experiments. Another example is the temperature of the burners in the welding with additional heating experiments. A small deviation between the temperature of the burners (left and right side of the welding torch) in different experiments can have an influence on the strain field and the distortion of the plate. In welding with additional heating experiments, new parameters are added compared to conventional welding, which make process reproducibility even more difficult. From the figure, the experimentally obtained minimum distortion index can be obtained where the burners are located 145 mm leading to the weld torch.

From the experimental results mentioned above, the case with the experimentally obtained minimum distortion is selected for AISI-316L (Case I-B) plates where the burners are located 145 mm leading the weld torch with a 287 mm separation distance and burner induced temperature of 380 ^{o}C. The out-of-plane deformation of this plate is measured and compared with that of conventional welding shown in **Figure 5.5**. It should be mentioned that the initial out-of-plane deformation of the plates before welding (and welding with additional heating) in the figure is subtracted from the out-of-plane deformation of the plate after welding.

As can be seen from the figure, the out-of-plane deformation of the plate is reduced when welding with additional heating is applied, compared with the conventionally welded plate. However, the deformation of the plate after welding with additional heating is still relatively high.

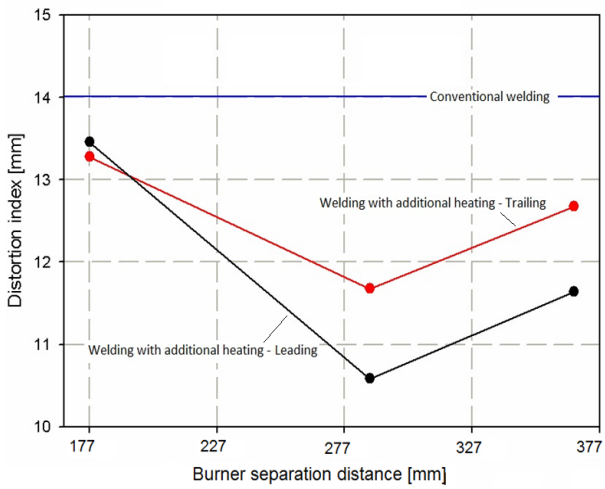

Figure 5.3. *The effect of the burner separation distance on the distortion index for AISI-316L (Case I-B) plate after conventional welding, welding with leading and trailing additional heating.*

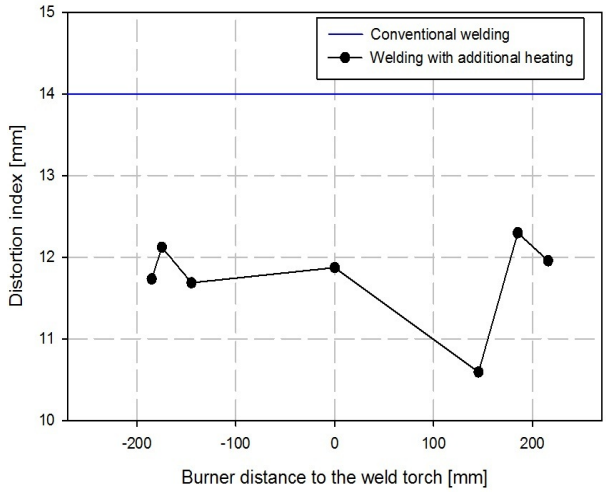

Figure 5.4. *The effect of the burner distance to the weld torch on the distortion index for AISI-316L (case I-B) plate after welding with additional heating.*

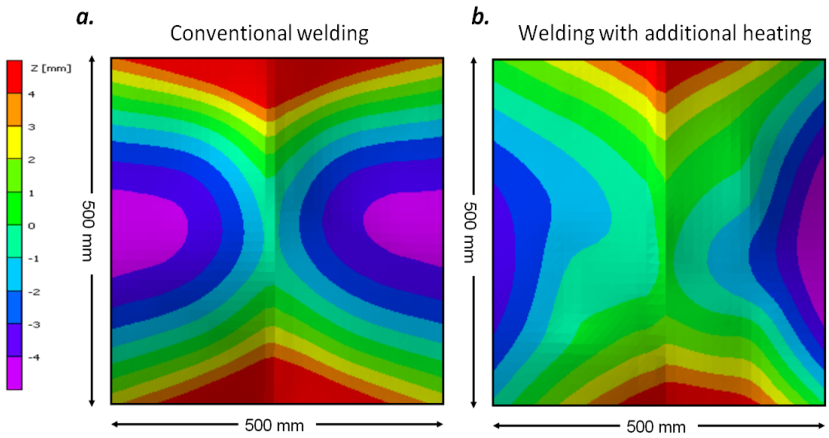

Figure 5.5. *The out-of-plane deformation of AISI-316L (Case I-B) plate after (a) conventional welding and (b) welding with additional heating for the case with the experimentally obtained minimum distortion. The weld is located in the centre of the plate.*

5.1.3 Experimental results of the out-of-plane deformation after welding and welding with additional heating of DP600 (Case II-B)

Similar experiments performed on AISI-316L were applied to dual phase steel DP600 (Case II-B). The effect of the burner induced temperature on the distortion index

for DP600 plate is shown in **Figure 5.6**. The results show a similar trend to the stainless steel AISI-316L plate. By increasing the burner induced temperature, the distortion index of the plate is decreased first after which it increases. The case with experimentally obtained minimum distortion is obtained when the temperature at the underside of the plate is around 320 ^{o}C. The results of the other process parameters on the distortion index are tested using this burner setting (temperature).

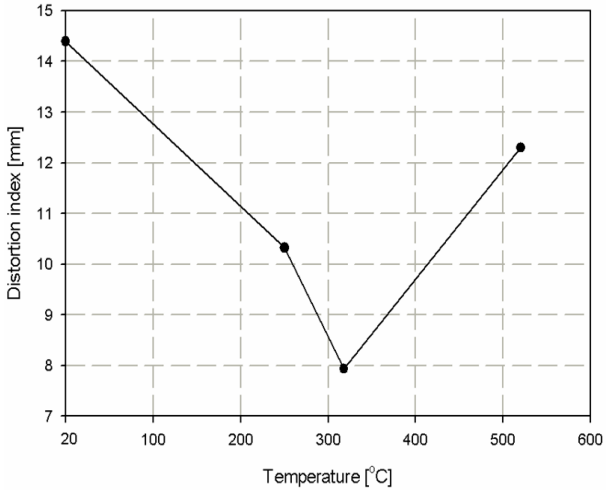

Figure 5.6. *The effect of the burner induced temperature at the underside of the plate on the distortion index for DP600 plate (Case II-B).*

Figure 5.7 shows the effect of burner separation distance on the distortion index for DP600 after conventional welding and welding with additional heating. The burners were positioned 145 mm leading and trailing to the welding torch. It is seen that for both leading and trailing situations when the burner separation distance is increased the distortion index is reduced. The best position of the burners in this case is the area close to edge of the plate edge 193.5 mm from the weld centre line. This difference between the position of the burners in DP600 and AISI-316L is related to the material properties of the steels. In DP600 steel, the thermal diffusivity (8.73 mm^2 s^{-1}) is more than twice of AISI-316L (3.35 mm^2 s^{-1}). Therefore, in order to reduce welding distortion in the same way as shown for AISI-316, the burners need to be placed further from the weld centre line. Both the leading and the trailing situations can reduce welding distortion. However, the leading situation leads to less out-of-plane deformation.

The effect of the position of the burners relative to the welding torch for a burner separation distance of 387 mm (leading and trailing) on the distortion index is shown in **Figure 5.8**. The trend of distortion change here is non-linear. The experimentally obtained minimum distortion case is obtained, where the burners are located 193.5 mm from the weld centre line and 145 mm leading to the welding torch.

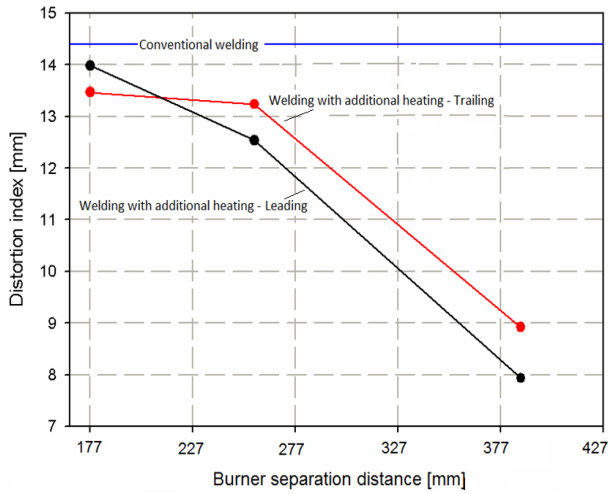

Figure 5.7. *The effect of the burner separation distance on the distortion index for DP600 (Case II-B) plate after conventional welding, and welding with leading and trailing additional heating.*

The result of the final out-of-plane deformation measurement after welding is compared to that of welding with additional heating in the experimentally obtained minimum distortion case for DP600 in **Figure 5.9**. The out-of-plane deformation after welding with additional heating has been decreased significantly for DP600. Nevertheless, the plate is not flat. Angular deformation can be seen after welding with additional heating. Again, the initial out-of-plane deformation of the plates is subtracted from the out-of-plate deformation after welding (and welding with additional heating).

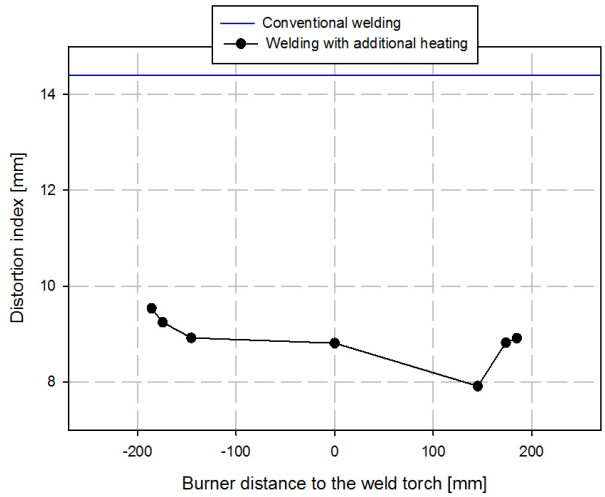

Figure 5.8. *The effect of the burner distance to the welding torch on the distortion index for DP600 (Case II-B) plate after welding with additional heating.*

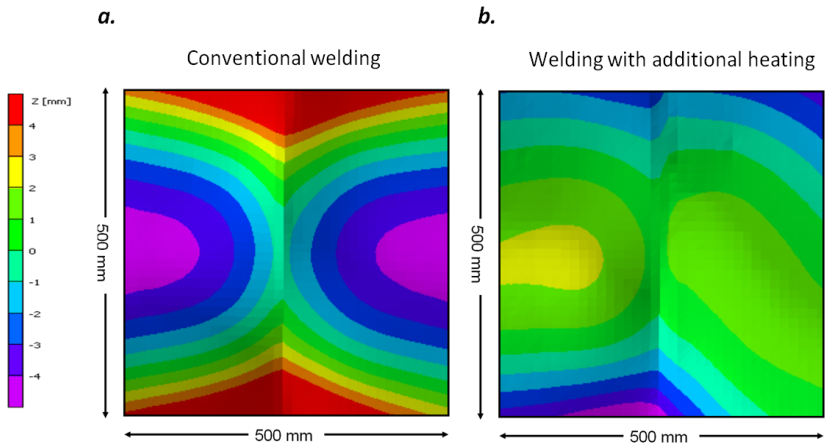

Figure 5.9. *The final out-of-plane deformation of DP600 plate after (a) conventional welding and (b) welding with additional heating for the case with experimentally obtained minimum deformation.*

5.1.4 Experimental results of the out-of-plane deformation after welding and welding with additional heating of AH36 (Case III)

The temperature effect of additional heating on the distortion index for AH36 plate is shown in **Figure 5.10**. The conventional welding has a distortion index of 5.5 mm.

Since the plate is thicker, the amount of out-of-plane deformation is significantly lower for the AH36 compared to the thin plate experiments (Cases I-B and II-B). By increasing the burner induced temperature, the distortion index is decreased first and then it starts to increase. The suitable temperature was found to be around 240 ^{o}C. This temperature is used for the other additional heating experiments. The effect of the burner separation on the distortion index is shown in **Figure 5.11**. The distortion index decreases when the burners are located 193.5 mm to the weld centre line. The distance of the burners to the welding torch was varied. The results are shown in **Figure 5.12**. The leading and the trailing positions of the burners both reduce the distortion index but there is hardly any effect. The case in which the burners are located 180 mm trailing the welding torch is selected as the case with experimentally obtained minimum deformation. The out-of-plane deformation of the plate after conventional welding is compared to that of welding with additional heating for the selected case in **Figure 5.13**. As can be seen, welding with additional heating reduces the plate deformation.

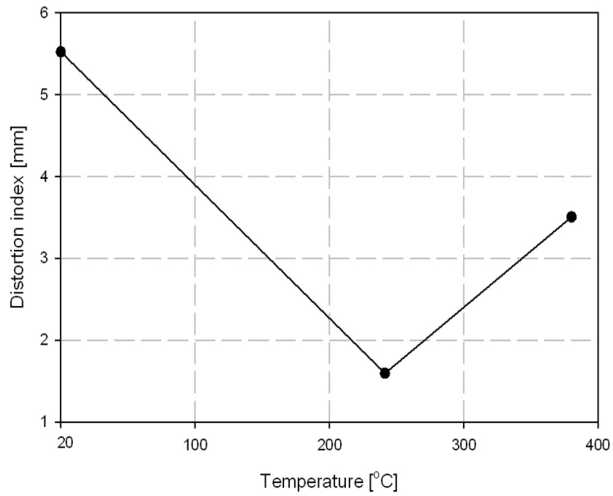

Figure 5.10. *The effect of the burner induced temperature on the distortion index for AH36 plate (Case III).*

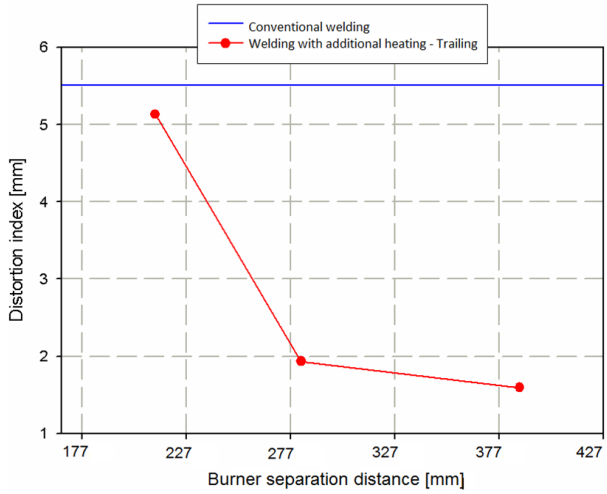

Figure 5.11. *The effect of the burner separation distance on the distortion index for AH36 (Case III) plate after conventional welding and welding with additional trailing heating.*

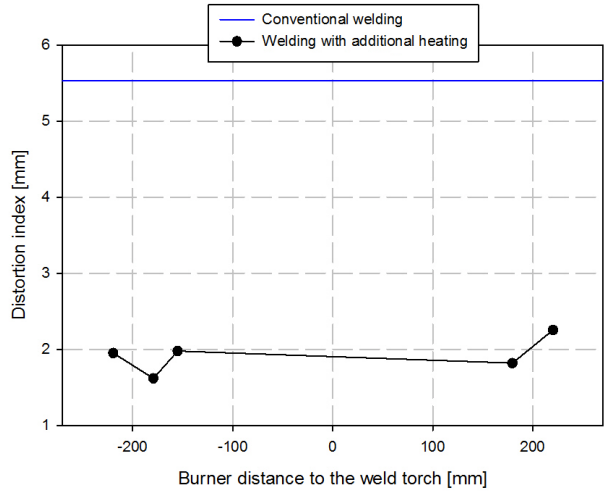

Figure 5.12. *The effect of the burner distance to the welding torch on the distortion index of AH36 plate after welding with additional heating.*

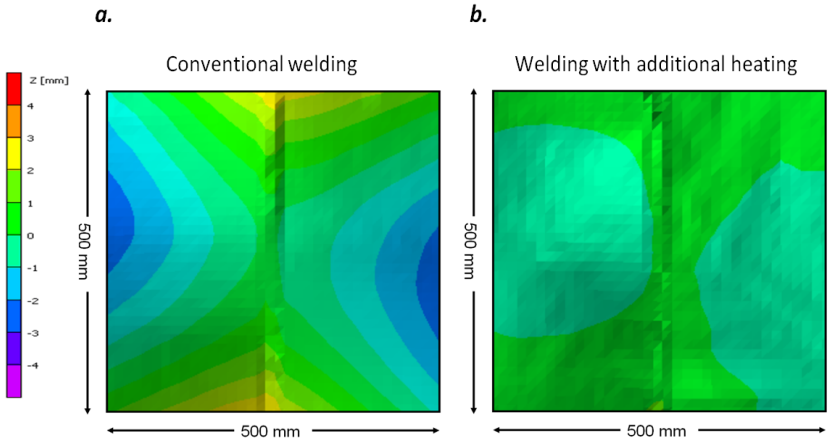

Figure 5.13. *The final out-of-plane deformation of AH36 plate after (a) conventional welding and (b) welding with additional heating with experimentally obtained minimum distortion.*

5.1.5 Plate deformation during welding and welding with additional heating

During both welding and welding with additional heating, plate movements were observed experimentally. It was indicated in **Chapter 4** that for all welding experiments (with and without additional heating), tack welds were employed. It was observed that the plate can move during both conventional welding and welding with additional heating even after using tack welds and clamping. **Figure 5.14** shows the plate movement during welding and welding with additional heating because of heat introduced by the welding arc and the burners. The movements are mainly due to the constraints and thermal expansion of the heated material. These effects are also visible after releasing the clamps.

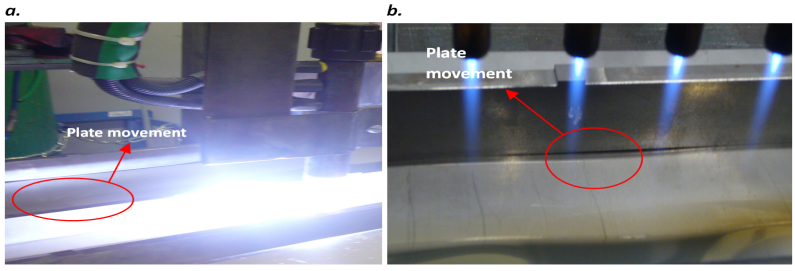

Figure 5.14. *Plate deformation during welding and welding with additional heating by (a) the welding arc and (b) the additional heating burners.*

5.2 Temperature measurement results

Welding involves localized heating of the workpiece. Each position within the workpiece experiences a specific thermal cycle, which can be defined by a heating rate, a peak temperature and a cooling rate. The heat generated by the arc is partially transferred to the workpiece. Heat is conducted away from the weld to the base material and supporting structure.

Numerous process and material parameters determine the thermal field during welding including the thermal material properties (thermal conductivity, specific heat), welding heat input, the latent heat of fusion and the cooling boundary conditions. The temperature distribution leads to formation of residual stresses, solid state phase transformations and permanent deformations (distortion). Therefore, an accurate description of the thermal field is necessary in order to analyse (or predict) the microstructural evolution and the stress fields.

In this section the results of temperature measurements during conventional welding and welding with additional heating sources are presented for the condition of the experimentally obtained minimum distortion. The thermal field during conventional welding is explained in the first part. The second part shows the results of heating trials by the burners, while the thermal field during welding with additional heating is presented in the third part. Since, the temperature of the clamps changes, the temperature measurements were also carried out on the clamps. The detailed position of thermocouples together with the results are described in **Section 5.2.4**.

5.2.1 Thermal field during conventional welding

The first set of measurements was made during conventional welding of AISI-316L, DP600 and AH36 steel plates. The welding parameters and conditions were listed in **Chapter 4**. Room temperature was 20 ^{o}C at the time of all measurements. **Figure 5.15** shows the temperature as a function of time at different positions from the weld centre line for conventional welding of AISI-316L samples (Case I-B). Temperature was measured at the underside surface of the plate. The results of temperature measurements for DP600 (Case II-B) and AH36 (Case III) steel plates with the same dimension as AISI-316L plates are shown in **Figure 5.16** and **Figure 5.17** respectively.

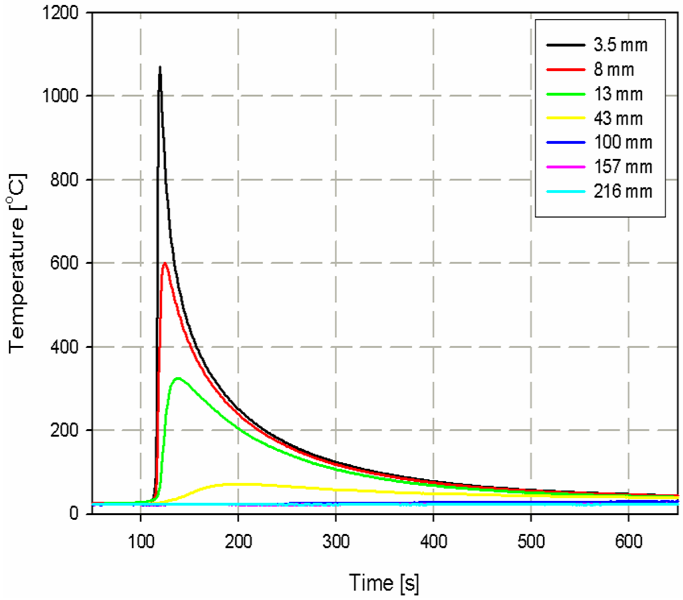

Figure 5.15. *Temperature as a function of time for conventional welding of AISI-316L plates (Case I-B) at several positions from the weld centre line.*

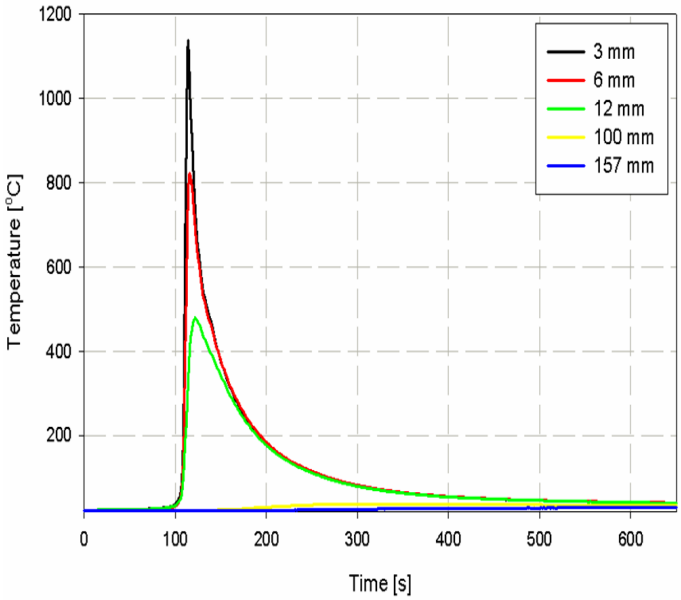

Figure 5.16. *Temperature as a function of time for conventional welding of DP600 plates (Case II-B) at several positions from the weld centre line.*

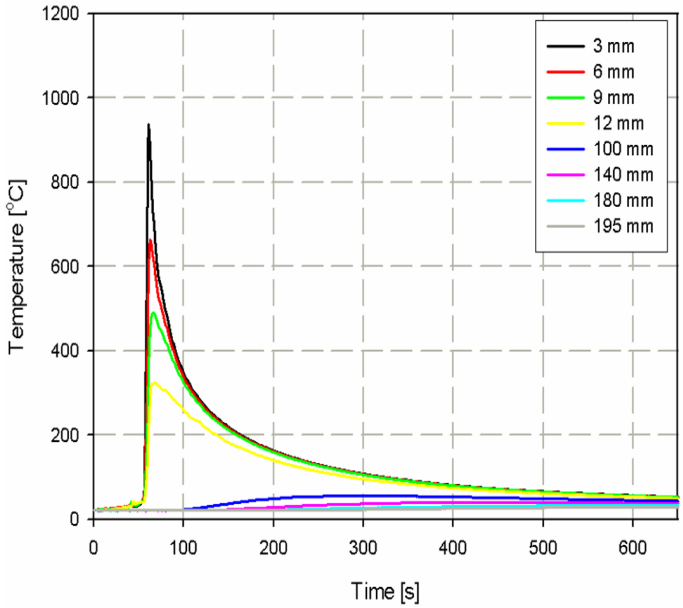

Figure 5.17. *Temperature as a function of time for conventional welding of AH36 plates (Case III) at several positions from the weld centre line.*

5.2.2 Heating source characterisation

The burners used in the additional heating experiments were introduced in **Chapter 4**. In this section the results of temperature measurements during heating by the burners are shown. In order to characterize the heating sources (the burners), the heating source was passed over the plates (materials) with the same speed as the welding speed (see **Table 4.6**). There were no welds made in these heating trials.

In the first series of the experiments, the plates were heated by the burner and the temperature of the underside surface of the plates was measured along the heating line. **Figure 5.18** shows a schematic picture of the experiment and the position of thermocouples.

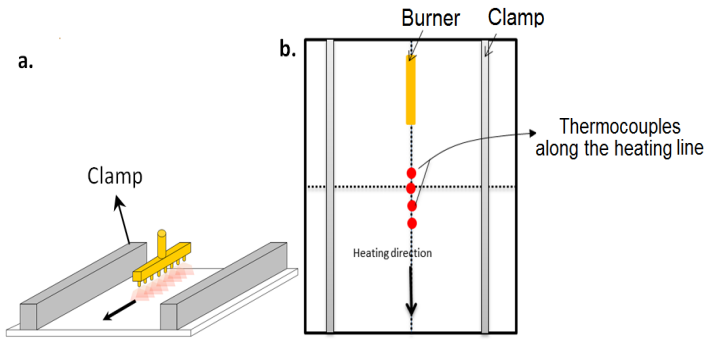

Figure 5.18. *Schematic picture of (a) the temperature measurement experiments during heating by the burner (The plate is clamped and the thermocouples are attached at the underside surface of the plate) and (b) the position of the thermocouples.*

The centre point is defined at the centre of the plate along the heating line. **Figure 5.19a** shows the temperature contour plot during heating of AISI-316L plate at a speed of 2.5 mms^{-1}. In this experiment, the maximum temperature obtained was 485 ^{o}C. In **Figure 5.19b** the temperature profile at different positions from the centre point along the heating line is plotted, while the maximum temperature for these points is shown in **Figure 5.19c**. The same experiments were repeated for DP600 and AH36 plates. Two examples are shown in **Figure 5.20** and **Figure 5.21**. Note that the burner was set to have a maximum induced temperature of 350 ^{o}C for DP600 and 250 ^{o}C for AH36 in the figures.

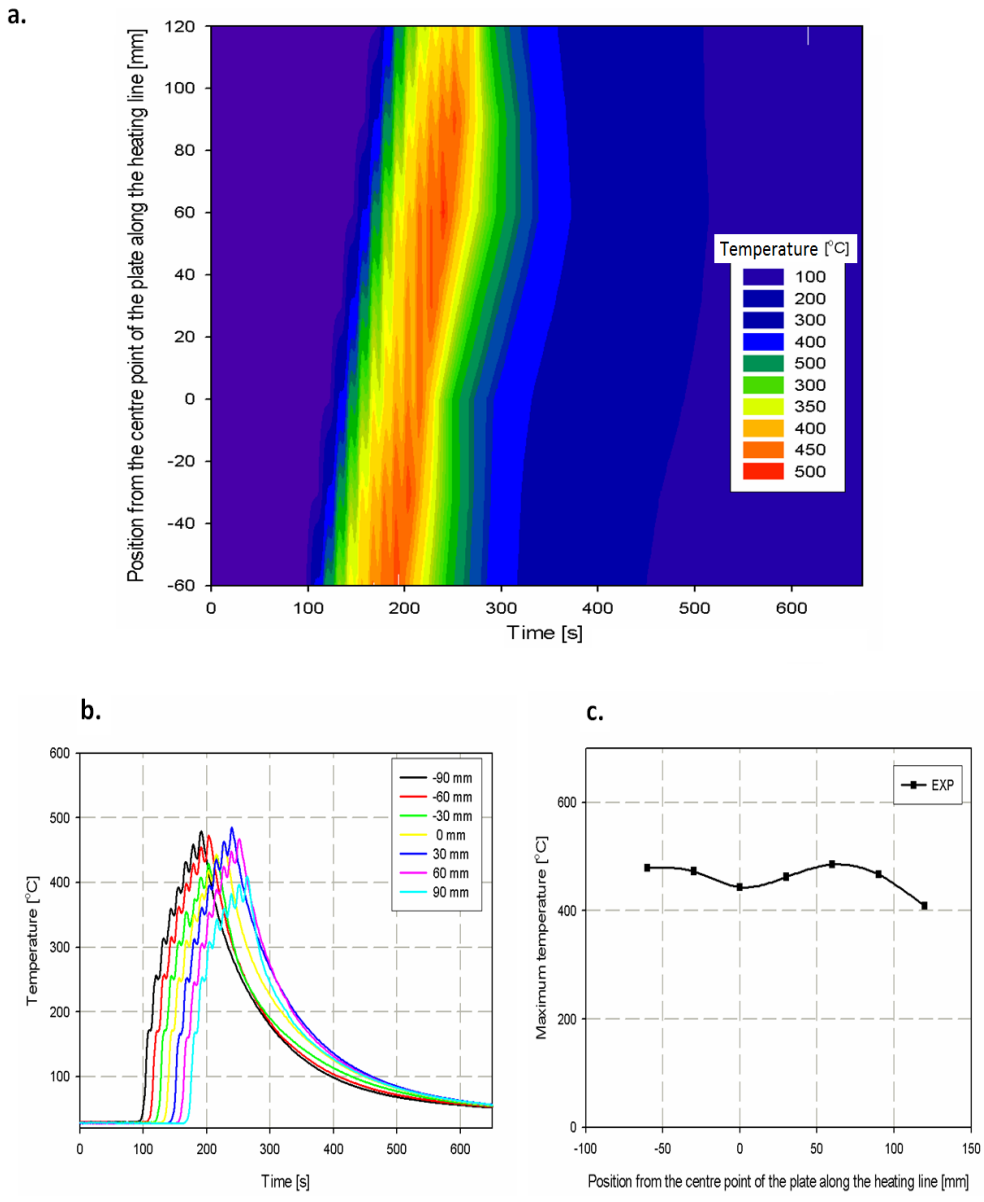

Figure 5.19. *(a) Contour plot (temperature as function of position and time), (b) the temperature profile at different positions along the heating line and (c) maximum temperature obtained during the heating process of AISI-316L plate using a burner. The thermocouples were attached at the underside surface of the plate along the heating line.*

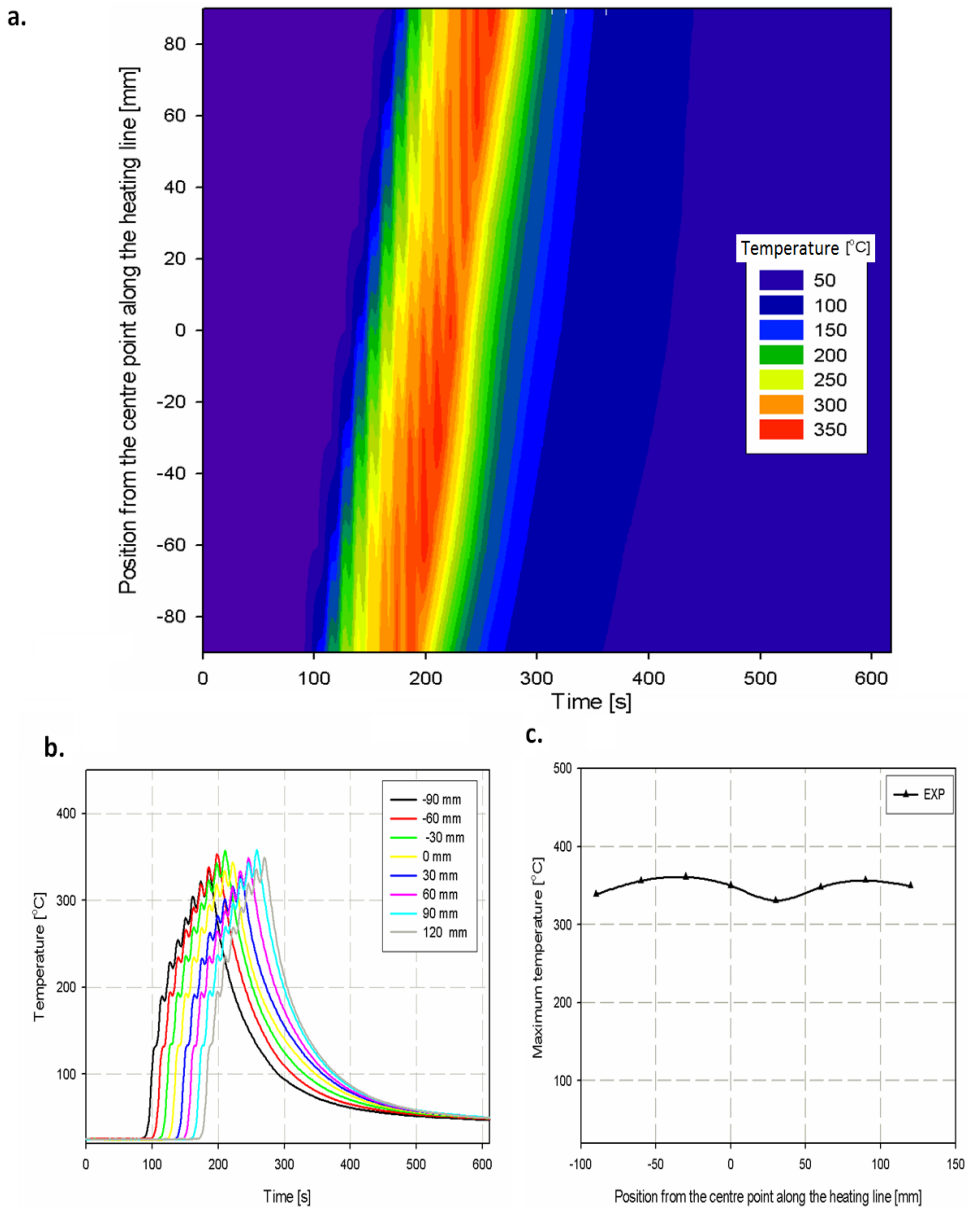

Figure 5.20. *(a) Contour plot (temperature as function of position and time), (b) the temperature profile at different positions along the heating line and (c) maximum temperature obtained during the heating process of DP600 plate using a burner. The thermocouples were attached at the underside surface of the plate along the heating line.*

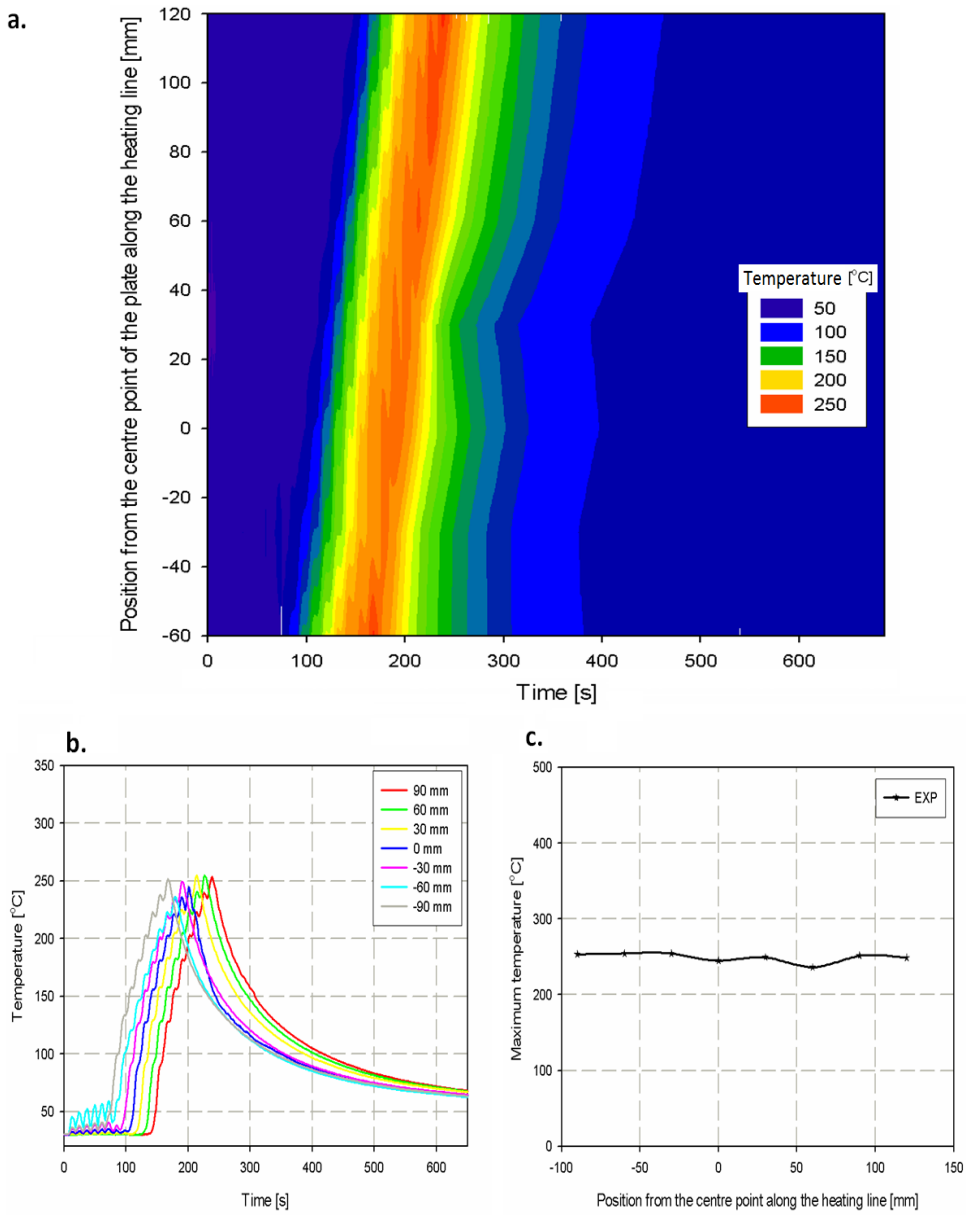

Figure 5.21. *(a) Contour plot (temperature as function of position and time), (b) the temperature profile at different positions along the heating line and (c) maximum temperature obtained during the heating process of AH36 plate using a burner. The thermocouples were attached at the underside surface of the plate along the heating line.*

It can be seen from the figures that there are eight peaks in the temperature profiles. The burner contains eight nozzles. It is seen that the temperature increases when the burner approaches. Once a nozzle has passed, a slight decrease in temperature is observed, before the temperature continues to rise until the 8th nozzle has passed. From this data the maximum peak temperature at each thermocouple position is derived. These peak temperatures are not constant over the plate length, especially for AISI-316L and DP600 steel plates. This may be due to the thermal distortion of the plate, which can alter the local heat transfer coefficient or to asymmetric distribution of gas between the nozzles in the burner. Since the thickness of AH36 plate is 6 mm, the out-of-plane movement of the plate is much less than that of AISI-316 and DP600 plates. Therefore, for this plate, the deviation of maximum temperature over the heating line is smaller than for the other two plates.

In the second series of the experiments, the plates were heated by the burner and the temperature of the underside surface of the plates was measured perpendicular to the heating line, see **Figure 5.22**. Three examples of the experimental results for different materials are shown in **Figure 5.23** to **Figure 5.25**. Note that the burner setting is not the same for these materials. It is clear that the maximum temperature is reached for all cases underneath the heat source (location 0 mm) where again temperature fluctuations are visible due to the passage of the different nozzles. The peak temperature decreases when the distance to the heat centre line is increased and the fluctuation in temperature due to passing of the nozzles diminishes. Furthermore, it can be seen that the positions with the same distance to the flame, reach different maximum temperatures. This may be due to the asymmetric distribution of gas between the nozzles in the burner.

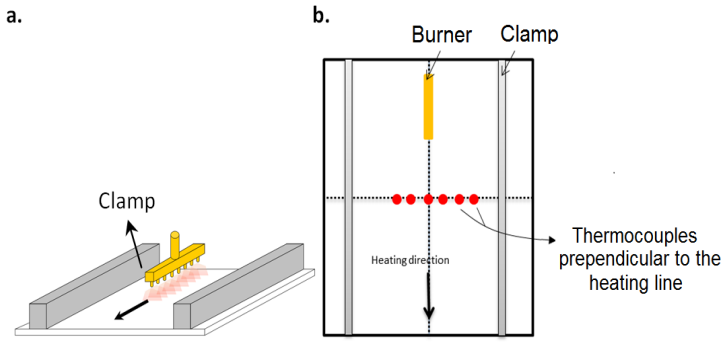

Figure 5.22. *Schematic picture of (a) the temperature measurement experiments during heating by the burner (The plate is clamped and the thermocouples are attached at the underside surface of the plate) and (b) the position of the thermocouples.*

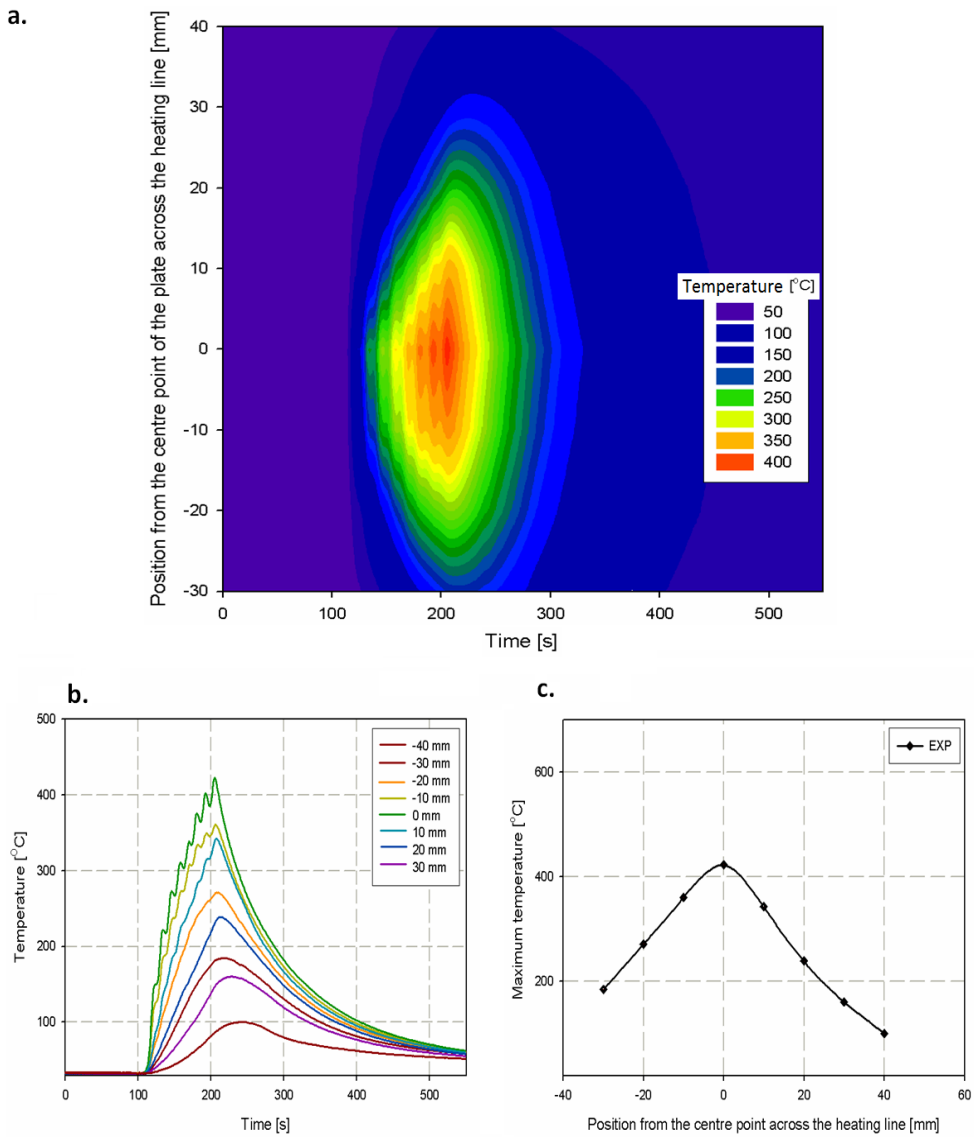

Figure 5.23. *(a) Contour plot (temperature as function of position and time), (b) temperature profile at different positions across the heating line and (c) maximum temperature obtained during the heating of AISI-316L plate using a burner. The thermocouples were attached at the underside surface of the plate transverse to the heating line.*

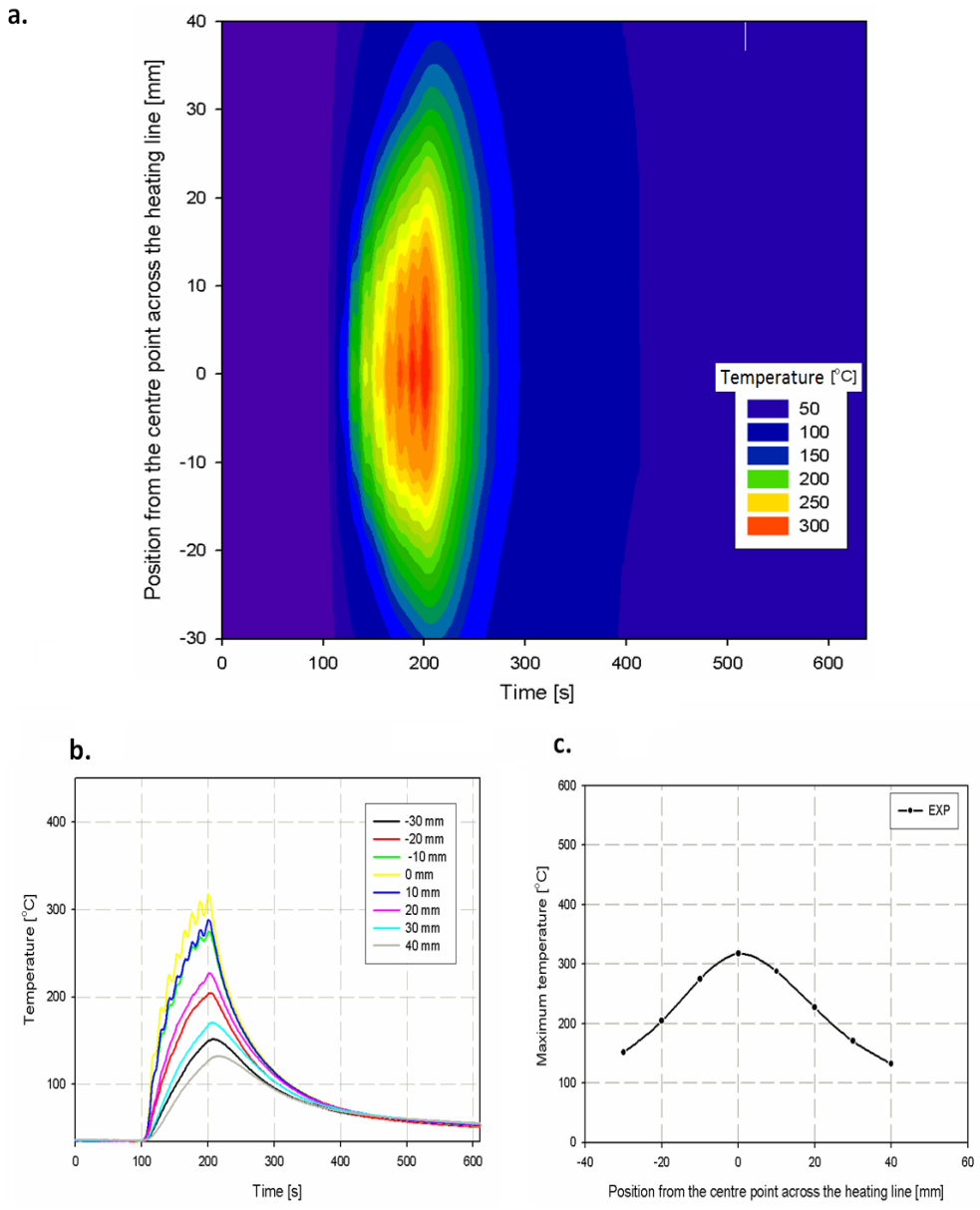

Figure 5.24. *(a) Contour plot (temperature as function of position and time), (b) temperature profile at different positions across the heating line and (c) maximum temperature obtained during the heating of DP600 plate using a burner. The thermocouples were attached at the underside surface of the plate transverse to the heating line.*

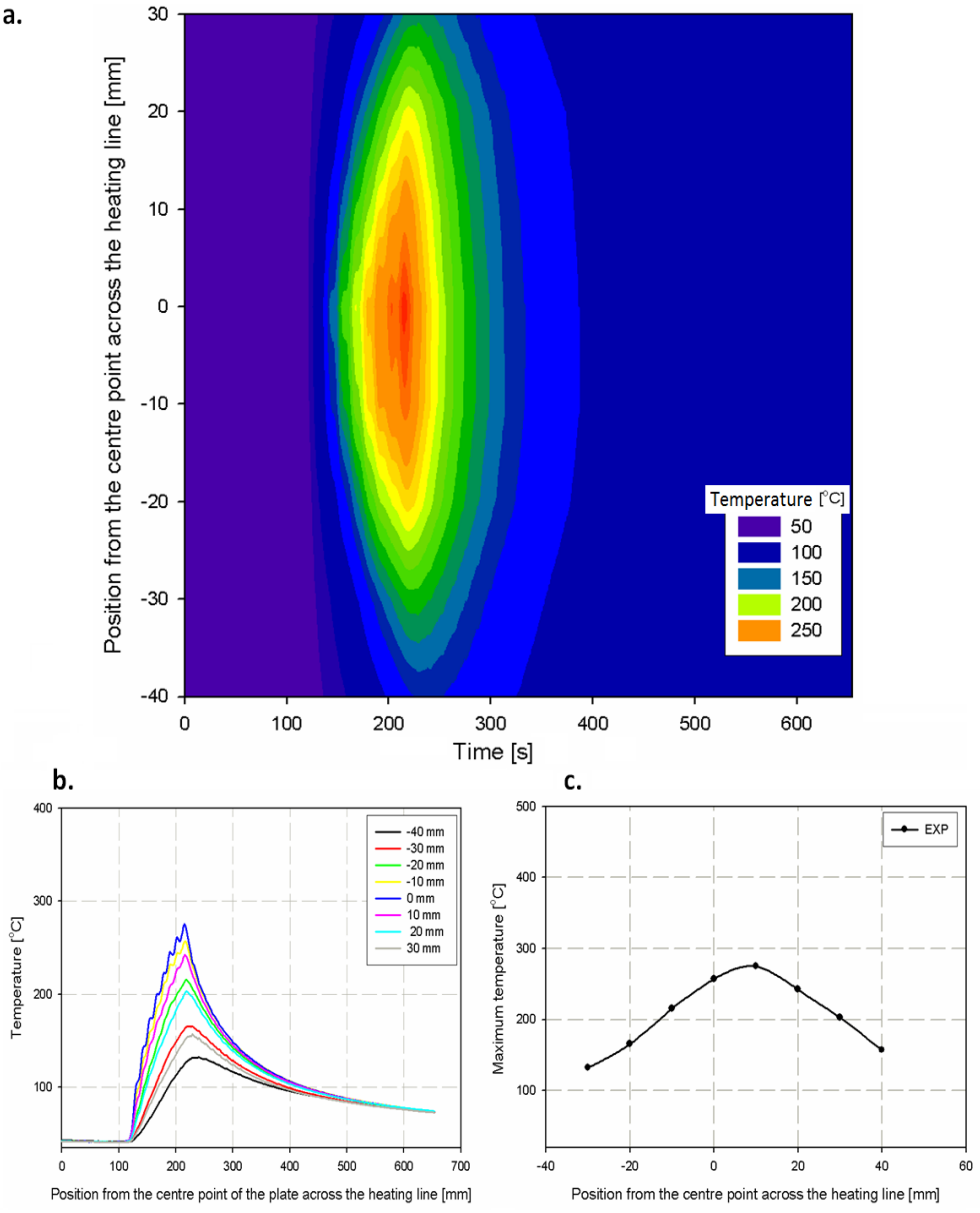

Figure 5.25. *(a) Contour plot (temperature as function of position and time), (b) temperature profile at different positions across the heating line and (c) maximum temperature obtained during the heating of AH36 plate using a burner. The thermocouples were attached at the underside surface of the plate transverse to the heating line.*

5.2.3 Thermal field during welding with additional heating

Figure 5.26 shows the results of temperature measurements during welding with additional heating of AISI-316L plate (Case I-B) for the case with experimentally obtained minimum distortion in which the burners are located at 143.5 mm from the weld centre line, 145 mm leading to the weld torch and the maximum temperature of the burners is 380 ^{o}C. The burners are coupled to the welding torch, therefore the speed of welding and heating are the same.

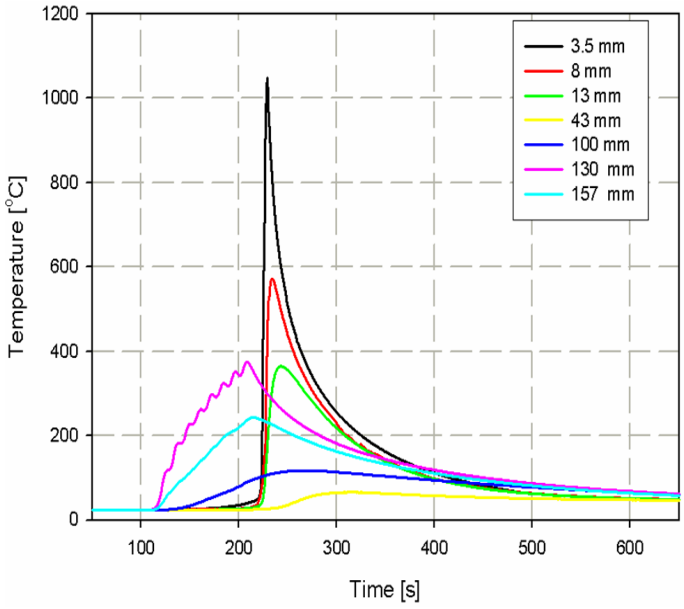

Figure 5.26. *Temperature measurements for welding with additional heating of AISI-316L plates (Case I-B) at different positions from the weld centre line.*

It is clearly seen that at the position of the burners, the temperature increases significantly. The temperature profiles for the point located at the weld region or the HAZ (of welding) are similar to that of conventional welding shown in **Figure 5.15**.

For DP600 steel plate (Case II-B), it was found that the experimentally obtained minimum distortion can be obtained where the burners are located 193.5 mm from the weld centre line 145 mm leading to the weld torch with a maximum temperature of around 320 ^{o}C. **Figure 5.27** shows the temperature profile during welding with additional heating for this plate. Again, the temperature of the positions located beneath the burners is increased significantly compared to that of conventional welding.

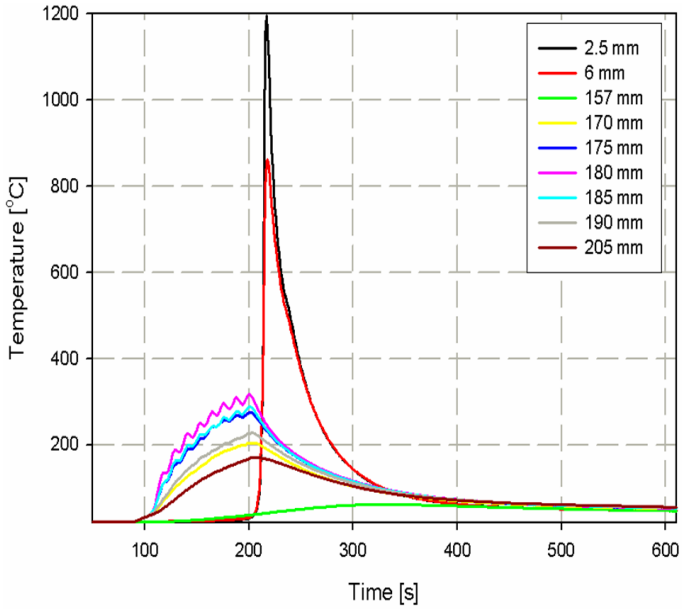

Figure 5.27. *Temperature measurements for welding with additional heating of DP600 plates (Case II-B) at different positions from the weld centre line.*

The same trend can be seen for AH36 plate (Case III). **Figure 5.28** shows the temperature profile during welding with additional heating for AH36 plate. It was found that the experimentally obtained minimum distortion condition for such a plate can be obtained where the burners are located 193.5 mm from the weld centre line at 180 mm trailing to the weld torch with a maximum temperature of 240 ^{o}C. The speed of the welding process and the additional heating was 4.5 mms^{-1}.

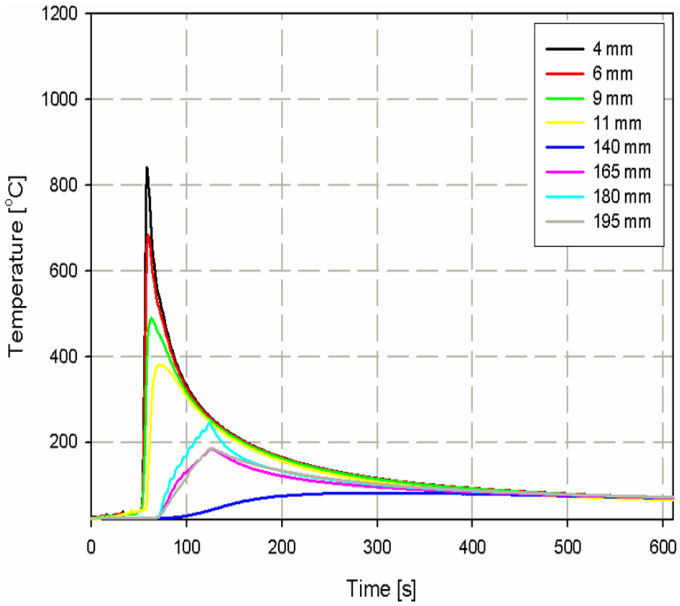

Figure 5.28. *Temperature measurements for welding with additional heating of AH36 plates (Case III) at different positions from the weld centre line.*

5.2.4 Temperature change of the clamps

The temperature of the clamps is not constant. In the conventional welding process, the temperature of the clamps close to the welding torch increased while the temperature of the clamps near the edges of the plate did not change. During welding with additional heating, the temperature of the clamps near the edges of the plate significantly increased.

The temperature change of the clamps close to the welding torch for both conventional welding and welding with additional heating depends on the welding heat input and the thermal material properties of the plate and the clamps. These clamps have a constant distance to the welding torch.

The temperature change of the clamps located near the edges of the plate when welding with additional heating depended on the heat input of the burner, the distance of the burner to the clamps and the thermal material properties of the clamps and the plate. An example of temperature change of the clamps during welding with additional heating of AH36 plate where the burners are located 30 mm from the clamps is shown in **Figure 5.29a**. Two thermocouples were attached to the clamps as shown in the **Figure 5.29b**. As can be seen, the temperature of the clamp increases. These measurements are used as the boundary conditions in the thermal

modelling in **Chapter 6**.

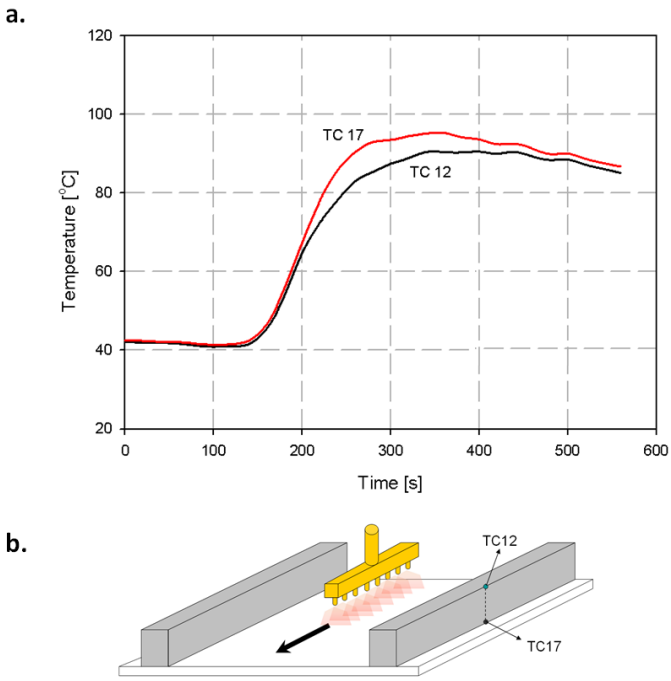

Figure 5.29. *(a) The temperatures change of the clamps located close to the edges of the plate during welding with additional heating of AH36 steel and (b) the position of thermocouples in the measurements.*

5.3 Microstructure analysis

In the previous section, the temperature cycle and distribution of conventional welding and welding with additional heating were measured for a number of conditions. The welding thermal field as well as the welding with additional heating temperature may change the microstructure of the materials, depending on the peak temperature reached and the cooling rate at that position. Any changes in the microstructure may alter mechanical properties and will have an influence on both the residual stress and the distortion fields.

The microstructure of the as-received materials used, described in **Chapter 4**. In this section the results of the study on the microstructural changes due to welding and welding with welding with additional heating are discussed.

5.3.1 Influence of welding and welding with additional heating on the microstructure of AISI-316L (Case I-B)

Stainless steel plates (Case I-B) were welded as described in **Chapter 4**. The experimentally obtained minimum distortion situation among the welding with additional heating experiments was obtained with the burners located 143.5 mm from the weld centre line and 145 mm leading to the welding torch. The burner induced temperature was found to be 380 ^{o}C at the underside of the plate.

This steel does not exhibit substantial solid state phase transformations during both conventional welding and welding with additional heating. Some ferrite may be formed in the weld metal and in the HAZ close to the weld. However, the heated areas beneath the burners in welding with additional heating are expected to have a large grain size.

Figure 5.30 shows the micrographs of the welded plates for different regions (at 0.5 mm from the top surface of the plate). The micrographs of the conventionally welded plate and the plate welded with additional heating for both weld zone and HAZ (of welding) were similar. The region located beneath the burner shows a larger grain size in the case of additional heating.

The grain size of the base material was approximately 20 μm. In the coarse grained HAZ of the weld, the grain size increases to approximately 100 μm. The heated area beneath the burner in the welding with welding with additional heating has a grain size approximately two times larger than that of the base material, *i.e.* 40 μm.

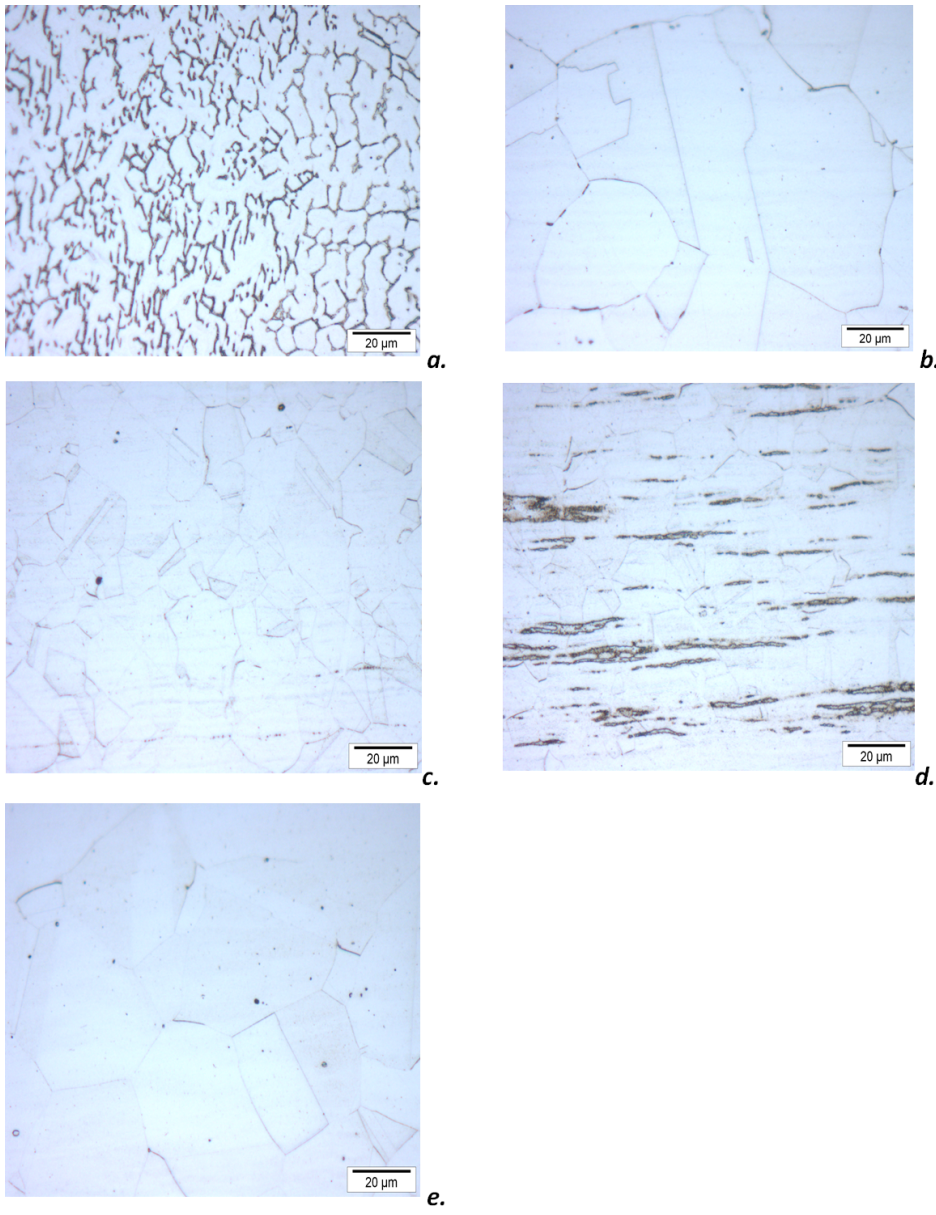

Figure 5.30. *Micrographs of the AISI316L stainless steel samples showing (a) weld metal, (b) coarse grained HAZ (of welding), (c) fine grained HAZ of welding, (d) base metal for both conventional welding and welding with additional heating and (e) the heated area beneath the burners in welding with additional heating. All micrographs are taken at 0.5 mm from the top surface of the plate.*

5.3.2 Influence of welding and welding with additional heating on the microstructure of DP600 (Case II-B)

DP600 steel contains approximately 80-90% ferrite and 20-10% martensite. This section shows the results of microstructure analysis of conventionally welded material and material welded with additional heating for DP600 steel plates (Case II-B). The experimentally obtained minimum distortion in the welding with additional heating experiment was obtained with the burners located 193.5 mm from the weld centre line and 145 mm leading to the welding torch. The burner maximum temperature was 320 ^{o}C.

During welding of DP600, the base material that consists of martensite in a ferrite matrix, will transform to austenite when the temperature exceeds the A_{c3}-temperature. Depending on the cooling rate, the austenite transforms back into acicular products, bainite or martensite [3].

For the transformation of austenite during cooling, a CCT diagram from [4] was selected with a chemical composition close to that of the material used in the present study, **Figure 5.31**. In order to use the diagram in calculations, this CCT diagram was parameterized using the procedure explained in **Chapter 3**. Results of phase fraction calculations are reported in **Chapter 6**.

Figure 5.32 shows the cooling cycle for two positions located 3 and 6 mm from the weld centre line during conventional welding of DP600 steel plate together with the parameterized CCT diagram. As can be seen from the figure for these two points, the formation of hard constituents (bainite and martensite) is expected.

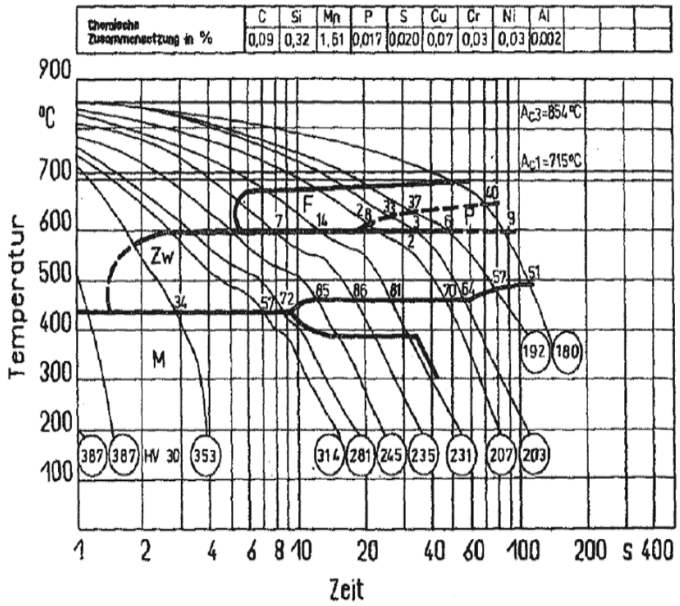

Figure 5.31. *Selected transformation diagram during continuous cooling of DP600 steel [4].*

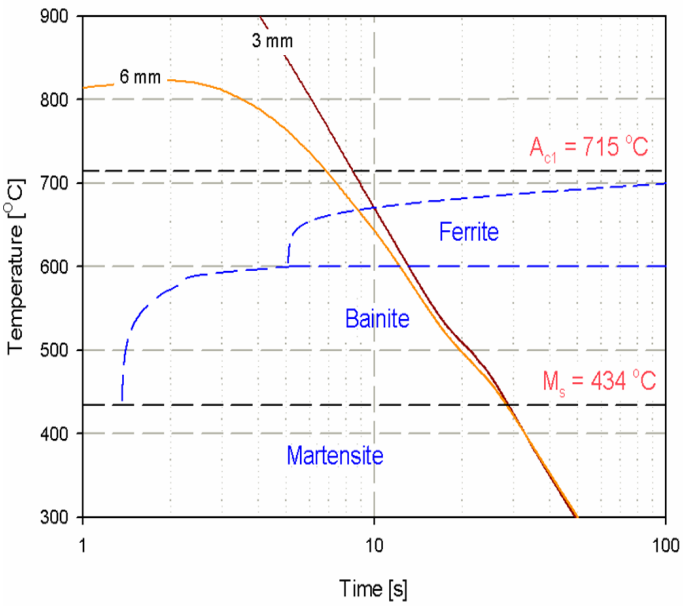

Figure 5.32. *Cooling cycle during conventional welding for two points located 3 and 6 mm from the weld centre line together with the parameterized DP600 CCT diagram.*

It was shown in the temperature measurement that the temperature profiles of the HAZ (of welding) and the weld zone for both conventional welding and welding with additional heating are the same, *i.e.* the heat of the burner does not influence the weld. Therefore, the development of microstructure in these regions should be very similar. **Figure 5.33** shows the micrographs of the weld, coarse grained HAZ (of welding), fine grained HAZ (of welding) and base metal of conventionally welded DP600 steel.

The areas beneath the burners have a similar microstructure to the base metal (**Figure 5.33d**). **Figure 5.34** shows a SEM photograph of the base material and the heated area beneath the burners in welding with additional heating experiments.

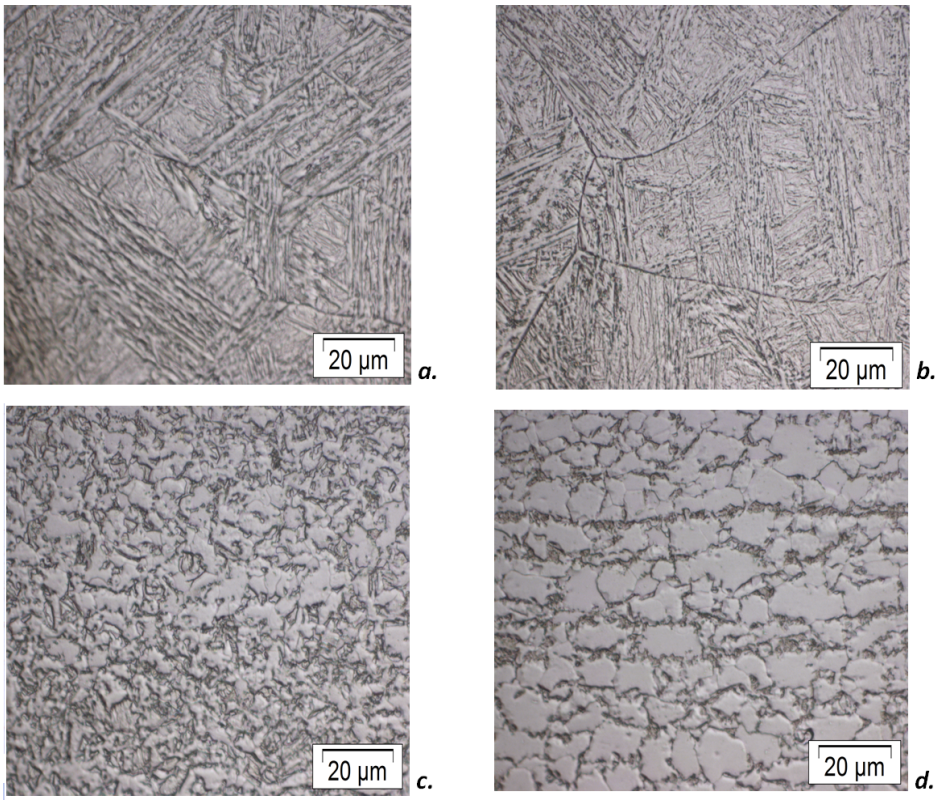

Figure 5.33. *Micrographs of the DP600 samples showing a close-up of the (a) weld metal, (b) coarse grained HAZ (of welding), (c) fine grained HAZ (of welding) and (d) base metal.*

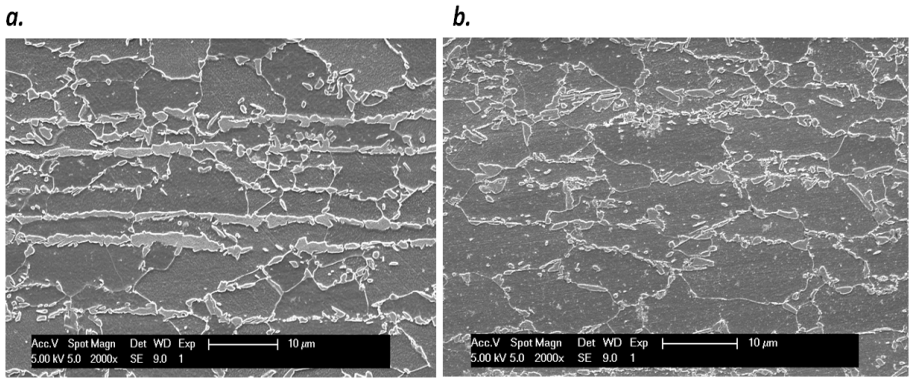

Figure 5.34. *SEM display of (a) base metal and, (b) the area beneath the burner in welding with additional heating experiments of DP600 plates.*

Hardness profiles were taken across the weld, the heat affected zone and the heated area beneath the additional heating burners. The locations of the measurements are shown in **Figure 5.35** and the hardness profiles are shown in **Figure 5.36**.

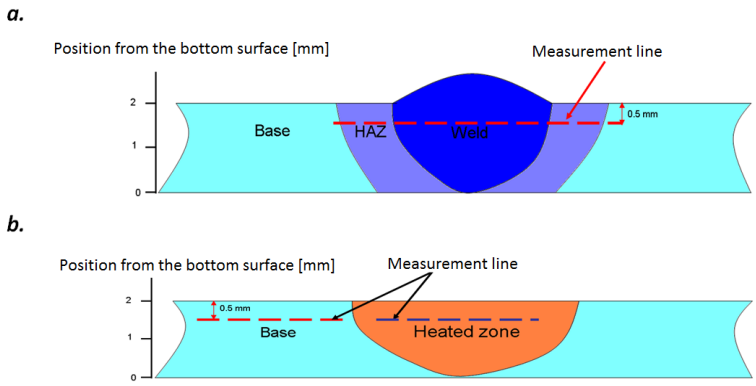

Figure 5.35. *The locations of hardness measurements of conventionally welded and welded with additional heating of DP600 plates. The measurements were performed for (a) HAZ (of welding) and weld zones and (b) beneath the burners.*

Figure 5.36a shows the hardness profile for the weld, HAZ (of welding) and base metal regions. The base metal hardness was approximately 200 HV. The maximum hardness in the conventional weld was around 250 HV. The hardness level of the weld with additional heating is more or less the same as for the conventional weld. In both cases, softening zones can be seen further away from the weld. The results indicate that additional heating does not affect the hardness levels around the weld.

Figure 5.36b shows the hardness profile of the heated area beneath the burners as a function of distance to the heating line. The figure includes the hardness of the base material. As can be seen from the figure, tempering of the martensite of the original base metal during additional heating, causes a reduction of hardness for the areas beneath the both burners.

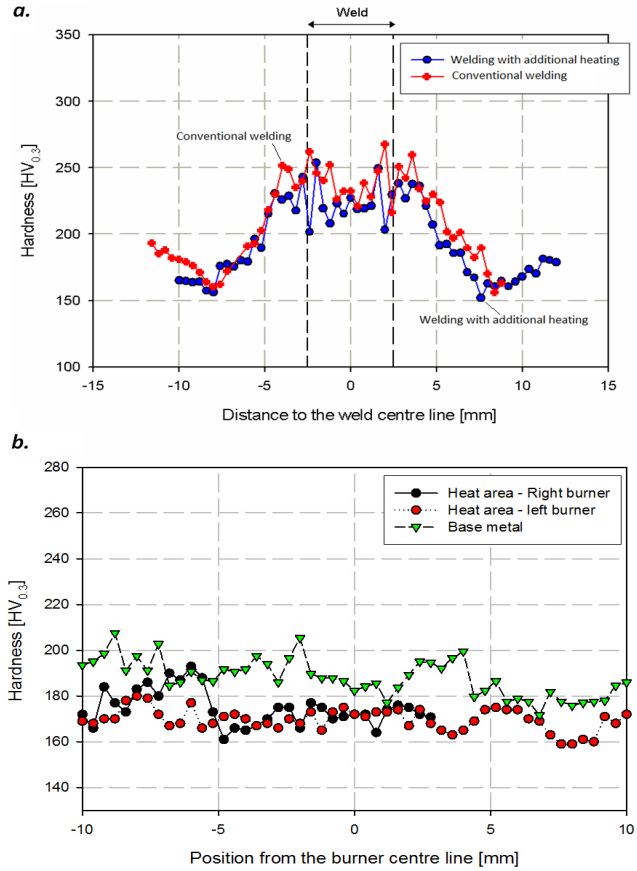

Figure 5.36. *The hardness profile for (a) both conventional welding and welding with additional heating and (b) the hardness profile in the side heated zones beneath the burners.*

5.3.3 Influence of welding and welding with additional heating on the microstructure of AH36 (Case III)

The experiments showed that the experimentally obtained minimum distortion case for AH36 occurs when the burners are positioned 193.5 mm from the weld centre line, 180 mm trailing to the welding torch with a maximum burner induced temperature of around 240 ^{o}C. In this section the micrographs of the conventional weld and weld with additional heating for the experimentally obtained minimum distortion case are discussed.

Figure 5.37 shows the micrograph of the weld metal, coarse grained HAZ (of welding), fine grained HAZ (of welding) and the base metal of both conventionally welded material and welded material with additional heating. The heated areas beneath the

burners in case of welding with additional heating for both the top and underside surfaces of the sample are shown in the figure.

Welding with additional heating has no influence on the microstructure of the weld metal and the HAZ (of welding). This is again because of the similar thermal histories of the weld and HAZ (of welding) for both cases. It can be seen that the top surface of the heated area beneath the burners has a re-crystallized microstructure, while the underside surface has a microstructure close to the base metal.

Hardness profiles were measured at locations shown in **Figure 5.38**. The hardness profile of the weld, HAZ (of welding) and the base metal for conventional welding and welding with additional heating is shown in **Figure 5.39a**, while the hardness of the heated area beneath the burners is shown in **Figure 5.39b**. The hardness of the heated area beneath the burners is slightly reduced. It is expected that such a reduction is due to the re-crystallization and reduction of internal energy.

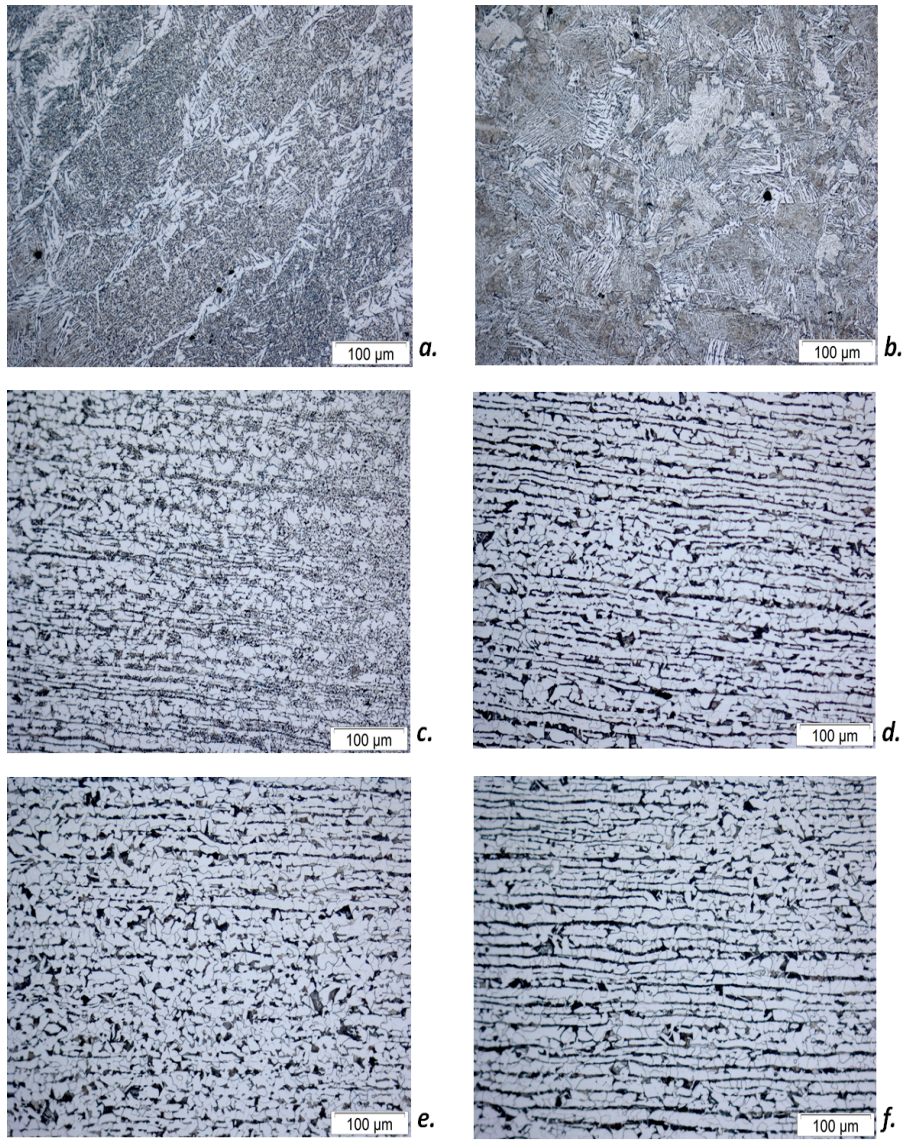

Figure 5.37. *Micrographs of the AH36 samples showing a close-up of the (a) the weld metal, (b) coarse grained HAZ (of welding), (c) fine grained HAZ (of welding) and (d) base metal, (e) the top surface of the heated area beneath the burner after additional heating and (f) the underside surface of the heated area beneath the burner in additional heating.*

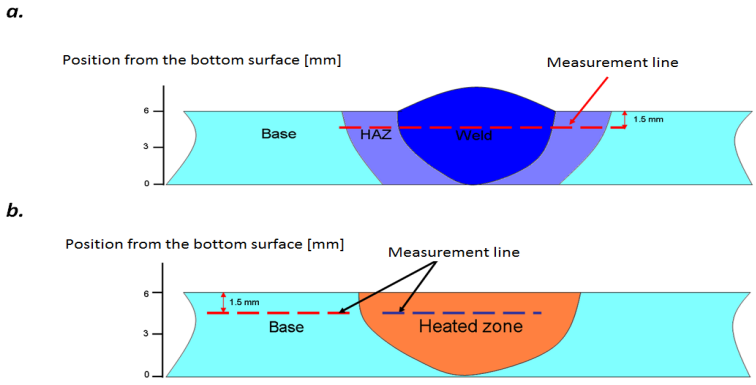

Figure 5.38. *The cross section of the welds in conventional welding and welding with additional heating.*

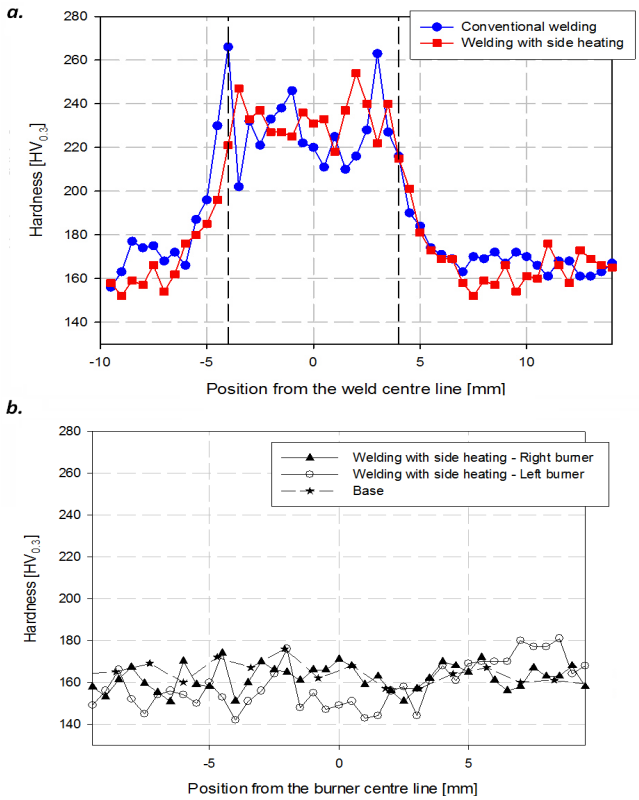

Figure 5.39. *The hardness profile for (a) both conventional welding and welding with additional heating and (b) the hardness profile in the side heated zones beneath the burners for AH36.*

The as-received condition of AH36 steel contains 15.5% pearlite and 84.5% ferrite. In large regions of the heat affected zone austenization will occur, but not enough time is available for homogenization. **Figure 5.40** shows the CCT diagram used for austenite transformations in AH36 steel [5]. The temperature profiles, for two points located at underside surface of the plate, 3 and 4 mm from the weld centre line are shown together with the parameterized CCT diagram in **Figure 5.41**. The temperature profiles are related to the points at the underside surface of the plate. As can be seen from the figure, at these two locations, the formation of hard constituents (like bainite) is expected.

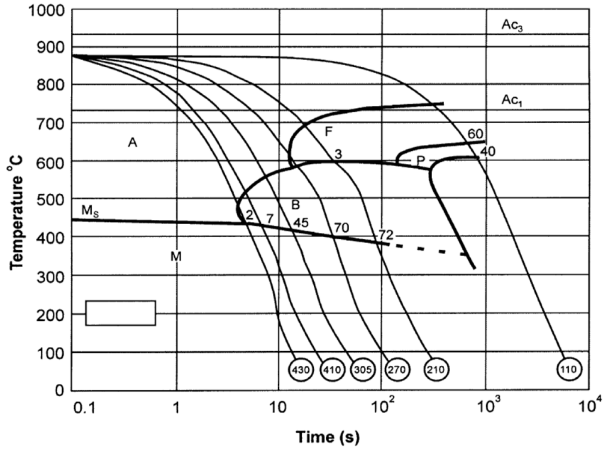

Figure 5.40. *Selected CCT diagram for transformation of austenite during cooling in AH36 steel [5].*

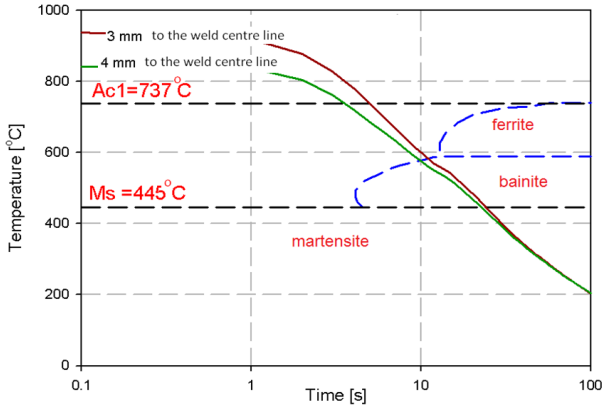

Figure 5.41. *The cooling cycle during conventional welding for two points located 3 and 4 mm from the weld centre line at the underside surface together with the parameterized CCT diagram.*

5.4 Residual stress measurement results

This section deals with the results of residual stress measurements for the conventionally welded AISI-316L (Case I-B), DP600 (Case II-B) and AH36 (Case III) sheets and material welded with additional heating. For the welds with additional heating, the results presented are related to the cases with the experimentally obtained minimum distortion as described in **Section 5.1**.

5.4.1 Residual stress measurement results and discussions for AISI-316L and DP600 plates (Case I-B and Case II-B)

Neutron diffraction residual strain measurements were conducted on $500\times250\times2$ mm^3 AISI-316L (Case I-B) and DP600 (Case II-B) samples. The samples were welded conventionally and welding with additional heating and full penetration was obtained. The experimentally obtained minimum distortion plates after welding with additional heating were used for comparing the influence of the additional heating on the residual stresses with conventional welding.

In order to calculate the residual stresses, the stress free lattice spacing is required. This value is not necessarily constant over the sample as it is affected by the variation in the chemical composition and the microstructure [3]. For both AISI-316 and DP600, a $280\times2\times2$ mm^3 sample was taken from the plate after welding with additional heating using electro-discharge machining (EDM). 24 measurements were carried out at different positions on the sample from the fusion line to the base material. The results of the measurements on the sample are shown in **Table 5.1**.

Table 5.1. *The stress free lattice spacing (d_o) measurement for AISI-316L and DP600.*

Material	**d_o**	**Error**
AISI-316L	1.08404 Å	±0.00005
DP600	1.17096 Å	±0.00004

The measured values are in good agreement with the reported values of 1.08405±0.0001 Å for AISI-316 and 1.1709 Å for DP600 steel from [3].

The stress free lattice spacing of the weld zone and the HAZ (of welding) of both the conventionally welded plates and the plate after welding with additional heating is assumed to be equal, since additional heating burners do not influence the temperature profile of the welded region.

The stress free lattice spacing was therefore measured for the plate after welding with additional heating from the weld zone to the base metal. The measured values for the weld zone, the HAZ (of welding) and the base material were used for conventionally welded plate as well. The residual stresses were calculated using the

reasonable assumption that the measurement directions are aligned with the principle stress directions. It is shown in [3] that the bi-axial and uni-axial stress state assumption show similar longitudinal residual stresses. Therefore, the stress state is assumed to be uni-axial here.

In the calculation of the residual stresses, the elastic constants for Fe(311) and (211) planes are listed in **Table 5.2**.

Table 5.2. *Elastic constants used in the calculation of residual stresses in this thesis (Data from [6]).*

Material	**Plane**	**E (GPa)**	α
AISI-316L	(311)	183.5	0.31
DP600	(211)	225.5	0.28

The residual stresses were measured on AISI-316L stainless steel samples that were welded conventionally and with additional heating. It was assumed that the stresses in the thickness direction of the plate are negligible. The origin is set at the plate centre. The rolling direction of the material is along the longitudinal direction. The diffraction data was analysed using two programmes: Poldiausfit8 and Poldilattfit8. Poldiausfit8 is the general POLDI fitting routine. Here all diffraction peaks are fitted independent of each other. Poldilattfit8 is a fitting routine using Pawley refinement. The diffraction peaks are fitted simultaneously in this programme assuming a certain crystal structure [7]. In the available beam time, the transverse stresses were not measured and the longitudinal residual stresses were determined from a longitudinal measurement only.

The longitudinal residual stress distributions for conventionally welded AISI-316L plates and after welding with additional heating are shown in **Figure 5.42**. The longitudinal residual stresses were measured for the weld with additional heating, the experimentally obtained minimum distortion. **Figure 5.42a** shows the results of conventional welding while the results of welding with additional heating are shown in **Figure 5.42b**. In the both cases, the longitudinal residual stresses are measured after releasing the clamps. The releasing of the clamps took place when the temperature of the plate had reached room temperature.

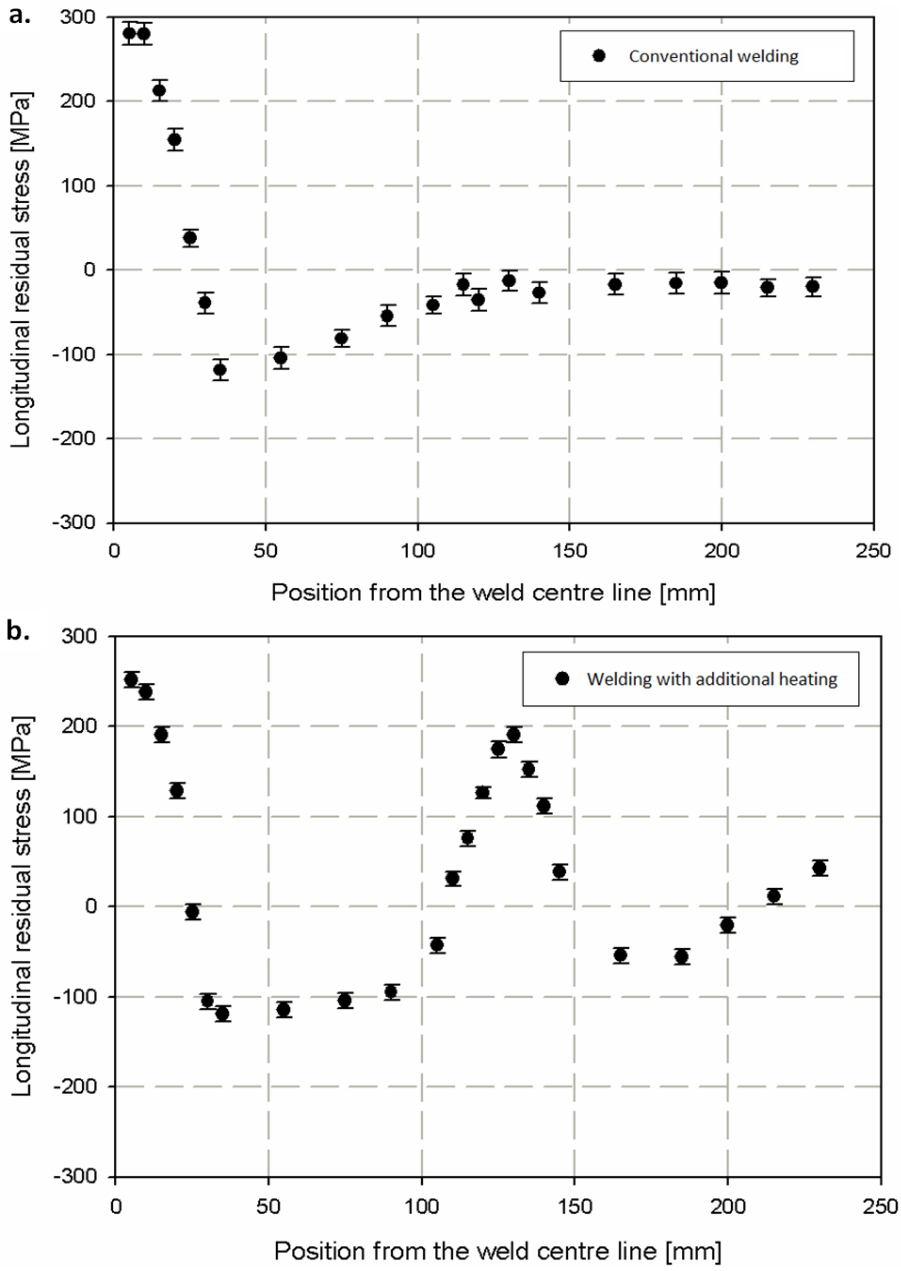

Figure 5.42. *Longitudinal residual stress measurement results for AISI-316L (Case I-B) after (a) conventional welding and (b) welding with additional heating.*

It can be seen from the figure that the maximum tensile stresses in the HAZ (of welding) for both cases are similar. This is also the case for to the maximum compressive stresses, present at approximately 25 mm from the fusion line. Welding with additional heating induces tensile stresses beneath the burner positions in the order of 200 MPa. The thermal conductivity of AISI-316L is relatively low ($\approx$25 $Wm^{-1}K^{-1}$ at 500^{o}C) and therefore, the heat introduced by the burners, remains localized. The thermal expansion and contraction of the additional heated areas cause the formation of stresses beneath the burner positions. It is also visible from the figure that the distribution of compressive residual stresses changes when additional heating is applied during welding.

The DP600 (Case II-B) steel plate undergoes solid phase transformations in the weld zone and the HAZ (of welding) during welding and welding with additional heating. Solid state phase transformations have a significant effect on the diffraction peaks. The diffraction peaks outside the HAZ (of welding) are of good quality, while in the HAZ (of welding), the peak intensity is reduced [3]. **Figure 5.43** shows the Full Width at Half Maximum (FWHM) of the diffracted peaks for both conventional welding and welding with additional heating. The FWHM increases in the weld zone and the HAZ (of welding). This can be attributed to microstructural changes, as it is also reported by van der Aa [3]. It can be seen that this increase is the same for conventional welding and welding with additional heating, indicating that the microstructure in the weld metal and the HAZ (of welding) is not different. The FWHM is somewhat larger for conventional welding compared to welding with additional heating. This can be ascribed to more deformation generated during conventional welding. The microstructure investigation of conventional welding and welding with additional heating was discussed in **Section 5.3**.

The measured longitudinal residual stress profiles for both conventionally welded plates and plates after welding with additional heating are shown in **Figure 5.44**.

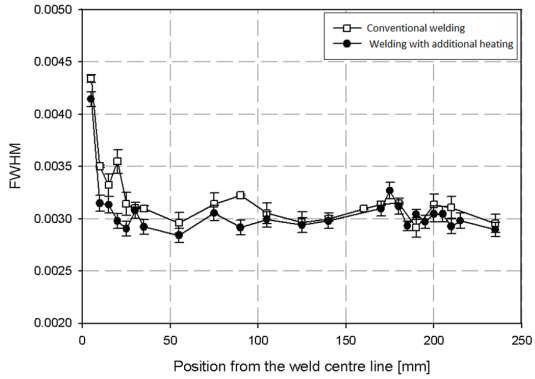

Figure 5.43. *FWHM for conventionally welded plates and the plates welded with additional heating as a function of distance from the weld centre line.*

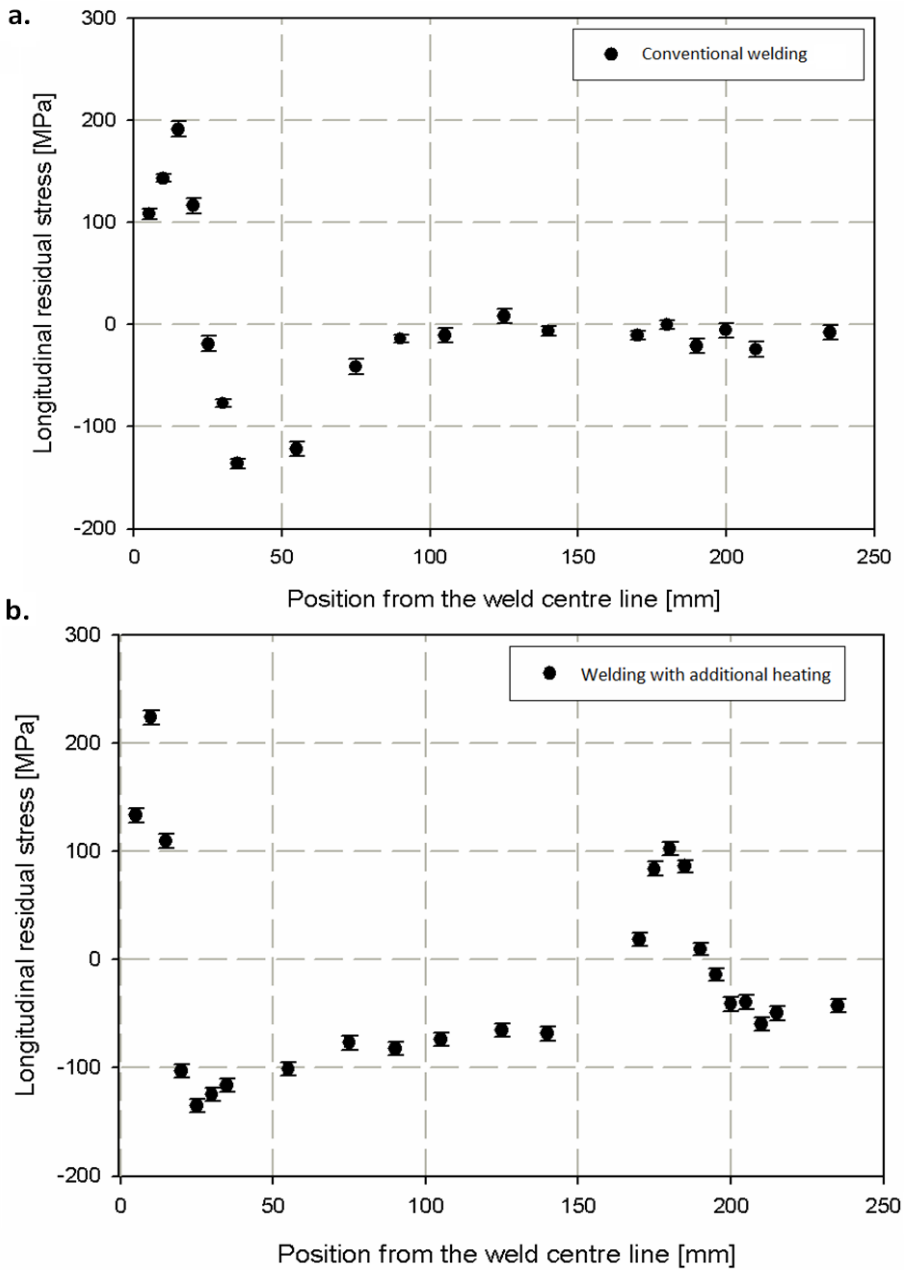

Figure 5.44. *Longitudinal residual stress measurement results for DP600 (Case II-B) after (a) conventional welding and (b) welding with additional heating.*

It is clear that welding with additional heating induces tensile stresses underneath the burner positions. The maximum tensile stresses at the weld and HAZ (of welding) for the conventional weld and welding with additional heating are more or less similar. The left most three points in **Figure 5.44a** and two points in **Figure 5.44b** demonstrate that the microstructure affects the tensile stresses. By approaching to the weld centre line, a drop can be seen in the residual stresses. This drop is attributed to the effects of solid phase transformations on the residual stresses in both cases. The maximum compressive stress for conventional welding occurs at a larger distance from the weld centre line compared to welding with additional heating. The level of the maximum compressive stresses is more or less similar for both processes. The area between the HAZ (of welding) and the heated area shows a significant difference in the stress levels.

5.4.2 Residual stress measurement results and discussions for AH36 plates (Case III)

Neutron diffraction residual stress measurements at LLB were performed on 500×250×6 mm^3 AH36 samples (Case III).

The samples were welded conventionally and with additional heating. The experimentally obtained minimum distortion plates after welding with additional heating were used for comparing the influence of the additional heating on the residual stresses with conventional welding. The diffraction measurements were performed on the Fe(211) planes.

In order to measure the stress free lattice spacing, a 280×2×6 mm^3 sample was taken from the plate after welding with additional heating using electro-discharge machining (EDM) and 24 measurements were carried out at different positions on the sample from the fusion line to the base material. The results of the measurements on the sample are shown in **Table 5.3**. The whole procedure is similar to that of the AISI-316L and DP600 plates explained previously.

Table 5.3. *The stress free lattice spacing (d_o) measurement for AH36.*

Material	$\mathbf{d}_o$	**Error**
AH36	2.02930 $\AA$	±0.000018

The longitudinal residual stresses were measured perpendicular to the welding direction as a function of distance from the weld centre line. The origin is set at the plate centre. The rolling direction of the material is along the longitudinal direction. The position of the measurement in the through thickness direction is shown in **Figure 5.45**. A gauge volume of 2×2×2 mm^3 was used here.

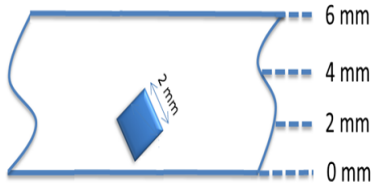

Figure 5.45. *The measurement position through thickness direction in AH36 plates.*

The longitudinal residual stress distributions for conventionally welded plates and after welding with additional heating are shown in **Figure 5.46a** and **Figure 5.46b** respectively. The longitudinal residual stresses are measured for the weld with additional heating with experimentally obtained minimum distortion. In both cases, the longitudinal residual stresses are measured after releasing the clamps. The releasing of the clamps takes place when the temperature of the plate had reached room temperature. It can be seen from the figure that the maximum tensile stresses of the welds in both conventional welding and welding with additional heating are at the same levels. However, the maximum compressive stresses in the case of welding with additional heating are slightly higher than that of conventional welding. By increasing the distance from the weld centre line to the plate edge, the compressive stresses in welding with additional heating decrease and change to tensile stresses. In **Chapter 6**, a detailed discussion is presented regarding the prediction of residual stresses after welding with additional heating of AH36, sources of deviation and expectations.

The longitudinal residual stresses were also measured for both the conventional weld and the weld with additional heating in the clamped conditions. In **Figure 5.47a** the result of the stress measurement for conventional welding for the plate in the clamped condition is shown and compared to the plate after releasing the clamps. It is seen that the absolute values of both tensile and compressive stresses are higher when the plate is in the clamped condition. The stress measurement for the plate before and after releasing the clamps in the case of the weld with additional heating is shown in **Figure 5.47b**. The tensile stresses are higher in the clamped condition. However, the compressive stresses in the clamped condition are close to the un-clamped cases. In order to interpret the results, numerical models for both cases are used and discussed in the next chapter. Only from the experimental point of view, such deviations (between clamped and clamped release stress measurements) can be attributed to errors in the measurement. The results of the stress measurement for the clamped conditions were obtained from portable X-Ray equipment. Therefore, different measurement methods are compared in the figure.

The main sources of errors in the measurements can be summarized as:

1. For thick material, an error is introduced by the simplification of the 3D stress tensor to in-plane stress condition;

2. Human related errors: Sample positioning, alignment, reading and typing errors, *etc.*
3. Sample positioning errors: Definition of the origin, Sample deformation, *etc.*
4. Data analysis errors: Peak fitting errors, Elastic constants, Stress free lattice parameter, *etc.*
5. Measurement errors: errors from neutron source, errors from measurement system (displacement), *etc.*
6. Errors from sample: Texture, Grain size, Shear stresses, Out-of-plane stresses, *etc.*

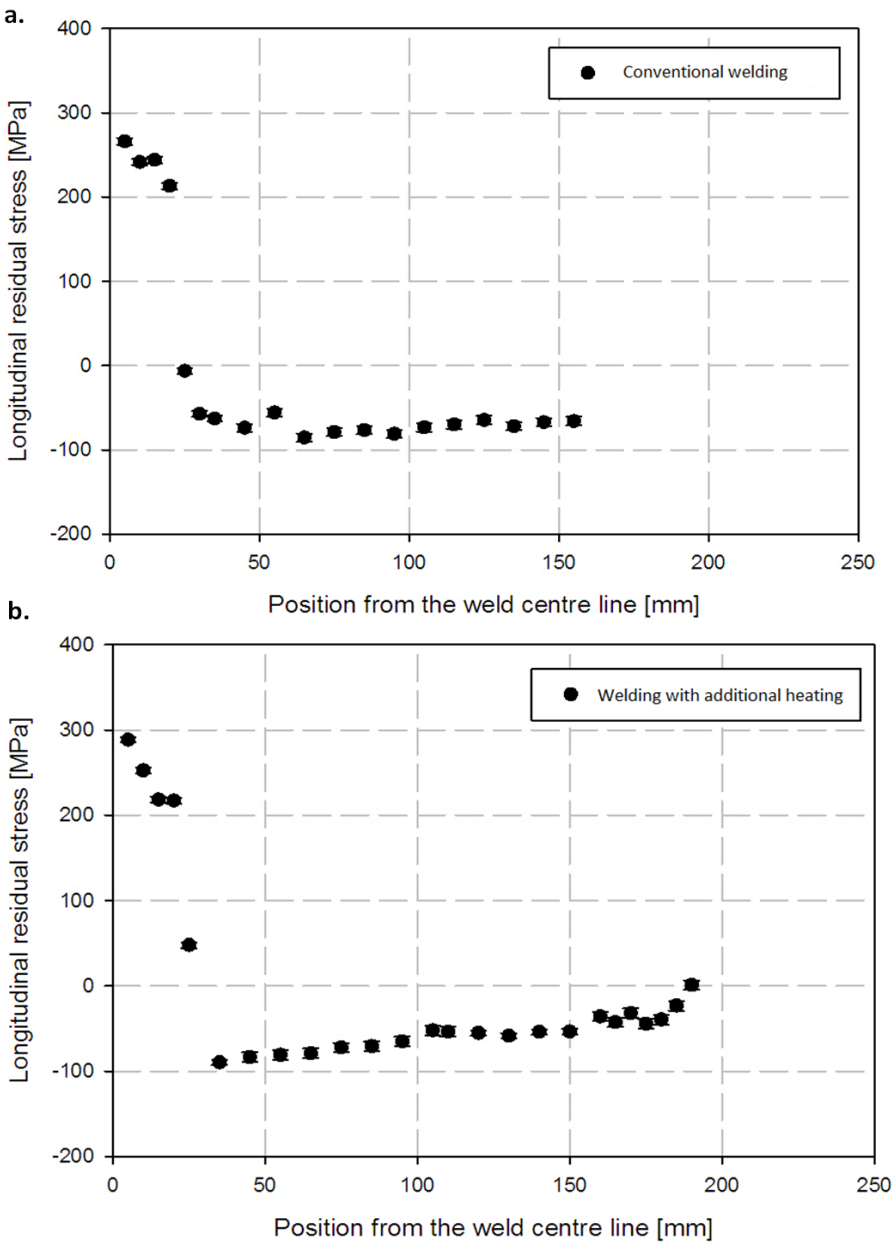

Figure 5.46. *Residual stress measurement results for AH36 (Case-III) after (a) conventional welding and (b) welding with additional heating.*

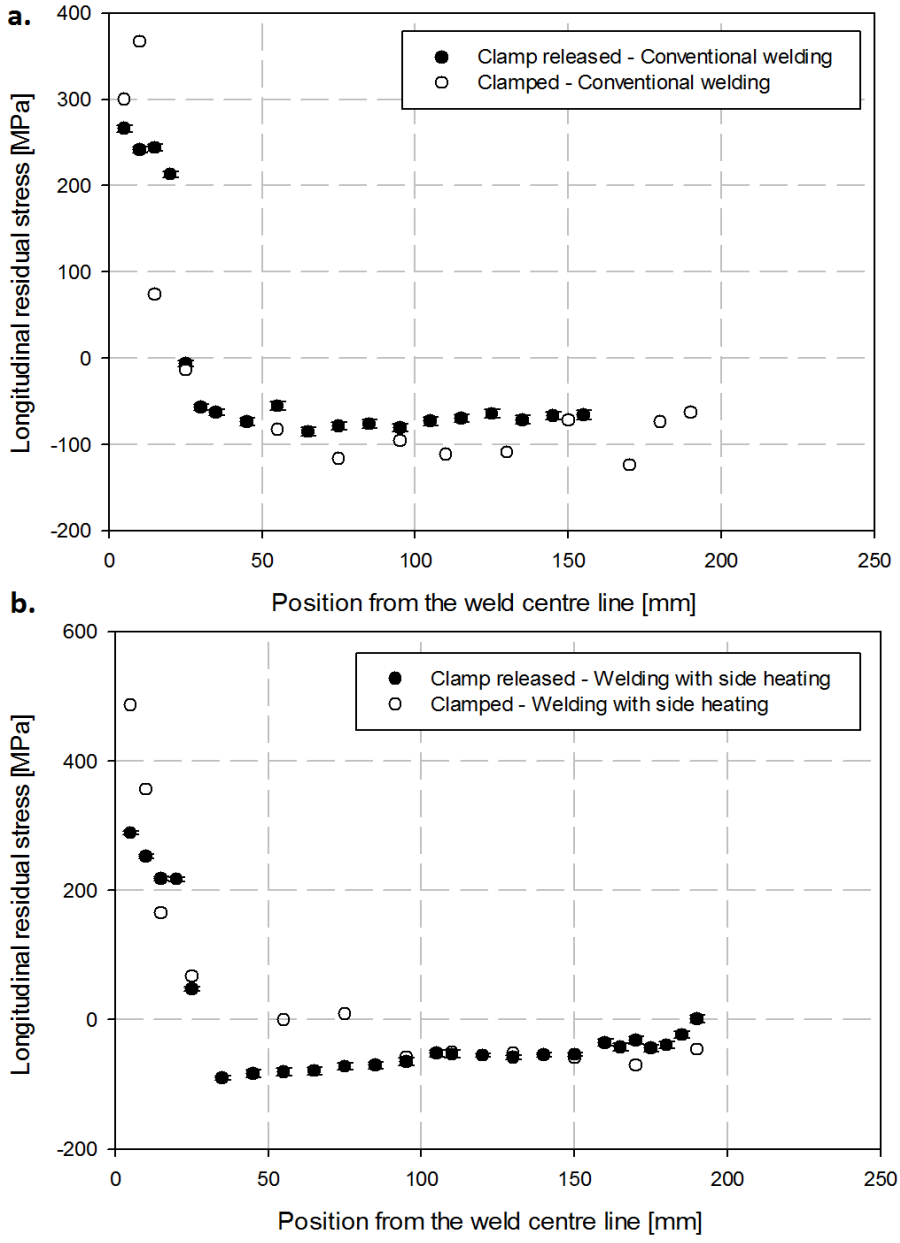

Figure 5.47. *Residual stress measurement results for AH36 (Case III) in the clamped condition for (a) a conventional weld and (b) a weld with additional heating.*

5.5 Concluding remarks

This chapter shows the experimental results of distortion, temperature, microstructure and residual stress measurements for both conventional welds and welds with additional heating.

The measured results of the out-of-plane deformation of the workpiece after conventional welding and welding with additional heating were presented first. The cases with experimentally obtained minimum distortion for different materials were defined and then the temperature measurements, microstructure investigation and the residual stress measurements were performed for conventionally welded plates and these defined additional heating experiments.

Welding with additional heating can successfully reduce out-of-plane deformation. The plate with experimentally obtained minimum distortion after welding with additional heating was obtained for AISI-316L (Case I-B) at the position 143.5 mm to the weld centre line and with a burner induced temperature around 380 ^{o}C. The burners were located 145 mm leading the weld. For D600 (Case II-B), the case with low distortion is obtained, when the burners are located 193.5 mm from the welding centre line and 145 mm leading the welding torch. The burner induced temperature was around 320 ^{o}C. The case in which the burners are located 180 mm trailing the welding torch was selected as the case with experimentally obtained minimum deformation for AH36 (Case III). The burners were located 193.5 mm from the welding centre line and produced a temperature of around 240 ^{o}C for the latter case.

The out-of-plane deformation of the plate has been reduced after welding with additional heating in comparison with conventional welding for AISI-316L. However, the deformation of the plate after additional heating is still high. The main reason for such high deformation is related to material properties of AISI-316L. The thermal thermal diffusivity of AISI-316L (3.35 mm^2 s^{-1}) is rather low, the generated heat is localized and the deformation of the heated area is much greater than other regions.

For all materials studied, it was found that the closer the burners were to the weld centre line the higher deformation is obtained. Moreover, the trend in distortion as a function of the distance between the burner and the welding torch was non-linear.

The temperature was measured for all materials during conventional welding and welding with additional heating. It was seen that for all materials, the temperature field around the welds is not changed by additional heaters when the temperature of conventionally welded plates is compared to that of welding with additional heating with experimentally obtained minimum distortion. In the temperature profile of welding with additional heating cases, eight peaks for the points beneath the burners were observed.

The effects of conventional welding and welding with additional heating on the microstructure of AISI-316L, DP600 and AH36 were shown. It was found that for all cases the microstructure of the weld and the HAZ (of welding) in conventional welding is the same as the weld with additional heating. The areas beneath the burners in AISI-316L plates show larger grain sizes. These areas in DP600 show a lower micro-hardness than the base metal, mainly because of tempering the martensite. For AH36 steel plate, the top surface of the heated areas beneath the burners shows a re-crystallized microstructure while the microstructure of the underside surface is not affected. The hardness for these areas is reduced slightly compare to the base metal. Such hardness changes could be due to stress relieving.

As explained in the **Chapter 2**, when the burners are far from the weld centre line the process of welding with additional heating is called side heating. The results explained in this chapter showed that successful distortion control can be obtained when the burners are not thermally influencing the welding process. In other words, side heating can reduce distortion compared to the transient thermal tensioning (with burners close to the welds). Since the implementation of additional heating during welding does not change the thermal field for the weld and HAZ (compared to conventional welding), the term side heating is used instead of welding with additional heating.

It was seen that the maximum tensile residual stresses in the HAZ (of welding) for both the conventional weld and the weld with side heating on AISI-316L were similar. This was also true for the maximum compressive stresses. Welding with side heating induces tensile stresses beneath the burner positions of the order of 200 MPa. The thermal diffusivity of AISI-316L is relatively low (3.35 $mm^2\ s^{-1}$) and therefore, the heat generated by the burners, remains localized. The thermal expansion and contraction of the side heated areas cause the formation of stresses beneath the burner positions. For DP600, the maximum tensile stresses at the weld and HAZ (of welding) for conventional weld and weld with side heating were again similar and there was a peak of tensile stress for the area beneath the burner. In the region beneath and close to the burners, the compressive residual stresses are reduced in welding with side heating compared with that of conventional welding of AH36. However, the tensile peak is not observed in AH36. It is expected that the stress relieving phenomenon is responsible for reduction of this tensile peak.

Reference

[1] T. Schenk, *Modelling Welding Distortion, the influence of clamping and sequencing and sensitivity analysis*, PhD thesis, Delft University of Technology, 2011.

[2] T. Nagy, S. Williams, P. Colegrove, C. Ikegu, I. Fafiolu, *Distortion mitigation in welded ship panels*, Proceedings of 2nd International Workshop on Thermal Forming and Welding Distortion IWOTE 2008, Bremen, pp. 265-275, 2008.

[3] E. M. van der Aa, *Local Cooling during Welding: Prediction and Control of Residual Stresses and Buckling Distortion*, PhD thesis, Delft University of Technology, 2007.

[4] P. Seyffarth, B. Meyer and A. Scharff, *Groβer Atlas Schweiβ-ZTU-Schaubilder*, Dusseldorf, DVS-Verlag, 1992.

[5] S. A. Tsirkas, P. Papanikos, Th. Kermanidis, *Numerical simulation of the laser welding process in butt-joint specimens*, Journal of Materials Processing Technology, No. 134, pp. 59-69, 2003.

[6] W. Reimers, A. R. Pyzalla, A. Schreyer and H. Clemens, *Neutron and Synchrotron Radiation in Engineering Material Science*, WILEY-VCH, 2008.

[7] http://poldi.web.psi.ch/index.shtml

Chapter 6

Numerical results and model validation

The modelling procedure was presented in **Chapter 3**. This chapter deals with the numerical results of the thermal field, residual stress and distortion models for conventional welding and welding with additional heating. The results of the previous chapter are used for validation of the constructed models.

The experimentally obtained minimum distortion situations after welding with additional heating for different materials are summarised in **Table 6.1**. The boundary conditions for such cases are implemented in the models and the results are shown and compared to those of the conventional welding model.

Table 6.1. *The experimentally obtained minimum distortion conditions after welding with additional heating.*

Material **Parameter**	**AISI-316L** **Case I-B**	**DP600** **Case II-B**	**AH36** **Case III**
Additional heating temperature [^{o}C]	380	320	240
Burner separation distance [mm]	287	387	387
Burner distance to the welding torch [mm]	145	145	-180

In the first part of the chapter, the temperature predictions during conventional welding and welding with side heating for AISI-316L, DP600 and AH36 plates are described. The out-of-plane deformation, phase fraction and the effects of phase transformation on distortion are shown and discussed in the subsequent sections. Finally the results of the residual stress prediction are addressed.

6.1 Numerical results of thermal field in conventional welding and welding with additional heating

The results of temperature predictions during conventional welding and welding with additional heating sources are presented. The thermal modelling input parameters are defined (based on experiments shown in **Chapter 5**) and the results of the predicted temperature of some points are compared to the measured results.

6.1.1 Numerical results of conventional welding

As stated in **Chapter 3**, the thermal modelling of conventional welding includes the modelling of heat input and heat losses. The heat input is modelled by the double ellipsoid model of Goldak [1]. The parameters of the model are defined experimentally. These parameters are related to the power input, the efficiency of the process and the size of the power density distribution, which can be estimated as 90% of the dimension of the weld [2]. However, the values in the model can vary in order to find a suitable value. The values of the heat input parameters used in this investigation for the modelling of AISI-316L, DP600 and AH36 welds are summarized in **Table 6.2**.

The heat losses by convection and radiation are incorporated in **Equations 3.10** and **Equation 3.11**. Near the weld, heat transfer is dominated by radiation. It should be noted that both the heat transfer coefficients of convection and radiation are temperature dependent. Therefore, the heat transfer coefficients are not the same for the whole plate. Different regions with different boundary conditions are defined in the model as shown in **Figure 6.1**. In the area 'A', the plate is exposed to the surroundings. Therefore, free convection and radiation are assumed for this area. Clamps are located in the area 'B' and 'C'. The heat loss in the area 'B' is due to the conduction to the clamps. This is also true for area 'C'. However, the temperature of the clamp increases in the zone 'C' much more than that in the area B in conventional welding. Therefore, the heat transfer coefficients are different for these two zones. There is heat loss due to conduction to the steel backing plate in the area 'E' where the plate is in a contact to the backing plate. The backing groove is located at 'F'. Convection and radiation is included in the model. The surfaces are cooled by free convection and radiation similar to the area 'A'. The heat transfer coefficient values for all these zones are listed in **Table 6.3**.

Table 6.2. *Parameter values for the heat input model used in the simulations. See* ***Figure 3.5*** *for the parameters definition.*

Parameter	AISI-316L	DP600	AH36
a [mm]	2.5	2.5	5
b [mm]	2	2	6
c_1 [mm]	a	a	a
c_2 [mm]	$2a$	$2a$	$2a$
f_1	1.2	1.2	1.2
f_2	0.8	0.8	0.8
Q[W]	940.22	1063.58	5185.18
η	65%	65%	75%

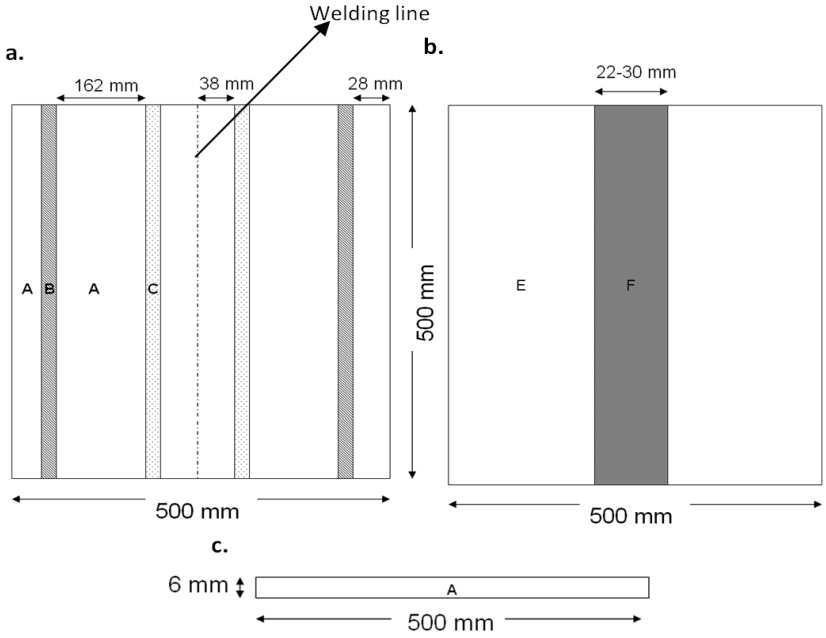

Figure 6.1. *Different regions for heat loss modelling at (a) the top side, (b) the underside and (c) thickness side surfaces of the plates.*

Table 6.3. *The heat transfer coefficients of the different regions defined for the heat losses of the top, underside and other surfaces of the plates in the modelling of conventional welding.*

Area	**Equation**	**Heat transfer coefficient** $[Wm^{-2}K^{-1}]$
A	3.10, 3.11	10
B	3.9	70
C	3.9	50
E	3.9	100
F	3.10, 3.11	10

The heat input and heat loss model parameters have been set by comparing the results of the simulations with the experimental temperature measurements. Therefore, a trial and error method has been used to fit the numerical output to the experimental results by variations in the parameters shown in **Table 6.3**. The predicted temperature profile during conventional welding of AISI-316L (Case I-B), DP600 (Case II-B) and AH36 at different positions from the weld centre line are shown in **Figure 6.2** to **Figure 6.4**.

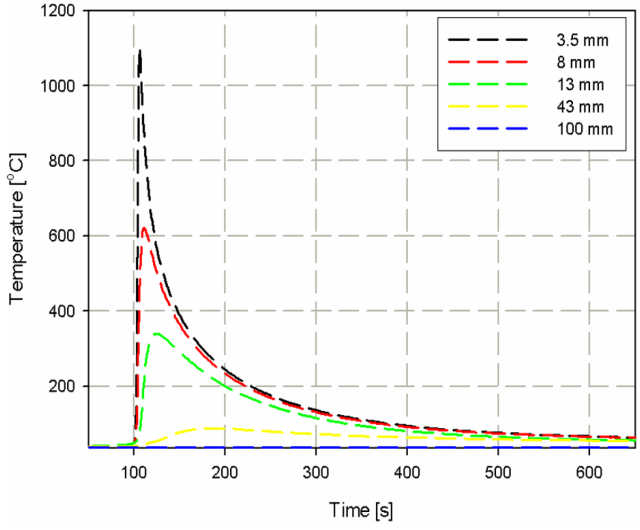

Figure 6.2. *Predicted temperatures for conventional welding of AISI-316L (Case I-B) plates at the underside surface for different positions from the weld centre line.*

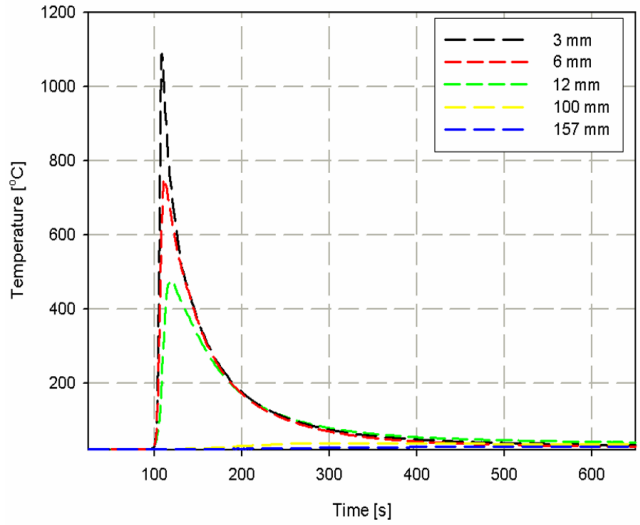

Figure 6.3. *Predicted temperatures for conventional welding of DP600 (Case II-B) plates at the underside surface for different positions from the weld centre line.*

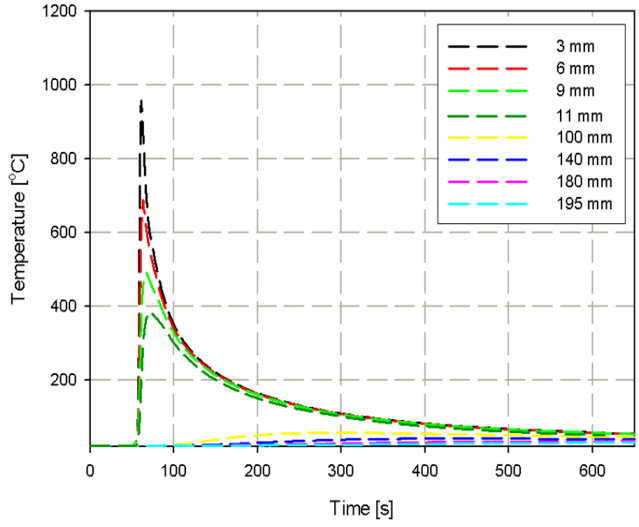

Figure 6.4. *Predicted temperature profiles for conventional welding of AH36 plates (Case III) at the underside surface for different positions from the weld centre line.*

The maximum temperature predictions are compared to the measurements for AISI-316L, DP600 and AH36 steel plates in **Figure 6.5**.

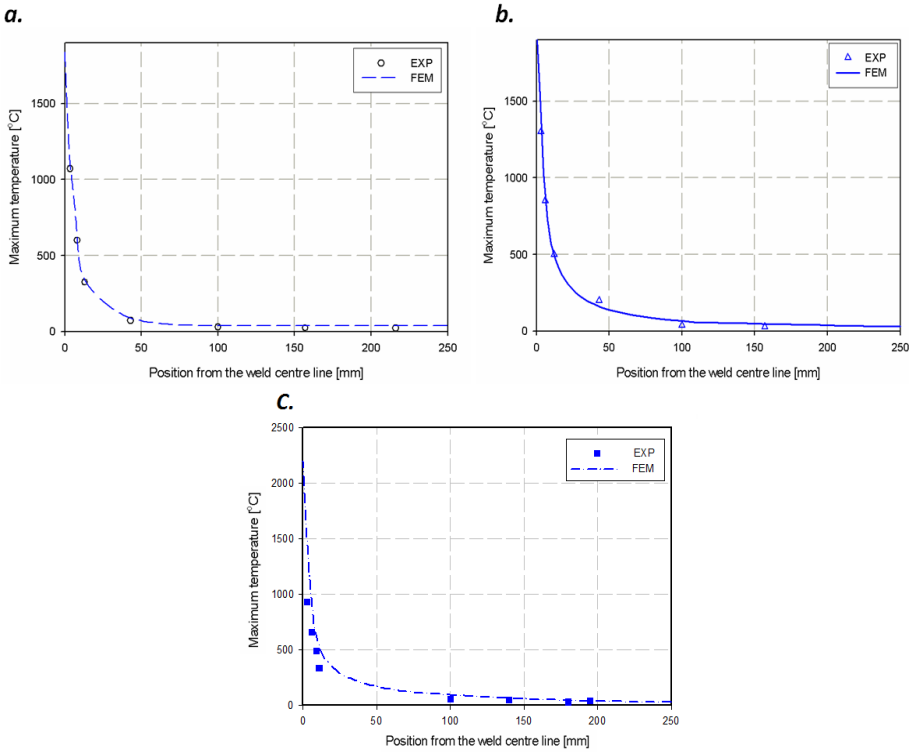

Figure 6.5. *Predicted maximum temperatures at different positions from the weld centre line are compared to the experimental temperature measurements for conventional welding of (a) AISI-316L (Case I-B), (b) DP600 (Case II-B) and (c) AH36 (Case III) steel plates. The prediction is shown for the underside surface.*

By comparing the results of the temperature predictions at different positions and materials to the experimentally measured results, a good agreement is clearly seen. The maximum temperature, the heating and the cooling rates are all very close to the measurements as shown in **Table 6.4** for some points. The agreement between the predictions and the measurements are good mainly because the heat input parameters and the power density distribution parameters are all based on the measurements. However, small deviations can be related to the following sources:

- Thermal material properties at high temperature are difficult to obtained.
- The heat transfer coefficients in the models are estimations.
- In the model, the weld pool is assumed to be a very soft solid and not a liquid.

Table 6.4. *Comparison of numerical and experimental results at specific positions in the thermal field. The positions are from the weld centre line. The heating rates are from room temperature to the maximum temperature. The cooling rates are from 800 °C to 500 °C.*

Material	Position [mm]	Heating rate [°C s^{-1}] NUM	EXP	Max Temp [°C] NUM	EXP	Cooling rate [°C s^{-1}] NUM	EXP
AISI-316L	3.5	50.38	48.75	1079	1069	-14.90	-15.19
DP600	3	72.45	76.61	1100	1113	-22.01	-24.93
AH36	3	28.76	28.03	930	910	-22.73	-25.28

6.1.2 Modelling of the additional heaters

Chapter 3 (**Section 3.2.7**) describes the modelling approach for the additional heat sources. It was stated that the burners have been modelled by a Gaussian heat flux distribution. Eight circular Gaussian heat flux distributions have been used to model the nozzles for welding with additional heating. In **Section 5.2.3**, the temperature profile during heating was shown using one burner for different materials. These temperature measurements are used to define the necessary parameters (intensity of the heat source and the dimensions) for the model. The model is shown again in **Figure 6.6**, where M is the inter-distance of the nozzles.

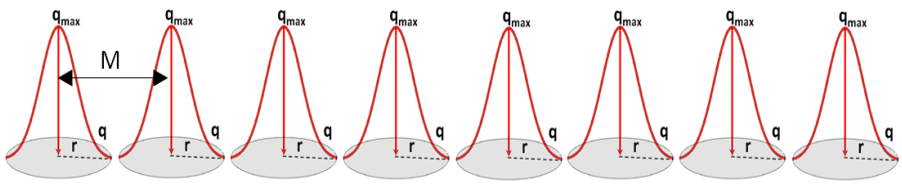

Figure 6.6. *The model of the burner including eight nozzles.*

In the model the power is distributed over a circle with a radius of r with a cut-off radius were the power is reduced to 1% of q_{max}. In order to find a suitable power density distribution, several FEM calculations were preformed until a good agreement between the temperature prediction and the temperature measurement was observed. **Figure 6.7a** shows typical power density distributions used in the simulations with different maximum values. The result of the temperature prediction at the underside surface of the plate from the centre point of the heat source toward the edges is compared to the temperature measurements for both AISI-316 (**Figure 6.7b**) and DP600 (**Figure 6.7c**). The values for the parameters in the heat source model that gave the best results are listed in **Table 6.5**. The speed of the heat source was set to 2.5 mm s^{-1} for both cases. It can be seen that the results from the model and the experiment are in good agreement. The same strategy was employed for AH36.

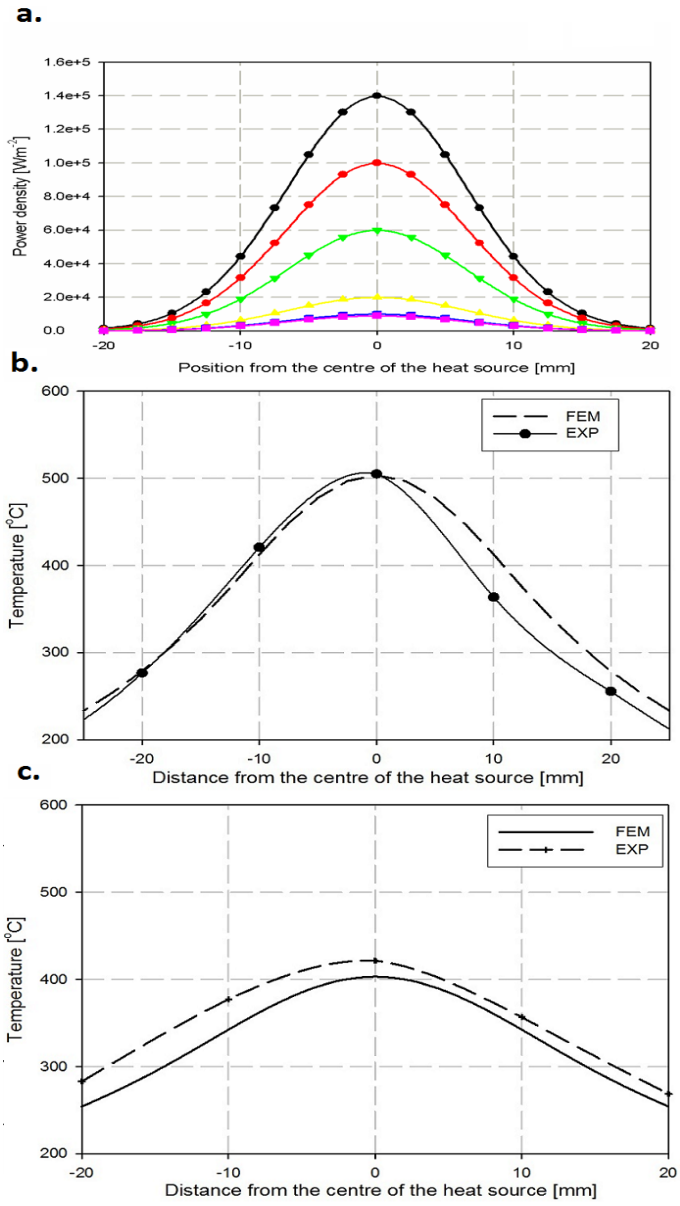

Figure 6.7. *(a) The different power density distributions used in the simulations. The temperature predictions are compared to the measurements for two examples: (b) AISI-316L and (c) DP600 steel plates.*

Table 6.5. *The values for the parameters in the heat source model in different materials.*

	AISI-316L	**DP600**	**AH36**
q_{max} [kW m^{-2}]	127.6	103.1	375.4
r [mm]	14	14	14
M [mm]	30	30	30
η [%]	47	47	47

6.1.3 Numerical results of welding with additional heating

In the modelling of welding with additional heating, the heat input is modelled exactly similar to that of the conventional welding model. Since the burners increase the temperature of the clamps, the cooling boundary conditions deviate from the conventional welding simulation. **Table 6.6** shows the values used for the heat transfer coefficients in modelling of welding with additional heating. Different regions were defined here similar to the conventional welding models as shown in **Figure 6.1**.

Table 6.6. *The parameter values of the different regions defined for the heat losses of the top, underside and perimeter surfaces of the plates used for the modelling of welding with additional heating.*

Area	**Equation**	**Heat transfer coefficient** $[Wm^{-2}K^{-1}]$
A	3.10, 3.11	10
B	3.9	50
C	3.9	70
E	3.9	100
F	3.10, 3.11	10

The prediction results of the temperature profile during welding with additional heating are shown for different materials in **Figure 6.8** to **Figure 6.10**. It is seen that the maximum temperature, the heating and the cooling rates are predicted close to the measurements as shown in **Table 6.7** for some points. The eight peaks observed during the experiments cannot be modelled by the approach adopted in this thesis. However, the predictions are in a good agreement with the temperature measurements.

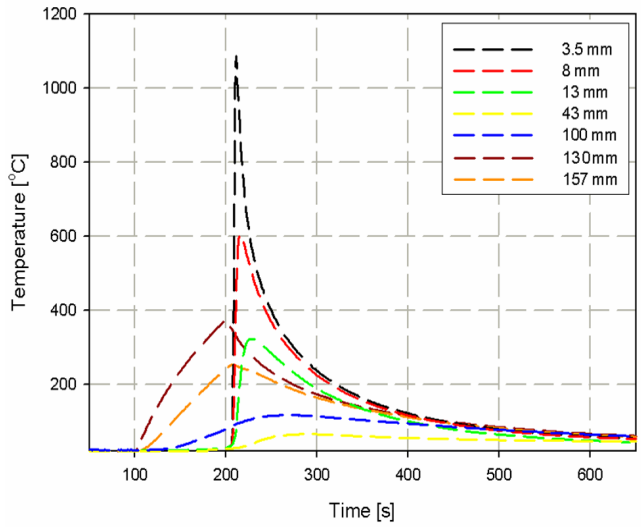

Figure 6.8. *Temperature prediction results for welding with additional heating of AISI-316L (Case I-B) plates at different positions from the weld centre line. The temperature cycles are shown for the underside surface.*

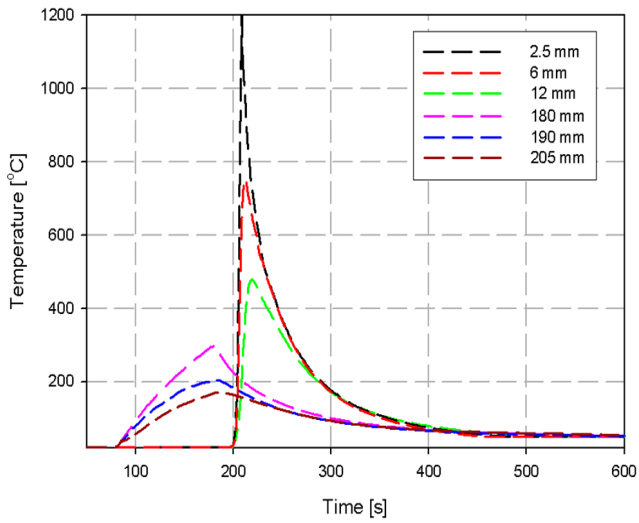

Figure 6.9. *Temperature prediction results for welding with additional heating of DP600 (Case II-B) plates at different positions from the weld centre line. The temperature cycles are shown for the underside surface.*

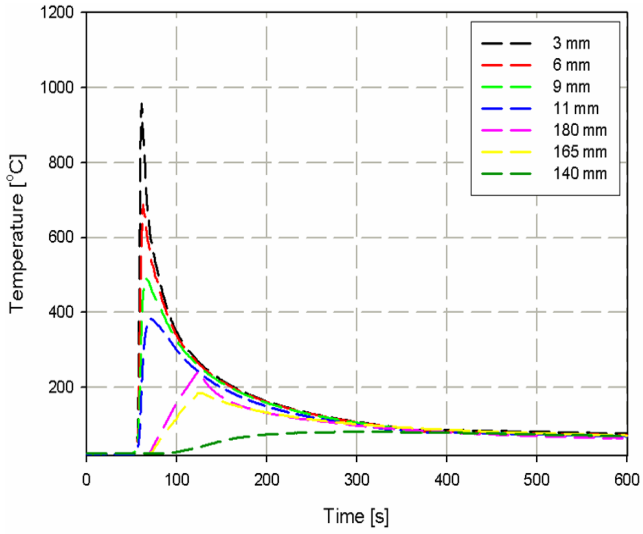

Figure 6.10. *Temperature prediction results for welding with additional heating of AH36 (Case III) plates at different positions from the weld centre line. The temperature cycles are shown for the underside surface.*

Table 6.7. *Comparison of numerical and experimental results at specific positions in the thermal field. The positions are from the weld centre line. The heating rates are from room temperature to the maximum temperature. The cooling rates are from 800 °C to 500 °C.*

Material	Positions [mm]	Heating rate $[^oCs^{-1}]$ NUM	EXP	Max Temp $[^oC]$ NUM	EXP	Cooling rate $[^oCs^{-1}]$ NUM	EXP
AISI-316L	3.5	44.13	47.01	1067	1057	-16.74	-16.89
DP600	2.5	85.45	80.61	1197	1194	-29.53	-26.76
AH36	4	25.76	23.6	830	815	-22.34	-23.16

Figure 6.11 shows the predicted through thickness temperature distribution of AH36 plate (Case III) beneath the burner during welding with additional heating. The burners are located 193.5 mm from the weld centre line. The maximum predicted temperature at the top surface of the plate beneath the burners when welding with additional heating for this material is 610 ^{o}C.

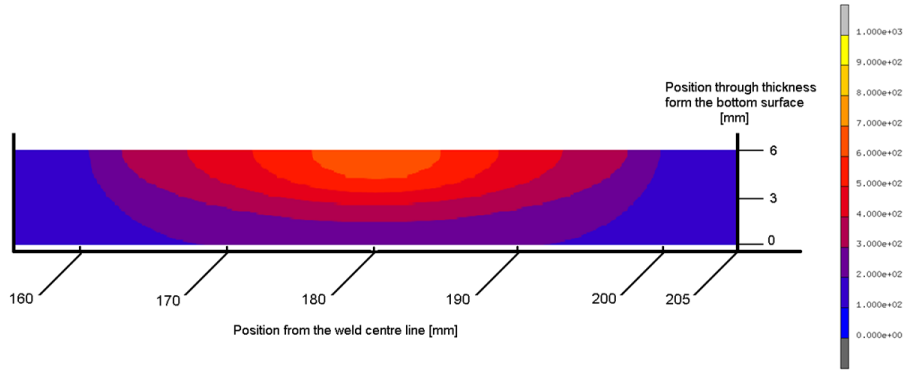

Figure 6.11. *Temperature distribution across the cross section of AH36 (Case III) steel during welding with additional heating at the position of a burner. The burner is located 193.5 mm from the weld centre line. The temperature is in degrees Celsius.*

6.2 Phase fraction calculations

Up to now, the results of thermal modelling for different materials and conditions (conventional welding and welding with additional heating) were shown. The validated thermal fields are used for prediction of out-of-plane distortion and residual stresses of the defined cases. However, temperature changes cause microstructural changes. Therefore, the next step is the prediction of phase fractions. The result of phase fraction predictions of different phases are shown and compared to the microstructure investigation of a conventionally welded DP600 (Case II-A) sample in this section. This model is used to investigate the effect of phase transformation on distortion and residual stresses.

Since the temperature changes cause solid state phase transformations, the first step is validation of thermal field for this case. **Figure 6.12** shows the temperature profile at different positions from the weld centre line during conventional welding of the plate. The measurements are compared to the numerical predictions.

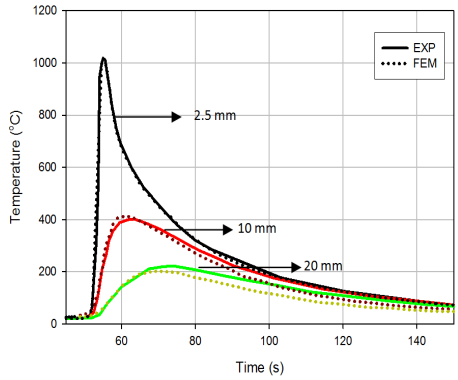

Figure 6.12. *The predicted and the measured temperature profiles at different positions from the weld centre line at the underside surface during conventionally welded DP600 (Case II-A).*

Cross sections of the welded sample were etched with different solutions (2% Nital solution, 5% Nital solution and LePera solution) to reveal the microstructure. A quantitative analysis of the phase fractions was performed using the point counting method with a 5×5 μm grid. The accuracy of this method is around 6%.

The fraction of phases obtained experimentally is compared with the numerical results in **Figure 6.13**. Since it is difficult to differentiate bainitic ferrite from Widmanstätten ferrite, the fraction of acicular products has been used to compare with the numerical results. As can be seen, the ferritic fraction is reduced from 80% in the base metal to below 20% in the fusion zone.

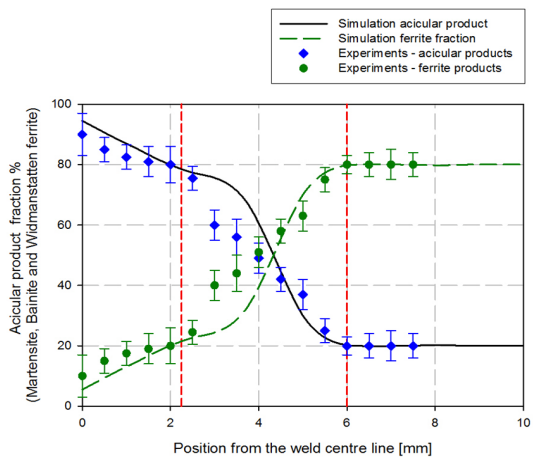

Figure 6.13. *The comparison of the predicted acicular products and experimental measurements.*

As can be seen from the figure, the predicted phase fractions are close to the measurements especially in the weld region. There are some deviations in the HAZ around 3 mm from the weld centre line. Since, the predicted temperatures for these points are close to the measurements, the main source of deviations is related to the CCT diagram employed, which was constructed for a material with a chemical composition close to that of the DP600 used here, but is not the same. Moreover, the CCT diagrams are obtained for heat treatments with lower heating and cooling rates compared to welding. The parameters (explained in **Section 3.3**) used in the simulations are summarized in **Table 6.8**.

Table 6.8. *The used parameters in the simulation of solid phase transformations.*

Parameter	**Transformation**	**Value**
n	Austenite → Ferrite	2.5
n	Austenite → Bainite	3
τ	Austenite → Ferrite	$exp(0.1027(T - 910.3)) + 32$
τ	Austenite → Bainite	$6.318 + 2.587 \times 10^{-9} \times 1.037^{(T-273)}$

The model explained in **Chapter 3**, including phase transformation predictions, was used and the effects of microstructural changes on distortion and residual stresses were investigated. The results are shown in subsequent sections. In all presented results, if not stated otherwise, the effects of phase transformations have been excluded.

6.3 Distortion prediction

This section deals with the numerical results of the de-coupled models described in **Chapter 3** for the out-of-plane deformation of the plates used. The numerical results are presented for conventional welding and welding with additional heating for the experimentally obtained minimum distortion plates.

Figure 6.14 shows the numerical results for the out-of-plane deformation of AISI-316L (Case I-B) after welding and welding with additional heating.

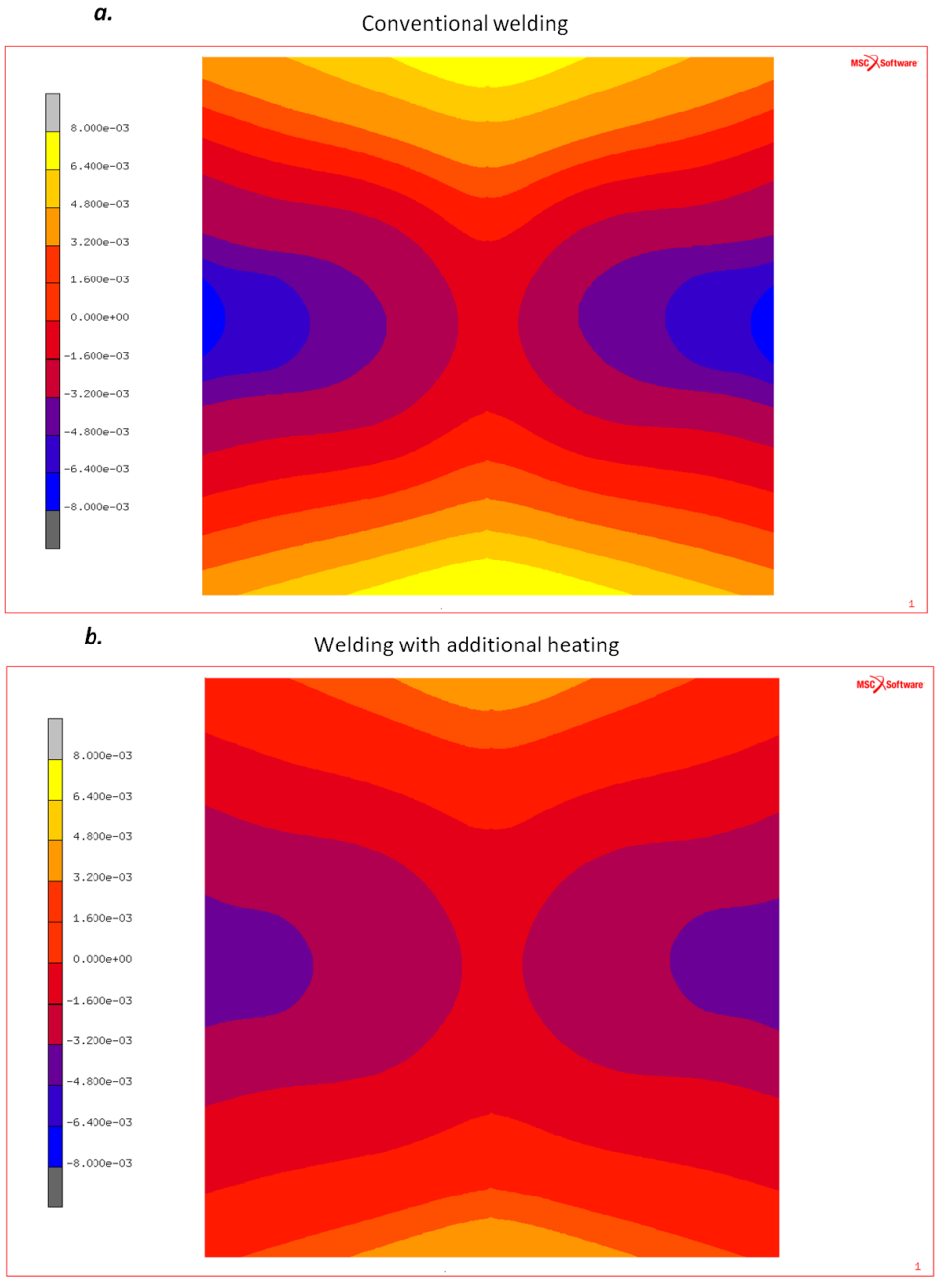

Figure 6.14. *The predicted final out-of-plane deformation of AISI-316L (Case I-B) steel plate after (a) conventional welding and (b) welding with additional heating for the experimentally obtained minimum distortion condition. The scale is -8 to +8 mm.*

Table 6.9 shows a comparison between the numerical results and the experimental results of the distortion index, after welding and welding with additional heating of AISI-316L. The welding with additional heating was modelled using the burners located 143.5 mm from the weld centre line and a burner induced temperature of 380 ^{o}C.

Table 6.9. *The simulation results compared to the experimental results for AISI-316L plates.*

	Distortion index [mm] **NUM**	**EXP**
Conventional welding	14.5	14.0
Welding with additional leading heating	9.5	10.5
Welding with parallel additional heating	10.9	11.8
Welding with additional trailing heating	12.3	11.6

It can be seen from the table above that the predictions approximate the experimental measurements very well. The predictions and the experiments show that the leading position of the burners results in a higher distortion reduction. The deviations between the model results and the measurements can have several reasons. For example, the uncertainty in the mechanical properties at elevated temperature and the clamping pressure.

The distortion index gives a global representation of the distortion of the plate. To obtain a better comparison, a distortion scan over the cross section of the middle of the plate is presented in **Figure 6.15**. The line scan was performed from one edge to the other edge of the plate along a line perpendicular to the weld centre line. The results are shown for conventional welding in **Figure 6.15a** and for welding with additional heating in **Figure 6.15b**. In both numerical results and measurement, the distortion reduction by welding with additional heating is visible. The prediction results are close to the measurements for conventional welding. However, there is a deviation between the measurements and the predictions for the welds with additional heating. In welding with additional heating, two heaters are used and therefore the effects of uncertainties such as material properties at high temperature and clamping behaviour (and pressure) on the final deformation are more significant than for conventional welding. It should be mentioned here that the room temperature releasing of clamps are different in practice compared to that in the numerical model. The clamps are released manually in practice. In the modelling activities, they are released all at once in both conventional welding and welding with additional heating. Moreover, in conventional welding (one heat source) the two clamps close to the welds can have a big influence on distortion but in welding with additional heating (three heat sources) all four clamps and their releasing manner can influence final distortion of the plate.

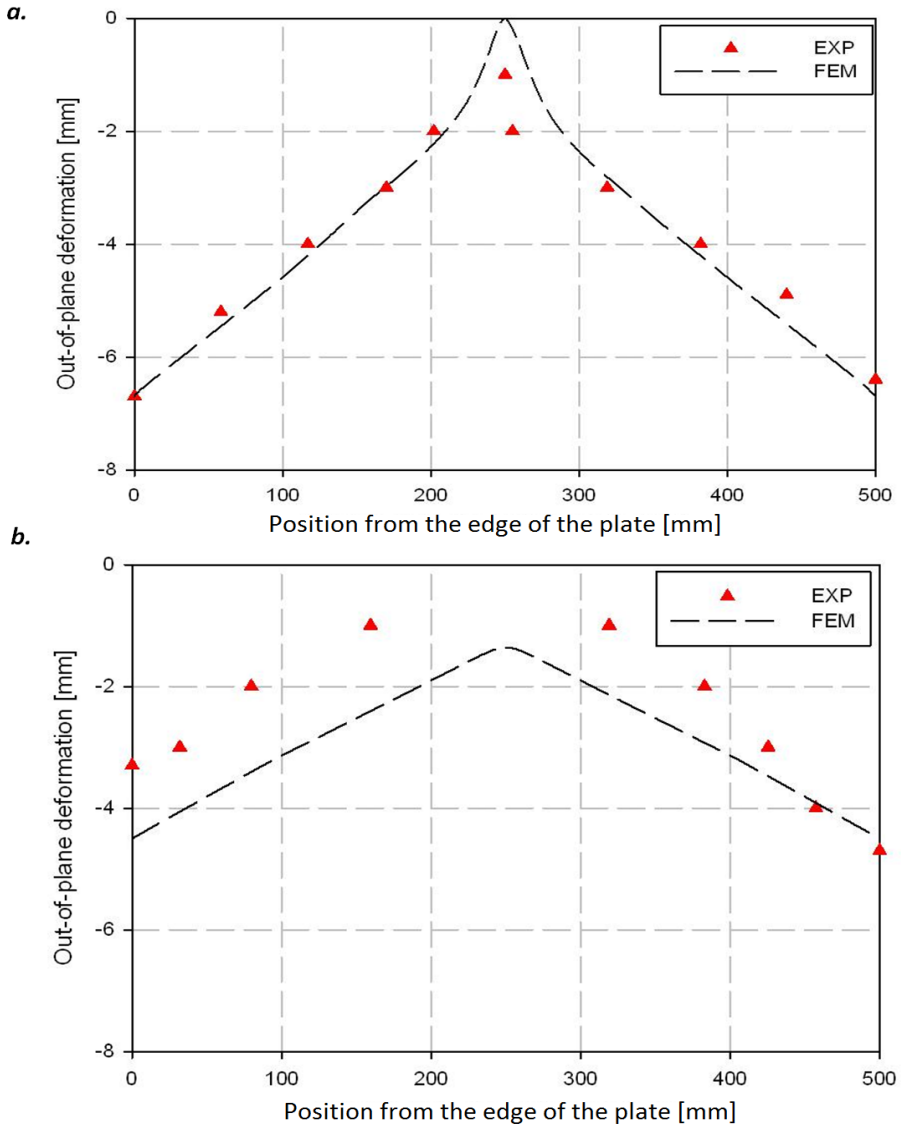

Figure 6.15. *Comparison between the predicted and measured out-of-plane deformation for points located at the middle part of an AISI-316L plate (Case I-B) from one edge to the other edge along a line perpendicular to the weld centre line for (a) conventional welding and (b) welding with additional heating.*

In the models used for DP600 (Case II-B) and AH36 (Case III) plates, solid phase transformations occur during welding and welding with additional heating, which may have significant effects on the out-of-plane deformation. In order to check this influ-

ence, a smaller plate of DP600 steel with dimension of 200×100×1.5 mm^3 (Case II-A) was conventionally welded and modelled. The simulation includes the effects of solid phase transformations occurring during the cooling cycle on the welding distortion and residual stress. The predicted phase fractions together with temperature profiles were shown in **Section 6.2**. **Table 6.10** shows the results of the maximum predicted out-of-plane deformation normalised to the experimental value for the model with and without phase transformation together with the calculations time for different cases.

Table 6.10. *Normalised maximum out-of-plane deformation and the computational time for the model including solid phase transformations.*

Model	**Normalized Max deformation [mm]**	**Calc. time [hours]**
Experiments	1	-
No phase transformation (Isotropic hardening)	1.10	7
Only yield strength increase (Isotropic hardening)	1.17	23.5
Only volume change (Isotropic hardening)	0.94	23.5
Both yield increase and volume change (Isotropic hardening)	1.01	23.5
Mixed hardening model with phase trans.	0.9	23.5

It can be seen that the phase transformation modelling increases the computational time significantly. The model without phase transformation predicts a higher out-of-plane distortion than the models with phase transformation. The isotropic hardening models predict a greater distortion in the out-of-plane direction compared to other model. The effects of solid phase transformations on the maximum out-of-plane deformation are predicted to be around 9%. However, these deviations can be adjusted by using different spring stiffnesses. The risk of computational instability and divergence is very high when phase transformation is implemented. For such reasons, solid phase transformations were excluded in all simulation tasks. In the subsequent sections, models for both conventional welding and welding with additional heating exclude the effect of solid state transformations.

Figure 6.16 shows the numerical results for the out-of-plane deformation of DP600 (Case II-B) steel after welding and additional heating. The welding with additional heating was modelled using the experimentally obtained minimum distortion. The results of the models are compared to the measurements for different burner positions in **Table 6.11**.

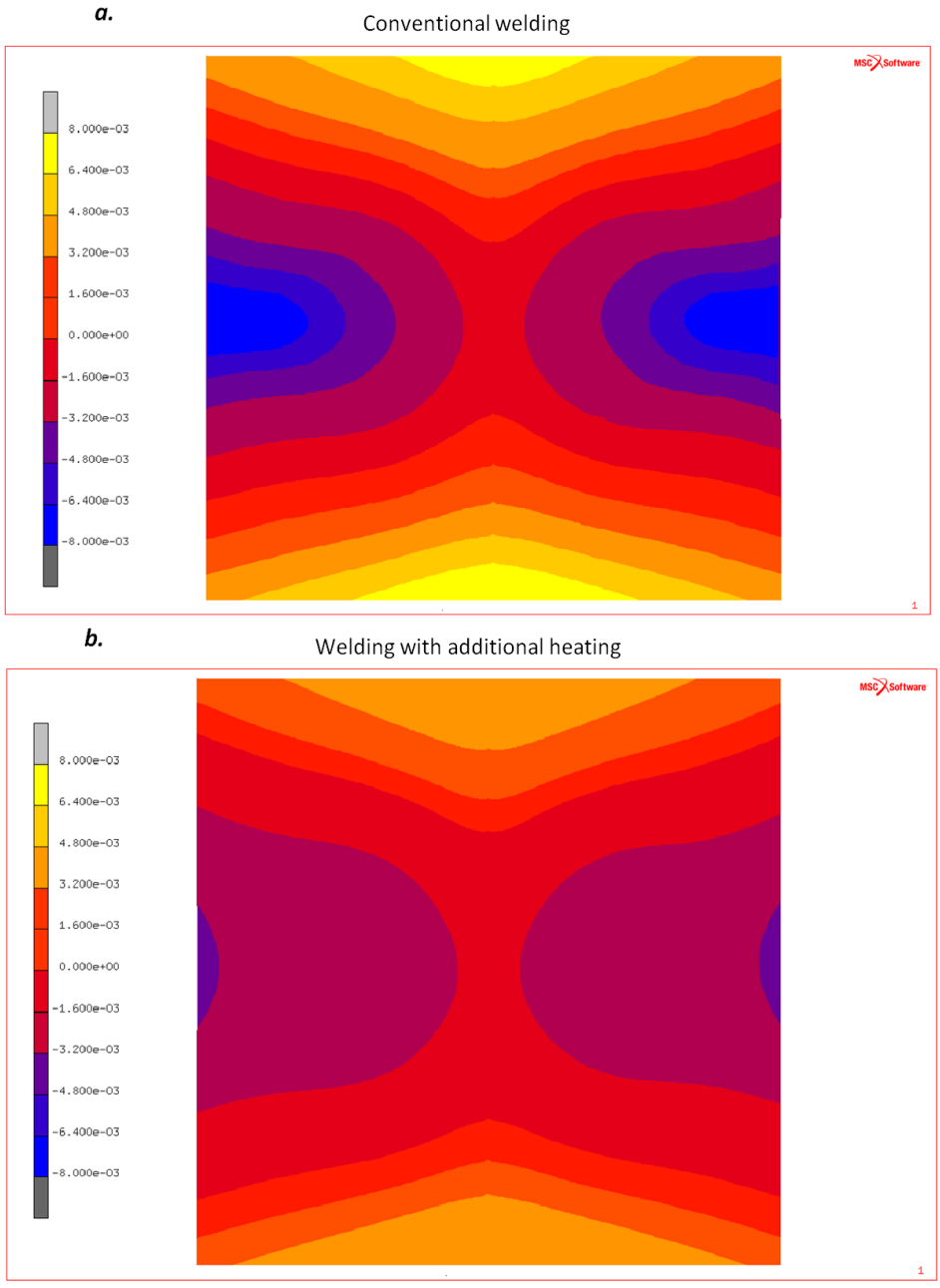

Figure 6.16. *The predicted final out-of-plane deformation of DP600 (Case II-B) steel plate after (a) conventional welding and (b) welding with additional heating in the experimentally obtained minimum distortion. The scale is -8 to +8 mm.*

Table 6.11. *The simulation results compared to the experimental results for DP600 plates, where the burners were positioned 193.5 mm from the weld centre line.*

	Distortion index [mm] **NUM**	**EXP**
Conventional welding	14.8	14.3
Welding with additional leading heating	8.3	7.9
Welding with parallel additional heating	9.5	8.7
Welding with additional trailing heating	9.2	8.9

In this set of experiments for DP600, leading burners reduce welding distortion better both in predictions and the measurements. The sources of deviation explained for AISI-316L (Case I-B) are valid here as well.

To obtain a better comparison, a distortion scan over the cross section of the middle plate is presented in **Figure 6.17**. The results are shown in **Figure 6.17a** for conventional welding and **Figure 6.17b** for welding with additional heating. In both numerical results and measurement, the distortion reduction after welding with additional heating can be seen. The sources of deviations and explanations (especially for additional heating) are the same as for the AISI-316L plates. Besides them, another deviation source between the experimentally obtained results and predictions in the case of welding with additional heating is related to the fact that the temperature gradients beneath the burners (through thickness direction) due to welding with additional heating are not captured in the model. Such gradients may cause angular deformation and after releasing the clamps, these localized deformations may change the final deformation of the plate.

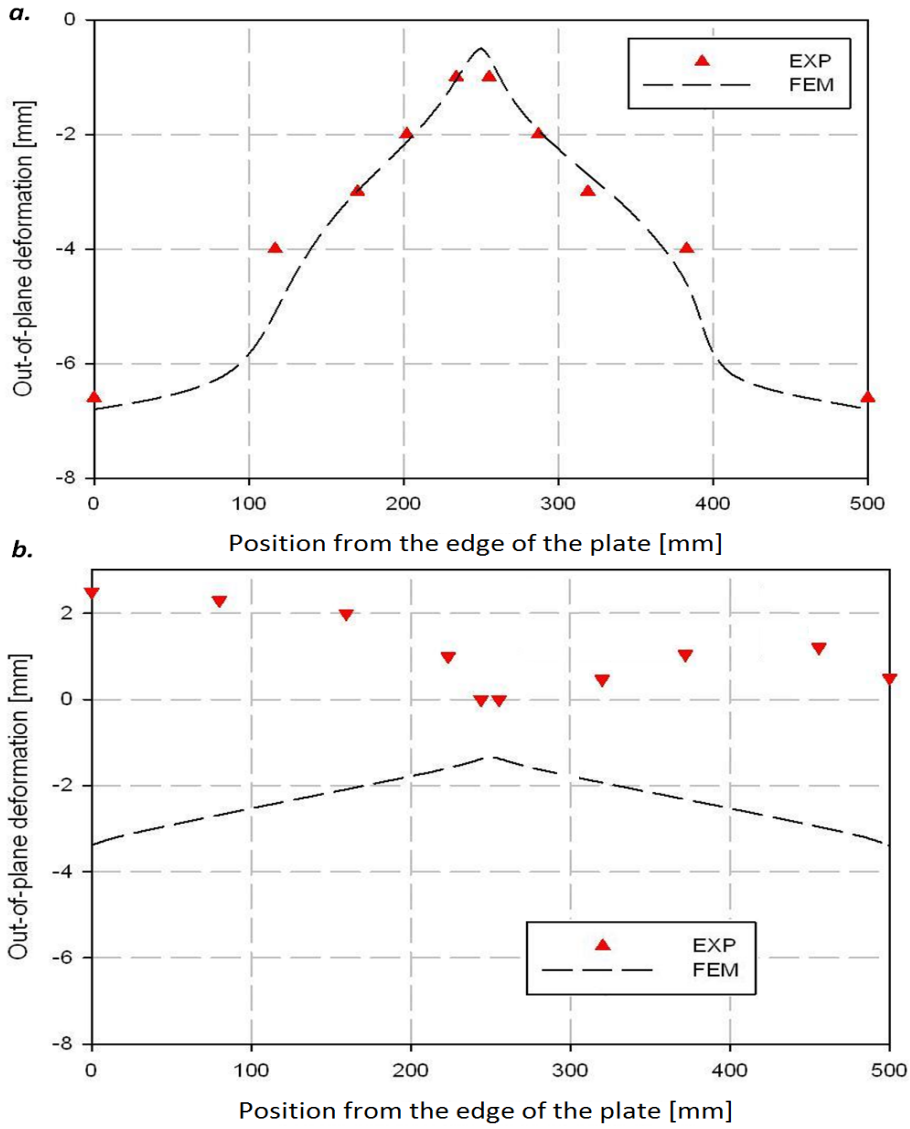

Figure 6.17. *Comparison between the predicted and measured out-of-plane deformation for points located at the middle part of a DP600 (Case II-B) plate from one edge to the other edge along a line perpendicular to the weld centre line for (a) conventional welding and (b) welding with additional heating.*

Figure 6.18 shows the numerical results for the out-of-plane deformation of AH36 steel (Case III) after welding and welding with additional heating. The welding with additional heating was modelled using the experimentally obtained minimum distor-

tion (trailing case). It is clear that the out-of-plane deformation of the plate is reduced using additional heating. However, as the plate is thicker than for the other steels, the out-of-plane deformation in this case is less.

Figure 6.19 shows the predicted and the measured out-of-plane deformation for points located across the middle part of an AH36 plate from one edge to the other edge along a line perpendicular to the weld centre line for conventional welding and welding with additional heating. Comparing the numerical results and the measurements for conventional welding, it is seen that the predicted deformations are close to the experimental measurements for the points at the middle part of the plate. At the edges of the plates, there is a small deviation. Since, the thermal field was predicted to be close to the measured field, the main source of the deviation is related to the mechanical field. This includes the material properties and the clamping model explained before for the other two materials. Although, the sources of deviations are valid here as well, there is another issue for AH36, which is less significant for the other materials. The modelling of clamps consists of series of springs with different stiffnesses. When the plate is thin (for example in the case of DP600 or AISI-316L), the springs can control the movement of plates (shell elements have been used) and the results are close to practice (through thickness strains can be ignored). If a plate is thick (like AH36), the constraints at the top and at the underside surfaces have an influence on the final distortion. The main reason for the different behaviour of the surfaces is related to the temperature gradient in the through thickness direction. In this situation, the clamps can control the movement of the underside surface in the numerical model. By releasing the clamps, the residual stresses are redistributed and the plate distorts to its final shape. For better modelling of clamps in thick materials, the constraint should be modelled using contacts at both the top and the underside surfaces.

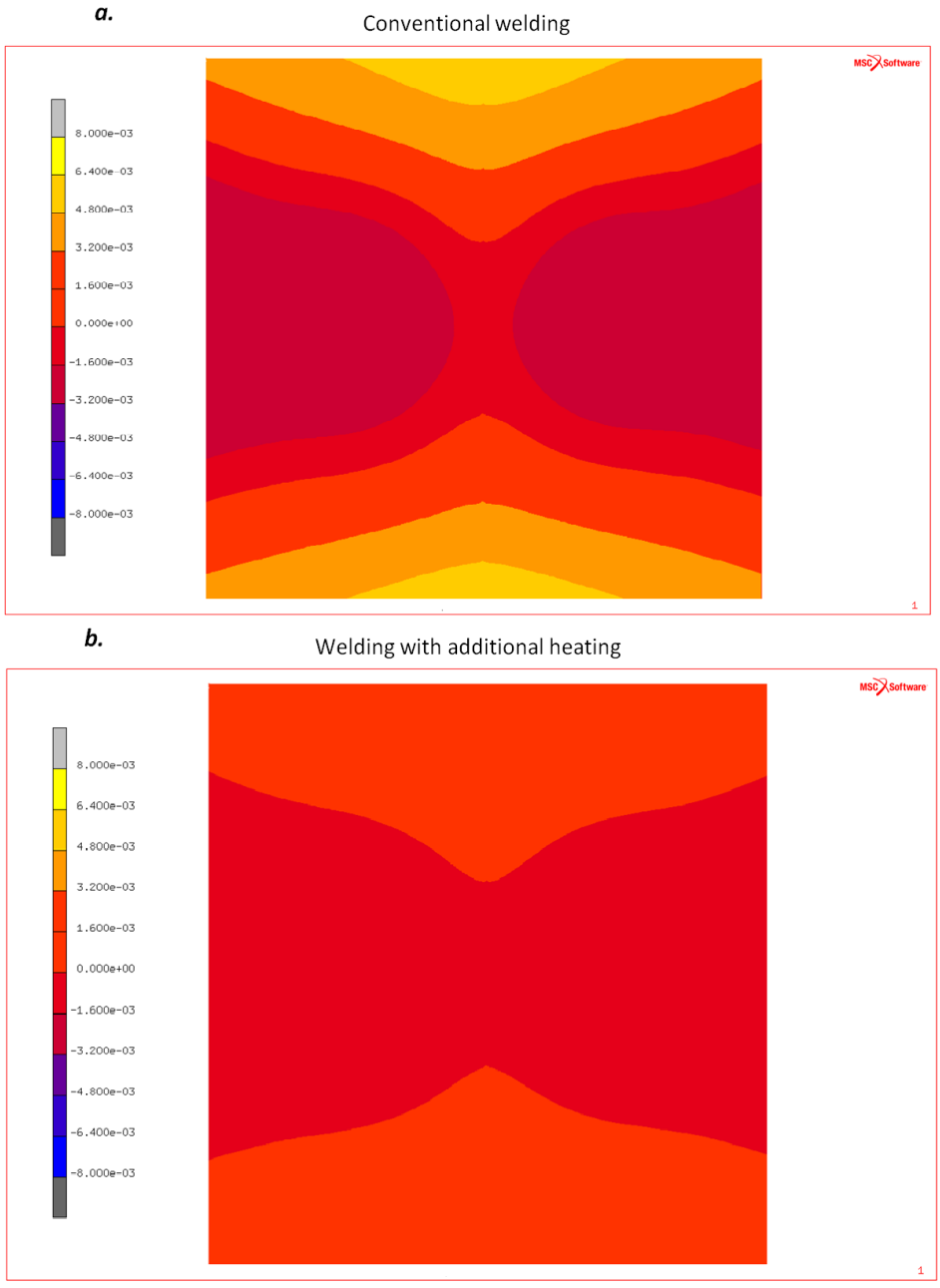

Figure 6.18. *The predicted final out-of-plane deformation of AH36 (Case III) steel plate after (a) conventional welding and (b) welding with additional heating in the experimentally obtained minimum distortion. The scale is -8 to +8 mm.*

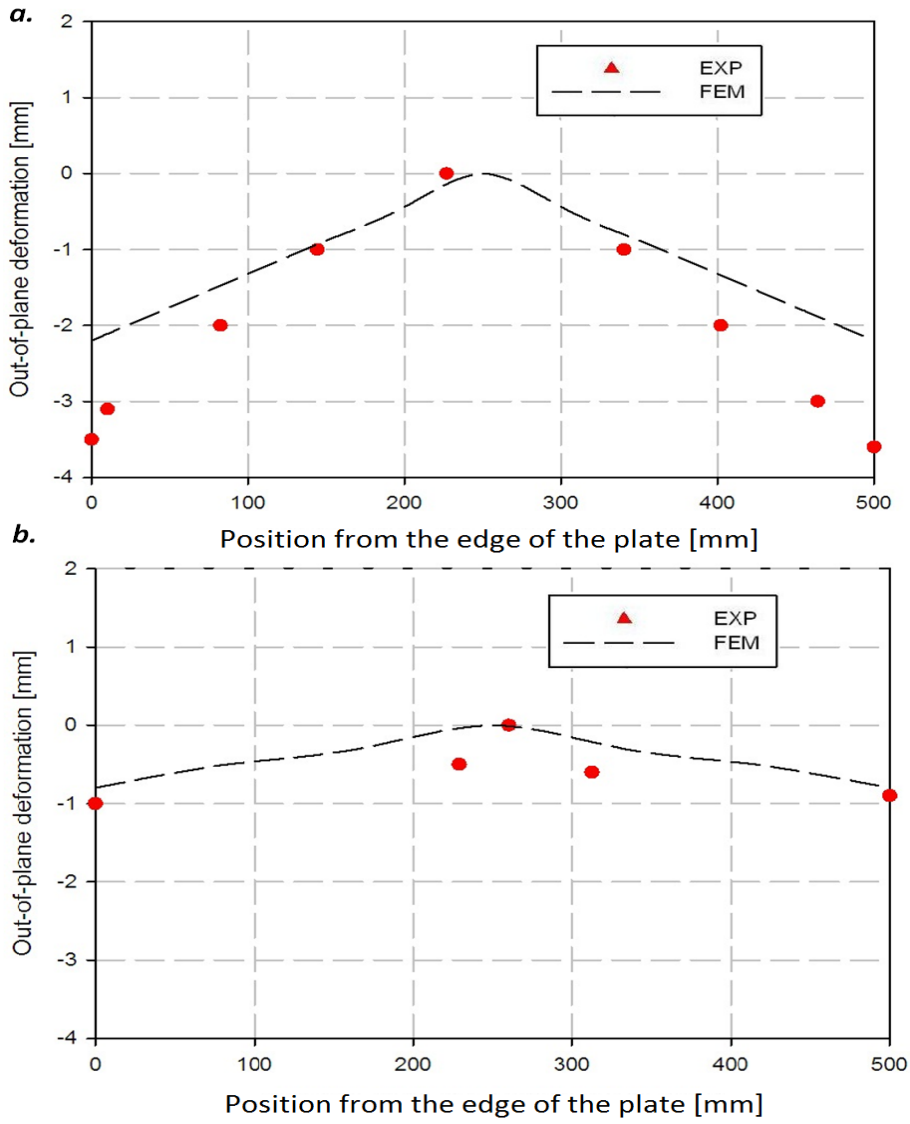

Figure 6.19. *Comparison between the predicted and measured out-of-plane deformation for points over the cross section across the middle of a AH36 (Case III) plate for (a) a conventional weld and (b) a weld with additional heating.*

Table 6.12 shows the numerical results of the out-of-plane deformation of AH36 steel plate for different burner positions. It can be seen that the trailing situation provides the minimum distortion index both in the numerical and measurement results. The predictions are in agreement with the experiments.

Table 6.12. *The simulation results compared to the experimental results for AH36 plates, where the burners were positioned 193.5 mm from the weld centre line.*

	Distortion index [mm] **NUM**	**EXP**
Conventional welding	8.8	5.5
Welding with additional leading heating	3.1	1.8
Welding with parallel additional heating	2.9	No data
Welding with additional trailing heating	2.6	1.5

6.4 Residual stress prediction

The main goal of the residual stress measurements is the validation of the constructed finite element models. The models were described in **Chapter 3**. In **Chapter 5**, the residual stress measurement procedure and the results were shown and discussed. In this section, the experiments are used to validate the models. The validated models are used to evaluate the stress evolution during welding and welding with additional heating for some critical positions and times. As explained in **Chapter 5**, the longitudinal residual stress is selected for all materials.

The modelled and experimentally measured longitudinal residual stresses for both conventional welding and welding with additional heating of AISI-316L after the release of the clamps are presented in **Figure 6.20**. It can be observed from the residual stress profiles that additional heating during welding does not have a significant effect on the residual stress level in the weld and HAZ of the weld.

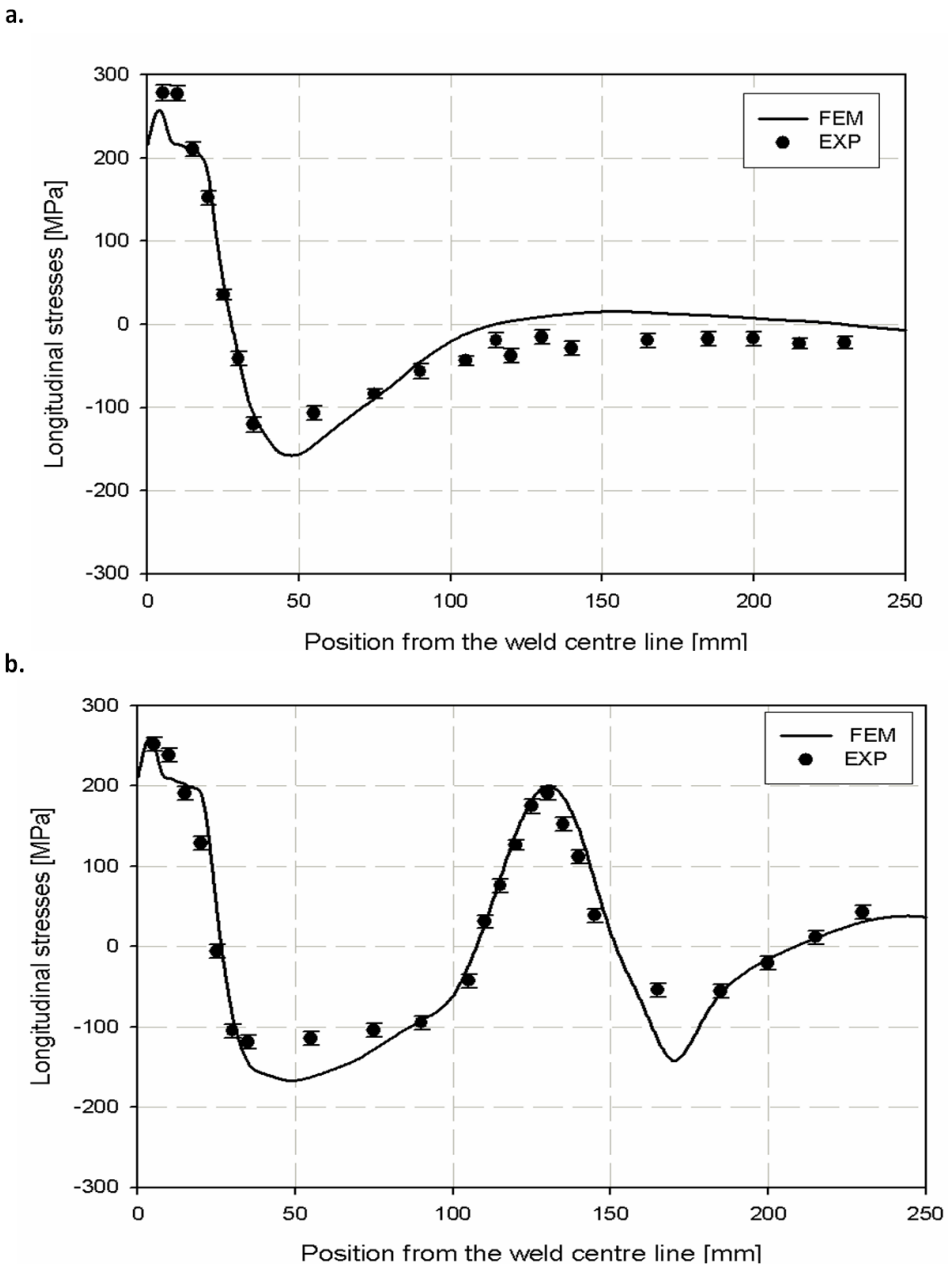

Figure 6.20. *Comparison between the modelled and the measured longitudinal residual stress results for AISI-316L (Case I-B) after (a) conventional welding and (b) welding with additional heating.*

Although, the predictions are in good agreement with the measurements, there are several discrepancies between the modelled and the experimental results for both conventional welding and welding with additional heating. As presented in **Section 6.1**, the temperatures closely matched. Therefore, the deviations from experimental data in the residual stress fields are mainly due to the mechanical material properties at elevated temperature, the modelling of the clamps using spring links and the stress annealing. For the weld with additional heating, there is a good agreement between the predictions and the experiments for the longitudinal residual stresses underneath the burner position. This shows that the assumptions used for the modelling of the burners are valid.

In order to obtain a better understanding of welding with additional heating, the stress development during conventional welding is compared to welding with additional heating. In this comparison, three different burner positions with respect to the welding torch (leading, trailing and parallel situations) are considered. The longitudinal stress development along a line in the middle of the plate transverse to the welding direction is displayed for four time steps and is shown in **Figure 6.21**. These time steps represent a situation where (a) the welding torch has not yet reached the middle line of the plate, (b) the welding torch has reached the middle line (c) the welding torch has passed the middle line and (d) the final residual stress profile when the work-piece has reached room temperature, and is still clamped.

For the conventional weld and the trailing configuration, the welding torch has not reached the middle line, the weld is under compressive stresses and the stress state far from the weld is negligible, **Figure 6.21a**. The material in front of the welding heat source already experiences the effects of the advancing arc. The material directly surrounding the arc will try to expand, inducing compressive stresses in these areas. In the parallel configuration, the welding torch has not reached the middle line, while the burners are already passing this line; because the burners have a length of 240 mm. Compressive stresses are introduced underneath the burners. These compressive stresses induce tensile stresses in the areas around the heated zone. In the leading configuration, the burner has passed the line completely and therefore the heated area already cools and compressive stresses in this area begin to fall.

Figure 6.21b shows the situation in which the welding torch has reached the middle line. Since the material is molten on the weld centre line in all cases, the stress state is zero up to the fusion line located 2.5 mm from the weld centre line. Due to the high temperatures near the fusion zone, the points located close the weld zone experience high compressive stresses accompanied by relative small tensile stresses outside the HAZ (of welding) for conventional welding. In the case of trailing heating, the effects of the additional heat sources are now experienced on the middle line. In the leading case, the burners have passed the middle line and the material has cooled causing a transition from compressive to tensile stresses.

Figure 6.21c shows the situation in which the welding torch has passed the middle line. The temperature of the weld zone is decreasing and therefore the compressive stresses at the weld centre line change to tensile stresses. For the leading and the parallel case, the temperature is also decreasing while for the trailing case the burner is still heating the material at the middle line area.

Figure 6.21d shows the stress profile when the plate has cooled to room temperature in the clamped condition. Tensile stresses are formed in all cases in the weld and HAZ (of welding). Along the track of the burners, tensile stresses are formed when welding with additional heating, while the stresses in this area are negligible for conventional welding. At the edges of the plate, tensile stresses are formed. These are in the order 100 MPa for welding with additional heating and approximately 30 MPa for conventional welding. During the cooling stage, the tensile stresses generated between the HAZ (of welding) and the areas heated by the burners become compressive due to redistribution and balancing of the stresses.

The stress development profiles and the final residual stresses for conventional welding and welding with additional heating indicate that additional heating does not reduce the compressive stresses ahead of the weld zone, nor does it increase the tensile stress in the weld zone during cooling. The tensile stresses generated by the burners redistribute the final residual stresses.

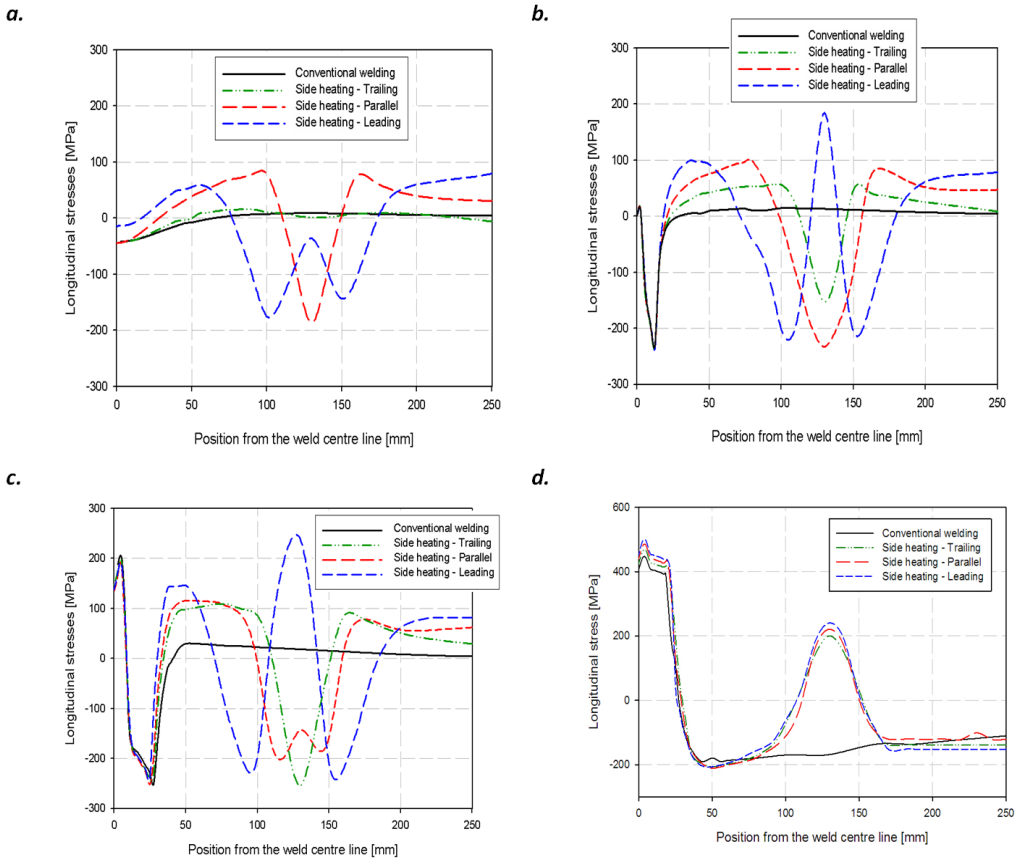

Figure 6.21. *The calculated stress development for conventional welding and welding with additional heating (Case I-B) when the welding torch (a) is approaching the plate centre line, (b) has arrived at the centre line, (c) has passed the plate centre line and (d) after cooling in clamped condition.*

The effects of solid state phase transformations on the residual stresses were investigated on a 200×100×1.5 mm^3 DP600 (Case II-A) steel plate. The numerical procedure and the implementation of phase transformations have been discussed in **Chapter 3**. The experimental procedure and the welding parameters were shown in **Chapter 4**. The temperature profiles of the points located at different positions to the weld centre line and the phase fractions were shown experimentally and numerically in **Chapter 5** and **Section 6.2** respectively.

Two effects of solid phase transformations have been modelled: the increase of the yield strength due to formation of hard phases and the volume change during phase

transformations. The measured residual stresses are form reference [2].

Figure 6.22 shows the longitudinal residual stress at different positions to the weld centre line for four different situations: (i) the model without phase transformation, (ii) the model with only the effect of martensite on the yield strength, (iii) the model with only the effect of volume change and (iv) the model including volume change and the increase of the yield strength. The residual stress profile upon releasing the clamps is also shown in the figure. All models predict the residual stresses close to the experimental results at the edges of the plate. In this area no phase transformation occurs in the base metal; however, there are some deviations in the stress predictions at the plate edges. These deviations are related to the equilibrium condition of residual stresses. In the model with only the effect of martensite on the increase of the yield strength, high tensile stresses are predicted in the fusion zone and consequently a high compressive stress is seen at 20 mm from the weld centre line. This model overestimates the residual stresses. The model with only volume change shows a very high compressive stress in the weld metal. This is related to the expansion of the material during phase transformation in the cooling stage in the welding process. Finally, the model including all aspects of phase transformation predicts residual stresses close to those found by experiment. It seems that the deviation of this model from the experimental result is related to the transformation plasticity. The model used does not include transformation plasticity. The transformation plasticity tends to increase the residual stresses as it induces some strains in the material. Comparing the results of these different models, it can be concluded that phase transformations can have a significant effect on the residual stress states. However, the effect of volume change counteracts the effects of the strength increase. The computational time for the models including the solid phase transformations (23.5 hours) is around three times greater than the model excluding these effects (7 hours).

Another issue in the mechanical modelling of phase transformations is the hardening models. As explained in **Chapter 3**, an isotropic hardening model and a mixed hardening model were used and the predicted results of the longitudinal residual stresses were compared. The effect of different hardening models in the prediction of residual stresses is shown in **Figure 6.23**. In these results, the effects of phase transformation are included. It can be seen that the isotropic hardening model predicts higher longitudinal residual stresses in the weld zone (and HAZ of welding) compared to the model with mixed hardening. The prediction of residual stress is almost similar for both cases at the edges of the plate. The agreement of the predictions and experiments is in an acceptable range for the areas located at the edges of the plate, while there are still some deviations for the areas in the welded zone.

The results show that different hardening models influence the residual stress prediction mainly in the weld zone and have minor effects at the edges of the workpiece. The isotropic hardening model overestimates the residual stresses, although most studies in the literature use a linear isotropic hardening model. During welding, the

temperatures are high and the mechanical properties at high temperature have low values. However, work hardening should be included. The mixed hardening model is able to predict residual stresses more accurately than isotropic hardening, but they need additional parameters which are difficult to obtain.

Figure 6.24 shows a comparison between the prediction and the measured results of longitudinal residual stresses for DP600 (Case II-B). Similar trends to the experiments are found in the numerical calculations. There is good agreement between the modeled and the experimental results. The model, however, excludes the effects of phase transformations.

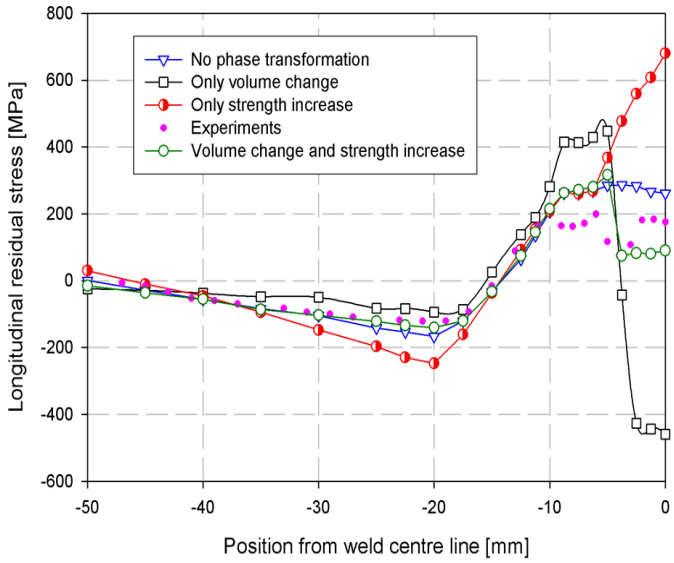

Figure 6.22. *Longitudinal residual stress predictions for four different cases: model with phase transformation, without phase transformation, with only the effect of volume change and with only the effect of yield strength increase due to martensite formation.*

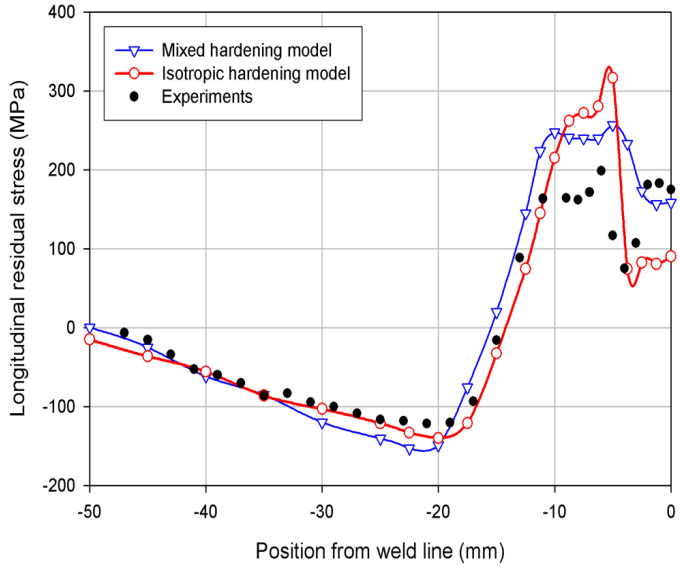

Figure 6.23. *The longitudinal residual stress profile for the model with isotropic hardening and the model with mixed hardening (both including phase transformation) compared to experiments.*

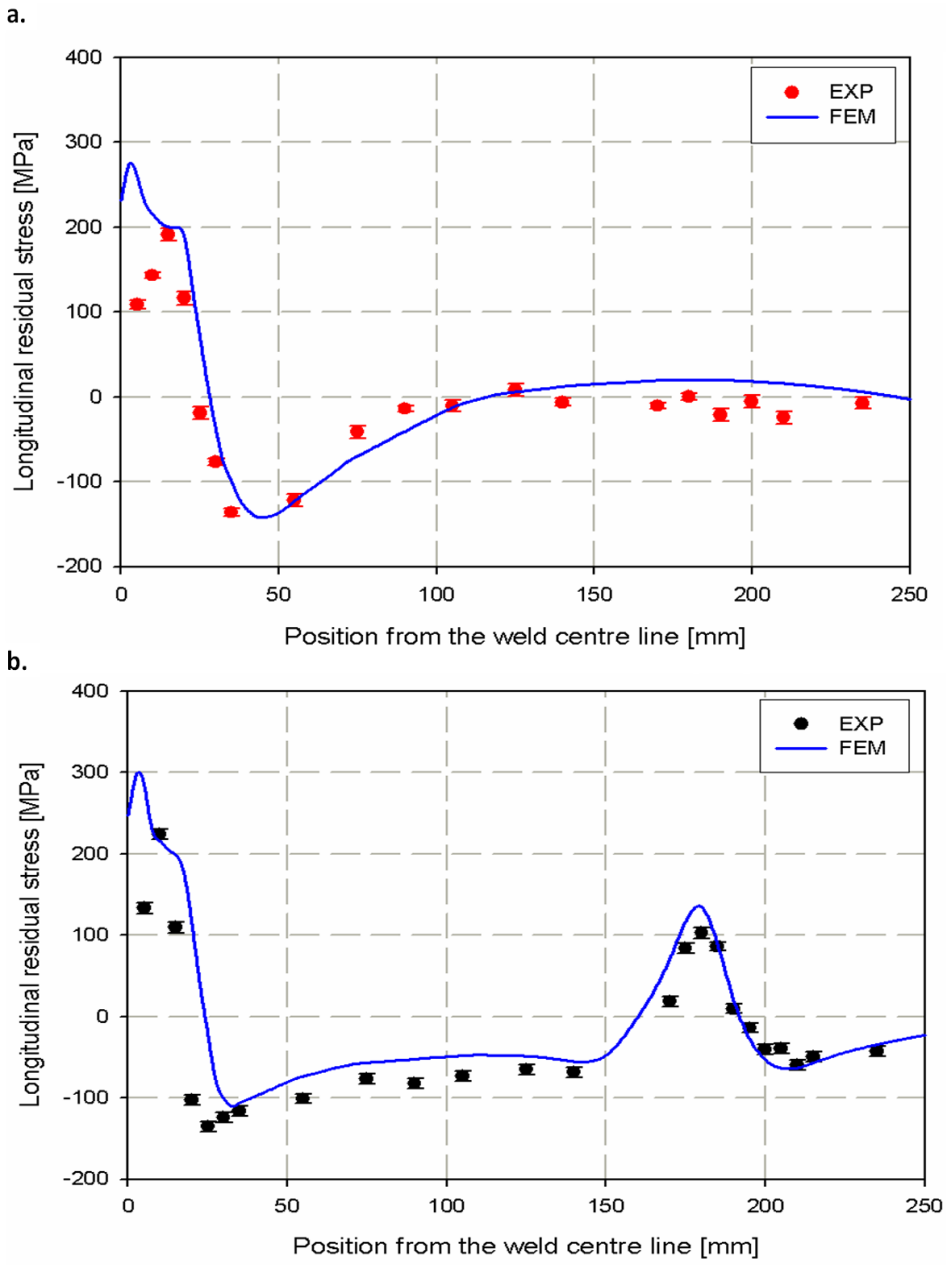

Figure 6.24. *Comparison between the modelled and the measured longitudinal residual stress results for DP600 (Case II-B) dimension after (a) conventional welding and (b) welding with additional heating.*

The stress development during conventional welding is compared to that when welding with additional heating. In this comparison, three different burner positions (leading, trailing and parallel situations) are considered. The longitudinal stress development in the line in the middle of the plate is displayed for four time steps as shown in **Figure 6.25**. These time steps represent when (a) the welding torch has not yet reached the middle line of the plate, (b) the welding torch is positioned at the middle line (c) the welding torch has passed the middle line and (d) the final residual stress profile when the workpiece has reached room temperature, but is still clamped.

Figure 6.25a shows a situation in which the welding torch has not reached the middle line. As can be seen, for the conventional weld and the welding with burners in the trailing configuration, the weld line is under compressive stresses and the stress state for the positions located at or near the plate edge is negligible. This means that the material in front of the welding heat source already experiences the effects of the advancing arc. The material directly surrounding the arc will try to expand resulting in compressive stresses in these areas.

In the parallel configuration, the welding torch has not reached the middle line while the burners are already passing this line, because the burners have a length of 240 mm. Again compressive stresses are introduced underneath the position of the burners as the expansion is counteracted by the surrounding materials. These compressive stresses induce tensile stresses in the areas around the heated zone.

In the leading configuration, the burner has passed the middle line completely and therefore the heated area already cools and the compressive stresses present in this area begin to decrease. **Figure 6.25b** shows the situation in which the welding torch has reached the middle line. Since the material is melting at the weld centre line in all cases, the stress state is zero for the points up to a distance of 2.5 mm from the centre line (*i.e.*, the fusion line). Due to the high temperatures near the fusion zone, the points located close the weld zone experience high compressive stresses. These compressive stresses are balanced by tensile stresses outside the HAZ (of welding) for conventional welding. In the case of trailing heating, the effects of the additional heat sources are now experienced by the material. In the leading case, the points at the position of the burner are cooled even further and a transition from compressive to tensile stresses has taken place.

Figure 6.25c shows the situation in which the welding torch has passed the middle line. The temperature of the weld zone is reducing and therefore the compressive stresses at the weld centre line change to tensile stresses. For the area where the burner is located, the temperature is also reducing for the leading and the parallel case while for the trailing case the burner is still heating. **Figure 6.25d** shows the stress profile when the plate is at room temperature in the clamped condition. Tensile stresses are formed in all cases in the weld and the HAZ (of welding). Near the edges of the plate, tensile stresses are formed when welding with additional heating, while

the stresses in this area are compressive for conventional welding. At the edges of the plate, compressive stresses are formed in welding with additional heating. In this area, compressive stresses are formed for conventional welding with higher absolute values.

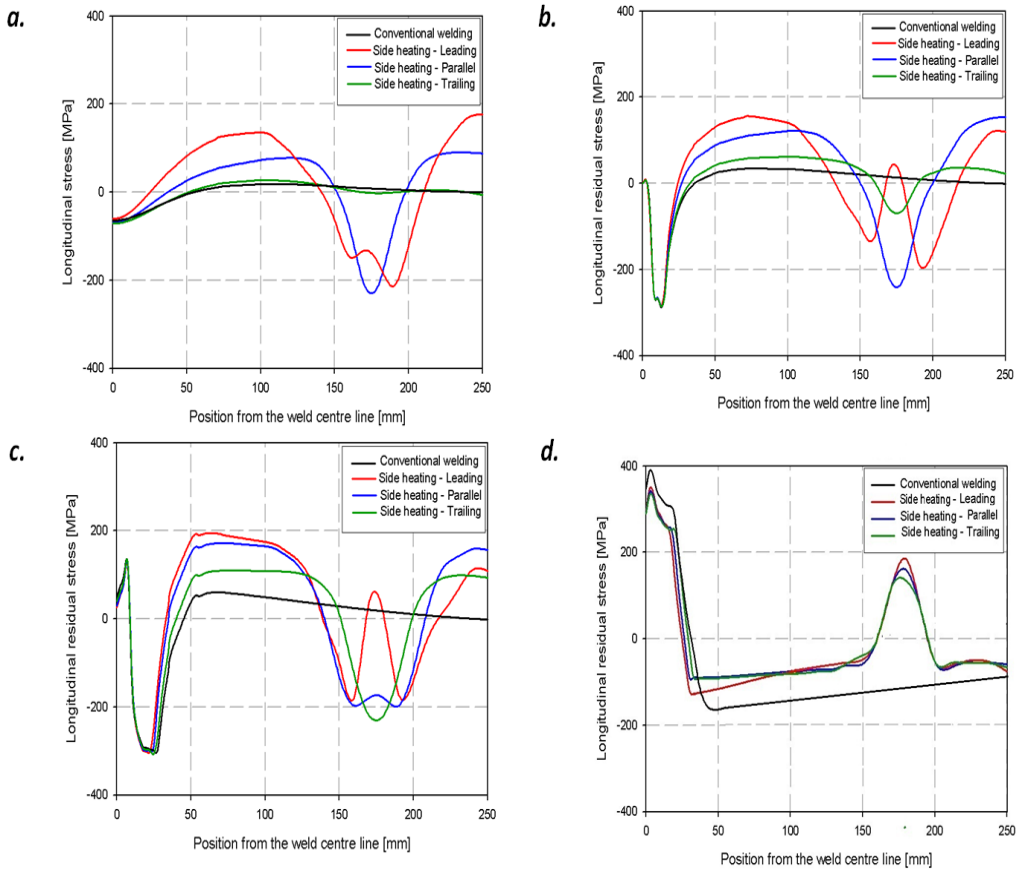

Figure 6.25. *The predicted stress development during conventional welding and welding with additional heating with different burner positions for three time steps when (a) the welding torch has not yet reached the middle line of the plate, (b) the welding torch reaches the middle line (c) the welding torch has passed the middle line and (d) the final residual stress at room temperature in the clamped condition.*

Welding with additional heating does not reduce the compressive stresses ahead of the weld zone, nor does it increase the tensile stress in the weld zone during cooling. The positions of the burners are far from the weld zone and thermal influences hardly change the stress state in this zone during heating or cooling. The tensile stresses

generated by the burners at or near the plate edges redistribute the final residual stresses upon release of the clamps.

Figure 6.26 shows a comparison between the prediction and the measured results of longitudinal residual stresses for AH36 (Case III) plate. In **Figure 6.26a** the results of conventional welding are presented while in **Figure 6.26b**, the results of welding with additional heating are shown. In both cases, the clamps are released after welding. In the numerical results, it is predicted that after welding with additional heating, a tensile stress region is formed at the location of the burners (193.5 mm from the weld zone). This area has a very low stress level in conventional welding. It can also be seen that the predictions indicate the same level of stresses in the weld and its HAZ in both conventional welding and welding with additional heating. However, the experimental results show a significant lower residual stress for the region beneath the burners in welding with additional heating. The main deviations between the numerical results and the experiments are attributed to the following:

1. There is a possibility that the heat generated by the burners causes stress relieving. The temperature of the top surface beneath the burners is predicted to be around 600 ^{o}C. The time of heating depends on the length of the burner (240 mm) and the heating speed (4.5 mm s^{-1}). Both temperature and time needed for stresses relieving are available. Therefore, it is expected that two competing phenomena are occurring here: (1) stress build-up by the burners and (2) stress reduction by stress relieving. The winning term determines the final level of residual stresses. In the numerical model, phase transformations and microstructure changes have been excluded. In the predicted results such tensile stress peaks at the position of the burners are expected. Implementation of these small changes in the numerical models is difficult. It should be noted here that the hardness measurement does not show significant change for the region beneath the burners. Full stress relieving needs more time than the heated time in the experiment. It is expected that stress relieving phenomenon occurs partially for this experimental heating time. Similar results have been observed in [3].

2. The experimental source of errors explained in **Chapter 5** should be taken into account in the interpretation.

3. The numerical models exclude the phase transformations. However the experimental results show lower stress in the region close to the weld in both conventional welding and welding with additional heating. Since the residual stresses are in a balanced condition, a change of these stresses somewhere in a plate causes a change somewhere else.

4. All errors in material related properties and the way of clamping in the numerical models explained for previous materials are valid here as well.

Figure 6.27 shows a comparison between the prediction and the measured results of longitudinal residual stresses for AH36 plate before releasing the clamps. In **Figure 6.27a** the results of conventional welding are presented while in **Figure 6.27b**, the results of welding with additional heating is shown. It is believed that the material properties contribute the most to the differences between the measured and the modeled residual stresses. Finally, it should be mentioned that the stresses have been measured only in the longitudinal direction. If more information for residual stresses in other directions were available for this thick material, it may be possible to determine more appropriate model parameters and obtain a better match between predictions and experiments.

a.

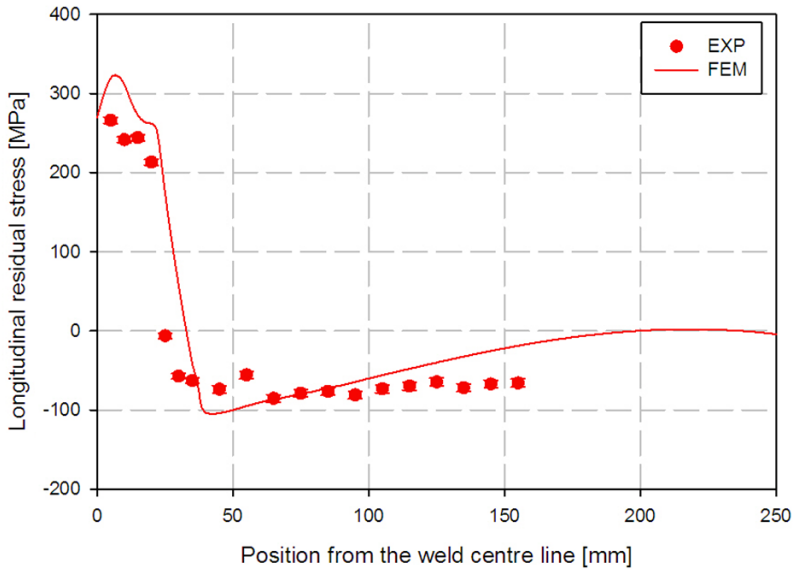

b.

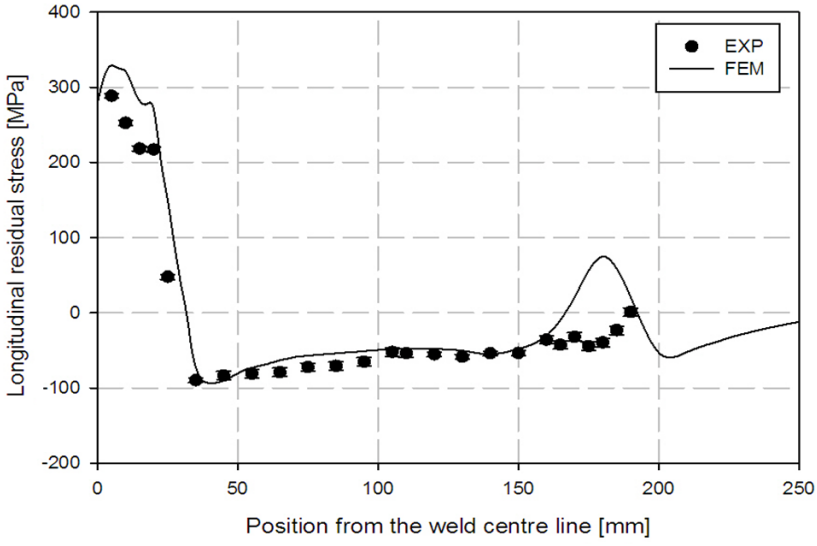

Figure 6.26. *Predicted longitudinal residual stresses after releasing the clamps for AH36 plates compared to the measurements for (a) conventional welding and (b) welding with additional heating.*

a.

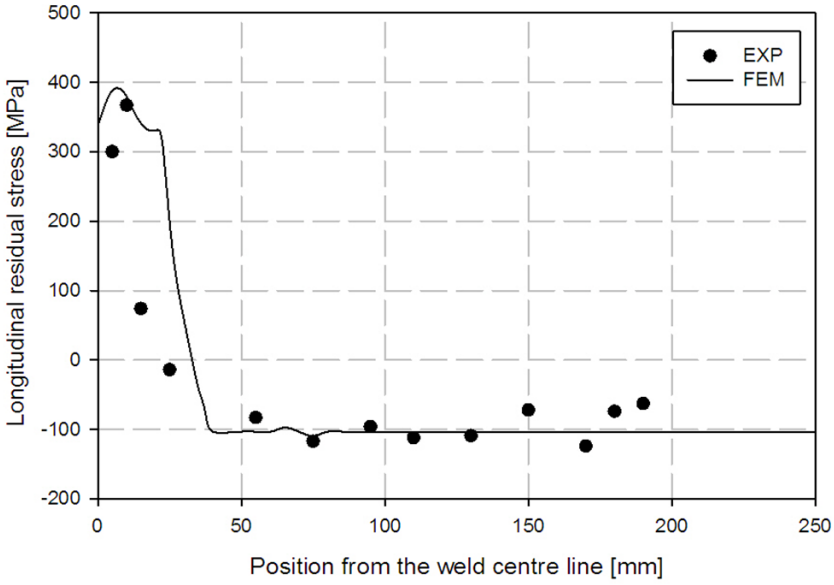

b.

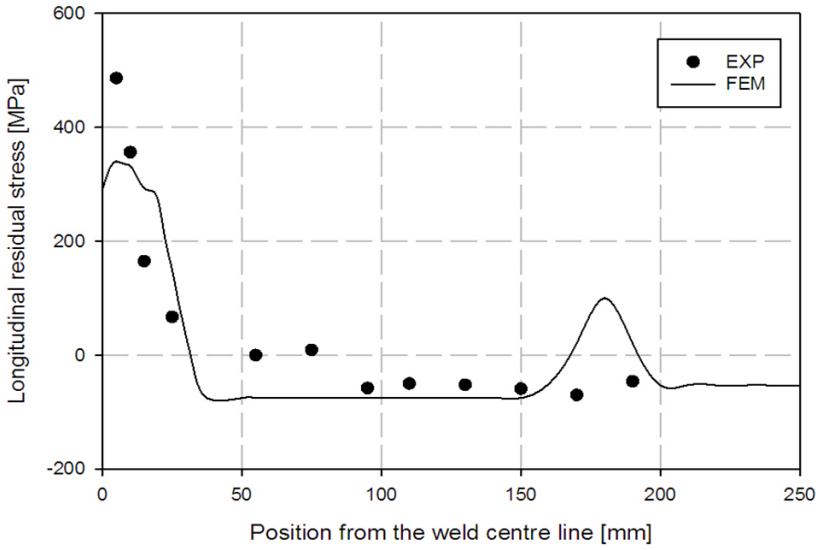

Figure 6.27. *Predicted longitudinal residual stresses before releasing the clamps for AH36 plates compared to the measurements for (a) conventional welding and (b) welding with additional heating.*

6.5 Concluding remarks

This chapter deals with the predicted results of temperature, phase fractions, out-of-plane deformation, stress development and residual stresses of AISI-316L, DP600 and AH36 steels conventionally welded and welded with additional heating.

The first part of the chapter describes the thermal field during conventional welding and welding with additional heating of AISI-316L, DP600 and AH36 steel plates. For the conventional welding process, close matches between the models and the measurements were observed. The burners were modelled using a Gaussian power density distribution on the top surface of the plates. Although, the presented model cannot predict the observed eight peaks in the temperature profiles of welding with additional heating at the location of the burners, the maximum temperature and the heating and the cooling rates modelled are close to the measurements. The main sources of deviation in the modelling of both conventional welding and welding with additional heating are related to the thermal material data at elevated temperature and the heat transfer coefficients. The essential feature of the weld with additional heating is the creation of a temperature peak at the location of the burners. The temperature distribution in the weld zone and the HAZ (of welding) remains unchanged.

The phase fractions were validated only for one case. Although, the predicted phase fractions were in an acceptable range compared to the experiments, it was found that the model with solid phase transformations predicts an out-of-plane deformation 9% lower than the model excluding the effects of the transformations. However, the risk of computational instability and divergence is high when phase transformations are included, therefore, for other cases the microstructure field was ignored.

The out-of-plane deformation of the workpiece after conventional welding and welding with additional heating were predicted and distribution was compared using different criteria: i) a distortion index, ii) an out-of-plane deformation contour and iii) a scan along a line perpendicular to the weld centre line. For all materials the predictions of conventional welding are in a good agreement with the experiments. Minor deviations are related to the material properties at high temperatures, the change of material stiffness during heating and cooling and the way that the clamps are models. In welding with additional heating these deviations are greater than for conventional welding. Besides the deviations sources explained before, which play a role here as well, there are some other possible sources. For example, the angular deformation due to the temperature gradient in the through thickness of thick materials may change the deformation of the plates upon clamp releasing. This type of deformation is not captured fully in the thin plate model. Another example is related to the phase transformation or stress relieving or being material related phenomena not captured in the models which may change the final deformation of the plates.

The predicted residual stresses are close to the measurements for both conventionally

welded plates and plates after welding with additional heating. The characteristic of additional heating from a numerical point of view is the creation of tensile residual stresses at the location of burners. This prediction is experimentally demonstrated for AISI-316L and DP600. The tensile peaks are not seen in the experimentally obtained results for AH36 and relieving is expected to be the main reason for this model limitation.

The stress development profiles and the final residual stresses in conventional welding and welding with additional heating indicate that (from numerical models), welding with additional heating does not reduce the compressive stresses ahead of the weld zone, nor does it increase the tensile stress in the weld zone during cooling. The tensile stresses generated by the burners redistribute the final residual stresses.

These validated models are used in **Chapter 8** to investigate the mechanism responsible for distortion reduction using additional heating and thermal tensioning. The models developed and validated here have been simplified and used in an industrial application at Damen Schelde Shipyard. The results of both experiments and numerical models are explained in the next chapter.

Reference

[1] J. Goldak, M. Gu, *Computational weld mechanics of the steady state*, Mathematical Modelling of Weld Phenomena 2, The Institute of Materials, pp. 207-225, 1995.

[2] E. M. van der Aa, *Local Cooling during Welding: Prediction and Control of Residual Stresses and Buckling Distortion*, PhD thesis, Delft University of Technology, 2007.

[3] M. N. IIman, R. Ismail, S. Iswahyudi, M. R. Muslih, *An experimental study of movingly localized heating based stress relieving for control of residual stress and its beneficial effect on fatigue crack growth rate of steel welded structure*, Proceedings of 64th annual assembly and international conference of International Institute of Welding, Chennai, pp. 583-591, 2011.

Chapter 7

Industrial implementation

The results obtained in the previous chapters showed that distortion reductions can be achieved using welding with additional side heaters. The mitigation technique is based on a redistribution of residual stresses in the welded plate, by a specific heating strategy by means of flames on the material surrounding the weld. Experiments were carried out on laboratory scale specimens. If distortion could also be reduced in large scale steel panels, a straightening step could be omitted and production speed could be increased.

In this chapter, the technique is applied in an industrial environment at Damen Schelde Naval Shipyards (DSNS). Large panels were submerged arc welded and the effects of additional heating investigated. During welding, temperature measurements were conducted and the initial and the out-of-plane deformation of plates measured. The numerical modelling knowledge is used to estimate suitable process parameters. The predicted position was then used as the starting point in the experiments. The main goal is a feasibility study on side heating of large panels together with the application of developed numerical models in the shipbuilding industry.

7.1 Background

Weld distortion is a real quality concern for manufacturers of naval ships, since weld distortion directly influences the performance (*e.g.* radar cross section) of the ship. Costly post weld heat treatments, like flame straightening, are often needed to control weld distortion. Any possibility to avoid or reduce weld distortion can lead to cost-savings and to increased competitiveness. For example, as reported in [1], re-work can encompass up to 20% of personnel time in the total metal working activities in shipbuilding, see **Figure 1.4**.

Figure 2.27 shows a comparison of out-of-plane deformation with and without side heating during welding. It was reported that the plate edge waves were eliminated

by side heating due to tensile stresses added by this technique in areas adjacent to the plate free edge.

The work presented in this chapter reports on a feasibility study of side heating during welding of large panels at DSNS using the lessons learned, which were described in the previous chapters. This chapter shows the numerical and the experimental approaches of the tests carried out at DSNS together with the results.

7.2 Numerical and experimental approaches

According to the available experimental facilities at DSNS, for both numerical and experimental activities, two AH36 plates with dimensions of $3600\times600\times6$ mm^3 were welded using Submerged Arc Welded (SAW). The welding was conducted in two runs, the first applied on one side of the plates and the plates were turned over, and the second run applied on the other side of the plate.

7.2.1 Numerical approach

The main goal of the numerical models presented in this chapter is to find the position of the burners with respect to the weld centre line to achieve minimum distortion.

The Case III in this thesis shown in **Chapter 1**, deals with AH36 welded plates with dimension of $500\times250\times6$ mm^3 using GTAW. The numerical approach was introduced in **Chapter 3** and the measurements and the simulation results were shown in **Chapter 5** and **6** respectively. The modelling was based on solid elements. The same approach is used here. However, in order to reduce the computational time, some assumptions are made. The model here is based on shell elements. The welding process is modelled only for one run. The addition of filler wire is not modelled. The solid state phase transformations are ignored. The speed of welding and side heating is set according to practice at 9.6 mm s^{-1}. The mesh used in the numerical models is shown in **Figure 7.1**. In both regions of the weld and the heated area by the side heaters, elements are re-meshed (as explained in **Chapter 3**).

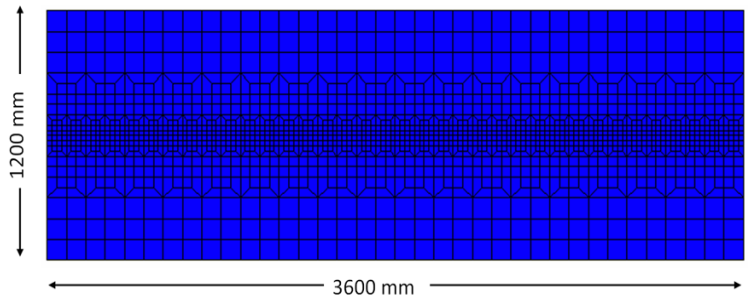

Figure 7.1. *Mesh used in the simulation.*

Based on the simulation approach mentioned above, it was calculated that the distortion index for conventional welding is 41 mm and for welding with side heating in the minimum distortion case is 13 mm. These values were obtained after 10 computational runs with different input parameters. The minimum case here is the case in which the burners are located 490 mm from the weld centre line. The simulation is more sensitive to the position of the burners relative to the weld centre line compared to the position of the burners relative to the welding torch (heat source). The parameters for the minimum distortion case were adopted as the starting point for the experiments.

7.2.2 Experimental approach

The experimental approach consists of three main steps:

1. Characterization of the burners and setting the burner parameters by temperature measurements;
2. Conventional submerged arc welding and measuring the out-of-plane deformation of the plates;
3. Side heating experiments for different situations and measuring the out-of-plane deformation of the plates.

AH36 plates with dimensions of 2000×1200×6 and 3600×600×6 mm^3 were used in the experiments. The chemical composition and all related material data can be found in **Chapter 4**. The plates were cut in the rolling direction. **Table 7.1** lists the experiments performed at DSNS.

In the first test, a 2000×1200×6 mm^3 plate was heated along the travelling direction. The burner was located at the middle of the plate. The test was repeated for both burners. The temperature of the plate was measured along a line located in the middle of the plate and perpendicular to the travelling direction, using eight K-type thermocouples attached at the underside surface of the plates at different positions as shown in **Figure 7.2**.

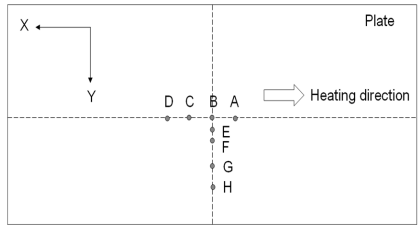

Point	(X mm,Y mm)
A	(-20,0)
B	(0,0)
C	(20,0)
D	(40,0)
E	(0, 10)
F	(0, 20)
G	(0, 40)
H	(0, 60)

Figure 7.2. *Thermocouple positions for tests 1 to 3 (see* ***Table 7.1****).*

Table 7.1. *The summary of the tests at Damen Schelde Naval Shipyard.*

Test	**Situation**
1	Heating 2000×1200×6 mm^3 with burners parallel to the welding direction plate with burners parallel to the welding direction
2	Heating 2000×1200×6 mm^3 plate with burners perpendicular to the welding direction
3	Heating 2000×1200×6 mm^3 plate with burners with 45^o to the welding direction
4	Conventional welding of 3600×600×6 mm^3 plates at both sides of the plate
5	Side heating during welding of 3600×600×6 mm^3 plates with burners parallel to the welding direction during both passes
6	Side heating, only during the first pass, while welding both sides of the 3600×600×6 mm^3 plates with burners parallel to the welding direction
7	Side heating during welding of 3600×600×6 mm^3 plates with burners with 45^o to the welding direction at both sides of the plate

The second and the third tests were similar to the first one. The differences were related to the burner direction with respect to the welding direction. In the second test the burner was perpendicular to the welding direction while in the third test it was at an angle of 45^o.

For conventional welding, two plates with dimensions of 3600×600×6 mm^3 were tack welded at different positions in order to prevent movement prior to submerged arc welded (SAW) with the parameters shown in **Table 7.2**. After the first pass (run), the plate was turned over and a second weld was made on the other side.

The plates were painted in order to measure the out-of-plane deformation with a 3D laser scanner (with accuracy of 40 μm) before and after welding, **Figure 7.3** and **Figure 7.4**. The out-of-plane deformation was always measured at the side of the plate that was being welded, and the thickness of the plate was subtracted for comparison.

Table 7.2. *Welding parameters used in SAW.*

Parameters	Value
Averaged welding current [A]	366
Averaged welding voltage [V]	32
Averaged welding speed [mms^{-1}]	9.6

Figure 7.3. *Two plates of AH36 with dimensions of* $3600 \times 600 \times 6\ mm^3$ *used in the SAW process. The plates are painted, in order to measure the out-of-plane deformation.*

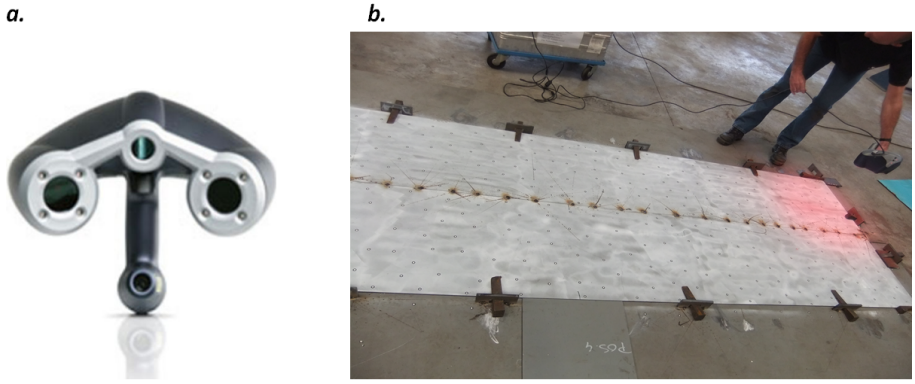

Figure 7.4. *(a) High resolution 3D laser scanner (EXAscan [2]) used for distortion measurements before and after welding and (b) measurements in progress.*

For test 4, temperature measurements were carried out at the underside surface of the plate at different distances from the weld centre line as shown in **Figure 7.5**.

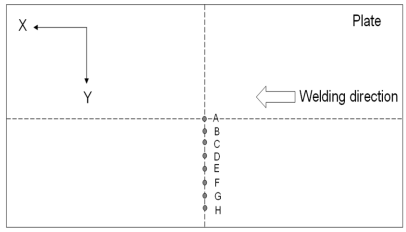

Point	(X mm.Y mm)
A	(0, 15)
B	(0, 20)
C	(0, 25)
D	(0, 30)
E	(0, 40)
F	(0, 50)
G	(0, 60)
H	(0, 70)

Figure 7.5. *Thermocouple positions for test 4; see* ***Table 7.1****.*

After welding the first pass, the plate was left to cool to room temperature, the clamps were released and then the other side of the plates were welded with the same welding conditions and parameters. The initial out-of-plane deformation of the plate was measured. These measurements were repeated after both weld passes. Since the welding parameters and conditions were the same for both sides, the temperature was measured just for the first pass.

It was mentioned in the numerical approach section that the simulations showed the minimum distortion case in which the burners are located 490 mm from the weld centre line. This point was used as the starting point for the side heating experiments. However, during experiments it was clear that, due to the clamping situation, the burners could not be placed more than 475 mm from the weld centre line. Otherwise, the burners heat the clamps.

In test 5, during welding of both sides of the plate, side heating was performed as shown in **Figure 7.6**. The burners were located along the welding direction 475 mm from the weld centre line and 380 mm leading the welding torch. Test 6 is similar to test 5. The only difference is that side heating is only applied during the first pass. For both tests 5 and 6, initial and final out-of-plate deformations were measured after each pass. The temperature measurements were performed just for one side in tests 5 and 6 at several positions as schematically shown in **Figure 7.7**.

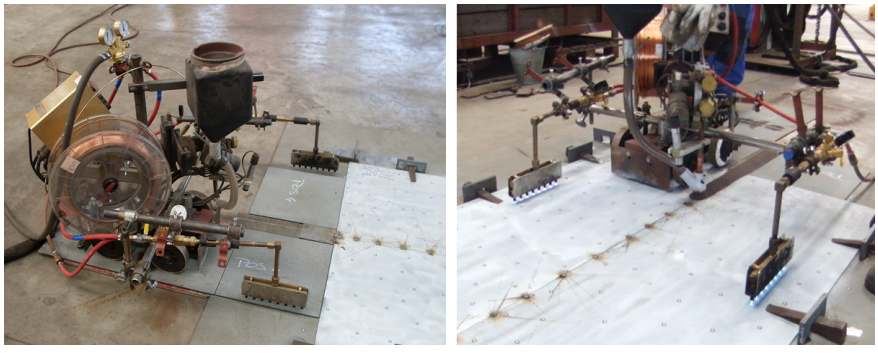

Figure 7.6. *Side heating during welding (test 5 and 6).*

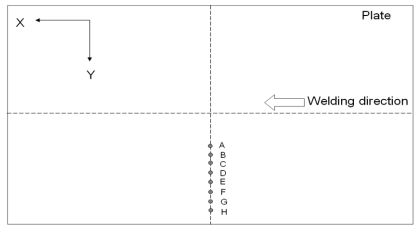

Point	(X mm,Y mm)
A	(0, 440)
B	(0, 460)
C	(0, 480)
D	(0, 500)
E	(0, 520)
F	(0, 540)
G	(0, 560)
H	(0, 580)

Figure 7.7. *Thermocouple positions for test 5,6; see* ***Table 7.1****.*

Finally, in the last test (test number 7), side heating during welding of both sides of the plate was performed using burners oriented 45^o to the weld centre line located 320 mm leading the welding torch and 360 mm from the weld centre line (from the centre of the burner) as shown in **Figure 7.8**.

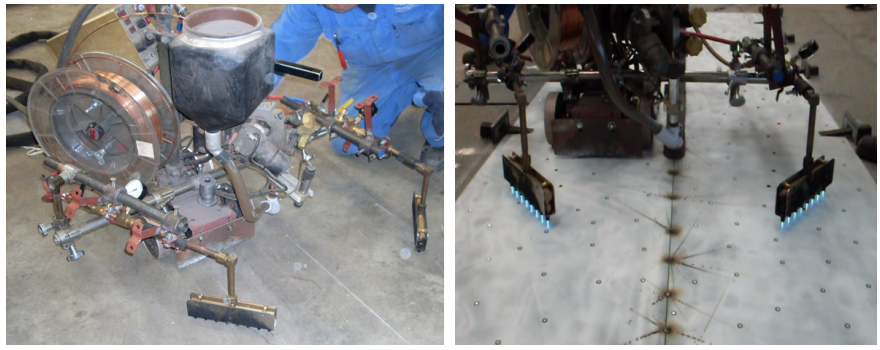

Figure 7.8. *Side heating during welding test 7.*

7.3 Experimental results and discussions

The results include the out-of-plane deformation measurements, the temperature measurements and the microstructural investigation.

7.3.1 Distortion measurement results

Figure 7.9 shows the initial plate deformation as well as the final out-of-plane deformation after conventional two pass welding. After the first pass, the distortion index of the plate reaches 29 mm. After the second pass the deformation stayed more or less the same.

The out-of-plane deformation of the plate after side heating during welding is shown in **Figure 7.10**. **Figure 7.10a** shows the initial plate deformation while the deformation after the first pass and the second pass is shown in **Figure 7.10b** and **Figure**

7.10c respectively. The final deformation of the plate after both passes is at the level of the initial deformation of the plate. The plate has low distortion after side heating.

Figure 7.11 shows the initial plate deformation together with the final deformation after side heating of the first pass. As mentioned in this experimental approach, the second pass at the underside of the plate was conventionally welded without side heating. It is clear that when side heating is applied the plate deformation is in the level of the initial plate deformation. After the second pass without side heating, a distortion index of 15 mm is found. Although this amount of deformation is much higher (7 mm) compared to the case where side heating is applied during both passes, it is still much less than the conventionally welded plates.

As mentioned in the experimental approach, the final test employed side heating on both sides of the plate using burners applied at an angle of 45^o to the welding centre line. The initial and the final out-of-plane deformation of the plate are shown in **Figure 7.12**. The distortion index is around 29 mm, which is same as that of the conventionally welded plate. This means that the burners with the mentioned configuration are not able to reduce welding distortion. **Figure 7.13** shows test plates 4 to 7.

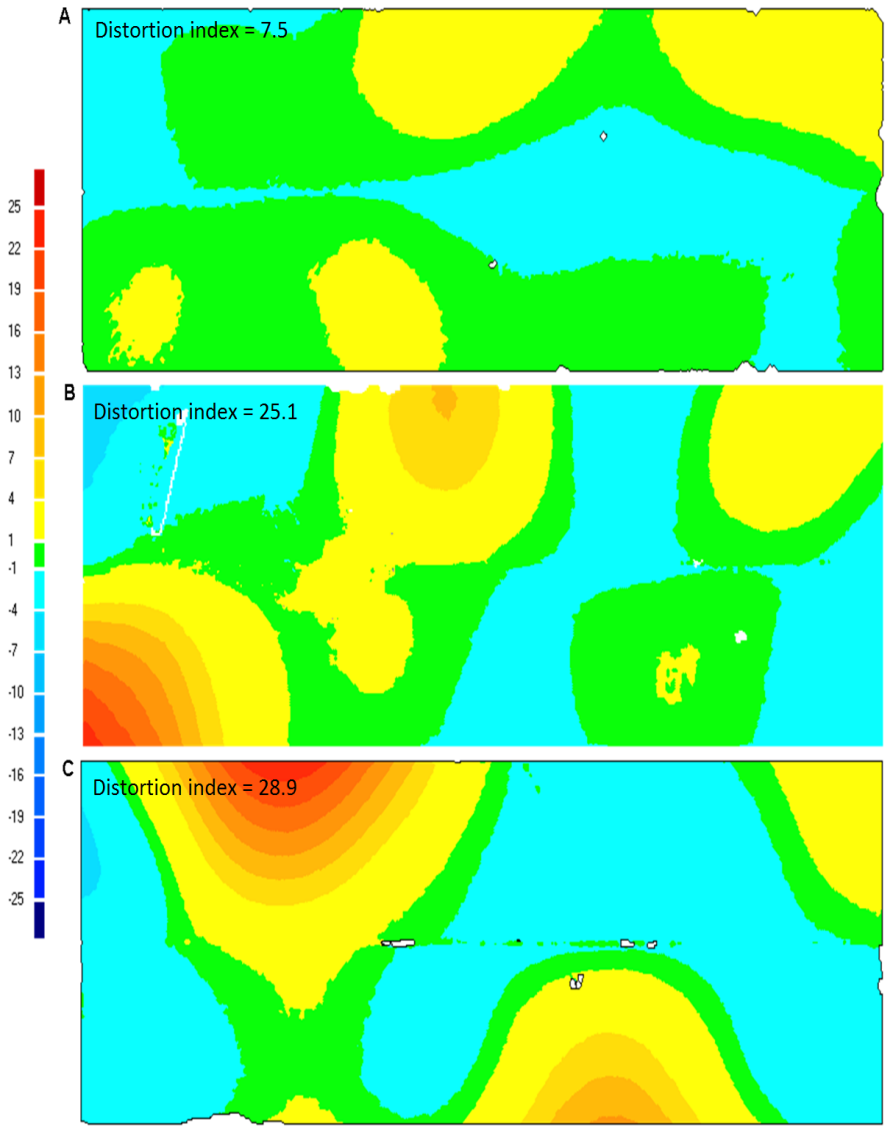

Figure 7.9. *The out-of-plane deformation of AH36 plate for conventional welding in test 4: (a) the initial deformation after tack welds, (b) the out-of-plane deformation after conventional welding of the first pass and (c) the final out-of-plane deformation after conventional welding of the second pass. The scale is -25 mm to +25mm.*

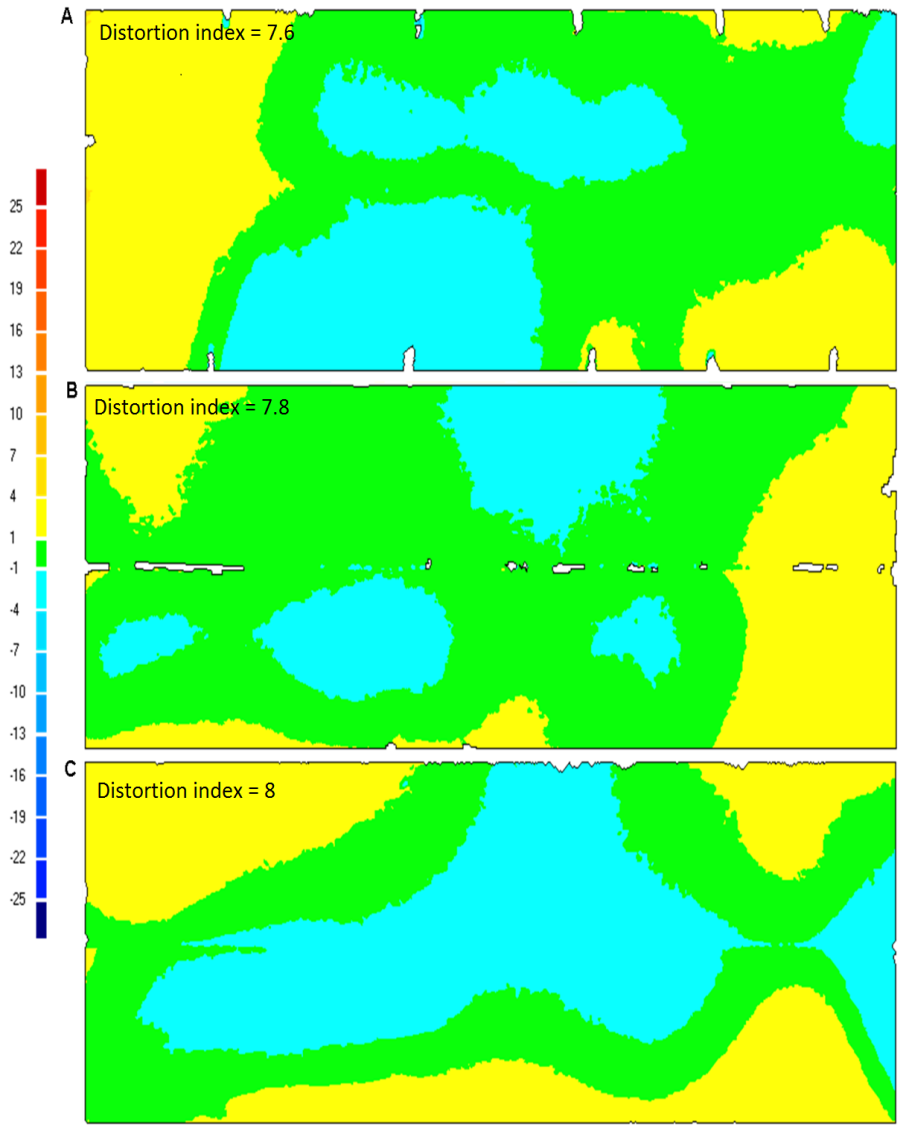

Figure 7.10. *The out-of-plane deformation of AH36 plate for welding with side heating in test 5: (a) the initial deformation after tack welding, (b) the out-of-plane deformation after side heating during welding of the first pass and (c) the final out-of-plane deformation after side heating during welding of the second pass. The scale is -25 mm to +25mm.*

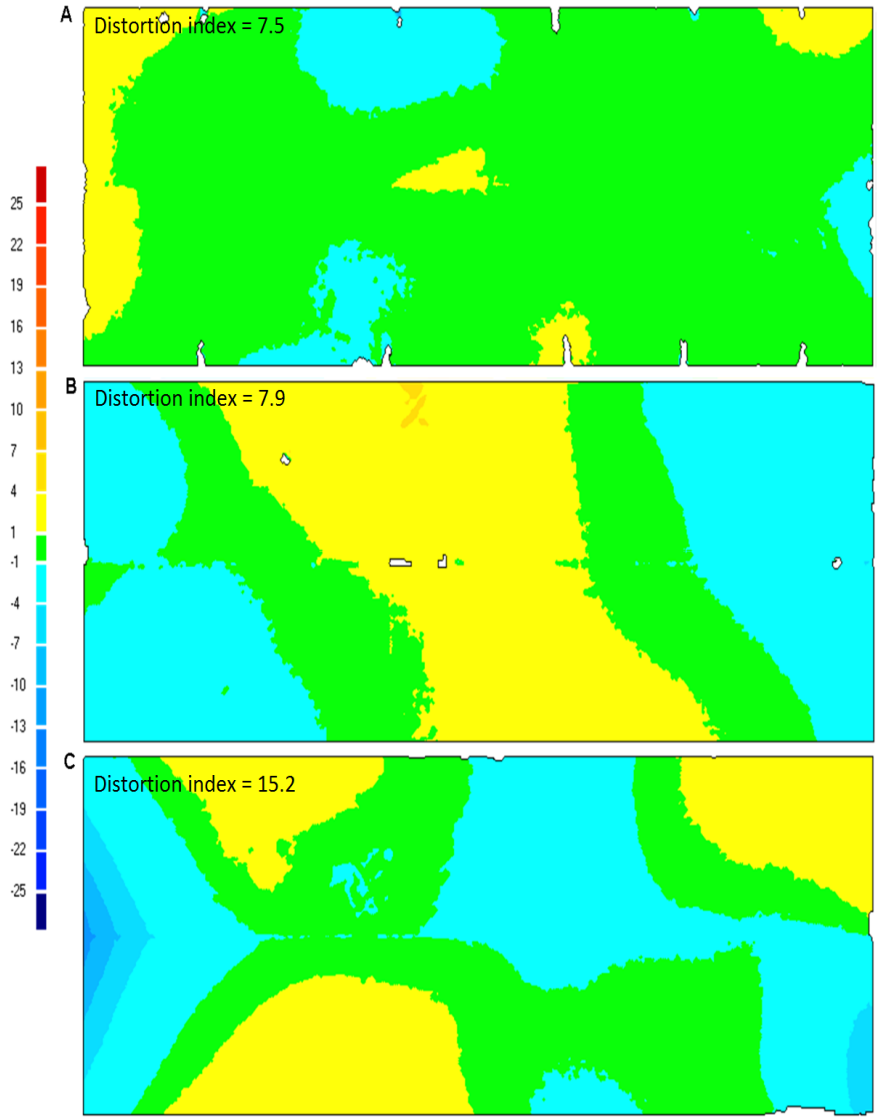

Figure 7.11. *The out-of-plane deformation of AH36 plate for several stages of production in test 6: (a) the initial deformation after tack welding, (b) the out-of-plane deformation after side heating during welding of the first pass and (c) the final out-of-plane deformation after conventional welding of the second pass (without side heating). The scale is -25 mm to +25mm.*

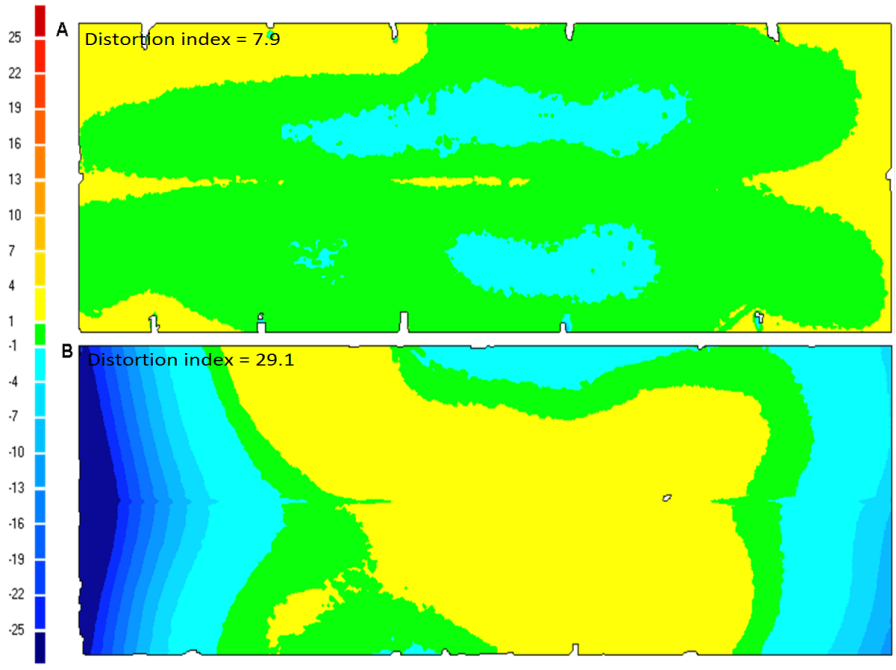

Figure 7.12. *The out-of-plane deformation of AH36 plate for different situations in test 7: (a) initial deformation after tack welds, (b) the final out-of-plane deformation after side heating during conventional welding of the two passes with burners with 45° to the weld centre line. The scale is -25 mm to +25mm.*

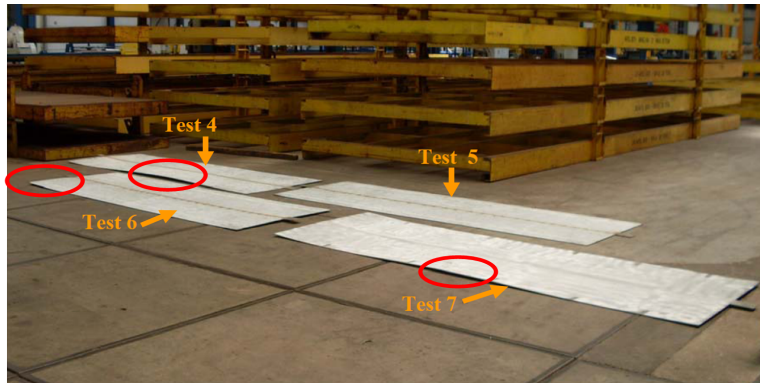

Figure 7.13. *AH 36 plates after Test 4, Test 5, Test 6 and Test 7. The red circles show the position of the maximum out-of-plane deformation of the plates.*

7.4 Conclusions

From the results, the following conclusions can be drawn:

1. Side heating during submerged arc welding reduces out-of-plane deformation of large panels of 6 mm thick AH36, considerably.
2. Simplified numerical models can be used efficiently to predict suitable positions of the burners in order to reduce the final out-of-plane deformation of the plate.
3. Side heating should be applied preferably during each welding pass, to obtain full benefit.

Reference

[1] P. Romero, N. Otero, A. Lopez, J. Otero, *Experimental comparison and analytical modelling of different industrial heating sources for thermal forming*, Proceedings of 3rd International Workshop on Thermal Forming and Welding Distortion IWOTE 2011, Bremen, pp. 121-132, 2011.

[2] http://www.3dscanco.com/products/3d-scanners/3d-laser-scanners/handyscan-3d/exascan.cfm

Chapter 8

General discussions

In the previous chapters, conventional welding and welding with additional heating were studied experimentally and by means of numerical models. In this chapter, the information already given is combined in a discussion of general features of welding with additional heating.

The first part of the chapter evaluates the experiments and the experimental results, while the numerical methods and results are discussed in the second part. The validated models are used to check the influence of process parameters for welding with additional heating on the final out-of-plane deformation. The results of these predictions are shown and considered in the third part of the chapter. The effects of the material properties on the final deformation are discussed in the subsequent sections. Transient Thermal Tensioning is compared to Side Heating during welding and different mechanisms of distortion reduction are explained in the last section of the chapter.

8.1 Discussion and comments on the experiments

It was explained that during conventional welding, non-uniform expansion and contraction of the weld and the surrounding material caused a permanent change in shape of a component (or instability), which is called welding distortion (or deformation). Different types of welding distortion may occur at the same time. One of the in-process strategies to reduce welding distortion employs two additional heating sources together with the welding source which is referred to as welding with additional heating. If the additional heaters are located close to the welding torch and contribute to the thermal field of the welds, the process is called Transient Thermal Tensioning. If there is no interference to the thermal field of the weld, the process is called Side Heating.

As shown in **Chapter 1**, three case studies were defined for laboratory tests and

one case study was arranged for industrial implementation. The experiments consisted of two main tracks: conventional welding and welding with additional heating. All welding tests were performed in a consistent manner. For example, the positions of the tack welds and the clamping bars together with the way of clamping and releasing of the clamps (the time and the sequence of clamp releasing) were the same throughout all the experiments. Therefore, it is expected that the deviations in the clamping forces are low, although the clamping forces during both conventional welding and welding with additional heating experiments were not measured. The results showed sound welds both in the conventional welding and the welding with additional heating tests.

During welding with additional heating, many tests were performed to find cases with distortion reduction in comparison to the distortion after conventional welding. The starting point of the trials was based on previously published literature. The detailed information of the experiments is given in **Chapter 5**. The out-of-plane deformation of the plates was measured before and after conventional welding and welding with additional heating in order to find the minimum distortion conditions. The out-of-plane deformation of welded plates was investigated using a distortion index, defined as the difference between maximum and minimum out-of-plane deformation of a plate. This definition makes the comparison between conventionally welded plates and welding with additional heating easy. However, as depicted schematically in **Figure 8.1**, for both cases A and B the distortion index is the same but the deformation modes are completely different. Therefore, other criteria (distortion contour) are used to gain a better understanding of the distortion modes.

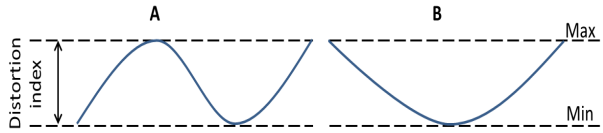

Figure 8.1. *Schematic presentation of similar distortion index, but different deformation modes.*

For the minimum distortion conditions obtained (for different materials), the temperature was measured using thermocouples on the underside of the plate during conventional welding and welding with additional heating. The errors in the temperature measurements related to the position of the thermocouples are small because the exact position of the thermocouples was measured before and after the experiments.

Since it is not possible to measure the temperature of the positions beneath the burners on the top surface (due to practical limitations, such as the attachment of thermocouples), the exact maximum temperature is not determined during welding

with additional heating for the region beneath the burners. However, numerical models developed in this investigation can be very useful for this purpose.

In some experiments with additional heaters, the temperature of the plate at the underside surface beneath the burners is different for the right and left burners. The maximum deviation is around 50 ^{o}C. A slight change in the acetylene and air mixture or the distance of the burners to the plate can lead to such variations. With the experimental facilities shown in this investigation, it was very difficult to eliminate such variations.

Comparing the thermal field during conventional welding and welding with additional heating, it is clear that the main characteristic of the thermal field of welding with additional heating is the creation of two hot zones at positions beneath the heaters. Results showed that the temperature of the weld is not influenced by the heaters for the cases with minimum distortion during welding with additional heating for all three materials. **Figure 8.2** shows schematically the maximum temperature obtained during welding (**Figure 8.2a**) and welding with side heating (**Figure 8.2b**) for different positions from the weld centre line. As shown in **Figure 8.3**, if the burners are very close to the welding torch, the two thermal peaks are close and contribute to the thermal field of the weld.

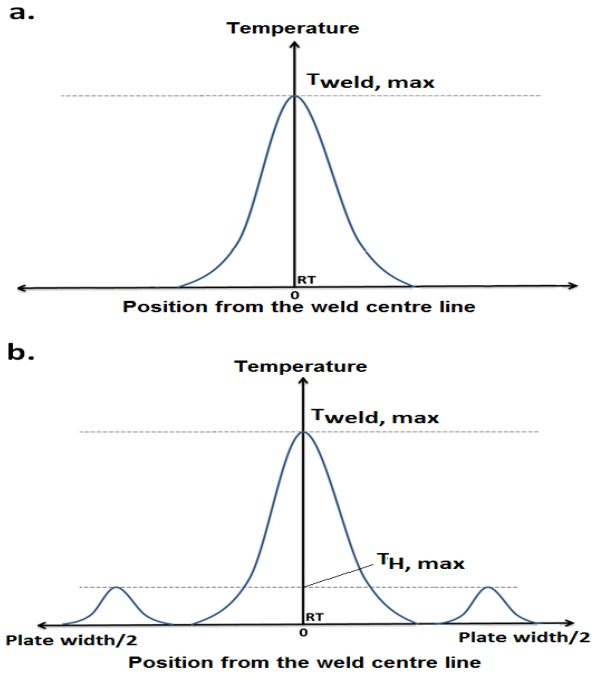

Figure 8.2. *Schematic representation of the maximum temperature during conventional welding and welding with side heating. RT is the room temperature.*

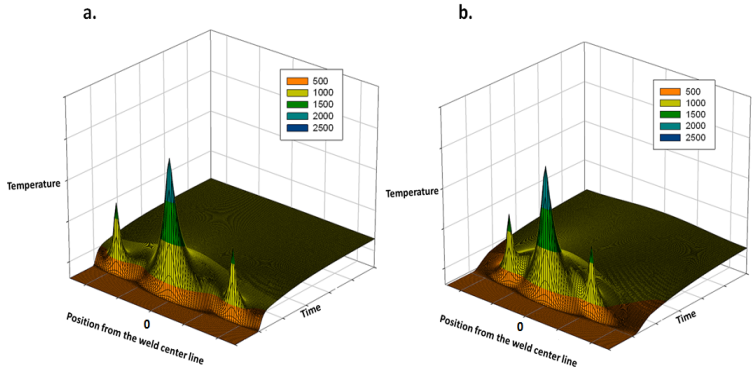

Figure 8.3. *Schematic representation of the thermal field during welding with additional heating where the burners are moved from (a) the edges toward (b) the region close to the welding torch for single nozzle burners.*

Figure 8.4 shows a schematic representation of the temperature profile for a point beneath the burners during welding with additional heating. The maximum temperature obtained during the process is T_{max} and the heating time to reach this maximum is defined by t_H. The maximum temperature depends on the burner settings (gas flow, pressure), the heating speed, the distance of the burners to the plate and the thermal material properties. The heating time (t_H) depends on the length of the burners, the travel speed and the material properties.

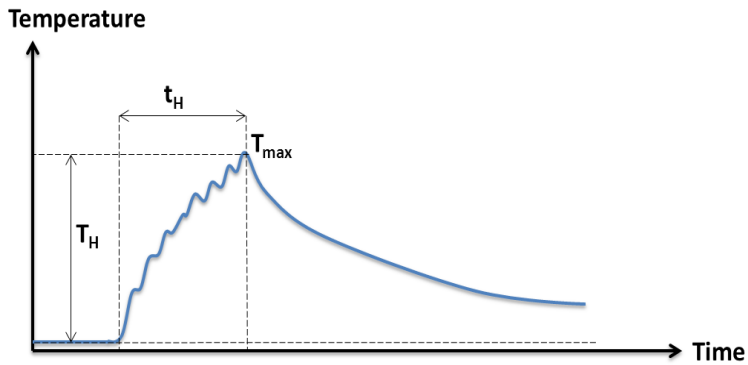

Figure 8.4. *Schematic representation of the temperature profile for the points beneath the burners during welding with additional heating.*

The temperature of the weld region (including the HAZ) remained unchanged when additional heating is applied for all materials. For the regions beneath the burners, microstructural changes may occur depending on the materials welded. In DP600, a hardness reduction was observed, which is attributed to tempering of the martensite.

In the case of AH36 steel, a slight reduction of hardness (around 5%) was seen. It is expected that such a reduction is due to the re-crystallization phenomenon. The temperature measurement at the underside surface of the plate showed a temperature of 240 ^{o}C. Since the thickness of this material is 6 mm, a high temperature is expected at the top surface of the plate beneath the burners (610 ^{o}C in the simulation). The two factors required for re-crystallization, the high temperature and the heating time (53 s), are both available during welding with additional heating.

The thermal history of conventional welding results in longitudinal residual stresses in the weld zone and compressive stresses further away. The thermal history of welding with additional heating results in the formation of tensile stresses along the line beneath the burners with compressive stresses in the surrounding area.

The samples used for residual stress measurements were exactly the same as the samples used for temperature measurements and the distortion measurements. Residual stress measurements were performed on the plates by means of the neutron diffraction. The uncertainties in the residual stress results are related to many factors summarized as:

- The errors in the sample positioning;
- The material texture and the grain size;
- The errors in the calculation of the residual stresses (like the plane specific elastic constants and the fitting equations);
- The assumption of a bi-axial stress state;
- The errors involved in the stress free lattice spacing and
- Human related errors.

Although there were many sources of errors in the measurements and challenges in the burner fuel mixture settings; the results of the experiments showed that distortion can be reduced by welding with additional heating. It was observed that the thermal field of the welds are not influenced by the heat generated by the additional heaters. It was also found that welding distortion can not be reduced when the additional heaters are located close to the welding heat source (using the burners shown in **Chapter 4**).

8.2 Discussions and comments on the numerical modelling

In order to investigate the influence of additional heating during welding on the thermal, the microstructural and the mechanical fields, 2D and 3D finite element models were constructed and extended. The numerical approaches used are explained

in **Chapter 3** and the results of the models were compared with the experimental results and discussed in **Chapter 6**.

The starting point of the simulation was conventionally welded plates and the cases where a minimum distortion after welding with additional heating was obtained experimentally.

In the thermal modelling of conventional welding of all materials, the main sources of uncertainties were classified as:

- The thermal material properties at elevated temperatures;
- The heat transfer coefficients by convection and contact;
- The emissivity of the material as a function of temperature and surface condition and
- The efficiency of the welding process.

The predicted temperatures of the conventionally welded plates were in good agreements with the measurements for all three materials. Therefore, it is concluded that the assumptions used in the models are valid.

Beside the parameters addressed above, in the thermal modelling of welding with additional heating of all materials, the main sources of uncertainties are classified as:

- The efficiency of the burners and
- The power distribution by the burners.

The only difference between conventional welds and welds with additional heating in the thermal models was the simulation of the heat sources. As explained in **Chapter 6**, eight circular Gaussian heat flux distributions have been used to model the heat flux during welding with additional heating. The use of such an assumption showed a small deviation from the measurements. The eight peaks observed experimentally in the temperature profile of the points beneath the burners are not captured in the models, but the maximum temperature obtained, the heating and the cooling rates are in acceptable agreements ($\leq 15\ ^{o}$C and $\leq 14\%$).

The microstructure modelling is very challenging due to the presence of many material parameters which are very difficult to obtain experimentally, *i.e.*, the parameters related to the solid state phase transformations when internal and external stresses are present. The effects of solid phase transformations on the welding distortion were investigated for conventional welding of DP600 plate and it was found that such effects are around 9%. The calculation time and the risks of divergence were considerably higher (by factor of 3.35, for calculation time) for the models including those effects.

The modelling of solid state phase transformations deals with micro scale phenomena, while the effects of those transformations on residual stress and distortion are on a macro scale (in this study). For other situations (DP600 welding with additional heating, AH36 conventional welding and welding with additional heating), the simulations excluded the microstructure modelling part. Since the temperature of the heated area by the burners is not high enough for significant solid state transformations and the volume (at the weld region and the HAZ of welding) in which solid state transformations take place is small compared to the volume of the rest of the plate, such assumptions do not lead to significant deviations between the predictions and the measurements. It should be added that the errors in the residual stress measurement for the area with solid state phase transformations are increased and therefore such measurements are not very reliable for validation.

It was seen from the measurement results that the side heating of AH36 plate does not lead to visible tensile peaks at the positions beneath the burners in the longitudinal residual stress profile. This was attributed to the microstructural phenomenon like re-crystallization. Such microstructural phenomenon cannot be represented by the models adopted in this investigation (**Section 3.3**). For such a purpose, for example, a model including re-crystallization should be developed.

The sources of errors in the microstructure modelling are classified as:

- The transformation temperatures;
- The amount of volume change due to solid phase transformations;
- The change of material strength due to the formation of hard phases and
- The phase fraction equations.

As stated in **Chapter 3**, the mechanical analysis uses the results from the thermal analysis as input files and the main outputs are the residual stress and the distortion predictions.

In the mechanical field for all materials studied, the following sources of errors are expected:

- The mechanical material properties at elevated temperatures;
- The plastic strain reset;
- The work hardening of the material at elevated temperatures and
- The clamping pressure and the manner of releasing the constraints.

The predicted results of the residual stresses in conventional welding of AISI-316L are close to the measurements ($\leq$ 50 MPa) but for welding with additional heating, there are some deviations between the measurements and the predictions. The deviations

are attributed to the number of errors involved in welding with additional heating, for example the effects of the mechanical material behaviour at high temperature and the clamping behaviour (and pressure) on the final deformation are more significant in welding with additional heating than in conventional welding. Besides these errors, another deviation source between the experimentally obtained results and the predictions in the case of welding with additional heating is related to the fact that the temperature gradients beneath the burners are not captured in the models (shell elements used in the model). Such gradients may cause angular deformation and after releasing the clamps, these localized deformations may change the final deformation of the plate.

Comparing the numerical results and the measurements for conventional welding of AH36, it is seen that the predicted deformations are close to the experimental measurements for the points at the middle part of the plate. At the plate edges, there is a deviation. Since, the predicted thermal field was in good agreement with the experiments and the microstructural field is excluded from the model, the main source of the deviation is related to the mechanical field. Although, the sources of deviations explained for AISI-316L are valid here as well, there is another issue for AH36 which is less significant for AISI-316L. The modelling of clamps consists of series of springs with different stiffnesses. When the plate is thin (for example in the case of DP600 or AISI-316L), the springs can control the movement of plates (shell elements have been used) and the results are close to practice (through thickness strains can be ignored). If a plate is thick (like AH36), the constraints on the top and on the underside surfaces influence the final distortion. The main reason for different behaviour on the top and on the underside surfaces is related to the temperature gradient in the through thickness direction. In this situation, the clamps constrain the movement of the underside surface. By releasing the clamps, the residual stresses are redistributed and the plate is deformed to its final shape. For better modelling of clamps in thick materials, the constraint should be modelled using contacts at both top and underside surfaces.

As indicated in previous chapters, the main focus of this study was on the longitudinal residual stresses. It was explained that these stresses are the greatest when compared with other directions. However, using only the longitudinal residual stress can lead to some deviations between the measurements and the predictions, as explained in **Chapter 5** and **Chapter 6**. Since the models were also validated based on the distortion field and the thermal field, such deviations are small.

The models developed in this study show a good agreement with the experimental results and are used to study the mechanisms responsible for distortion reduction when additional heating is used.

8.3 Influence of process parameters on the deformation

In this section, a developed and validated model is used to investigate the influence of process parameters during welding with additional heating on the final out-of-plane deformation. Since the distortion reduction was significant in the experiments for DP600 steel plates and the calculation is fast for this material, all calculations in this section are performed for DP600 steel. The effect of solid state phase transformations is excluded from the calculations. The welding parameters as well as the clamping conditions are kept constant.

The main parameters involved in welding with additional heating can be summarized as (see **Figure 8.5**):

- The distance of the burners to each other;
- The distance of the burners to the welding heat source;
- The parameters related to the shape of the burners, such as:
  The length of the burners, the width of the burners, the radius of the nozzles, the inter-distance of the nozzles, the number of the nozzles;
- The maximum power of the burners and the distance of the burners to the plate.

It was shown in the previous chapters that the burners contain eight nozzles of 20 mm diameter with inter distance of 30 mm. The total length of the burners was 240 mm while the total width of the burners was 27 mm. For modelling purposes, it is assumed that the width of the burner is twice the radius of the nozzles.

A very rapid method for predicting residual stresses is shown by Van der Aa [1] using 1D bar models. Selecting an appropriate number of bars and spring stiffnesses between the bars, result in a very good approximation of the residual stresses compared to the experiment and very short computational time compared to 2D and 3D FE models. However, the model cannot predict the distortion of the plates after welding. In this section, in order to study the effects of the process parameters involved, the 2D numerical model developed for stress and strain predictions in DP600 steel plate after conventional welding and welding with additional heating explained in **Chapter 3** is again used.

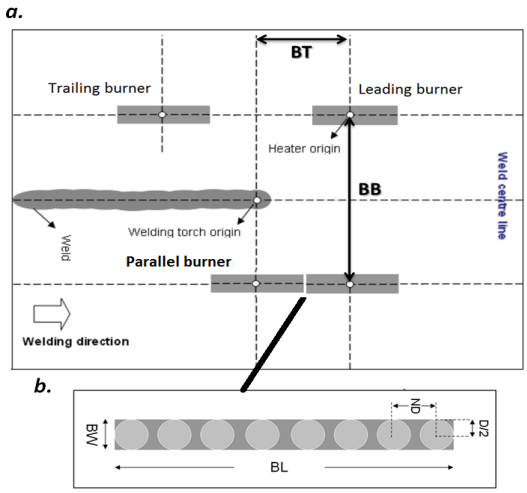

Figure 8.5. *The parameters involved in side heating and (b) the shape of the side heaters.*

8.3.1 Burner separation distance

Figure 8.6 shows the influence of the separation distance of the burners on the final distortion index for DP600 steel plate. The burners are positioned 145 mm leading the welding torch. Other process parameters are the same for different points in the figure (for example, the intensity). In the figure the results of the predicted distortion index are shown as a function of the separation distance of the burners; moreover, the figure also shows the experimental results.

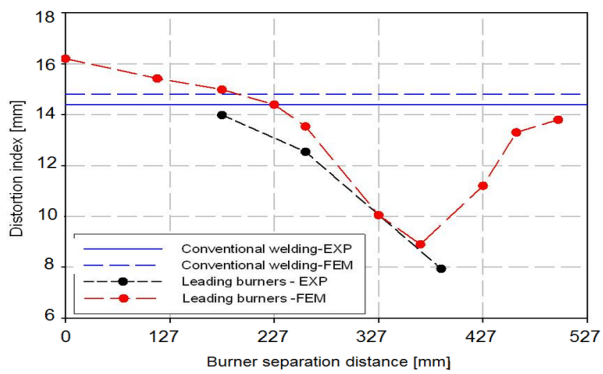

Figure 8.6. *The effect of the burner distance to the weld centre line on the distortion index for DP600 steel plate.*

When the burners are close to each other, the maximum distortion index is obtained. This is mainly because of the contribution of the generated heat by the burners to

the welding thermal and mechanical fields. In this case the distortion index is higher than that of conventional welding.

By increasing the distance between the burners, the distortion index decreases first and then it starts increasing again. When the burners are located 118 mm from the weld centre line, the distortion index is reduced because of the cooling influence of the clamps. In the thermal model, the clamps are modelled as heat losses by a contact heat transfer coefficient. The generated heat by the burners in this region is thus reduced by the clamps and therefore the predicted distortion index is close to the conventional welding case.

If the distance between the burners increases, the thermal contribution of the burners to the thermal field of the weld zone is reduced and therefore, the main reason of distortion reduction is not related to manipulation of the thermal field of the weld zone. For the case shown in **Figure 8.6**, the optimum position for the burners is predicted to be around 183.5 mm from the weld centre line. In the experiments, the lowest distortion was found when the burners were located at 193.5 mm from the weld centre line.

Further increasing the distance between the burners increases the distortion index. The main reason is that the edges of the plate are able to move freely. When the burners are applied, the plate beneath the burners can move more easily in this case compared to the other situations.

8.3.2 Distance of the burners from the welding torch

In this section a case study is performed in order to find out the effects of the distance of the burners to the welding torch on the distortion index for DP600 steel plate. All process parameters and the numerical inputs are the same as the case explained in previous chapters. The burners are located 193.5 mm from the weld centre line at different positions relative to the welding torch in the numerical models. The results of the predictions are shown and compared to the experimentally obtained results.

Figure 8.7a shows the effects of the burners distance to the welding torch on the distortion index both in the experiments and the numerical models. It is clear from the numerical results that if the burners are located far behind or in front of the welding torch, the distortion index increases and the locations close to the welding torch are the best places to install the burners. However, for all points distortion reduction can be seen.

When the burners are located far behind the welding torch, the weld has enough time to cool. When the weld has been cooled, the welding tensile stresses have been formed at the weld centre line and the compressive stresses have been created at the plate edges. In this situation, during side heating when the burners arrive, the com-

pressive stresses generated by the burners are added to the compressive stresses of the welding process and can reach the yield point of the material. Therefore, the final out-of-plane deformation of the plate increases. This is also true when the burners are far in front of the weld, in which the compressive stresses due to the weld are added to the pre-existing compressive stresses due to the burners.

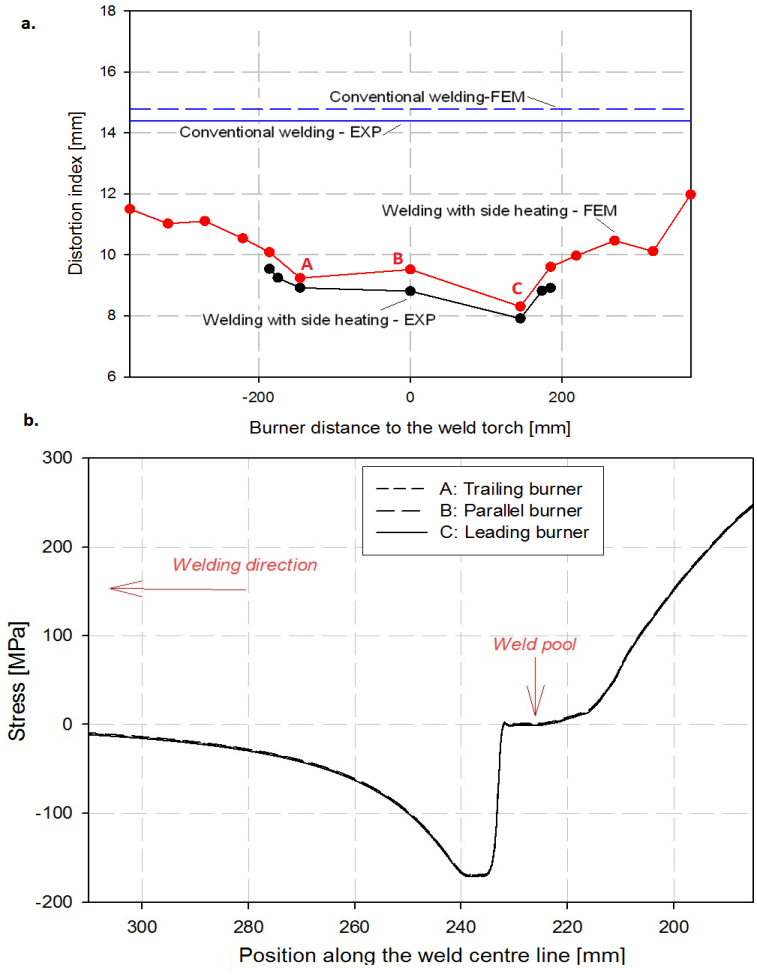

Figure 8.7. *(a) The effect of the burner distance to the welding torch on the distortion index for DP600 steel plate and (b) the stresses along the weld centre line for different burner positions (A:Trailing, B:Parallel and C:Leading burners).*

It can be seen from the figure that minimum distortion index can be obtained where the burners are placed in front of the welding torch. In order to check if the stresses along the weld centre line are different for burner positions relative to the welding

torch, three points are selected (A: Trailing, B: Parallel and C: Leading burners, see **Figure 8.7a**). The stresses along the weld centre line for these points are plotted in **Figure 8.7b**. It is clearly seen that there is no influence of the burner locations relative to the welding torch on the stresses along the weld centre line. In **Chapter 6** (**Figure 6.21**), it was shown that there are some slight changes on the tensile longitudinal residual stresses at the position beneath the burners for different burner locations relative to the welding torch. The higher the peak, the less distortion is obtained. Therefore, the distortion index differences for different burner locations are attributed to the residual stress distribution for the regions beneath and adjacent to the burners (and not the stresses of the weld zone).

It is concluded that side heating is more sensitive to burner separation distance than the distance between the burners and the welding torch. When side heating is applied at the appropriate position to the weld centre line during welding, the distortion of plates can be reduced. It should be added that if the burners are applied (in a suitable location) before or after welding, the final deformation of the plate is reduced but not as significant as for the case in which the burners are applied during welding. This is attributed to the tensile peaks that form at the location beneath the burners. When such peaks are present in the longitudinal residual stress profile, the plate distortion is reduced regardless of the position of the burners relative to the welding torch. All results are valid if the plates are in the clamped condition when welding and side heating are applied. When the weld has been cooled, it is recommended to place the burners on the weld centre line (also reported in [2]). Since, for the regions beneath the burners, compressive stresses are formed during the heating cycle, tensile stresses in the weld will be reduced and therefore less residual stresses will remain.

8.3.3 Burner shape

The length of the burners (BL) is assumed to be equal to:

$$BL = (j - 1) \times ND + D; \tag{8.1}$$

in which j is the number of the nozzles, ND is the inter-distance of the nozzles and D is the diameter of the nozzles. The width of the burners is assumed to be the same as the diameter of nozzles.

A change in the shape of the burners causes a change in one of the parameters in the **Equation 8.1**. As stated before, the eight peaks in the temperature profile during side heating experiments at the place of the burners cannot be modelled using the strategy explained in **Chapter 3**. Therefore, a 20% change of the distance between the nozzles will not change the out-of-plane deformation of the plate.

When the number of nozzles is constant, any change in the length of the burners means a change either in the diameter of the nozzles or in the distance between the nozzles.

When the generated heat for each nozzle is constant and the diameter of the nozzles increases, the heat flux is reduced. The maximum temperature will decrease and in the residual stress profile, the width of the tensile zones at the position of the burners will change. A 20% change in the nozzle diameter can change the heat flux by a factor of 1.5. **Table 8.1** shows the effect of 20% variation of the width of the burners on the final out-of-plane deformation of DP600 steel plates. If the diameter is very wide then the heat flux is reduced and the effect of the side heating burners (tensile stress peaks) is reduced and the final deformation is increased. When the diameter is reduced, the generated heat is localized and at that location beneath the burners high plastic deformation takes place and the final deformation increases again.

Table 8.1. *The effect 20% variation of the burners shape on the out-of-plane deformation of DP600 steel plate.*

Condition	**Maximum out-of-plane deformation [mm]**
Conventional welding	14.8
Side heating - reference	8.3
Side heating 20% larger D	10.8
Side heating 20% smaller D	9.7

Table 8.2 shows the effect of the number of nozzles on the final out-of-plane deformation of DP600 steel plate. By increasing the number of the nozzles and keeping the heat flux density of each burner constant, the total heat generated is increased. This means the maximum temperature obtained is increased. Another point here is related to the heat pattern by the nozzles. When just one nozzle is used the heat flow is almost identical in all directions. However, using an eight nozzle burner produces a rectangular heat flow. The heat in this case flows more in the width direction of the burner than the length direction.

Table 8.2. *The effect of the number of nozzles on the out-of-plane deformation of DP600 steel plate.*

Condition	**Maximum out-of-plane deformation [mm]**
Conventional welding	14.8
Side heating eight nozzles	8.3
Side heating four nozzles	10.6
Side heating one nozzle	14.8

It was shown in the experimental and the numerical results that when side heating during welding, the tensile peaks generated for the region beneath the burners lead to distortion reduction. In order to create such peaks, a specific temperature profile has to be obtained on the plate beneath the burners. **Figure 8.4** shows such a temperature profile schematically. In that profile, a heating time and a maximum temperature are required. If the heating time and the maximum temperature are

enough then the number of nozzles or the length of the burners or the distance of the burners to the plate do not play a role in the distortion reduction. This is also true for the power of the additional heaters. If the heating power of the burners leads to such a temperature profile, distortion can be reduced. If the power is too high, more plastic deformation can occur and distortion increases. If the power is too low, the maximum temperature required is not achieved.

Since it is easier in the numerical models to vary the position of the burners compared to the experiments, a series of calculations was run in order to find a suitable position for a single nozzle burner. For this purpose, a similar heat flux to the eight nozzle burners was used in which a single nozzle burner and the distance of the burners to the welding torch and the weld center line were changed until a distortion reduction similar to the eight nozzle burners was achieved. The results are shown in **Table 8.3**.

Table 8.3. *Comparison between eight and single nozzle burners.*

Condition	Max distortion [mm]	Burners separation	Burners to the welding torch
Eight nozzle burners	8.3	387 mm	+145 mm
Single nozzle burners	8.3	80.2 mm	+70 mm

It can be seen from the table above that it is possible to reduce welding distortion using single nozzle burner. However, in this situation the burner should be located close to the welding torch and therefore the final residual stress distribution for this situation is not similar to the eight nozzle burner configuration explained in previous chapters. For the single nozzle burner located close to the welding torch, the thermal field of the weld is affected by the heat generated by the burners. An example of such localized burners can be achieved by the use of laser beams. Preston *et al.* [3] demonstrated the use of laser heating during welding to reduce welding distortions.

8.4 Sensitivity analysis

In this section, the effects of the thermal diffusivity (k_a), the thermal expansion coefficient (α) and the yield stress (σ_y) on welding distortion and the effects of side heating are discussed, followed by the role of the plate thickness and the initial plate deformation on the final out-of-plane distortion.

In the developed 2D model, the material properties are changed by factors of 0.5 and 2 and the out-of-plane deformation of the plate (W) is compared as shown in **Figure 8.8**. When changing of one of these parameters, the other parameters remained unchanged.

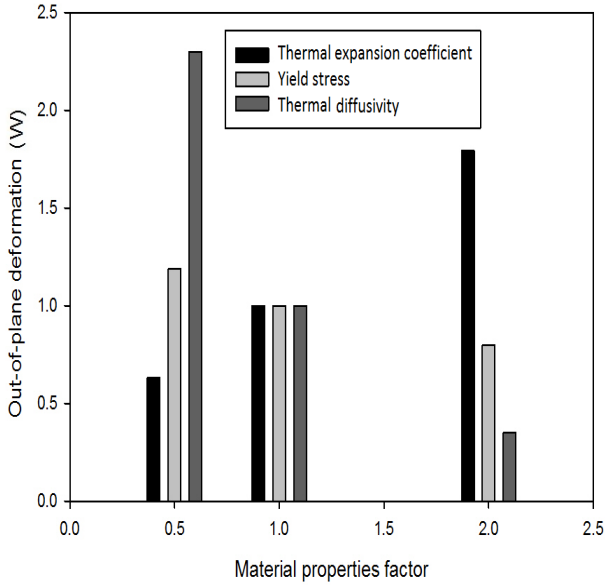

Figure 8.8. *The effects of the thermal diffusivity, the thermal expansion coefficient and the yield stress on the final out-of-plane deformation of a plate.*

As can be seen from the figure, a material with a high thermal diffusivity, has a lower final distortion compared to a material with a low thermal diffusivity. During welding with side heating of this material (with high thermal diffusivity) the temperature obtained (when the burner power is constant) is lower and therefore, the burners should be placed closer to the weld centre line compared to a material with lower thermal diffusivity.

A material with high thermal expansion coefficient, expands more during heating (and shrinks more during cooling) and the final distortion is higher than a material with a lower thermal expansion coefficient. During side heating of such a material (high thermal expansion coefficient), more expansion occurs beneath the burners during heating and plastic deformation can occur at the heated region. The reduction of distortion using side heating in this situation is challenging and needs less heating power.

The higher the yield stress of the material, the lower is the distortion. A higher yield stress makes higher residual stresses possible. Materials with a low yield stress deform more easily than materials with a high yield stress. During side heating of a material with a lower yield point, the power of the burners should be set in such a way that excessive plastic deformation does not occur.

In a thicker plate, the generated heat (either by welding heat source or additional

heaters) dissipates faster than in a thin plate. In general, the out-of-plane distortion of thick plates is less than of thin plates; however, this depends on the type of deformation. One of the main deformation types for thick plates is angular distortion. During side heating of thick material a higher power is needed.

Table 8.4 shows the effects of the initial deformation of a plate on the final out-of-plane deformation after welding. The calculations are based on the model developed and validated for DP600, excluding the microstructure field. In the model, the plate is bent with a deflection height of 0.5 mm and 1 mm and is clamped before welding. The results of the distortion index after welding are compared to that of a plate without any initial distortion (flat plate). It can be seen that the pre-deformation of the plates increases the final plate deformation after welding. In this study only bending deformation was considered. In general, the type of distortion of the initial plate is as important as the magnitude of the initial deformation. As shown in **Figure 2.18**, the initial distortion of a plate can be such that after welding, the final distortion is reduced.

Table 8.4. *Effect of the initial deformation of a plate on the final out-of-plane deformation after welding and side heating.*

Conditions	Distortion index after welding [mm]
Initial distortion of 0 mm - Flat plate	14.8
Initial distortion of 0.5 mm (Bending)	15.5
Initial distortion of 1 mm (Bending)	16.9

8.5 Mechanism of distortion reduction

Transient Thermal Tensioning

Thermal tensioning is a group of in-process methods to reduce welding distortion. In **Chapter 2**, a review of published research about these methods is presented. Unfortunately, the amount of literature published about the mechanisms of these methods is limited. The lack of both understanding of the process and of predicting models are the main reasons why these techniques have not yet been implemented extensively in industry. In this study explanation of the distortion reduction mechanisms during welding with additional heating (side heating and transient thermal tensioning) is discussed.

It was mentioned that side heating refers to the process of heating during welding in which the burners are positioned leading, trailing or parallel to the welding torch but further from the weld centre line than in transient thermal tensioning. The thermal field of the weld in transient thermal tensioning is influenced by the thermal field generated by the burners.

The specific and essential feature of TTT is to provide a desired tensioning effect during welding to prevent welding distortion. Efforts for this method [4-8] mainly focused on buckling distortion. It has been reported that the higher the tensioning stress on the weld, the better the results of buckling distortion control. The tensioning effect becomes stronger as the temperature gradient increases, while the distance of the additional heating sources to the weld centre line decreases [8].

Figure 8.9 shows the longitudinal stresses along the weld centre line during conventional welding and transient thermal tensioning when the burners are located in front of the welding torch. As can be seen from the figure, in transient thermal tensioning, the weld is under tensile stresses. These stresses are formed by the leading burners. The transient compressive stresses along the weld centre line are reduced and when the weld has cooled, relative low tensile stresses have been formed. The mechanism of distortion reduction in this case is related to lower transient compressive stresses along the weld centre line. This is also valid for the parallel burners.

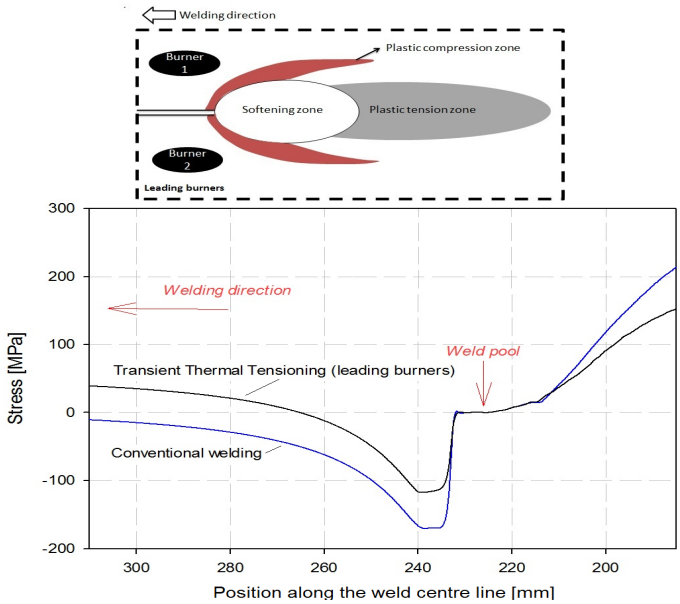

Figure 8.9. *The longitudinal stresses along the weld centre line during conventional welding and transient thermal tensioning using leading burners.*

Figure 8.10 shows the longitudinal stresses along the weld centre line during conventional welding and transient thermal tensioning when the burners are located trailing the welding torch. As can be seen from the figure, the weld is under tensile stresses during cooling. Those stresses are more pronounced in transient thermal tensioning. The transient tensile stresses along the weld centre line are increased until yielding occurs. The mechanism of distortion reduction in this case is related to the increase of

the transient tensile stresses along the weld centre line to the yield point and yielding of the weld metal during cooling.

For all burner locations, the distortion reduction mechanism in transient thermal tensioning is based on manipulation of the welding induced stresses (increase or decrease). It was mentioned in **Section 2.4.3**, that the relevant literature proposes three different mechanisms of distortion reduction by thermal tensioning methods:

(A) The redistribution and not a reduction of longitudinal residual welding stresses increase the critical buckling load. Therefore, buckling distortion is prevented [9-10].

(B) The compressive longitudinal welding stresses are reduced by means of the heat sources [3, 8].

(C) Thermal tensioning generates tensile stresses, which increase the tensile stress level in the weld zone. The stresses reach the yield stress of the material and therefore local plastic deformation occurs. During cooling the final residual stresses are reduced due to this plastic deformation [10-11].

According to this classification, the responsible mechanism of distortion reduction for transient thermal tensioning using leading (and parallel) burners can be classified as category B, while for trailing burners category C is applicable.

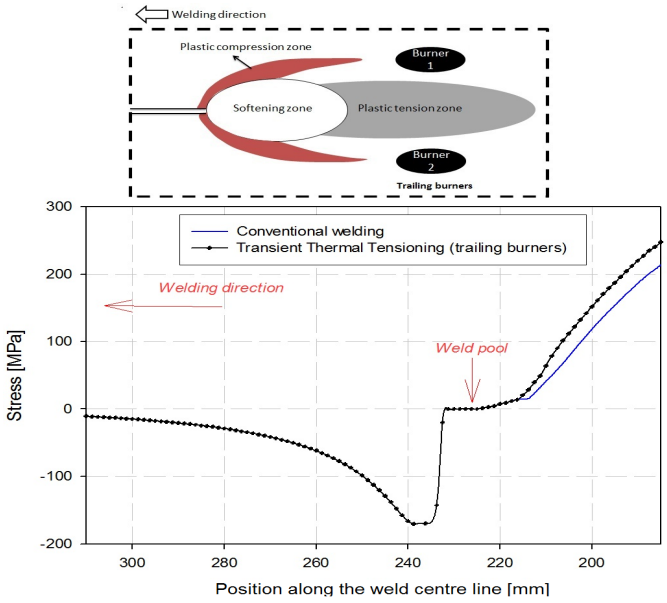

Figure 8.10. *The longitudinal stresses along the weld centre line during conventional welding and transient thermal tensioning using trailing burners.*

Side Heating

In 1990 a Japanese patent was filed [12] involving a method to prevent buckling distortions in welding of thin metal sheets using transient heating sources parallel to the welding torch (side heating). The method looks similar to transient thermal tensioning, but it reduces buckling by an entirely different mechanism. As indicated in **Chapter 2**, it was claimed that in this method the compressive residual stresses further away from the weld are reduced, which is the main reason for reduction of buckling distortion [8]. The reduction of buckling distortion using side heating has also been reported by Feng [9] and Yang [13]. Nagy [10] reported that when welding and side heating are applied simultaneously, opposite rotations of the plate occur and produce tensile stress peaks at the location of the burners. These additional tensile regions reduce buckling distortion.

In this study, it was shown that in side heating, the position of the burners relative to the weld centre line is more critical than the position of the burners relative to the welding torch. Moreover, the transient stresses along the weld centre line are not influenced by the stresses generated by the side heaters. During side heating, the plate is heated locally beneath the burners. These areas expand and shrink non-uniformly and therefore stresses are formed. Tensile stresses are formed at the positions beneath the burners. The area with tensile residual stresses (at the position beneath the burners) with side heating during welding tends to increase the strain required for out-of-plane deformation. The redistribution of final stresses (stresses formed due to the welding process in combination with the stresses formed due to the additional heating) reduce the final deformation of the plate.

Figure 8.11a schematically shows the plate rotations during conventional welding (No 1), and welding with side heating (No 2 and 3) in the heating cycle of the weld. In the conventional welding case, the fusion zone is expanding. In side heating during welding, the heated areas beneath the burners are either heating and expanding (No 2) or cooling and contracting (No 3), depending on the location of the burners. If the heated area is expanding together with the expansion of the weld region (No 2, for example side heating with parallel burners), the rotations of the plate at the weld zone and the two heated zones are in the same direction. Plastic deformation can take place in three regions, the weld region and the heated regions beneath the burners. The plastic deformation of the weld zone is much greater than in the other regions. If the heated areas beneath the burners are contracting during the expansion of the weld zone (No 3, for example side heating with leading burners), the rotations are opposite. Although the plastic deformation may occur in all three regions, the expanding of the plate during heating in this case is less than that of the conventional weld (No 1).

Figure 8.11b schematically shows the plate rotations during conventional welding (No 1), and welding with side heating (No 2 and 3) in the cooling cycle of the weld,

depending on the location of the burners. In the conventional welding case, the fusion zone is contracting. In side heating during welding, the heated areas beneath the burners are either heating and expanding (No 2) or cooling and contracting (No 3). If the heated area is expanding during the contraction of the weld region (No 2), the rotations of the plate at the weld zone and the heated zones are opposite, therefore, the out-of-plane deformation of the plate is reduce because of these opposite rotations. If the heated areas beneath the burners are contracting during the contracting of the weld zone (No 3), the rotations of the plate at the weld zone and the heated zones are in the same direction. Since the plate beneath the burners has been plastically deformed in the heating cycle, the out-of-plane deformation of the plate is less than that of conventional welding.

In conventional welding, the welded area is the only region where plastic deformation takes place. In welding with side heating, the weld region and the region beneath the burners are plastically deforming. The rotation of the plate in the weld zone and the heated zones during heating and cooling stages can be in the same or opposite direction.

It is shown by Masubuchi [4] that the Critical Buckling Load (CBL) for a welded plate with a non-uniform load depends on the width of the tensile region. The larger the width of tensile region, the larger the CBL becomes. During side heating, there are three regions with tensile peaks, two more than in conventional welding. Therefore, the width of tensile region is increased after side heating and the CBL will be larger than that of conventional welding. In other words, side heating reduces buckling deformation by increasing the CBL and not by the reduction of compressive stresses. This is in agreement with the results reported by Nagy [10].

The main focus of this study is on the out-of-plane deformation in general (combination of different types of distortion) and not on buckling distortion only. It was shown that the out-of-plane distortion can be reduced by the side heating. According to the classification presented before, the responsible mechanism of distortion reduction for side heating is under category A. The dimensions of the plates used in the industrial implementation experiments, shown in **Chapter 7**, are such that buckling is the dominant distortion type. Significant distortion reduction was shown in that case. If the dominant distortion type is buckling, the distortion reduction mechanism is still classified as category A.

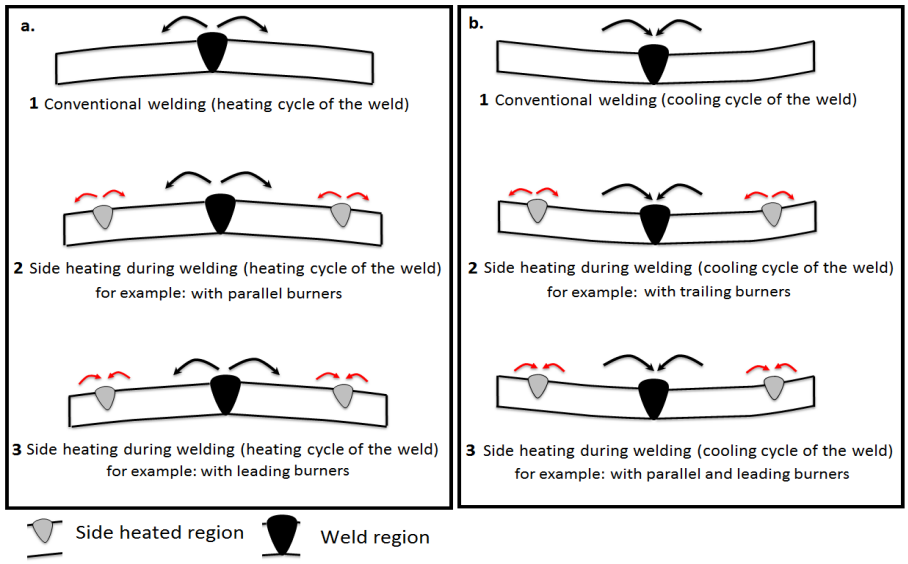

Figure 8.11. *The rotations of the weld and the heated zones during conventional welding and welding with side heating for (a) weld heating and (b) weld cooling cycles.*

In conclusion, **Figure 8.12** shows the classification of dynamic thermal tensioning using additional heaters including the mechanisms of distortion reduction based on the results of this thesis. Comparing side heating with different thermal tensioning (TT) methods [5-7, 14-18], the following additional benefits are summarized:

- Cheap and accessible tools (oxy-acetylene burners);
- No risk of the formation of hard constituents (like formation of martensite as a result of the LSND Active Cooling) for the region beneath the burner;
- Reduction of stiffeners needed in Shipbuilding and therefore cost reduction.

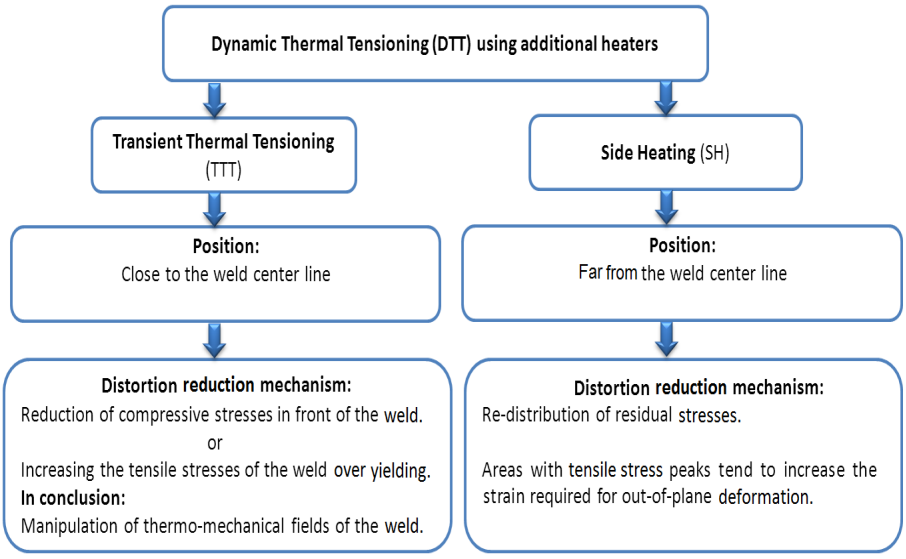

Figure 8.12. *Classification of thermal tensioning process using additional heaters.*

Reference

[1] E. M. van der Aa, *Local Cooling during Welding: Prediction and Control of Residual Stresses and Buckling Distortion*, PhD thesis, Delft University of Technology, 2007.

[2] D. Radaj, *Heat Effects of Welding: temperature field, residual stress, distortion*, Springer-Verlag, 1992.

[3] R. V. Preston, *Modelling of residual stresses in welded aerospace alloys*, PhD thesis, University of Cambridge, 2000.

[4] K. Masubuchi, *Analysis of welded structures: residual stresses, distortion and their consequences*, Oxford: Pergamon Press Ltd., Edition anonymous. 1980.

[5] Y. I. Burak, L. P. Besedina, Y. P. Romanchuk, A. A. Kazimirov and V. P. Morgun, *Controlling the Longitudinal Plastic Shrinkage of Metal during Welding*, Avt. Svarka (Automated Welding), Vol. 3, pp. 27-29, 1977.

[6] Q. Guan, *A Survey of Development in Welding Stress and Distortion Controlling in Aerospace Manufacturing Engineering in China*, Welding in the World, Vol. 43, No. 1, pp. 64-74, 1999.

[7] Q. Guan, D. L. Guo, C. Q. Li and R. H. Leggatt, *Low Stress Non-Distortion (LSND), Welding - a New Technique for Thin Materials*, Welding in the World (UK), Vol. c33(3), pp. 160-167, 1994.

[8] *Minimization of Welding Distortion and Buckling, Modeling and Implementation*, Edited by P. Michaleris, Woodhead Publishing, May 2011.

[9] Z. Feng, *Processes and Mechanisms of Welding Residual Stress and Distortion*, Woodhead Publishing Ltd, 2005.

[10] T. Nagy, *Investigation of thermal techniques to mitigate buckling distortion in welded panels*, Phd thesis, Cranfield University, 2012.

[11] N. A. McPherson, *Thin plate distortion - The ongoing problem in shipbuilding*, Journal of Ship Production, May 2007.

[12] S. Takeno, *Method for preventing welding distortion of sheet metals*, Japanese Patent JP 4052079, 20 February 1992.

[13] Y. P. Yanga and G. Juang, *Advancement in Prediction and Control of Welding Residual Stress and Distortion*, Materials Science Forum, Vols. 539-543, pp. 3943-3948, 2007.

[14] R. M. Dull, J. R. Dydo, J. J. Russell and J. Shanghvi, *Method of reducing distortion by transient thermal tensioning*, US Patent 6861617.

[15] J. Li, Q. Guan, Y. W. Shi and D. L. Guo, *Stress and distortion mitigation technique for welding titanium alloy thin sheet*, Science and Technology of Welding and Joining, Vol. 9, pp. 451-458, 2004.

[16] M. V. Deo and P. Michaleris, *Mitigation of welding induced buckling distortion using transient thermal tensioning*, Science and Technology of Welding and Joining, Vol. 8, No. 1, 2003.

[17] T. Nagy, S. Williams, P. Colegrove, C. Ikegu, I. Fafiolu, *Distortion mitigation in welded ship panels*, Proceedings of 2nd International Workshop on Thermal Forming and Welding Distortion IWOTE 2008, Bremen, pp. 265-275, 2008.

[18] J. Song, J. Y. Shanghvi, P. Michaleris, *Sensitivity analysis and optimization of thermo-elasto-plastic processes with applications to welding side heater design*, Computational Methods in Applied Mechanical Engineering, 193, pp. 4541-4566, 2004.

Chapter 9

General conclusions

Thermal tensioning using heating strategies (welding with additional heating sources) is one of the more promising in-process welding distortion control techniques and can be classified into two groups: Transient Thermal Tensioning (TTT) and Side Heating (SH). In this work, the process of welding with additional heating sources has been extensively investigated using numerical and experimental approaches. The thermal, microstructural and mechanical fields during conventional welding and welding with additional heat sources were examined by means of finite element models, and validated by comparison with experimental observation of temperature, distortion and residual stresses and microstructure investigations. The combined numerical and experimental approaches used in this thesis provide a better understanding of thermal tensioning using heating strategies during welding. The main conclusions of the investigation presented in this thesis are summarized here:

- The mechanisms of distortion reduction in side heating during welding are based on the formation of tensile stresses in the workpiece at positions beneath the burners. Such areas act as specific stiffening supports against possible deformation. The areas with tensile stress peaks in side heating during welding tend to increase the strain required for out-of-plane deformation. In other words, side heating during welding does not reduce but redistributes the residual stresses. Moreover, buckling deformation can be reduced by increasing the critical buckling load and not by the reduction of compressive stresses in side heating.

- From numerical predictions, it was found that the main mechanism of distortion reduction in transient thermal tensioning is based on the manipulation of the transient stresses along the weld centre line. The responsible mechanism for distortion reduction during transient thermal tensioning using leading and parallel burners is the reduction of the transient compressive stresses along the weld centre line. In the transient thermal tensioning using trailing burners, the responsible mechanism for distortion reduction is related to the increase of

the transient tensile stresses along the weld centre line to the yield point and yielding of the weld metal during cooling.

- Due to the complexity of stress and strain fields during conventional welding and welding with side heating (or transient thermal tensioning) and due to the number of parameters involved in these methods, in order to estimate the most appropriate position of the burners and the most appropriate process parameters, numerical modelling is required. Finite element models were constructed for simulation of thermal, stress and strain fields for both conventionally welded plate and plate welded with side heating (or TTT). The assumptions made in the high temperature material properties, plastic strain resetting and modelling of clamps and the side heaters resulted in some discrepancies between models and measurements but generally provided a good agreement.

- The important process parameters in side heating or transient thermal tensioning are the position of the heat source with respect to the weld centre line and the welding torch (leading, parallel or trailing), the heat source shape, size and intensity. In side heating during welding, a burner position relative to the plate edges can always be found at which distortion is at minimum. The position of the burners with respect to the welding torch (leading, parallel or trailing) in side heating is not as critical as the position of the burners relative to the weld centre line. By increasing the burner induced temperature in side heating, the out-of-plane deformation of the plate decreases. However, if the material is overheated during side heating the final out-of-plane deformation is increased.

- The thermal field generated by the welding process is not affected by the thermal field of the side heaters in side heating during welding of AISI-316L, DP600 and AH36 for the case with the experimentally obtained minimum out-of-plane deformation. The essential feature of welding with side heating is the creation of a temperature peak at the location beneath the burners. The temperature distribution in the weld zone and the HAZ (of welding) remains unchanged. Therefore, minor changes in microstructure and mechanical properties are observed. For example, the areas beneath the burners in DP600 showed a lower micro-hardness than the base metal. For AH36 steel plate, the top surface of the heated areas beneath the burners showed a re-crystallized microstructure, while the microstructure of the underside surface was not affected.

- A model was constructed to investigate the effects of solid phase transformations on the residual stress and distortion for conventionally welded DP600 steel. Two main effects of phase transformation are included: volume change and the increase of the yield strength due to the formation of hard phases. It was seen that the effect of volume change counteracts the effects of the strength increase. Phase transformations tend to reduce the tensile residual stresses in the fusion zone. The model including solid phase transformations predicts less out-of-plane deformation than the model excluding phase transformations and is in

closer agreement with experiments. However, phase transformation modelling increases the computational time and the risk of divergence.

Although significant distortion reduction was obtained using side heating during welding (by oxy-gas burners) of large plates in the shipbuilding industry, it is recommended to use induction heaters in order to have repeatable and robust heating strategies with more control on the generated power. Moreover, the development of simplified models is suggested to predict the position of the additional heaters to reduce welding distortion.

Summary

Distortion Control during Welding

The local material expansion and contraction involved in welding result in permanent deformations or instability *i.e.*, welding distortion. Considerable efforts have been made in controlling welding distortion prior to, during or after welding. Thermal Tensioning (TT) describes a group of *in-situ* methods to control welding distortion. In these methods local heating and/or cooling strategies are applied during welding. Additional heating and/or cooling sources can be implemented either stationary or in a transient state. In static methods, a pre-set temperature distribution is imposed on the workpiece, while in transient methods, the temperature depends on the position and the time.

The mechanisms of distortion reduction in thermal tensioning are complex. The complicated nature of welding stress and strain fields is increased by the large number of parameters involved in thermal tensioning. Type, intensity and characteristics of the additional heating and/or cooling sources play an important role in the development of the stress and strain fields during welding with thermal tensioning. The positioning of the additional sources with respect to the welding centre line and the welding torch are other critical parameters involved in thermal tensioning. In this work the focus is on dynamic method using heating strategies (welding with additional heating) and can be classified into two types, Transient Thermal Tensioning and Side Heating. If the additional heaters are located close to the welding torch and contribute to the thermal field of the welds, the process is called transient thermal tensioning. If there is no interference to the thermal field of the weld, the process is called side heating.

In this study, the thermal, the microstructural and the mechanical fields for both conventional welding and welding with additional heating were investigated by means of numerical models and by experimental methods including temperature, distortion and residual stress measurements and by microstructural investigations. The usage of both experimental and numerical work has provided valuable insight into welding with additional heating.

Three case studies were defined for laboratory tests (with different materials: AISI-

316L, DP600 and AH36 steels) and one case study was set for industrial implementation (AH36 steel). The experiments consisted of two tracks: conventional welding and welding with additional heating. Welding parameters were selected to obtain a sound weld. The parameters concerning the additional heating sources were systematic investigated. The conditions where deformation was reduced, referred to as 'experimentally obtained minimum distortion' were used for further study and to validate numerical models.

For the experimentally obtained minimum distortion (for different materials), temperature was measured using thermocouples at the underside of the plate during conventional welding and welding with additional heating. The out-of-plane distortions of the plates before and after welding and welding with additional heating were measured by means of the digital image correlation method. The microstructure of the weld metal, the heat affected zone of the weld (HAZ-welding), the base metal and the heated area beneath the burners (HAZ-welding with additional heating) were studied at a cross section perpendicular to the weld and in the middle of the plate for all materials. Residual stress measurements were performed on AISI-316L and DP600 steel plates by means of neutron diffraction (ND) at the Paul Scherrer Institute. At the Laboratoire Leon Brillouin, the residual stress profiles of AH36 plates were also measured by ND.

It was found from the experiments that transient thermal tensioning using the burners applied in this study cannot reduce welding distortion (with the materials and experimental conditions employed in this study), while side heating can successfully reduce out-of-plane deformation for the selected materials. In order to apply transient thermal tensioning, the heating source should be localized, for example by laser heating. In side heating, for all of the materials studied, it was found that the closer the burners were to the weld centre line the higher deformation obtained. Moreover, the trend in distortion as a function of the burner positions (leading, parallel or trailing) relative to the welding torch was non-linear. The results of distortion measurements indicated that the distortion of the plates is less sensitive to this parameter.

Experiments showed that side heating temperatures in the range of 200-400 ^{o}C, defined at the underside of the plate, can reduce deformations for all materials. Higher temperatures cause severe plastic deformation and with lower temperatures no visible change will occur. The best temperature for welding with additional heating depends on many factors such as the position of the burners, the thermal and the mechanical material properties, the clamping system around the weld, the area heated by the burners, the geometry of the plate, the welding process and so on. It was seen that for all materials, the thermal field around the welds is not changed by additional heaters.

The introduction of the additional heat by the burners is limited. Although at the top surface of the plate, higher temperatures are obtained. This causes minor changes in

microstructure and mechanical properties. For example, the areas beneath the burners in DP600 showed a lower micro-hardness than the base metal. For AH36 steel plate, the top surface of the heated areas beneath the burners showed a re-crystallized microstructure, while the microstructure of the underside surface is not affected.

It was seen that the maximum tensile residual stresses in the HAZ (of welding) for both the conventionally welded plates and AISI-316L plates welded with side heating were similar. This was also true for the maximum compressive stresses. Welding with side heating induces tensile stresses beneath the burner positions in the order of 200 MPa. For DP600, the maximum tensile stresses at the weld and HAZ (of welding) for conventional welds and welds with side heating were again similar and there was tensile stress peaks at the areas beneath the burners. In the region beneath and close to the burners, compressive residual stresses are reduced in welding with side heating compared with those of conventional welding of AH36. However, the tensile stress peak was not observed in AH36.

Finite element models were constructed to simulate and investigate the thermal, the microstructural and the mechanical fields in both conventional welding and welding with additional heating (both for side heating and transient thermal tensioning). The assumptions made in the high temperature material properties, plastic strain resetting, modelling of clamps and the additional heaters resulted in some discrepancies between the models and the measurements.

For the conventional welding process, close matches between the temperature, residual stress and distortion measurements and the numerical predictions were observed. The main sources of deviation in the thermal modelling of both conventional welding and welding with side heating are related to the thermal material data at elevated temperature and the heat transfer coefficients. The essential feature of the welding with side heating is the creation of a temperature peak at the location of the burners. The temperature distribution in the weld zone and the HAZ (of welding) remains unchanged.

The effect of phase transformations on residual stress and distortion was studied only for DP600. The phase fractions were validated. Although, the predicted phase fractions were in an acceptable range compared to the experiments, it was found that the model with solid state phase transformations predicts an out-of-plane deformation 9% lower than the model excluding the effects of the transformations and closer to the measured values. However, the risk of computational instability and divergence is high when phase transformations are included; therefore for other cases, the microstructural field was ignored.

The out-of-plane deformation of the workpiece after conventional welding and welding with side heating was predicted and the distributions were quantified using different criteria: i) a distortion index, ii) an out-of-plane deformation contour and iii) a scan

along a line perpendicular to the weld centre line. For all materials the predictions of conventional welding are in a good agreement with the experimental measurements.

The predicted residual stresses are close to the measured values for both conventionally welded plates and plates after side heating. The characteristic of side heating from a numerical point of view is the creation of tensile residual stresses at the location of the burners (even for AH36 steel, tensile peaks were observed in the numerical results for the regions beneath the burners).

The predictions of the numerical models developed in this study showed a good agreement with the experimental results and were used to study the mechanisms responsible for distortion reduction when additional heating (side heating or transient thermal tensioning) is used. The results of the simulations indicate that the responsible mechanism of distortion reduction for transient thermal tensioning using leading and parallel burners is the reduction of the transient compressive stresses along the weld centre line. In transient thermal tensioning using trailing burners, the responsible mechanism of distortion reduction is related to the increase of the transient tensile stresses along the weld centre line to the yield point and yielding of the weld metal during cooling. In side heating, it was found that the transient stresses along the weld centre line are not influenced by the stresses generated by the side heaters. The area with tensile residual stresses (at the position beneath the burners) tends to increase the strain required for out-of-plane deformation. The redistribution of final stresses (stresses formed due to the welding process in combination with the stresses formed due to the additional heating) reduce the final deformation of the plate. During side heating, there are three regions with tensile peaks, two more than in conventional welding. The total width of tensile stress regions is increased due to side heating and the critical buckling load will be larger than that of conventional welding. In other words, side heating reduces buckling deformation by increasing the critical buckling load and not by the reduction of compressive stresses.

The implementation of side heating during welding of large plates in the shipbuilding industry showed that side heating can significantly reduce welding distortion.

A.M.A.Pazooki, Apeldoorn, October 2014.

Samenvatting

Vervormingsbeperking tijdens lassen

Het plaatselijk uitzetten en krimpen van materiaal als het gevolg van lassen resulteert in permanente vervorming of instabiliteit, met andere woorden in lasvervormingen. Om vervorming te beheersen voor, tijdens of na het lassen zijn aanzienlijke onderzoeksinspanningen verricht. Thermal Tensioning (TT) is een groep van *in-situ* methoden om lasvervorming te beheersen. Bij deze methoden wordt tijdens het lassen plaatselijk aanvullende warmte of koude strategieën toegepast. Deze extra warmte of koude bronnen kunnen zowel op een statische als op een tijdsafhankelijke manier worden gemplementeerd. Bij statische methoden wordt het werkstuk onderworpen aan een bepaalde temperatuurverdeling, terwijl voor de tijdsafhankelijke (dynamische) methode de temperatuur afhangt van positie en tijd.

De mechanismen van vervormingsvermindering bij thermisch spannen/rekken zijn complex. De gecompliceerde aard van spannings- en rekvelden ten gevolge van lassen neemt toe door het grote aantal parameters dat betrokken is bij thermal tensioning. Het type, de intensiteit en de karakteristieken van de aanvullende warmte en/of koude bronnen spelen een belangrijke rol in de ontwikkeling van de spannings- en rekvelden tijdens het lassen. De positionering van deze aanvullende bronnen ten opzichte van de las en de lastoorts is tevens een kritische parameter bij het thermisch spannen/rekken. In dit onderzoek ligt de nadruk op de dynamische methode waarbij gebruik wordt gemaakt van warmtebronnen. Deze methode kan onderverdeeld worden in twee typen. Als de aanvullende warmtebronnen dicht bij de lastoorts geplaatst worden en bijdragen aan de temperatuurverdeling rond de las wordt het proces 'transient thermal tensioning' genoemd. Indien er geen invloed is op de temperatuurverdeling ten gevolge van de lasbron wordt het proces 'side heating' genoemd.

In het vervolg van deze samenvatting zal de Engelse benaming voor de processen gebruikt worden: 'transient thermal tensioning' en 'side heating'. In deze studie zijn het thermische, het microstructurele en het mechanische veld voor zowel conventioneel lassen als het lassen met aanvullende warmtebronnen onderzocht met behulp van numerieke modellen en experimenteel door middel van temperatuur-, spannings- en vervormingsmetingen en door microstructuur onderzoek. Het gebruik van zowel ex-

perimentele als numerieke methoden heeft een waardevolle bijdrage geleverd aan het inzicht ten aanzien van lassen met aanvullende warmtebronnen. Drie casussen zijn gedefinieerd voor de laboratoriumproeven (met verschillende materialen AISI-316L, DP600 en AH36 staal) en een casus is opgezet voor industriële implementatie (AH36 staal).

De lasparameters zijn zodanig gekozen dat goede lassen worden verkregen. De parameters van de aanvullende warmtebronnen zijn systematisch onderzocht. De condities waarbij de vervorming werd gereduceerd, wordt aangeduid als 'experimenteel behaalde minimale vervorming', en zijn in de verdere studie gebruikt voor het valideren van numerieke modellen.

Temperatuurmetingen aan de onderkant van de plaat zijn uitgevoerd door middel van thermokoppels voor de situatie met de 'experimenteel behaalde minimale vervorming' (voor de verschillende materialen) voor conventioneel lassen en het lassen met side heating. De vervorming uit-het-vlak van de platen voor en na het lassen en voor lassen met side heating is gemeten met behulp van de digitale beeldcorrelatie methode. De microstructuur van het lasmetaal, de warmtebenvloede zone van de las (WBZ-las), het basismetaal en het verwarmde oppervlak onder de branders (WBZ-side heating) is voor alle materialen bestudeerd aan een dwarsdoorsnede loodrecht op de las en in het midden van de plaat. Restspanningsmetingen zijn uitgevoerd aan AISI-316L en DP600 staalplaten met behulp van neutronendiffractie (ND) aan het Paul Scherrer Instituut te Villigen, Zwitserland. Aan het Laboratoire Leon Brillouin te Saclay, Frankrijk, zijn de restspanningsprofielen van gelaste AH36 platen gemeten door middel van ND. Uit de experimenten is gebleken, dat transient thermal tensioning voor de experimentele omstandigheden en materialen van dit onderzoek, lasvervorming niet kan reduceren, terwijl side heating voor de geselecteerde materialen wel een verlaging van de vervorming geeft. Om transient thermal tensioning succesvol te kunnen toepassen moet de warmte over een kleiner oppervlak worden ingebracht, door bijvoorbeeld een laser. Bij side heating werd voor alle materialen vastgesteld dat als de branders dichter bij de las worden geplaatst, de vervorming toeneemt. Tevens blijkt dat de trendmatige vervorming als functie van de afstand van de branders tot de lastoorts (voorafgaand, parallel of volgend) niet lineair is. De resultaten van de vervormingsmetingen laten zien dat de vervorming van de platen minder gevoelig is voor deze parameter.

Experimenten hebben aangetoond dat side heating aan de bovenzijde van de plaat waarbij aan de onderzijde temperaturen in het bereik van 200-400 ^{o}C worden bereikt de vervorming voor alle gebruikte materialen kan reduceren. Hogere temperaturen resulteren in ernstige plastische vervorming en bij lagere temperatuur treden geen zichtbare veranderingen op. De optimale temperatuur voor het lassen met side heating hangt van vele factoren af zoals de positie van de branders, de thermische en mechanische materiaaleigenschappen, de kleminrichting rond de las, het oppervlak dat door de branders verwarmd wordt, de geometrie van de plaat, het lasproces, en-

zovoort. Het is vastgesteld dat bij het toepassen van side heating het thermische veld rond de las niet merkbaar verandert.

De introductie van extra warmte door de branders is beperkt. Hoewel het bovenoppervlak van de plaat een hogere temperatuur bereikt, veroorzaakt dit slechts kleine veranderingen in de microstructuur en de mechanische eigenschappen. Voor DP600 heeft de zone onder de branders een lagere hardheid dan het basismateriaal. Bij AH36 treedt rekristallisatie op aan het oppervlak onder de branders, terwijl aan de onderkant van de plaat de microstructuur niet merkbaar wordt beïnvloed.

Er is geen verschil geconstateerd in de grootte van de maximale residule trekspanning in de WBZ van de las tussen conventioneel gelast AISI-316L platen en platen gelast met side heating. Dit is ook het geval voor de maximale drukspanningen. Lassen met side heating genereert trekspanningen op de locaties van de branders in de orde van grootte van 200 MPa. Voor DP600 zijn de maximale trekspanningen in de las en haar warmte benvloede zone voor conventioneel lassen en het lassen met side heating wederom gelijk en ontstaan pieken in het verloop van de trekspanning in de gebieden van de branders. In de regio van de branders worden in het geval van AH36 drukspanningen verlaagd als side heating wordt toegepast. De piek in de trekspanning wordt voor AH36 echter niet gemeten.

Eindige elementen modellen zijn geconstrueerd voor het simuleren en het onderzoeken van het thermische, het microstructurele en het mechanische veld voor conventioneel lassen en lassen met additionele warmtebronnen (zowel side heating als transient thermal tensioning). De aannamen ten aanzien van de materiaaleigenschappen op verhoogde temperatuur, het resetten van de plastische rek, het modelleren van de kleminrichting en additionele warmtebronnen resulteerde in enige afwijking tussen de resultaten van modellen en metingen.

Voor het conventionele lasproces is een goede overeenkomst waargenomen tussen de temperatuur-, de restspanning- en de vervormingsmetingen en de numerieke voorspellingen. De belangrijkste bron van afwijking in het modelleren van het thermische veld voor conventioneel lassen en het lassen met side heating is gerelateerd aan de data van de thermische materiaaleigenschappen op verhoogde temperatuur en de warmteoverdracht coëfficiënten. Een essentieel kenmerk van lassen met side heating is het creëren van een temperatuurpiek op de locatie van de branders, terwijl de temperatuurverdeling in de zone van de las en de warmte benvloede zone van de las niet merkbaar verandert.

Het effect van fasetransformaties op de restspanningen en vervorming is alleen onderzocht voor DP600. De fracties van de aanwezige fasen zijn gevalideerd. Hoewel de voorspelde fracties van de fasen in een acceptabele range in vergelijking tot de metingen liggen, voorspellen de modellen de vervorming uit het vlak 9% lager dan de modellen die het de transformaties niet meenemen. Deze metingen liggen dan ook

dichter bij de gemeten waarden. Het risico van numerieke instabiliteit en divergentie is groot als fasetransformaties in de modellen worden opgenomen; daarom is voor de andere casussen het microstructurele veld genegeerd.

De uit-het-vlak vervorming van het werkstuk na conventioneel lassen en lassen met side heating is berekend en de mate van vervorming is gekwantificeerd met behulp van verschillende criteria: *i)* een vervormingsindex, *ii)* een uit-het-vlak vervormingscontour en *iii)* een scan over een lijn loodrecht op de centrale lijn van de las. Voor alle materialen zijn de voorspellingen in goede overeenstemming met de metingen.

De voorspelde restspanningen liggen in de buurt van de gemeten waarden voor zowel de conventioneel gelaste platen als de lassen waarbij gebruik is gemaakt van side heating. Het karakteristieke van side heating vanuit een numeriek standpunt is het creëren van residuele trekspanningen op de locatie van de branders (zelfs voor AH36 staal worden trekspanningen waargenomen in de numerieke resultaten in de regio onder de branders).

De voorspellingen van de in deze studie ontwikkelde numerieke modellen toonde een goede overeenkomst met de gemeten resultaten en werden gebruikt om de mechanismen verantwoordelijk voor vervormings vermindering bij het gebruik van aanvullende verwarming (side heating of transient thermal tensioning) te bestuderen. Uit de resultaten van de simulaties blijkt dat het mechanisme verantwoordelijk voor de reductie in vervorming voor transint thermal tensioning met leidende en parallele branders de vermindering van de transinte drukspanningen langs de hartlijn van de lasnaad is. In transient thermal tensioning met volgende branders, is het mechanisme voor vervormingsvermindering gerelateerd aan de verhoging van de trekspanningen langs de lasnaad tot de vloeigrens en het deformeren van het lasmetaal tijdens afkoelen. Bij side heating, bleek dat de transiënte spanningen langs de lasmiddellijn niet benvloed worden door de spanningen die door de aanvullende verwarming wordt gentroduceerd. Het gebied met residuele trekspanningen (ter plaatse onder de branders) neigt de rek die nodig is voor deformatie uit-het-vlak van het werkstuk te verhogen. De herverdeling van spanningen (spanning ten gevolge van het lasproces in combinatie met de spanningen ontstaan door side heating) vermindert de uiteindelijke vervorming van de plaat. Tijdens lassen met side heating ontstaan drie gebieden met een piek in de trekspanning, twee meer in vergelijking tot conventioneel lassen. De totale breedte van de trekspanningsgebieden neemt toe door side heating en de kritische kniklast is groter ten opzichte van die bij conventioneel lassen. Met andere woorden, side heating vermindert knikvervorming door het verhogen van de kritische knikbelasting en niet door de reductie van drukspanningen. Implementatie van side heating tijdens het lassen van grote platen in de scheepsbouw heeft aangetoond dat side heating vervorming ten gevolge van lassen aanzienlijk kan reduceren.

A.M.A.Pazooki, Apeldoorn, Oktober 2014.

Acknowledgements

The last few years, I have enjoyed every moment of my time during my PhD research and there are a lot of great people who I would like to thank. First and foremost, I would like to express my sincere gratitude to my daily supervisor Dr.ir M.J.M. Hermans for his guidance, advises and supports. I would like to extend my thanks to my promoter Prof.Dr. I.M. Richardson for providing me the opportunity to work on my thesis in his group. I have learned a lot from him, especially clear scientific writing. It was a great pleasure to work with both Marcel and Ian.

Many thanks go to all of my colleagues of the former Joining and Mechanical Behavior group (JMB); Anneke van Veen, I would like to explicitly express my great appreciation to your supports and wishes. Special thanks also go to Frans Bosman and Jurriaan van Slingerland without whom my experiments never worked.

My sincere thanks are due to my neutron diffraction measurement team conducting experiments at LLB and PSI: Dr.ir. Marcel Hermans, Dr. Murugaiyan Amirthalingam, Rangan Kaushik Dutta, and He Gao.

I would like to thank the industrial partners of the project for their interest and their collaborations. Special thanks go to Dr.ir. Ellen van der Aa for her supports and constructive comments especially on numerical modelling of welds. I thank M2i for the financial support for the project.

I extend my thanks to my friends in the Netherlands for their supports during my stay in Delft. I will never forget the joyful times being together.

Not in the last place, I would love to express my deepest gratitude to my family. Dear Mom and Dad, I am very grateful for all your love, support, encouragement and patience. I would also like to express my gratitude to my parents-in-law for their care, concern and encouragement. I am particularly thankful to my lovely wife, Maryam, for her understanding and supports.

Yours,
A.M.A.Pazooki, Apeldoorn, October 2014.